

7TH INTERNATIONAL CONFERENCE
ON ADDITIVE TECHNOLOGIES - iCAT 2018

Proceedings

Maribor, Slovenia
10. - 11. October 2018

Editors:
Igor Drstvenšek,
Dietmar Drummer,
Nataša Ihan Hren and
Nicolae Balci.

 www.icat.si



Title:	7th International Conference on Additive Technologies iCAT 2018
Type:	<i>Proceedings of 7th International Conference on Additive Technologies</i>
Editors:	Igor Drstvenšek <i>(University of Maribor, Faculty of Mechanical Engineering, Slovenia)</i> Dietmar Drummer <i>(Institute of Polymer Technology (LKT), Friedrich-Alexander-Universität Erlangen-Nürnberg, Germany)</i> Nataša Ihan Hren <i>(Department for Oral and Maxillofacial Surgery, University clinical Centre, Ljubljana)</i> Nicolae Balc <i>(Department of Manufacturing Engineering, Technical University of Cluj Napoca, Romania)</i>
Layout & Design:	Dušan Pogačar
Publisher:	Interesansa - zavod, Ljubljana
Impression:	Digital edition
Year of publishing:	2018

Disclaimer:

The Organizing Committee of 7th International Conference on Additive Technologies – iCAT2018 accepts no responsibility for errors or omissions in the papers. The Organizing Committee shall not be liable for any damage caused by error or omissions in published papers.

All rights reserved.

This publication may not be reproduced in whole or in part, stored in retrieval system or transmitted in any form or by any means without written permission of the Organizing Committee of 7th International Conference on Additive Technologies – iCAT 2018.

© 2018, The Organizing Committee of 7th International Conference on Additive Technologies – iCAT 2018
Publisher Interesansa - zavod, Ljubljana

CIP - Kataložni zapis o publikaciji
Univerzitetna knjižnica Maribor

621.9:681.5(082)

INTERNATIONAL Conference on Additive Technologies.
(7 ; 2018 ; Maribor)

Proceedings [Elektronski vir] / 7th International
Conference on Additive Technologies iCAT 2018, Maribor,
Slovenia, 10. - 11. October 2018 ; editors Igor Drstvenšek ...
et al. - Digital ed. - Ljubljana : Interesansa-zavod, 2018

Sistemske zahteve: bralnik za format PDF
Način dostopa (URL): <http://www.icat.si/icat2018/icat2018proceedings.pdf>. - El. publikacija v PDF formatu.

ISBN 978-961-288-790-2 (pdf)
1. Drstvenšek, Igor
COBISS.SI-ID 95317761

Table of Contents

I. Organisers	07
II. Committees	08
III. List of Authors	10
IV. Foreword: Aiming at knowledge dissemination	11
V. Invited Speakers	13

PAPERS BY CATEGORY

1. MEDICAL APPLICATIONS OF ADDITIVE MANUFACTURING
2. AM PROCESS - METALS
3. CAE AND TESTING
4. EDUCATION AND ARTS & DESIGN
5. AM PROCESS - POLYMERS

1. MEDICAL APPLICATIONS OF ADDITIVE MANUFACTURING

Helena Barbara Zobec Logar, Robert Hudej	22
INDIVIDUAL APPLICATORS FOR BRACHYTHERAPY OF GYNECOLOGICAL CANCERS	
Snehashis Pal, Gorazd Lojen, Vanja Kokol, Igor Drstvensek	26
MELTING CHARACTERISTICS IN SELECTIVE LASER MELTING OF TI-6AL-4V PRODUCT FOR BIOMEDICAL APPLICATION	
Amir Mahyar Khorasani, Ian Gibson, Moshe Goldberg, Guy Littlefair	40
THE EFFECT OF MACHINING AND HEAT TREATMENT ON CUTTING FORCES OF SLM MEDICAL COMPONENT	
Ioan Alexandru Popan, Nicolae Balc, Alina Ioana Popan	48
STUDY ON MANUFACTURING IMPLANTS OF BIOCOMPOSITE MATERIALS BY WATER JET CUTTING	
Ioan Turcin, Cosmin Cosma, Ali Abdallah, Nicolae Balc	51
DESIGN FOR ADDITIVE MANUFACTURING OF A SWEAT GLAND SIMULATOR	

2. AM PROCESS - METALS

Igor Shishkovsky, Pavel Peretyagin	58
ELECTRON BEAM MELTING OF TI6AL4V ALLOY: THIN-WALL SAMPLES FABRICATION, MICROSTRUCTURE, AND PROPERTIES EVALUATION	
Igor Shishkovsky, Vladimir Sherbakoff	62
INFLUENCE OF ADDITIONAL HEATING ON PHASE STRUCTURE AND RESISTIVITY OF INTERMETALLIC SMA MANUFACTURED BY PBF PROCESS	
Andreas Wimmer, Christian Zeller, Fabian Bayerlein, Dominik Scherer, Michael F. Zaeh, Pierre Forêt and Jürgen Scholz	66
INFLUENCE OF THE PROCESS GAS ON THE LASER BEAM MELTING PROCESS	
Max Horna, Georg Schlicka, Felix Wegnera, Christian Seidela, Christine Anstaetta, Gunther Reinharta	71
DEFECT FORMATION AND INFLUENCE ON METALLURGICAL STRUCTURE DUE	
Tobias Schwanekamp, Martin Reuber	78
PARAMETER STUDY ON LASER BEAM MELTING OF WC-Co AT 800°C PRE-HEATING TEMPERATURE	

Platt, Sebastian; Wegner, Jan; Kleszczynski, Stefan; Witt, Gerd	85
EFFECT OF SCAN STRATEGY, RE-MELTING AND EXPOSURE TIME ON THE MICROSTRUCTURE OF STAINLESS STEEL 17 - 4 PH FABRICATED BY LASER POWDER BED FUSION OF METALS	
Massimo Lorusso, Diego Manfredi, Flaviana Calignano, Marco Actis Grande	92
NANO- MICRO- MACRO- HARDNESS OF LPBF 316L AUSTENITIC STAINLESS STEEL	

3. CAE AND TESTING

Marius Rimašauskas, Tomas Kuncius	98
TENSILE TESTING OF 3D PRINTED CONTINUOUS CARBON FIBRE-REINFORCED PLA COMPOSITES	
D. Hübner, M. R. Gotterbarm, A. Kergaßner, J. Köpf, C. Pobel, M. Markl, J. Mergheim, P. Steinmann, C. Körner, M. Stingl	102
TOPOLOGY OPTIMIZATION IN ADDITIVE MANUFACTURING CONSIDERING THE GRAIN STRUCTURE OF INCONEL 718 USING NUMERICAL HOMOGENIZATION	
D. Hübner, M. Stingl	112
ON A COMBINED GEOMETRY AND MULTIMATERIAL OPTIMIZATION APPROACH FOR THE DESIGN OF FRAME STRUCTURES IN THE CONTEXT OF ADDITIVE MANUFACTURING	
Luca Kotroczy, Péter Bakonyi	120
THE EXAMINATION OF PHOTOPOLYMER-BASED 3D PRINTED PRODUCTS IN THE CASE OF PINPOINT LOADING	

4. EDUCATION AND ARTS & DESIGN

Stefan Junk	126
IMPLEMENTATION OF INTERDISCIPLINARY STUDENT TEAMS IN DESIGN EDUCATION FOR ADDITIVE MANUFACTURING	
Tanja Nuša Kočevar, Aja Knific Košir, Eva Razložnik, Luka Dakskobler, Matej Pivar, Marjeta Čuk, Deja Muck, Helena Gabrijelčič Tomc	131
3D INTERPRETATION OF SNEŽNIK CASTLE AND ITS SURROUNDINGS IN A FORM OF A SCALE MODEL	

Bernhard Heiden, Ulrich Leitner	136
ADDITIVE MANUFACTURING – A SYSTEM THEORETIC APPROACH	
Havenga, S.P., De Beer, D.J., Van Tonder, P.J.M., Campbell, R. I., Van Schalkwyk, F.	140
DEVELOPMENT OF AN ADDITIVE MANUFACTURING EDUCATION AND TRAINING STRATEGY FOR SOUTH AFRICA, USING THE I2P LAB CONCEPT	

5. AM PROCESS - POLYMERS

J.S. Gómez Bonilla, A. Chiappina, M.A. Dechet, J. Schmidt, A. Bück, K.-E. Wirth, W. Peukert	149
THERMAL ROUNDING OF PARTICLES IN A DOWNER REACTOR: DIRECT VS. INDIRECT HEATING (MANUFACTURING AND CHARACTERIZATION)	
Sandra Greiner, Lydia Lanzl, Meng Zhao, Katrin Wudy, Dietmar Drummer	153
INFLUENCE OF POWDER BED SURFACE ON PART PROPERTIES PRODUCED BY SELECTIVE LASER BEAM MELTING OF POLYMERS	
Lydia Lanzl, Sandra Greiner, Katrin Wudy, Dietmar Drummer	162
GLASS-FILLED POLYPROPYLENE-SYSTEMS FOR ENHANCING REPRODUCIBILITY DURING SELECTIVE LASER BEAM MELTING AND EFFECT OF THE MIXING STRATEGY ON POWDER PROPERTIES	
Maximilian A. Dechet, Juan S. Gómez Bonilla, Jochen Schmidt, Andreas Bück, Wolfgang Peukert	168
SPHERICAL BLEND PBT-PC PARTICLES FOR SELECTIVE LASER SINTERING MANUFACTURING AND CHARACTERIZATION	
T. Antunes, S. P. Magalhães da Silva, M. E. V. Costa, J. M. Oliveira	173
CORK-BASED FILAMENTS FOR ADDITIVE MANUFACTURING THE USE OF CORK POWDER RESIDUES FROM STOPPERS INDUSTRY	

I. Organisers

Rapid Prototyping and Innovative
Manufacturing Network



University of Maribor, Faculty of Mechanical
Engineering - Department of Production Engineering



University of Ljubljana, Medical Faculty, Department of
Maxillofacial and Oral Surgery



Collaborative Research Center 814 –
Additive Manufacturing



II. Committees

MEMBERS OF THE ORGANIZING COMMITTEE

Drstvenšek, Igor (President, SI)
Ihan Hren, Nataša (President, SI)
Balc, Nicolae (President, RO)
Drummer, Dietmar (President, DE)
Brajlih, Tomaž (SI)
Campbell, Ian (UK)

Kostevšek, Urška (SI)
Lazarescu, Lucian (RO)
Leordean, Dan (RO)
Pogačar, Dušan (SI)
Schmidt, Michael (DE)

iCAT REVIEW COMMITTEE FOR 2018

Abdel Ghany, Khalid (EG)
Balc, Nicolae (RO)
Bartolo, Paulo (PT)
Brajlih Tomaz (SI)
Campbell, Ian (UK)
Cardoon, Ludwig (NL)
DeBeer, Deon (RSA)
Dolinsek, Slavko (SI)
Drstvenšek, Igor (SI)
Fabio Miani (ITA)
Gibson, Ian (SGP)
Godec, Damir (HR)
Gonzales, David (ES)
Hagiwara, Tsuneo (J)
Harl, Bostjan (SI)
Hudak, Radovan (SVK)

Iuliano, Luca (IT)
Jay, Olivier (DEN)
Kegl, Marko (SI)
Legutko, Stanislaw (POL)
Levy, Gideon (CH)
Mehrle, Andreas (AUT)
Moraca, Slobodan (SRB)
Predan, Jozef (SI)
Rahmati, Sadegh (IRN)
Rännar, Lars-Erik (SVE)
Schmid, Manfred (SUI)
Smurov, Igor (FR)
Traussnigg, Udo (AUT)
Truscott, Michelle (RSA)
van der Walt, Kobus (RSA)

iCAT SCIENTIFIC AND PROGRAMME COMMITTEE FOR 2018

Abdel Ghany, Khalid (EG)	Hadzistevic, Miodrag (SRB)	Reinhardt, Andrea (DE)
Agarwal, Mukesh (IND)	Hagiwara, Tsuneo (J)	Rotaru, Horatiu (RO)
Avellan, Lars (S)	Homa, Johannes (AUT)	Schaefer, Martin (DE)
Balc, Nicolae (RO)	Hudak, Radovan (SK)	Schermer, Scott (USA)
Balic, Joze (SI)	Ihan Hren, Natasa (SI)	Schindel, Ralf (CH)
Bartolo, Paulo (PT)	Iuliano, Luca (IT)	Schmidt, Michael (DE)
Bernard, Alain (FR)	Janse van Vuuren, Michaela (SAR)	Schwartz, Dieter (DE)
Bertrand, Phillippe (FR)	Jay, Olivier (DEN)	Sinkovic, Andreja (SI)
Bjork, Lennart (S)	Junghanss, Michael (D)	Smurov, Igor (FR)
Campbell, Ian (UK)	Katalinic, Branko (AUT)	Stamenkovic, Dragoslav (SRB)
Cardoon, Ludwig (NL)	Kosica, Olga (SLO)	Strojnik, Tadej (SI)
Cus, Franci (SI)	Kostal, Peter (SK)	Sercer, Mladen (HR)
Dean, Lionel T (UK)	Kramberger, Slavko (SI)	Tetsuzo, Igata (J)
DeBeer, Deon (RSA)	Krenicky, Tibor (SK)	Tomazic, Tomaz (SI)
Dickens, Philip (UK)	Kruff, Walter (NL)	Tromans, Graham (UK)
Dolinsek, Slavko (SI)	Kyttanen, Janne (FI)	Tuomi, Jukka (FI)
Drstvenšek, Igor (SI)	Levy, Gideon (CH)	Velisek, Karol (SVK)
Drummer, Dietmar (DE)	Malisa, Viktorio (AT)	Wimpenny, David (UK)
Dybala, Bogdan (PL)	Mateazzi, Paolo (IT)	Wang, Xiaohong (PRC)
Frost, Noel (AUS)	Murphy, Michael (IRL)	Wong, Martin (HKG)
Fuzir, Bauer Gabrijela (SI)	Ohigashi, Norihito (J)	Wood, Duncan (UK)
Gerrits, Anton (NL)	Ostojic, Gordana (SRB)	Yan, Yongnian (PRC)
Gibson, Ian (SGP)	Pogacar, Vojko (SI)	Yang, Dong-Yol (KOR)
Godec, Damir (HR)	Porter, Ken (AUS)	Yeung, Millan (CDN)
Gonzales, David (ES)	Poukens, Jules (NL)	Zhang, Qiqing (PRC)
Grzesiak, Andrzej (D)	Preez, Willie, du (RSA)	
Grzic, Renata (HR)	Pritrznik, Lidija (SLO)	
Haas, Franz (AUT)	R. Vulicevic, Zoran (SRB)	

III. List of Authors

Abdallah, Ali	Heiden, Bernhard	Pobel, C.
Anstaetta, Christine	Horna, Max	Popan, Alina Ioana
Antunes, T.	Hübner, D.	Popan, Ioan Alexandru
Bakonyi, Péter	Hudej, Robert	Razložnik, Eva
Balc, Nicolae	Jan, Wegner	Reinharta, Gunther
Bayerlein, Fabian	Junk, Stefan	Reuber, Martin
Bück, A.	Kergaßner, A.	Rimašauskas, Marius
Bück, Andreas	Knific Košir, Aja	Scherer, Dominik
Calignano, Flaviana	Kočevár, Tanja Nuša	Schlicka, Georg
Campbell, R. I.	Kokol, Vanja	Schmidt, Jochen
Chiappina, A.	Köpf, J.	Scholz, Jürgen
Cosma, Cosmin	Körner, C.	Schwanekamp, Tobias
Costa, M. E. V.	Kotrocz, Luca	Sebastian, Platt
Čuk, Marjeta	Kuncius, Tomas	Seidela, Christian
Dakskobler, Luka	Lanzl, Lydia	Sherbakoff, Vladimir
De Beer, D.J.	Leitner, Ulrich	Shishkovsky, Igor
Dechet, M.A.	Littlefair, Guy	Stefan, Kleszczynski
Dechet, Maximilian A.	Lojen, Gorazd	Steinmann, P.
Drstvenšek, Igor	Lorusso, Massimo	Stingl, M.
Drummer, Dietmar	Magalhães da Silva, S. P.	Turcin, Ioan
Forêt, Pierre	Mahyar Khorasani, Amir	Van Schalkwyk, F.
Gabrijelčič Tomc, Helena	Manfredi, Diego	Van Tonder, P.J.M.
Gerd, Witt	Markl, M.	Wegnera, Felix
Gibson, Ian	Mergheim, J.	Wimmer, Andreas
Goldberg, Moshe	Muck, Deja	Wirth, K.-E.
Gómez Bonilla, J.S.	Oliveira, J. M.	Wudy, Katrin
Gómez Bonilla, Juan S.	Pal, Snehashis	Zaeh, Michael F.
Gotterbarm, M. R.	Peretyagin, Pavel	Zeller, Christian
Grande, Marco Actis	Peukert, W.	Zhao, Meng
Greiner, Sandra	Peukert, Wolfgang	Zobec Logar, Helena Barbara
Havenga, S.P.	Pivar, Matej	

IV. Foreword

IGOR DRSTVENŠEK

Aiming at knowledge dissemination

In the last 20 years communities like RAPDASA¹, FIRPA², RAPIMAN³ and others mainly grouped into GARPA⁴, struggled to move the use of Additive Manufacturing onto a higher, predominantly industrial level. Nowadays this role has been taken over by more commercially oriented networks that are making impact in the public awareness about the additive technologies. This awareness also reflects in the response of the mainstream and even the yellow-press media providing some promotion of the new technologies. The promotive messages are mainly positive with some annoying exceptions, like questions about printed guns and printed people... But, whatever the message is it triggers some new ideas that push the industry forward.

Early industrial adopters of AM were mainly companies that have seen its potential in their development departments but some of them also tried them in production of low series parts. In the last 5 years we are witnessing a huge growth of interest for the new technologies, especially in so-called metal 3D printing. Thus we have been seeing spare parts but also some serially made products entering the market directly from AM machines. Some new start-ups have been founded, mainly in medical area that have seen their possibilities in providing bespoke parts to their potential customers. AM also became a popular keyword in different research and development tender calls released by national agencies worldwide. These range from pure technologically to more socially oriented pointing out that the community is well aware of the potential impact these technologies

1 Rapid Product Development Association fo South Africa
2 Finish Rapid Prototyping Association
3 Rapid Prototyping and Innovative Manufacturing Network
4 Global Alliance of Rapid Prototyping Associations

will have to our future. These calls have a positive impact because they enable the big industrial partners to try the new technologies without a big risk, provide the financial support for R&D and also enable the start-ups to move over the turbulent times...

What surprises in this fast developing industrial field is that the producers of »AM machine tools« struggling to catch up with the industrial development pace. We are still witnessing the commercial approach that is typical for dealing with academia and their research labs. Instead of providing the productivity, reliability and maintainability data the companies handing over the same old maintenance plans where the mean time to repair (MTTR) is measured in days instead of minutes, where the accuracy requires building the part twice to reach the standard and where the material management is not an issue as long as it provides income to the providers of the machines.

All these reflects in the papers collected in this proceedings of the 2018 International Conference on Additive Technologies (iCAT). The research interest in the last 14 years since the RAPIMAN has been established moved from applicability of technologies to the conditions of their acceptability. The authors are dealing with different technological aspects ranging from material science to specific behaviour of technology in different working conditions. Some typical properties of Additive Manufacturing are becoming obvious as the technology has been explored in more details. Dependence of productivity and accuracy on the shape complexity of parts is certainly one of these typical properties that differ from other production technologies and that help us improve the reliability of the AM machine tools if taken into account...

Taking all the new knowledge into account is the task of AM machine producers and users of these technologies. The task of the academics and all the research community is to make them aware of this knowledge by providing forums and disseminating the knowledge in other ways. The iCAT is aimed to gather industrial users and users in medical institutions with the researchers from AM field to push the limits of AM usability and the barrier of its acceptability forward.

With the speakers that honoured us with their presence in all these years I am sure that iCAT is still on the right track providing some applicable guidelines to the industry based on scientific results.

Igor Drstvenšek

V. Invited Speakers

Christian Fang / Hong Cai / Andrej Moličnik / Miha Verdenik / Helena Barbara Zobec Logar / Matjaž Merc / Ismo Mäkelä / Luka Prodnik / Boštjan Vihar / Deon de Beer



Christian Fang

Department of Orthopaedics and
Traumatology, Queen Mary Hospital, The
University of Hong Kong

Experience in using free software for cost effective clinical 3D printing - the Hong Kong experience

The use of 3D printing technology in the clinical management of disease conditions is rapidly gaining popularity. Yet, best practices remain to be defined and validation studies are lacking.

As industry standard commercialised software may not be affordable for all clinics, it is of interest to explore advantages and drawbacks of more cost-effective alternative means in conducting the clinical 3D printing workflow.



Hong Cai

Orthopaedic Department, Peking University, Third Hospital Beijing, China

Application of Metal 3D Printing in Orthopaedics – Current Status in China

Due to the features of 3D printing that are particularly suitable for the field of orthopaedics, more and more innovative medical devices have been developed based on metal 3D printing.

The CFDA has continuously approved the listing of multiple metal 3D printing implants, but this is only the beginning. 3D printing is showing great potential in the treatment of certain special diseases, such as a bone tumour, huge bone defect. As research progresses and customized regulations are being developed, patient-customized implants will bring new therapeutic concepts.



Andrej Moličnik

Orthopaedic department, University Clinical Centre Maribor, Slovenia

The use of Patient Specific Instruments in Clinical Praxis

Revision hip arthroplasty presents a huge challenge in front of the surgeon because of the defects caused by the loose acetabular component. Using modern 3D planning techniques combined with additively manufactured patient-specific instruments and implants surgical problems can be foreseen and surgical outcome predicted.

A process of 3D planning of replacement of an acetabular component will be presented on a case of a defect with a huge bone loss estimated at level IIIa according to Paprosky. The planning was based on CT scans of the affected area and performed in interdisciplinary cooperation among surgeons and mechanical engineers. This cooperation combined surgical experiences and knowledge of surgeons with knowledge of engineers in using 3D design tools and mechanical calculation. The cooperation resulted in a virtual 3D plan and 3D printed communication models and implants that enabled flawless communication among the team members and predictable outcome of the surgery.



Miha Verdenik

Department of Maxillofacial and Oral
Surgery Medical Faculty Ljubljana,
Slovenia

The 3D imaging as clinical and research tool in the patient with dentofacial deformities

Dentofacial deformities are severe skeletal changes of the face which are connected with the functional and esthetic problems. They are corrected with surgical procedures known as orthognathic surgery. The classical 2D diagnostic procedures are more and more replaced with 3D methods.

They became also a strong tool in the treatment planning (simulation), with virtual patient becoming a reality. With merging cone beam CT, 3D facial and intraoral scan we are able to create virtual (digital) patient with all possibilities to make exact diagnosis and treatment plan. To transfer this plan to real world we need different templates, custom implants, etc. At this point, the process can be completed with additive technologies, which offers a new possibilities and some advantages over traditional methods. In addition to clinical usefulness of the 3D methods they have also a big role in research area. The cross-sectional studies on normal population and populations with different dental and skeletal deformities, evaluation of different surgical techniques are more and more based on 3D method, such as cone-beam CT and 3D photography. A lot of these studies are transferred to the clinical work at the end.



Helena Barbara Zobec Logar

Institute of Oncology Ljubljana, Ljubljana,
Slovenia

Individual Applicators for Brachytherapy of Gynecological Cancers

Application of additive manufacturing in medicine has the potential to significantly improve the clinical practice in MRI-based image-guided adaptive brachytherapy (IGABT). The standard applicators available on the market do not always enable an acceptable dose coverage of a tumour and sometimes do not fit the patient anatomy.

Additive manufacturing is an attractive new technology that offers many possibilities of adapting standard applicators and designing new ones. This paper represents two clinical cases with individually designed applicators for brachytherapy of gynaecological cancers. The results showed excellent coverage when using individual applicators.



Matjaž Merc

Orthopaedic department, University
Clinical Centre Maribor,
Slovenia

An Additively Manufactured multi-level drill guide template for pedicle screw placement in the lumbar and sacral spine

Pedicle screw placement using a freehand technique has a high incidence of pedicle perforation. The said risk can be reduced with intra-operative fluoroscopy or navigation, which have some disadvantages. A promising principle for solving most of the issues is the use of Additive Manufacturing technology.

It makes manufacturing of patient-specific drill guide templates possible that enable optimal pedicle screw placement. In the last decade, many studies have featured relatively successful implantations of pedicle screws through the use of drill guide templates, though mostly on cadavers. We performed a similar clinical study involving the manufacture of templates for the lumbar and sacral regions that enable simultaneous multiple-level screw implanting.



Ismo Mäkelä

DeskArtes Oy, Helsinki,
Finland

Data preparation for Additive Manufacturing

In his talk, Ismo will describe the use of DeskArtes software tools for data preparation for Additive Manufacturing. DeskArtes has been a pioneer for AM software development since 1993 and becoming the de-facto-standard software provider for 3D Color printing in mid-2000. Since then DeskArtes has expanded its software portfolio to include support generation tools for metal, stereolithography and DLP based AM systems. Currently, DeskArtes is also participating in EU H2020 “I AM RRI” project investigating Responsible Research and Innovation methods for AM.

Ismo graduated in 1989 from Helsinki University, majoring in computer sciences. After graduation he worked as a researcher at the Computer Science Laboratory of HUT (currently Aalto University), specializing in geometric modelling and computational geometry especially targeted for Additive Manufacturing. He joined DeskArtes 1996 to continue the development of special AM tools, becoming the product manager for the tools in 1998 and since 2001 he has been the managing director of the company. He is also a board member for the Finnish Rapid Prototyping Association, FIRPA.



Luka Prodnik

Department for Oral and Maxillofacial
Surgery, University clinical Centre,
Ljubljana

Virtual surgical planning of complex bony defects in maxillofacial surgery

The complex anatomy of maxillofacial skeleton increases the complexity of its reconstruction and presents a challenge when trying to achieve acceptable functional and aesthetic outcomes. Facial skeleton provides support for the soft tissues and is crucial in determining the shape of the face. That's why bony reconstruction has to be done as precisely as possible. To achieve this goal, the bony reconstruction has to be planned

Traditionally, reconstructive surgery in the maxillofacial region has relied on the surgeon's subjective assessment of form and aesthetics pre and intraoperatively, with intraoperative decision making based on experience. Important factors such as position and direction of the osteotomies, shape of the bone fragments and thus the shape of the face were unpredictable, and further rehabilitation (e.g. dental) of the patient hindered. In the last 10 years, the advent of virtual surgical planning has brought a large improvement in the precision, speed and predictability of the reconstructions, performed at the Department for Oral and Maxillofacial Surgery in University clinical Centre in Ljubljana. By presenting our clinical cases we will guide you through preoperative planning, virtual surgery, fabrication of cutting guides, and 3D models and show you how additive technologies meet medicine in practice with excellent results.



Boštjan Vihar

Institute IRNAS Rače,
Slovenia

Open-source 3D bioprinting for scientific and industrial applications

Tissue engineering and regenerative medicine have been developing rapidly over the last few years, and bioprinting as a supportive technology has also seen a lot of advances. The availability of 3D bioprinters has increased substantially, however, certain challenges still prevent successful fabrication of complex tissues and other applications.

Broad biocompatibility, controlled biodegradability, shape fidelity retention, etc. require advanced material formulations, which need highly customized fabrication strategies to be formed into complex shapes with high precision. This is something we wish to approach at Institute IRNAS, using open-source philosophy and collaborative design to create adaptive and future-proof solutions.



Deon de Beer

Central University of Technology,
Free State, SAR

South African AM Outlook - Latest results, developments and strategies

Additive Manufacturing (AM) in South Africa started with humble beginnings in the early 1990's. Whilst still developing an AM industry in the country, research and industry/research relationships, complemented by well-designed technology

transfer strategies, have developed into an interesting model for countries wishing to develop an AM industry, to follow.

Progress have been made with government funding models, backed by a national AM Strategy, which also impacted on trade and industry and industrial development policies and strategies. The presentation will highlight key successes, and discuss the results achieved in terms of successful development of an AM Ecosystem in SA.

CHAPTER 1.

Medical Applications of Additive Manufacturing

Individual Applicators for Brachytherapy of Gynecological Cancers

Helena Barbara Zobec Logar, Department of Radiotherapy, Institute of Oncology, Ljubljana, Slovenia,
hlogar@onko-i.si

Robert Hudej, Department of Radiophysics, Institute of Oncology, Ljubljana, Slovenia, rohudej@onko-i.si

Abstract—Application of additive manufacturing in medicine has the potential to significantly improve the clinical practice in MRI-based image-guided adaptive brachytherapy (IGABT). The standard applicators available on the market do not always enable an acceptable dose coverage of the tumor and sometimes do not fit the patient anatomy. Additive manufacturing is an attractive new technology that offers many possibilities of adapting standard applicators and designing new ones. This paper represents two clinical cases with individually designed applicators for brachytherapy of gynecological cancers. The results showed excellent tumor coverage when using individual applicators.

Keywords—gynecological cancer; additive manufacturing; SLS; individual applicator; multi-channel vaginal cylinder; brachytherapy; IGABT

1. INTRODUCTION

The principles of IGABT were introduced in brachytherapy at the beginning of the 21st century. The historical 2D approach based on X-ray imaging and applicator reconstruction without visualization of the tumor was changed with 3D magnetic resonance imaging (MRI)-based approach. The basis of concepts and terms in 3D image-based brachytherapy for cervix carcinoma was introduced by gynecological (GYN) GEC-ESTRO (The Groupe Européen de Curiethérapie-European society for radiotherapy and Oncology) working group in 2005 and 2006 [1, 2]. The recommendations for applicator reconstruction and MRI followed later on [3, 4]. With the introduction of the MRI the tumor and the organs at risk (OAR) could be clearly identified and accurately delineated. Available are commercially developed MRI-compatible applicators for cervical cancer that combine intracavitary (IC) and interstitial (IS) component [5, 6]. Consequently, the dose to the target is adapted to the shape of the tumor, taking into account the dose limits for the OAR. With such an approach an excellent local control

and improvement in overall survival of 10 % was reached while the side effects to the OAR were markedly reduced [7-10]. It has been proven that adding the IS component with inserting needles in the tumor is mandatory for the proper tumor target coverage in advanced cervical cancer [6-10]. Commercially available applicators offer only the possibility of inserting parallel needles, although oblique needles are sometimes needed to cover the target. For patients with large tumors and anatomy unsuitable for the applicator insertion, the individual solution has to be used [11, 12]. The additive manufacturing is a promising new method in brachytherapy for designing and production of individual applicators. It is fast and relatively cheap. It enables better needle guidance to predetermined locations in the tumor with consequently less trauma to the surrounding tissue.

2. APPLICATION OF ADDITIVE MANUFACTURING TECHNOLOGY IN CLINICAL PRACTICE

The same principles that were developed for MRI-based IGABT for cervical cancer can be used for other gynecological cancers as well. The tumor target volume for brachytherapy visible on the MRI is defined as the clinical target volume CTV-T_{HR} [13]. The dose prescribed to the CTV-T_{HR} is always balanced with the dose received to the OAR. The dose delivered to the CTV-T_{HR} is defined with the following parameters:

- D90 (D98)-the minimum dose delivered to 90% (98%) of the target volume
- V100-percentage of the volume covered with 100% isodose. This is an indirect measure of the proportion of the underdosed area of the target volume.

The OAR for gynecological brachytherapy are the organs in the proximity of the CTV-T_{HR} and brachytherapy sources.

They are usually:

- bladder
- rectum
- sigmoid
- bowel
- urethra
- vagina

The dose restrictions to the CTV-T_{HR} and the OAR are defined according to clinical evidence, taking into account our institutional practice and patient specific issues. Finally, all these factors culminate in a specific treatment plan which is highly individual for every patient. The planning-aim isodose level that encompasses the CTV-T_{HR} as much as possible is determined as 100% isodose level. It gives the visual information about conformity of single brachytherapy treatment.

The dose constraints to the OAR are usually defined in terms of the dose to the maximally exposed tissue volume of 2 cm³ indicating the most irradiated tissue volume adjacent to the applicator.

Two clinical cases where individual applicators were manufactured with selective laser sintering (SLS) technology are presented here. A biocompatible polyamide PA2200 material and Formiga P100 system were used.

2.1. Add-On for Cervical Cancer

A 52-year-old woman was diagnosed with advanced cervical cancer, histologically squamous cell carcinoma grade 2 (G2), stage IIIB. She was treated with external beam radiotherapy (EBRT) with concomitant cisplatin-based chemotherapy first in order to shrink the tumor at the time of brachytherapy. After EBRT 1st MRI-based brachytherapy was performed using standard Varian applicator with ring for parallel needles. It was obvious that the CTV-T_{HR} delineated on the MRI could not be properly covered with the 100% isodose (see Figure 1).

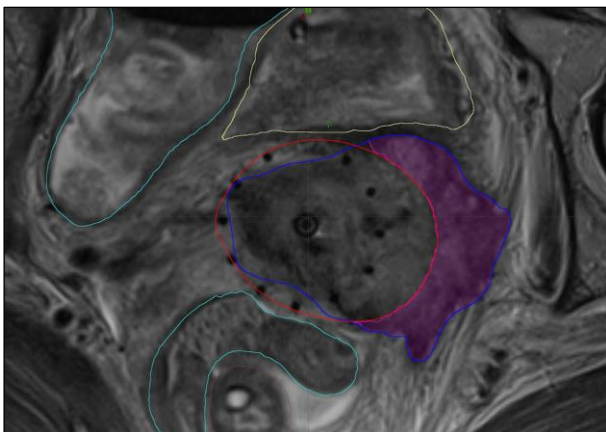


Figure 1. Schematic presentation of the underdosed CTV-T_{HR} tumor target area (purple colour) if a Varian ring applicator with parallel needles is used (100% isodose level in red). CTV-T_{HR} (blue), bladder (yellow), rectum (brown) and bowel (light blue) are delineated.

MRI served as the basis for designing the 3D-printed add-on for the ring which was shaped according to the CTV-T_{HR}, delineated on the MRI. To cover the target volume properly, four additional oblique needles were added to Varian ring applicator at different positions and angles (see Figure 2).

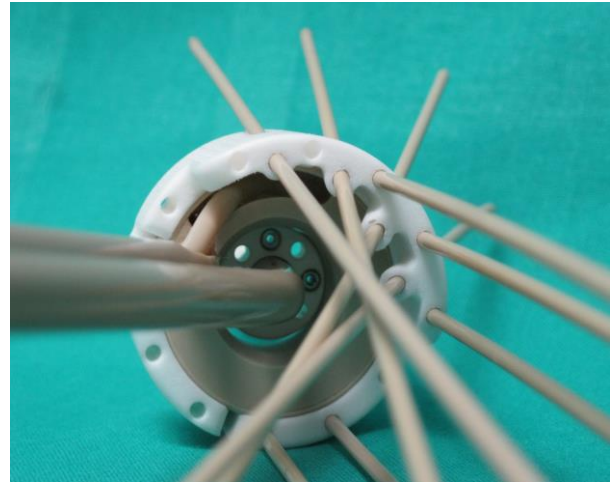


Figure 2. Add-on for the Varian ring applicator. Parallel and oblique needles are inserted through the add-on. Precise needle guidance is achieved.

The 2nd brachytherapy was performed with the Varian ring applicator with an individually designed add-on. Excellent target coverage was achieved (see Figure 3).

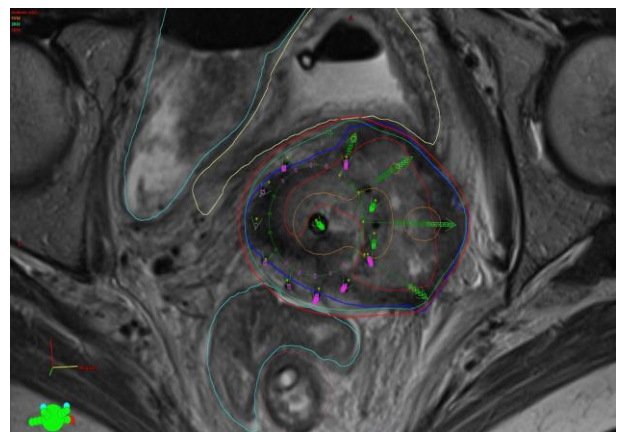


Figure 3. The CTV-T_{HR} (blue) is covered with 100% isodose (red) if the Varian ring applicator with individually designed add-on is used. The dose to the OAR is respected for the bladder (yellow), rectum (brown) and bowel (light blue). Four oblique needles are presented with green arrows.

2.2. Multi-Channel Vaginal Cylinder for Recurrent Endometrial Cancer

A 56-year-old woman was operated for endometrial cancer stage IB, G3. She was planned for post-operative EBRT. Before the radiation treatment started, the recurrent disease was histologically proved at two different sites of the vagina: at the vaginal cuff and above the external urethral orifice. She received EBRT first and finished her treatment with brachytherapy later. The 1st brachytherapy was performed with a Varian vaginal applicator, which was used as a template to design individual applicator multi-channel vaginal cylinder (see Figure 4). Exact needle positions were designed according to MRI-predetermined locations in the tumor. The 2nd brachytherapy was performed with a multi-channel vaginal cylinder using rectal ultrasound for needle guidance.

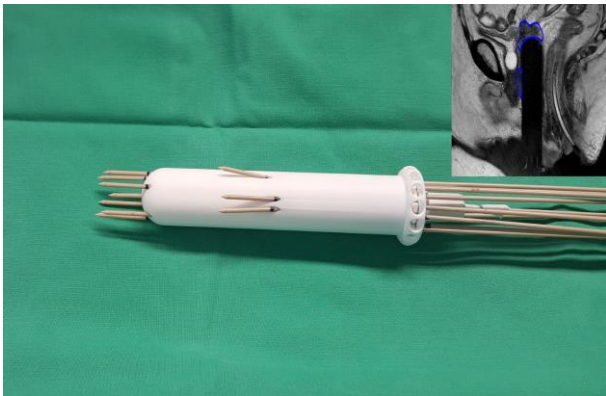


Figure 4. Multi-channel vaginal cylinder with inserted needles for interstitial implantation. The applicator enables precise target coverage at two different locations in the vagina (marked with blue colour on small picture).

3. RESULTS

Individual applicators produced with additive manufacturing technology enabled highly individualized and precise needle guidance to the exact position in the tumor. The dose-volume parameters for the CTV-T_{HR} were significantly improved in the range of 15-38% for the first and in the range of 73-90% for the second patient, while the dose to the OAR was not exceeded (see Table 1).

TABLE I. THE CTV-T_{HR} COVERAGE WITH STANDARD OR INDIVIDUAL APPLICATOR

CTV-T _{HR} (%)	Standard applicator			Individual applicator		
	D98	D90	V100	D98	D90	V100
Patient 1	51	71	78	81	109	93
Patient 2	20	27	20	93	117	97

4. CONCLUSION

Additive manufacturing technology has an important advantage in prototyping and manufacturing of applicators for clinical use in brachytherapy when compared to traditional industrial technology. The time frame between designing the applicator and manufacturing the end product is short and allows individual adaptation of the applicator for the specific patient. Better dose distribution to the target is achieved, which is expected to translate to better tumor control probability. Precise needle guidance causes less trauma of the surrounding tissue and less perioperative side effects are anticipated.

ACKNOWLEDGEMENT

We would like to thank all the colleagues working on the project with great enthusiasm, in general without extra payment for the good of our patients. We also appreciate good cooperation with Assoc. Prof. Igor Drstvenšek from the University of Maribor, Faculty of Mechanical Engineering.

REFERENCES

- [1] Haie-Meder C, Pötter R, Van Limbergen E, Briot E, De Brabandere M, Dimopoulos J, et al. Recommendations from Gynaecological (GYN) GEC-ESTRO Working Group (I): concepts and terms in 3D image based 3D treatment planning in cervix cancer brachytherapy with emphasis on MRI assessment of GTV and CTV. *Radiother Oncol* 2005;74:235–45. doi:10.1016/J.RADONC.2004.12.015.
- [2] Pötter R, Haie-Meder C, Limbergen E Van, Barillot I, De Brabandere M, Dimopoulos J, et al. Recommendations from gynaecological (GYN) GEC ESTRO working group (II): Concepts and terms in 3D image-based treatment planning in cervix cancer brachytherapy—3D dose volume parameters and aspects of 3D image-based anatomy, radiation physics, radiobiology n.d. doi:10.1016/j.radonc.2005.11.014.
- [3] Hellebust TP, Kirsits C, Berger D, Pérez-Calatayud J, De Brabandere M, De Leeuw A, et al. Recommendations from Gynaecological (GYN) GEC-ESTRO Working Group: considerations and pitfalls in commissioning and applicator reconstruction in 3D image-based treatment planning of cervix cancer brachytherapy. *Radiother Oncol* 2010;96:153–60. doi:10.1016/j.radonc.2010.06.004.
- [4] Dimopoulos JC, Petrow P, Tanderup K, Petric P, Berger D, Kirsits C, et al. Recommendations from Gynaecological (GYN) GEC-ESTRO Working Group (IV): Basic principles and parameters for MR imaging within the frame of image based adaptive cervix cancer brachytherapy. *Radiother Oncol* 2012;103:113–22. doi:10.1016/j.radonc.2011.12.024.
- [5] Jürgenliemk-Schulz IM, Tersteeg RJHAHA, Roesink JM, Bijmolt S, Nomden CN, Moerland MA, et al. MRI-guided treatment-planning optimisation in intracavitary or combined

intracavitary/interstitial PDR brachytherapy using tandem ovoid applicators in locally advanced cervical cancer. *Radiother Oncol* 2009;93:322–30. doi:10.1016/j.radonc.2009.08.014.

- [6] Kirisits C, Lang S, Dimopoulos J, Berger D, Georg D, Pötter R. The Vienna applicator for combined intracavitary and interstitial brachytherapy of cervical cancer: Design, application, treatment planning, and dosimetric results. *Int J Radiat Oncol Biol Phys* 2006;65:624–30. doi:10.1016/j.ijrobp.2006.01.036.
- [7] Pötter R, Georg P, Dimopoulos JCA, Grimm M, Berger D, Nesvacil N, et al. Clinical outcome of protocol based image (MRI) guided adaptive brachytherapy combined with 3D conformal radiotherapy with or without chemotherapy in patients with locally advanced cervical cancer. *Radiother Oncol* 2011;100:116–23. doi:10.1016/j.radonc.2011.07.012.
- [8] Dimopoulos JCA, Kirisits C, Petric P, Georg P, Lang S, Berger D, et al. The Vienna applicator for combined intracavitary and interstitial brachytherapy of cervical cancer: clinical feasibility and preliminary results. *Int J Radiat Oncol Biol Phys* 2006;66:83–90. doi:10.1016/j.ijrobp.2006.04.041.
- [9] Sturdza A, Pötter R, Ulrik Fokdal L, Haie-Meder C, Tee Tan L, Mazon R, et al. Image guided brachytherapy in locally advanced cervical cancer: Improved pelvic control and survival in RetroEMBRACE, a multicenter cohort study. *Radiother Oncol* 2016;120:428–33. doi:10.1016/j.radonc.2016.03.011.
- [10] Fokdal L, Sturdza A, Mazon R, Haie-Meder C, Tan LT, Gillham C, et al. Image guided brachytherapy in cervical cancer with combined intracavitary and interstitial technique improves the therapeutic ratio in locally advanced cervical cancer: Analysis from the retroEMBRACE study. *Radiother Oncol* 2016;120:434–40. doi:10.1016/j.radonc.2016.03.020.
- [11] Zobec Logar BH, Hudej R. EP-1978: Individualized approach to brachytherapy in cervical cancer patient: a case report study. *Radiother Oncol* 2016;119:S936–7. doi:10.1016/S0167-8140(16)33229-7.
- [12] Lindegaard JC, Madsen MLL, Traberg A, Meisner B, Nielsen SK, Tanderup K, et al. Individualised 3D printed vaginal template for MRI guided brachytherapy in locally advanced cervical cancer. *Radiother Oncol* 2016;118:173–5. doi:10.1016/j.radonc.2015.12.012.
- [13] Report 89. *J ICRU* 2013;13:NP.3-NP. doi:10.1093/jicru/ndw042.

Melting characteristics in Selective Laser Melting of Ti-6Al-4V product for biomedical application

Snehashis Pal, Faculty of Mechanical Engineering, University of Maribor, Maribor, Slovenia,
snehashiseu@gmail.com

Gorazd Lojen, Faculty of Mechanical Engineering, University of Maribor, Maribor, Slovenia,
gorazd.lojen@um.si

Vanja Kokol, Faculty of Mechanical Engineering, University of Maribor, Maribor, Slovenia,
vanja.kokol@um.si

Igor Drstvensek, Faculty of Mechanical Engineering, University of Maribor, Maribor, Slovenia,
igor.drstvensek@um.si

Abstract— Melting of powder by laser is the principal mechanism used in Selective Laser Melting to build a biomedical implant as entrusted computer-aided designed model. The process is done by layer by layer fusion technique using laser energy input and rapid sonification. The volumetric Energy Density (ED) depends on the energy input employed by laser power, scanning speed, hatch spacing and layer thickness. Several thermal-related phenomena occur during melting and solidification which are powder particles melting, molten pool formation, rapid solidification, re-melting, high thermal-gradient, reheating and re-cooling. There are several chances of inconsistencies in the mentioned phenomena which are improper melting, material spattering, imperfect pool formation, gaseous bubble presence, keyhole effect, Marangoni effect, and thermal stress. These problems result in several types of pores, starting layer defect, irregular surface, bending and residual stress in the product. This study focused on three steps to overcome these problems in Ti-6Al-4V alloy product considering laser power, scanning speed, hatch spacing, and ED. Results show that the influence of ED is significantly higher compared to its technological parameters. Partial re-melting during consecutive scanning track overlapping has a great impact on defects reduction. Influence of Laser power and scanning speed are lesser in improving product quality.

Keywords- melting mechanism; porosity; Ti-6Al-4V alloy; selective laser melting; biomedical implant.

1. INTRODUCTION

Tens of micron thick layer by layer melting of the metal powder particles and rapid solidifying method is used to build a product as entrusted Computer-Aided Design (CAD) model in Selective Laser Melting (SLM)

technology [1]. Therefore, there is high manufacturing flexibility in complexly designed perspective to transform a CAD model into a metallic product. Comparatively lower cost and manufacturing time than traditional manufacturing process to fabricate a product allure the SLM technology in industrial applications especially in aerospace, automobile and biomedical implantation [2], [3]. As the melting of metallic powder particles is considered to fuse them layer by layer, therefore, there are the possibilities for improper melting [2], improper fusion [4], spattering [5], improper pool formation, Marangoni effect inside the molten pool [6], asymmetry heat distributional effect, instability and spreading of molten metal [7], metallic gas evaporation due to high Energy Density (ED) [8], high thermal-gradient [9], gaseous bubble formation inside the pool by inert gas entrapment [10], crescent shape formation during the solidification of the molten pool, downwards movement of the pool in-between the gap of supportive points of the beneath layer and burning. The phenomena mentioned above can cause porosity, void space on the exposed surface area, irregular surface, bending, and residual stress [11], [12]. Void spaces decrease the density and quality of a product. An irregular pore initiates microcrack from its corner point and accumulates stress at the trench zone [13]. Void space on the exposed surface area leads to the decreasing of the strength of a product. Burning minimises the overall quality of a product. High thermal-gradient causes bending and residual stress [12]. Uneven void spaces on the surface create a higher surface area which provokes higher chemical corrosion when it gets simulated body fluid in biomedical implantation.

Defects mentioned earlier with their probable causes, and plausible solutions have been described using several thermal mechanisms in the several kinds of literature. Yu et al. [14] and Vilaro et al. [10] observed the occurrence of gas entrapment inside the melt pool which comes from the inter gas presence in interparticle gaps. Liu et al. (2016) [15] have described a void space formation mechanism inside the molten pool which is a result of trapped tiny metal vapour caused by keyhole effect during a high cooling rate of the pool. Krakhmaleva and Yadroitsev [16] reported that a keyhole effect caused by metal evaporation during slow scanning speed. Similarly, Attar et al. [17] have been observed that keyhole effect was decreased while both laser power and scanning speed increased at a constant ED. On the other hand, using thermo-mechanically coupled finite element model, Luo et al. [18] have been stated that vaporisation gradually weakens along with the decreasing of the laser power and the increasing of the scanning speed during SLM process of thermoelectric tin telluride (SnTe). Investigating by both high-speed imaging observation and computational fluid dynamics calculation on the porosity of Ti-6Al-4V alloy product fabrication, Qui et al. [7] concluded that scanning speed does not influence much on porosity and porosity can be decreased with high laser power. They also observed that layer thickness above 40 μm leads to significant porosity and surface roughness, which are comparatively higher. Qui et al. [7] and Zopp et al. [19] have believed that layer thickness above 30 μm causes stair effect on the surface of Ti-based alloys. Spattering behaviours have been looked by Liu et al. [5] using the high-speed camera; they observed that oxygen content and higher energy input increases spattering of Stainless steel powder in the SLM process. Kasperovich et al. [13] have correlated the relation between the porosity in Ti-6Al-4V alloy product and its manufacturing parameters, they have ascertained that the void formation is mostly influenced by the ED and scanning speed where the hatch distance exerting over ED; eventually, shorter hatch spacing can decrease the porosity in the same ED. Producing a flawless SLM product is still a challenging assignment in industrial application.

In the SLM process, laser ray melts metallic powder particles with a duration, and it can reheat or re-melt those during consecutive scanning. The absorption of energy is done by the powder particles in the particular action zone. Therefore, the volumetric ED (E) is directly proportional to the laser power (P) and inversely proportional to the scanning speed (v), hatch spacing (h) and layer thickness (H). Fig. 1 shows the schematic diagram of technological parameters in the SLM process. The ED can be defined by the Equation (1) [20], [21].

$$E = \frac{P}{v \cdot h \cdot H} \tag{1}$$

Observing the adverse effect of thermal behaviour in SLM process, it is cleared that there is a need to deal with ED and its technological parameters such as laser power, scanning speed and hatch spacing by keeping the layer thickness below 30 μm to overcome the defects remained in the internal structure of the product. Therefore, to improve the product quality, this study has investigated the porosity that occurs in the case of several sets of samples manufactured using different combinations of parameters. Seven samples have been produced in the high range of ED between 39 to 206 J/mm³ and scanning speed between 150 to 1000 mm/s to investigate the defects with the help of scanning electron microscopy (SEM) image in the first step of study. The second step and the third step have been focused on five different laser powers and ten different hatch spacings in the range of 55 W to 95 W and 49.5 μm to 99 μm (10% to 55% consecutive scanning track overlapping) respectively. Eventually, part with about 100% relative density has been obtained from Ti-6Al-4V alloy.

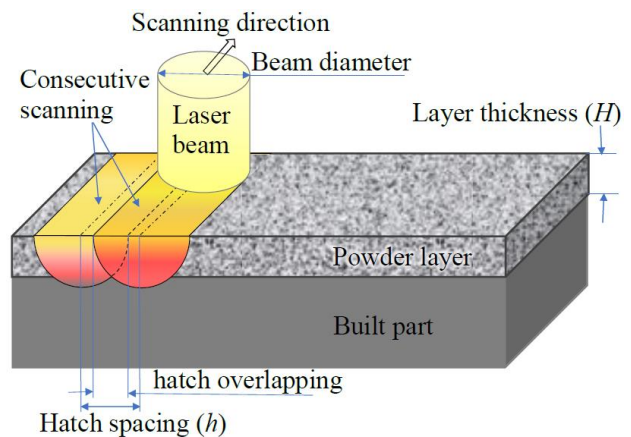


Figure. 1. The schematic diagram of technological parameters in the SLM process

2. MATERIALS AND METHODS

2.1. Materials

The fully dense powder particles of Ti-6Al-4V extra low interstitial alloy (Ti - grade-23) were used to fabricate the samples using several combinations of manufacturing parameters.

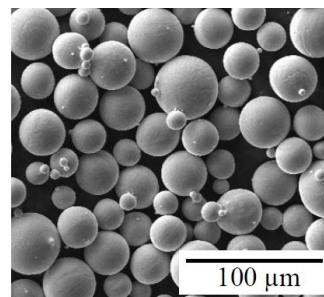


Fig. 2. SEM image of the powder particles of the Ti-6Al-4V alloy.

The powder particles were almost spherical having a diameter in the range of 5 to 40 μm provided by Dentaurem, Germany which is shown by SEM image in Fig. 2. The build substrate material was a Ti-6Al-4V alloy to avoid the uneven heat conduction.

2.2. Maintaining the Integrity of the Specifications

Considering the above-mentioned thermal behavior and defect formation in the SLM process, the study has been focused at first on different EDs by changing scanning speed to manufacture the samples. Thereafter, getting optimum ED as well as an optimal range of scanning speed from the first step, different laser powers has been set in the second step. With the help of obtained optimal parameters from the previous step, several hatches overlapping scanning strategy have been implemented in the third step of study. The SLM process has been conducted in an expedient atmosphere almost filled with Argon and 0.8% oxygen admissible level. Concept Laser LLC, Lichtenfels, Germany has provided the mLAB SLM machining set up where the used laser was Yb:glass fibre laser having a beam diameter of 0.11 mm provided by IPG Photonics, Germany. The machining chamber environment, preheated build substrate, and powder material temperature were set at 20 °C. The samples have been started to build up after having 2 mm height support structure on build substrate. The layers thicknesses were kept constant at 25 μm for the entire study. The consecutive scanning track overlapping, and hatch distance were 30% and 0.77 μm respectively during the first and second step, and the third step has been executed with different values of these parameters.

Cubic samples with the dimension of 8x8x8 mm³ have been manufactured from Ti-6Al-4V alloy powder to perform the experiments. The first step of the study was intended to observe the influences of different EDs over the quality of the product. Seven sets of scanning speeds have been considered to obtain different EDs as shown in Table 1. Table 2 contains the list of five different laser powers along with different scanning speeds which have been considered in the second step of the study. The observation in the third step was the occurrence of track overlapping during consecutive scanning where the hatch distance has been measured by the central distance between two consecutive scanning of the laser beam. The third experiment has been accomplished with ten different hatch distances keeping the laser power and ED at a constant value and the scanning speed in an optimal range as shown in Table 3.

All the samples have been done grinding up to 1 mm from a side surface and then by polishing them to observe the SEM images of the vertical cross-sectioned planed. Therefore, the SEM images in this report are showing a few layers, e.g., a product that was built in the upper direction is represented from the bottom in the upper direction within the SEM image.

TABLE I. PROCESSING PARAMETERS OF THE SAMPLES IN THE FIRST STEP OF THE STUDY WHILE SCANNING SPEEDS AND EDs WERE VARIED

Sample Set number	Laser power (W)	Scan speed (mm/s)	Track over-lapping (%)	Hatch space (mm)	Layer thickness (mm)	Energy Density (J/mm ³)
I-1	75	1000	30	0.077	0.025	39
I-2	75	800	30	0.077	0.025	49
I-3	75	600	30	0.077	0.025	65
I-4	75	400	30	0.077	0.025	97
I-5	75	300	30	0.077	0.025	130
I-6	75	200	30	0.077	0.025	195
I-7	75	150	30	0.077	0.025	260

TABLE II. PROCESSING PARAMETERS OF THE SAMPLES IN THE SECOND STEP OF THE STUDY WHILE LASER POWERS AND SCANNING SPEEDS WERE VARIED

Sample Set number	Laser power (W)	Scan speed (mm/s)	Track over lapping (%)	Hatch space (mm)	Layer thickness (mm)	Energy Density (J/mm ³)
II-1	95	760	30	0.077	0.025	65
II-2	85	680	30	0.077	0.025	65
II-3	75	600	30	0.077	0.025	65
II-4	65	520	30	0.077	0.025	65
II-5	55	440	30	0.077	0.025	65

TABLE III. PROCESSING PARAMETERS OF THE SAMPLES IN THE THIRD STEP OF THE STUDY WHILE SCANNING SPEEDS AND HATCH SPACINGS WERE VARIED CONSIDERING DIFFERENT TRACK OVERLAPPING

Sample Set number	Laser power (W)	Scan speed (mm/s)	Track over-lapping (%)	Hatch space (mm)	Layer thickness (mm)	Energy Density (J/mm ³)
III-1	65	405	10	0.099	0.025	65
III-2	65	430	15	0.0935	0.025	65
III-3	65	455	20	0.088	0.025	65
III-4	65	485	25	0.0825	0.025	65
III-5	65	520	30	0.077	0.025	65
III-6	65	560	35	0.0715	0.025	65
III-7	65	605	40	0.066	0.025	65
III-8	65	660	45	0.0605	0.025	65
III-9	65	725	50	0.055	0.025	65
III-10	65	805	55	0.0495	0.025	65

3. RESULTS AND DISCUSSIONS

3.1. Consequences of the first step of the study

The results in the first step of the study show that the ED has high influences on melt pool formation which contains metallic vapor, gaseous bubble, and improper melted particles and spattering of the material occurs from the action zone. It is difficult to achieve an optimal melting of all the powder particles in the action zone with low ED.

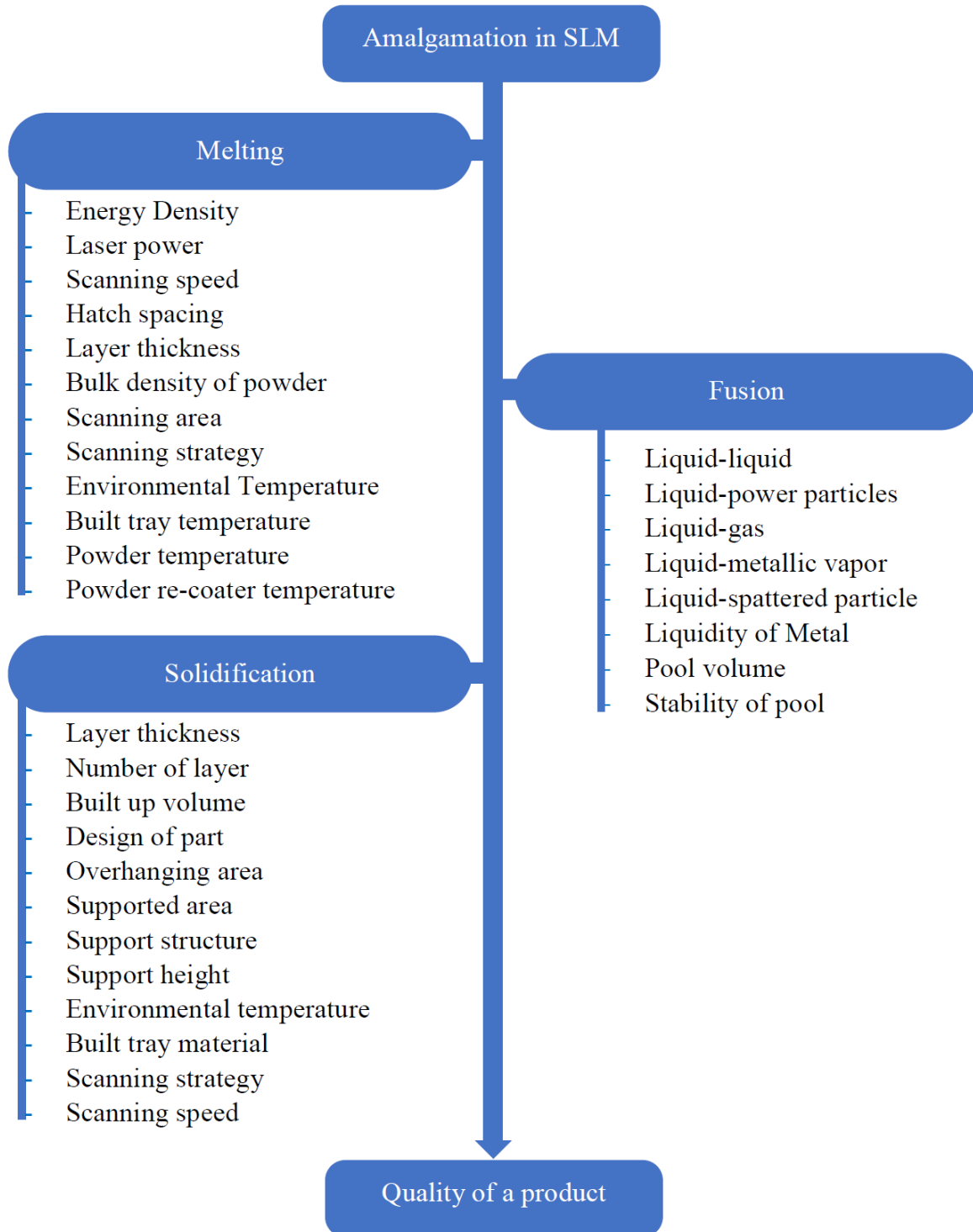


Figure 3. Dependent conditions to regulate a product quality in SLM technology.

High ED results in several types of spattering of powder particles as well as liquid metal. High scanning speed leads to the formation of keyhole vacuum space inside the molten pool. Low scanning speed generates high energy in the action zone which leads to the formation of big pool

volume and provides optimal temperature required for the melting of the powder particles. Inter-particle void spaces contain gas, which could mix up in the molten pool and remains even after the solidification of the pool. As the void and related defects are the main factors which significantly

influence the quality of an SLM product, therefore, this research has gone through an in-detailed analysis of the void formation mechanism during the process of melting-fusion-bonding. The melting happens in powder particles, the preceding layer and the adjacent scanned zone. The fusion is responsible for the purpose of dissolving powder particles, the preceding layer and adjacent scanned zone and the formation of a tiny pool. The bonding occurs among three sides of the pool with the preceding layer, adjacent scanned zone and behind the zone present along in the direction of scanning.

The pores do not have regular shape and volume and are not distributed equally within a sample due to various undesirable reasons and uncertain void formation. The porosity in an SLM product relies upon its numbers, shape, volume, contain and location and plays an influential role on the quality of a product. Porosity decreases the density of a product, and thus it reduces machinal strength. An open pore on the surface increases the surface area by which it gets more diverse effect chemically. Porosity could provoke stress concentration and initiation of microcracks. The pores in an SLM product may exist in various shapes such as spherical, elongated, irregular, etc. Additionally, the presence of critical corner(s), wavy inner periphery, and open pores on the product's outer surface can be observed. A pore contains any or more of these elements which are

the inert gas, loose powder particles, partially melted particles which adhered on the pore inner periphery, and spattered particle or it can be a vacuum.

These critical pores occur due to inconsistent melting influenced by technological parameters, surrounding temperature and environmental condition. The environmental conditions which play an influential role are the presence of gases, initial temperatures of substances and heat spreading constitutions. The gases contain inert gas and oxygen. The initial temperatures are of gas, powder, built tray and powder re-coater. Spreading out of heat from the melt pool depends upon heat conduction, convection and radiation rate into the metallic-materials, gases and inside the chamber respectively. Heat conduction rate relied on the support structure, number of the layer during scanning, the plane area of scanning and built up the volume. Fabrication of the starting layer with and without support has a powder bed or scaffolded support below. Therefore, heat conduction rate differs with or without support and design of the support. All of the mentioned conditions and technological parameters included in ED influence the action of melting zone, pool formation and stability of a pool. Therefore, a proper fusion and solidification process, as shown in Fig. 3, are needed by the influencing parameters to get a high-quality biomedical implant by a specific metal.

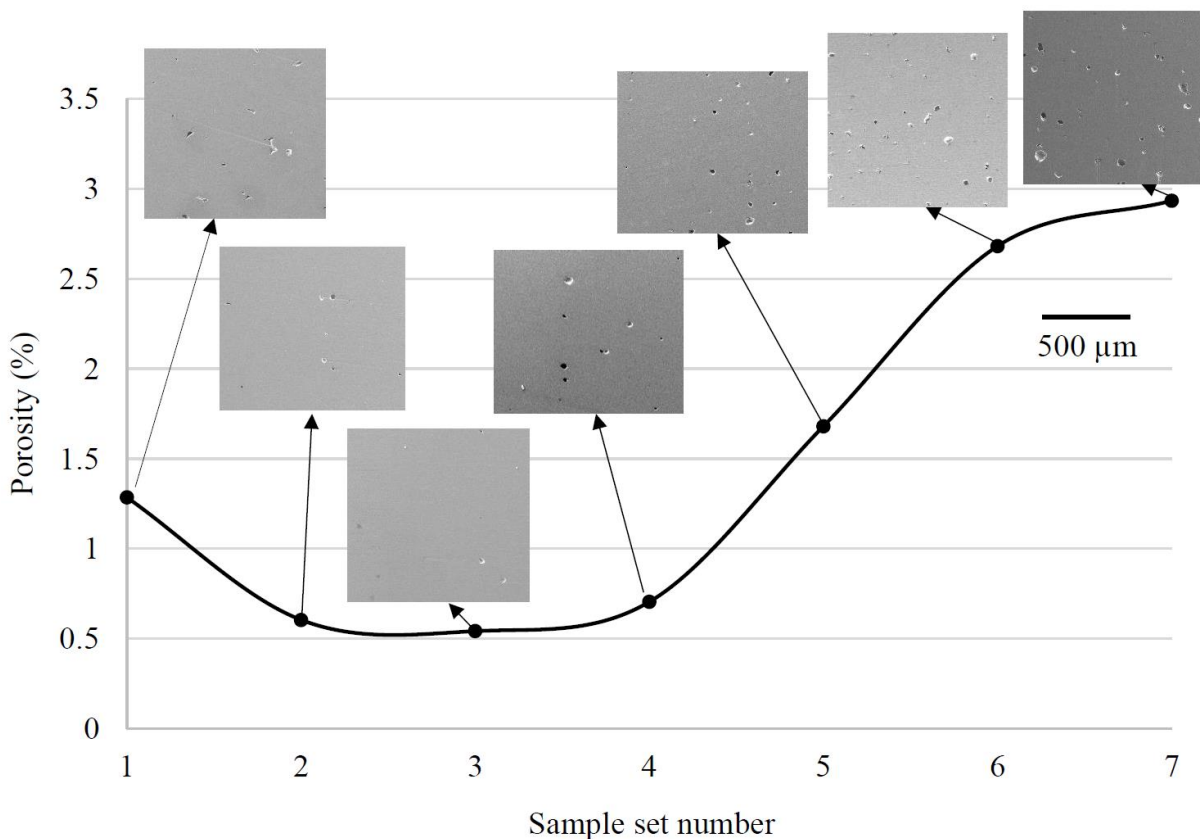


Figure 4. The porosity of the Ti-6Al-4V alloy samples fabricated with different Energy Densities and scanning speeds in the first step of the study.

However, the porosity decreased initially along with an increased ED up to set-3 which have an ED value of 65 J/mm³. Afterwards, the porosity decreased along with increased ED up to set-7 which have the highest ED value of 260 J/mm³. Fig. 4 shows the percentage of porosity in each sample in the first step. The pore structure also changed from set-1 to set-3 which is from an irregular shape to spherical-like shape and volume also decreased. Then the pores became critical and bigger sized due to increase ED till set-7. Low ED caused keyhole effect and insufficient melting which results in irregular pore formation with critical corner points. Comparatively, mediocre ED has melted all the particles but have some spattered defect as well as the spherical void resultant of keyhole effect. High ED causes a high amount of spattering which leads to more irregular shaped void spaces which contain powder particles and inert gas. The detailed melting-fusion-solidification mechanism and unwanted physical behavior, which happen during the SLM manufacturing process [15], [22] are described as follows. The resultant defects and reasonable solutions have also been described considering the causations in the SLM process.

3.1.1. Melting-fusion-solidification mechanism

A nonequilibrium thermal model in the SLM process is described and illustrated in Fig. 5. Seven different thermodynamic and physical regions can be observed during laser melting process which are metal vapor zone, liquid zone, mushy zone, re-melt zone, heat affected zone, powder zone and sintered zone. The mentioned zones are crucial for understanding and controlling to get a flawless and high-quality product. The laser starts to scan after depositing a powder layer with higher thickness than its desired layer thickness; then the gaps exist between the particles disappeared and became a solid part. The laser ray enters into the powder bed and also scatters in between the powder particles. Hence, the laser energy absorbed partially at first by the powder bed in the action zone, and temperature increases up to the melting point of the metal. Afterwards, melting occurs as the temperature increases further. Due to the rapid increase of the heat in the active zone and high ED, the heat doesn't get sufficient time to spread around which causes evaporation of the metal. After melting the particles, the volume shrinks when the gas removed from the action zone. Mushy zone refers to the soft and pulpy area where the powder is partially melted, and it occurs where the solid and liquid coexist in-between the un-sintered powder zone and liquid zone. Beneath portion of the melt pool is the re-melted zone which connects the actioning layer to the preceding layer. After a first track of the scanning, there exists another re-melted zone caused by overlapping of hatch or scanning. Three sides are considered as heat affected zone which all belong to the neighbor zone which helps to amalgamate the pool and its surroundings during solidification. Therefore, the heat-affected zones are existing below the melt pool, beside

the consecutive scanned track and behind the actioning zone. When the melt pool and heat affected zone cooled down, the part makes the solid sintered zone.

Practically, all the mentioned 'zones' could be in an unstable situation during manufacturing caused by thermodynamic, dynamic, and metallurgical instability. Though there are several factors influence the stability of the 'zones', however, the technological parameters include in ED can be considered as key factors to regulate the stability of the 'zones'. Changing the technological parameters namely laser power, scanning speed, hatch spacing and layer thickness, the ED changes and eventually all of these parameters significantly influence the stability of those 'zones', which have been explained in most of the articles mentioned in the reference part.

In the SLM process, the fusion belongs to the amalgamation of several states of the material, which are partially melted powder particle, nonmelted powder particle, liquid and solid segment. Solidification is referred to the formation of the solid segment with a track by track and layer by layer to build up the product. The bottom portion of the pool is connected to the solid part. The sides of the pool are generally in contact with powder particles or the latest scanned zone. The upper part is connected with the gaseous environment. Therefore, the heat spreading rate is highest towards the bottom area. Thus, the pool usually initiates solidification from the bottom area.

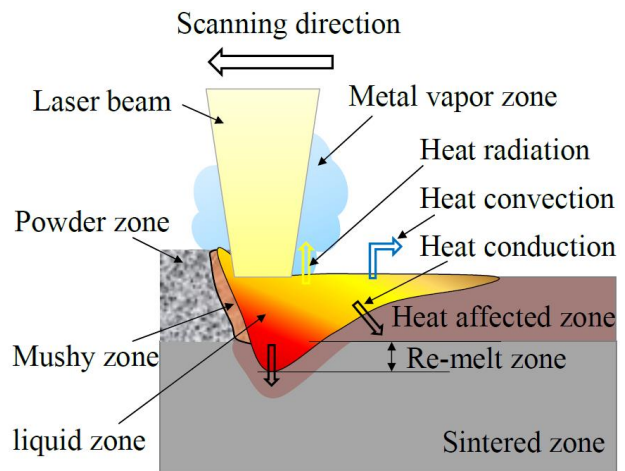


Figure 5. A schematic model of the physical zones occurs at the scanning zone in selective laser melting process.

3.1.2. Spattering behavior during melting

Ti-6Al-4V alloy has poor thermal conductivity and additionally the powder bed exhibit significantly lower thermal conductivity than the solid segment [23]. During laser scanning, the heat at the action zone increases very rapidly. As the heat in the melt pool is not easily transmitted to the surrounding materials, the temperature at the action zone rise up to its evaporation temperature.

As the laser ray primarily penetrate into the powder and scatter inside, therefore, the lower part of the layer gains much higher temperature than its upper level. Such wise, the metal vapor is being generated rapidly at the down part of the pool and forms an intense metallic vapor. Thereafter, the vapor enlarges rapidly which causes high recoil pressure inside the molten metal pool. A high recoil pressure results in the melt expulsion by its instinct phenomenon of removal from melt pool [5]. On the other hand, the inert gas remains in the inter-particular space. During scanning, the gas could mix up with the molten metal [10]. Due to the high temperature, the gas bubble

could also create an explosion of the liquid metal during its expansion.

Uneven heat conduction and presence of gaseous bubbles and metallic vapor provoke the melt pool to perceive instability which results in a spattering of some materials from the action zone. The spattering of materials can be classified into four types concerning its reasons and way out which are powder particle spattering, jet spattering, small droplet spattering and big spattering, which are shown in Fig. 6.

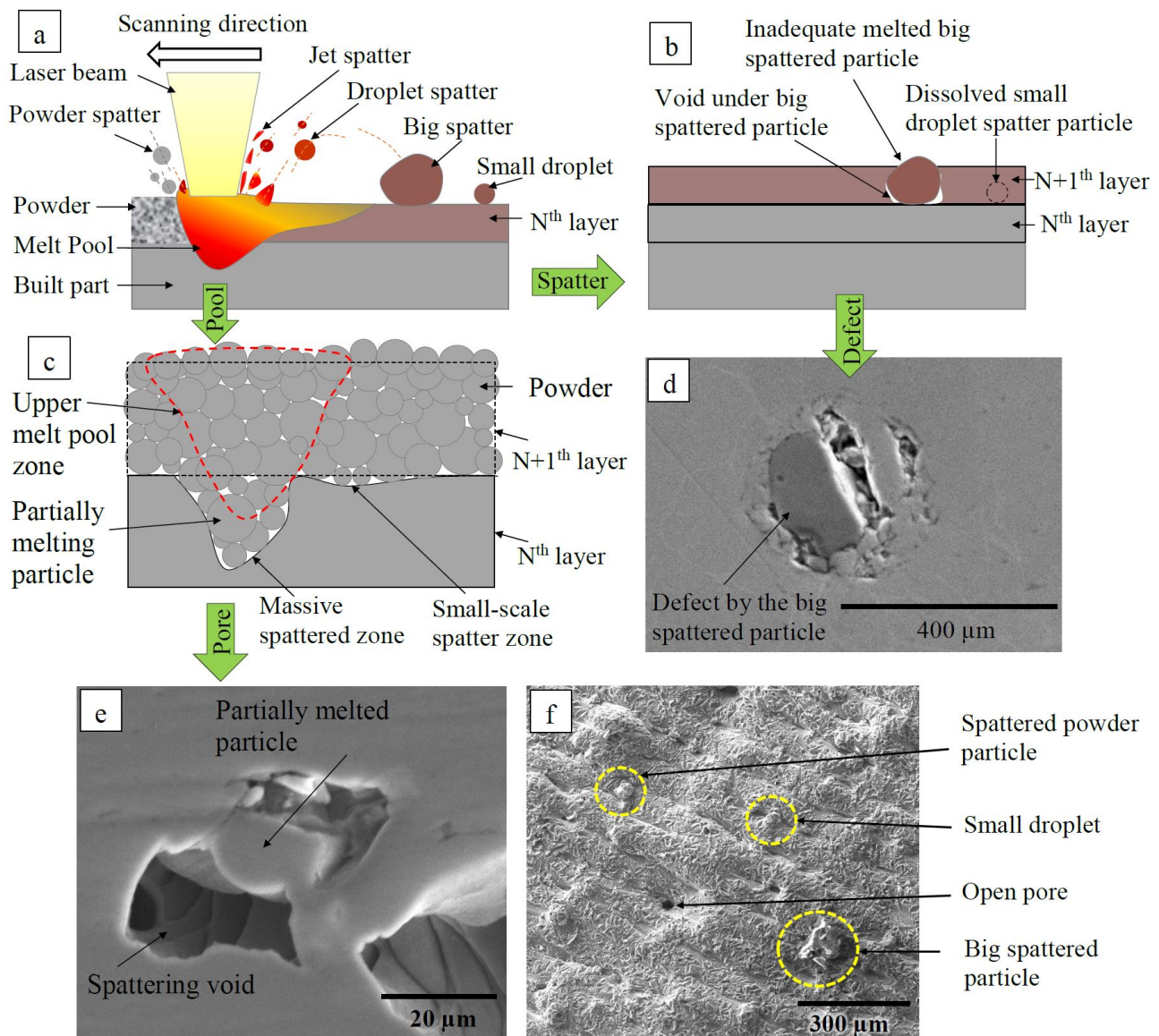


Figure 6. Spattering of material and the defects caused by it, where (a) – (c) are diagram and (d) – (f) are SEM images, (a) various types of spattering, (b) the effects of different sized spattered particles, (c) void formation caused by massive spattering, (d) a defect caused by big spattered particle, (e) pores caused by spattering, (f) a top surface including spattered particles.

The high energy input in a very short time and uneven head conduction cause spattering of the powder particles from the powder zone at beside and the front side of the scanning direction. A sudden high explosion is responsible for the jet spattering of the liquid metal. The explosion also causes small droplet and big spattering. A small droplet spatters as shown in Fig. 6(a) and (b) are completely being melted and dissolve during the next scanning. Accordingly, it metallurgically bounds with the product and disappeared. The powder re-coater device can't usually remove the big spattered object during next powder layer deposition. Currently, there is no available technology or device has that ability to remove it from the scanning region. Therefore, big spattered particle stays on the scanning area, and if the input energy is not sufficient to melt it completely, it stays as the mixture of impurities as shown in Fig. 6(b) and (d). It gets smaller after scanning from its original size after falling into the scanning zone. Due to the particle mixture with impurities and not bond properly with the surrounding layers, they accumulate and contribute to internal defects within the product. This type of spattered defect exhibit brittleness character. If the top surface of the product doesn't re-melt or rescan, the spattered particles lead to the uneven surface. Fig. 6(f) shows an SEM image of the top surface of an SLM product where several types of the spattered particles can be

observed. The small droplet and the spattered powder particle dropped after the scanned tracks, and this phenomenon happened during the next consecutive scanning(s). The big spattered particle marked in Fig. 6(f) might drop before or after scanning. A little void can be present in the sides and the beneath portion of the big spattered particle which may not fill with a sufficient amount of powder particles. The spattered particle also impedes the proper circulation of powders and thus causes voids nearby. Comparatively, a big powder particle prevents flowability, which is needed to occupy the gap with molten metal or melt pool. Fig. 6(b) illustrates the influence of spattering particles on the void formation and internal defects. Scanning by low scanning speed with low laser power and sintering the layer with low ED before its original scanning could be the possible solutions to avoid the spattering of the material.

3.1.3. Keyhole effect in the melt pool

The effect of the keyhole in a melt pool has a significant effect on producing a void space. The laser ray penetrated the powder particles at the action zone and scattered much at the lower portion of the layer than its upper portion.

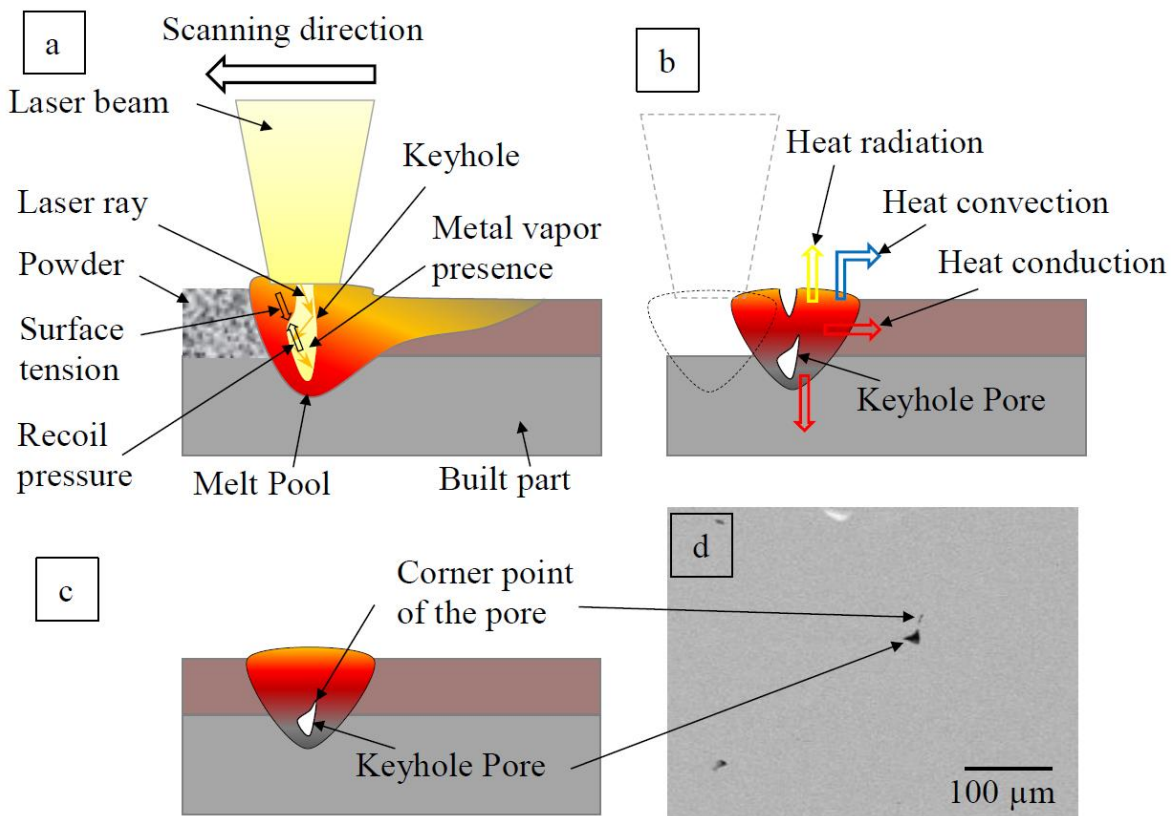


Figure 7. The keyhole effect in a melt pool, (a) keyhole formation by metallic vapor, (b) formation of a pore by keyhole effect, (c) remaining pore in a pool, (d) SEM image of a sample with pore caused by keyhole effect.

Therefore, the lower portion of the layer gain higher temperature and produce high metallic vapor, which causes a recoil pressure, thus form a keyhole in the melt pool [24] as shown in the Fig. 7(a). The laser ray also enters through the keyhole and reflected by the inner surface of it which make more vapor [15]. Two forces occur inside the melt pool, which contains keyhole and those are recoil pressure by the metal vapor and surface tension by the liquid metal. The surface tension occurs higher than the recoil pressure if the solidification of the pool become faster. The melt pool cools faster during high scanning speed. Thus, high scanning speed causes conically shaped void space having a corner point as shown in Fig. 7 (b) and (c). Fig. 7(d) shows an SEM image of the vertical cross-sectional plane as an example of such a keyhole void which is manufactured by 1000 mm/s in sample set-I-1. On the other hand, high scanning speed produces a low ED which is responsible for low vapor creation. High ED increases the temperature of the melt pool which drops surface tension and greater recoil pressure with a higher level of vaporization. This type of keyhole has the tendency to make spherical shaped pore.

3.1.4. Improper melting of powder particles

Xia et al. [25] have reported that high scanning speed induces low energy in the powder bed, which generates a melt pool having low depth. Due to the insufficient energy input with ED of 39 J/mm³ and 49 J/mm³ and faster solidification rate, few powder particles are not melted well which caused voids as shown in Fig. 8. Such voids are the irregular shape and contain some unfused powder particles, partially melted and stuck particles on the void wall and inert gas [1] as shown in Fig. 8(c) by SEM image. The SEM image in Fig. 8(c) shows a corner point exist in-between the stuck particle and next scanned pool. This type of zone is highly sensitive to be separated from each other and initiate a microcrack. As the powder particles are not equally distributed everywhere, some portions have remained like mounded [10] as shown in Fig. 8(a). Low ED is not able to melt all particles well at the mounded zone, and the molten pool stays at a higher level than regular level as illustrated in Fig. 8(b). Therefore, this phenomenon forms an irregularly shaped void space.

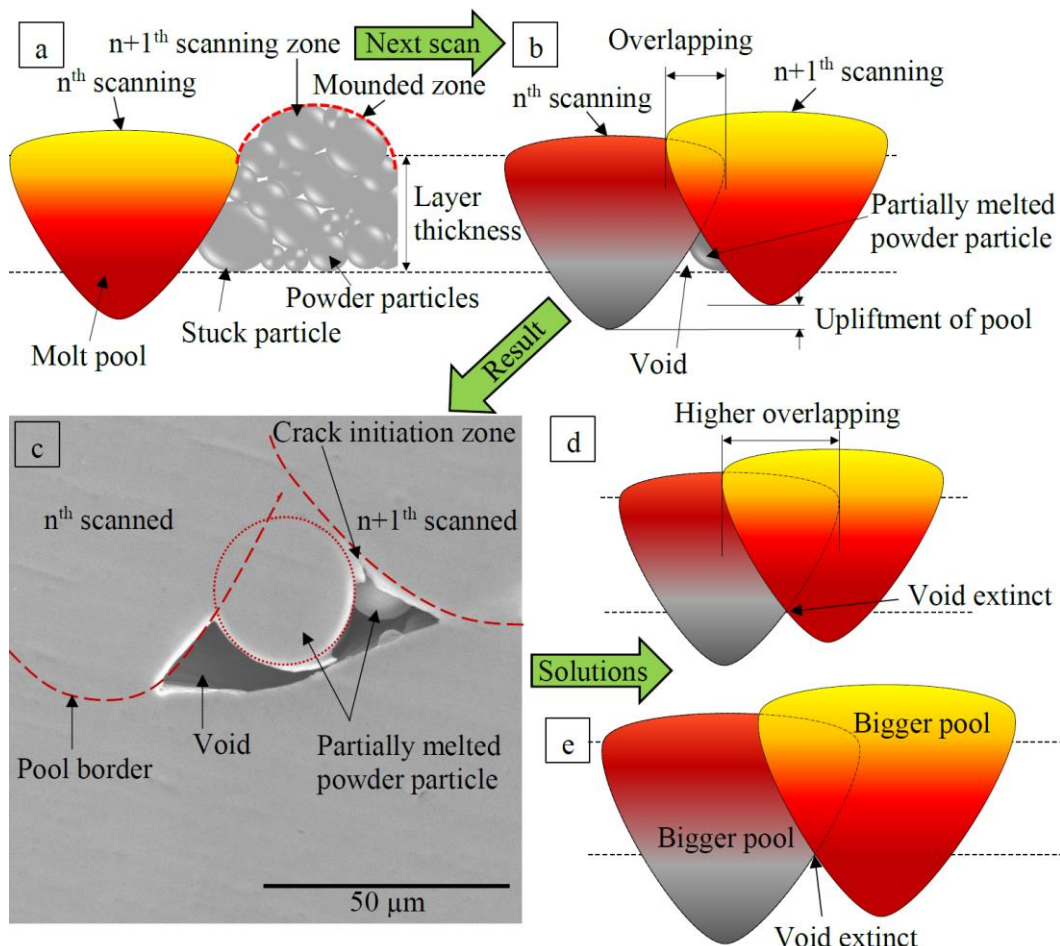


Figure 8. The defects caused due to low ED, (a) a pool and a mounded region, (b) next adjacent pool during next consecutive scanning and the pool position (with upliftment) due to presence of excessive powder particles, (c) SEM image of a pore of set-I-1, (d) a possible solution to decrease the void space by higher track overlapping (smaller hatch spacing), and (e) omitting void space by bigger sized pool formation with higher ED value.

If the overlapping is not high, then there might be a possibility of having some zones without proper molten flow. The flow of liquid metal can be interrupted by a big powder particle, which is not melted enough. Fig. 8(a) presents an action zone, where a big powder particle adheres to the pool. During consecutive scanning, as shown in Fig. 8(b), the pool (besides the previously mentioned action point) is unable to melt the big particle because of having low ED.

Therefore, the possible solution could be higher track overlapping, which can fill the gap of unmelt zone [2] as illustrated in Fig. 8(d). Another way, as shown in Fig. 8(e), the molten pool can be made bigger with higher energy input facilitating by low scanning speed and high laser power. Re-melting of the scanned layer could be a solution to avoid unmelt zone.

3.1.5. Entrapment of the gaseous bubble in the molten pool

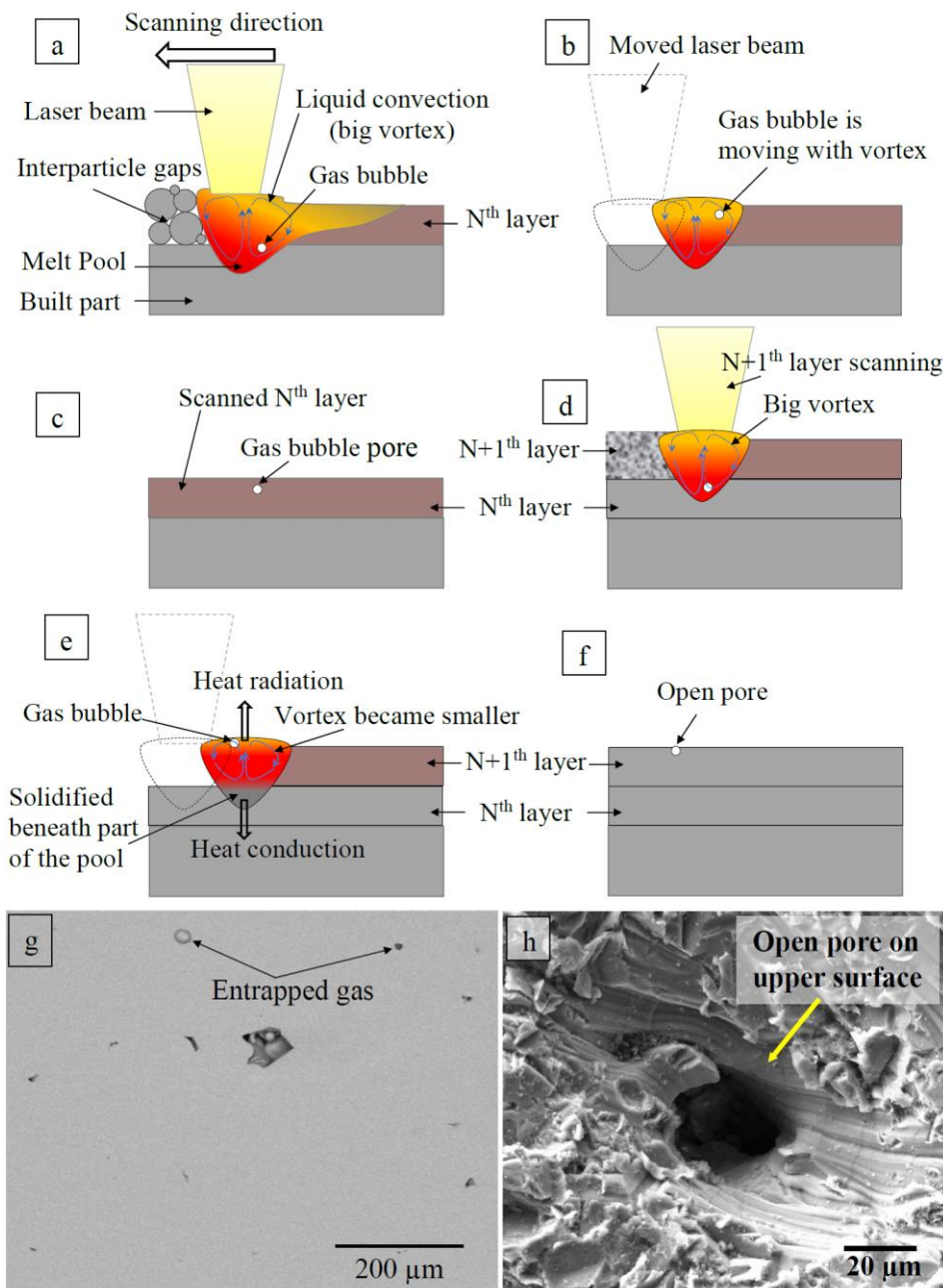


Figure 9. Entrapment of gaseous bubble in the pool and pore formation, (a) presence of a gaseous bubble, (b) entrapping of a gaseous bubble and its motion with vortex, (c) pore formation by the bubble, (d) inclusion of the last bubble in to the next layer's pool, (e) occurrence of bubble upliftment as the vortex became smaller, (f) pore formation with the bubble and its possibility to create open pore, (g) SEM image of the pores caused by the entrapment of gaseous bubble, (h) SEM image with open pore exist on the top surface of a sample.

Entrapment of gases is well known in the casting process where the pores are usually spherical and very small. Few pores have been seen in SLM Ti-6Al-4V products which were caused by the entrapment of intern gaseous bubble as illustrated in Fig. 9. Such pore remains almost spherical and small, and thus, these pores must contain an inert gas. Fig. 9 (g) shows an SEM image of a vertical cross-section of a sample manufactured with ED of 39 J/mm³ and scanning speed of 1000 mm/s, and here the presence of entrapped gas can be observed. There is a possibility to have open pores as shown in Fig. 9(h) on the orientation wise top surface of the product caused by gaseous bubble entrapment. Fig. 9(a) – (f) illustrating the formation of the void by the entrapment of gas. The inert gas, which exists between inter-particle gaps, is mixed with the liquid metal during the melting process [10]. Then the bubble moves with vortex inside melt pool and may not goes out from the melt pool due to the high cooling rate and as a result, it remains as spherical void [10] as shown in Fig. 9(c). Therefore, the pores created by the gas entrapment have mostly found in the samples manufactured with high scanning speed such as 1000 mm/s and 800 mm/s. Interestingly, the gaseous bubbles tended to move up in the melt pool under the joint action of buoyancy, convection within the molten pool, and solidification of the melt pool from bottom to upper side [14]. The vortex in the melt pool becomes smaller and upwards with the solidification of the pool as illustrated in Fig. 9 with a schematic diagram.

The void may again mix up with the next upper layer pool and may stay inside the melt pool or goes out or again mixed with the next upper layer and so on. There is also a chance to create an open pore by the bubble. It is not a problem if the open pore exists in some layer before the top layer because it then starts to behave as an inter-particles gap. If the open pore remains at the top layer of the part segment, then it stays as an open pore on the surface of the product as shown in Fig. 9(h). As Delannay et al.'s [26] argument, increasing the layer's apparent density by increasing the coordination number of the powder particles leads to reduce the interparticle gaps, and thus the chances of gaseous bubble formation would be less. Reducing the cooling rate of the pool by reducing the scanning speed can be another solution to provide time to the bubble to escape itself from the pool. Scanning twice could be a possible solution to remove the entrapped gaseous bubble. Melting of the top layer twice is a possible solution to reduce the open pore on the top surface of the part.

3.1.6 Capillary effect

The existence of capillary effect in the melt pool sucks the powder particles into it, or the particles stuck onto the

pool wall [1], [5]. By this phenomenon, the melt pool becomes bigger in volume which could have a diverse effect for next scanning. If the bigger volume pool occurred in the top layer, it causes uneven surface as well as inaccurate dimension. The occurrence causes lack of sufficient material at the next adjacent zones which form a smaller pool there and thus there is a chance of void formation. Full powder particles adhere to the pool at the surface area and partially melted particles as shown in Fig. 10. Thus, the surface gets higher roughness with partially and nonmelted particles as shown in Fig. 10 (b). As the particles stuck by the side of the pool, therefore, this type of roughness dwelt on the side surface of an SLM product.

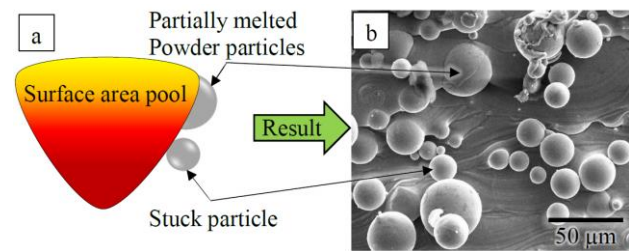


Figure 10. The capillary effect, (a) a diagram of a pool and its capillary effect on pooling of powder particles, (b) SEM image of the side surface and adhesion of powder particles on the side surface of any SLM product.

3.2. Consequences of the second step of the study

The substantial influences of the laser power on the melting behavior in the SLM process have been observed. Fig. 11 displays that the overall porosity decreased slightly along with the decrement of laser power. Though it has been seen that the porosity slight increased from the laser power 95 W to 85 W which has no such significant difference. As the ED was fixed at a previously obtained optimum value, the range between maximum and minimum porosity is not much high which is 0.23% to 0.99%. The pore size and shape are small and spherical respectively. The sample manufactured with the lowest laser power of 55 W has the lowest porosity in the second step of the study. At low laser power, the intensity of the metal stream decreases, so, the liquid metal in the melt pool flow with less violent and thus less spattering occurs [27]. As there are the influences of scanning speeds too, therefore, the consequences happened by the influence of both parameters together, laser power and scanning speed. Higher laser power worked with higher scanning speed, and thus, the pools solidified in faster rate which has higher effects on porosity formation from the keyhole effect.

However, higher density samples were achieved by the lesser laser powers of 65 W and 55 W in the second step than the first step. As there is no significant porosity

difference between these two samples, hence, 65 W could be considered as in the range of optimal laser powers. Therefore, to keep other parameters in their optimal range,

the laser power of 65 W has been considered for the next step of the study.

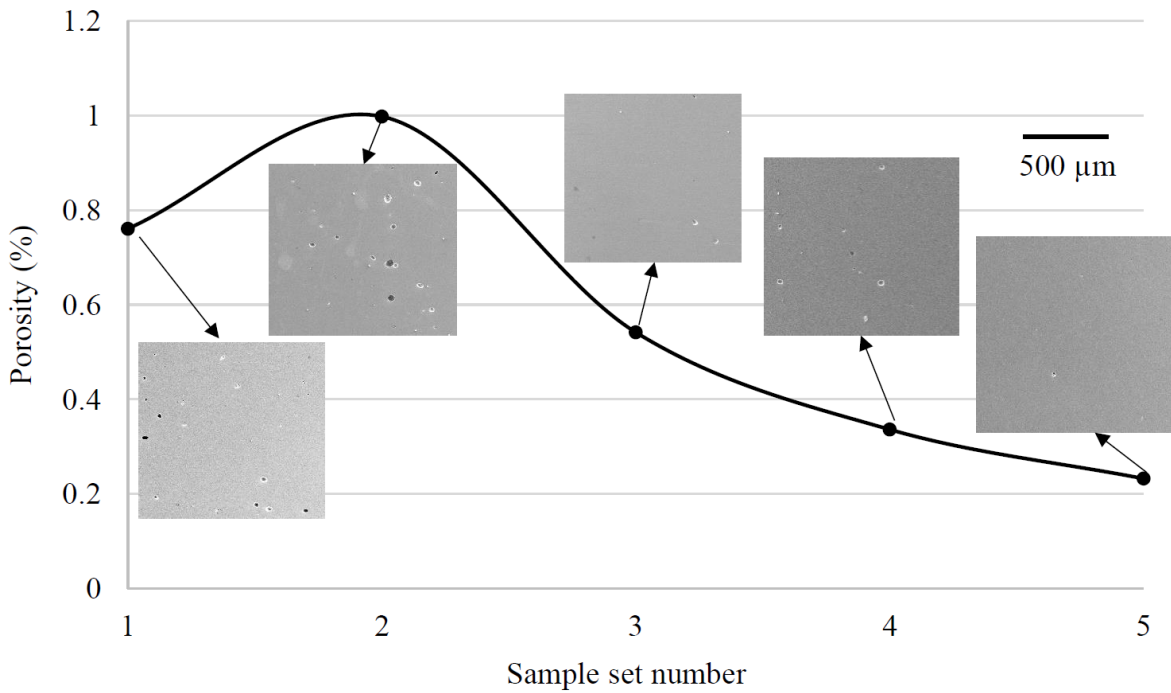


Figure 11. The porosity of the Ti-6Al-4V alloy samples fabricated with different laser powers and scanning speeds in the second step of the study.

3.3. Consequences of the third step of the study

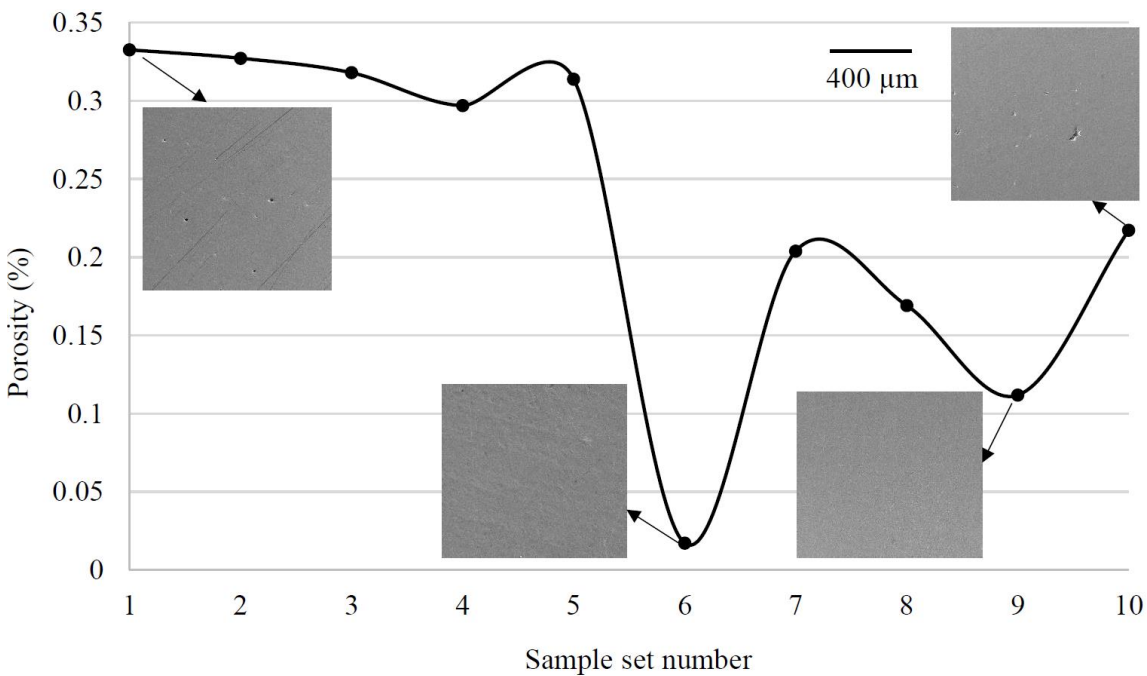


Figure 12. Porosity of the Ti-6Al-4V alloy samples fabricated with different track overlapping (hatch spacings) and scanning speeds in the third step

Considering the availability of pores, the remarkable results have been acquired in the third step of the study focusing on track overlapping. The porosity is diminished in the samples manufactured with more than 30% track overlapping which is presented in Fig. 12. Almost 100% relative density sample has been obtained in the sample having 35% track overlapping where no pore was observed except small voids at the starting layer which are caused by manufacturing problem on the support structure. The further increment of track overlapping will facilitate to the manufacturing of the better flawless product. However, scanning speed also increased along with higher overlapping. Therefore, higher scanning speeds are responsible here for the occurrence of a higher number of pores. The results also show that there was a tension between the increment of track overlapping and increment of scanning speed in melting-fusion-solidification process.

4. CONCLUSIONS

The melting characteristics have been studied with different values of laser power, scanning speed, hatch spacing, and ED in SLM technology to reduce porosity difficulties in the product. Powder-melting-solidification transformations results were observed in Ti-6Al-4V alloy samples, and the phenomena were analyzed evidently.

By the consequences and the analysis of the first step of the study, it can be concluded that the formation of pores is the resultants of possible uncertainties of the phenomena of melting, fusion and solidification. Therefore, the pores have occurred uncertainly and do not have any regular position in the SLM product. Similarly, the shape, size, numbers are different, and the constituents are different as well in every pore. Using low ED caused insufficient melting of powder particles whereas using average ED favor sufficient melting with few spattering of materials and keyhole effect by metallic vapor. High ED is responsible for the high rate of spattering. High scanning speed leads to faster cooling and thus produced high surface tension which caused irregular keyhole pore. ED having a value of 65 J/mm³ has performed optimally when considering the numbers, shape and volume of pores. Whereas, scanning speed in the range of 400 mm/s to 800 mm/s can be considered as an optimal fabrication range.

The second step has been dealt with different laser powers, keeping the optimum ED in a fixed value and scanning speed in the optimal range obtained from the first step. Lowest laser power (55 W) has low intensity, which has less effect on spattering and disparity of molten metal inside the molten pools. Thus, 55 W laser power performed the highest density in the second step of the study.

The effect of the re-melting amount of a pool by consecutive track has been observed by the increments of track overlapping from 10% to 55% in 10 distinct values. The 35% track overlapping has performed the best fusion process and solidification to build a flawless product. Thus,

desired mechanical properties in a biomedical implant can be induced with the SLM parameters of 65 W laser power, 600 mm/s scanning speed, 35% track overlapping, 25 μm layer thick and 65 J/mm³.

ACKNOWLEDGEMENT

Authors are in debt to the Orthotip, Maribor, Slovenia for manufacturing the samples used in this study. Authors are thankful to the Faculty of Mechanical Engineering, University of Maribor, Slovenia for providing all the necessary equipment and machinery needed for the study. The authors are grateful to the supporting staff for their continuous efforts and support. Authors thank Erasmus Mundus EUPHRATES (2013-2540/001-001-EMA2) scholarship program for financial assistance.

REFERENCES

- [1] A. M. Khorasani, I. Gibson, M. Goldberg, and G. Littlefair, "Production of Ti-6Al-4V acetabular shell using selective laser melting: Possible limitations in fabrication," *Rapid Prototyp. J.*, 2017.
- [2] J. Stef *et al.*, "Mechanism of porosity formation and influence on mechanical properties in selective laser melting of Ti-6Al-4V parts," *Mater. Des.*, vol. 156, pp. 480–493, 2018.
- [3] D. Leordean, C. Dudescu, T. Marcu, P. Berce, and N. Balc, "Customized implants with specific properties, made by selective laser melting," *Rapid Prototyp. J.*, 2015.
- [4] M. Simonelli *et al.*, "A comparison of Ti-6Al-4V in-situ alloying in Selective Laser Melting using simply-mixed and satellited powder blend feedstocks," *Mater. Charact.*, 2018.
- [5] Y. Liu, Y. Yang, S. Mai, D. Wang, and C. Song, "Investigation into spatter behavior during selective laser melting of AISI 316L stainless steel powder," *Mater. Des.*, vol. 87, pp. 797–806, 2015.
- [6] D. Gu *et al.*, "Densification behavior, microstructure evolution, and wear performance of selective laser melting processed commercially pure titanium," *Acta Mater.*, vol. 60, no. 9, pp. 3849–3860, 2012.
- [7] C. Qiu, C. Panwisawas, M. Ward, H. C. Basoalto, J. W. Brooks, and M. M. Attallah, "On the role of melt flow into the surface structure and porosity development during selective laser melting," *Acta Mater.*, vol. 96, pp. 72–79, Sep. 2015.

- [8] X. Zhou *et al.*, “3D-imaging of selective laser melting defects in a Co–Cr–Mo alloy by synchrotron radiation micro-CT,” *Acta Mater.*, vol. 98, pp. 1–16, Oct. 2015.
- [9] Y. Huang, L. J. Yang, X. Z. Du, and Y. P. Yang, “Finite element analysis of thermal behavior of metal powder during selective laser melting,” *Int. J. Therm. Sci.*, vol. 104, pp. 146–157, Jun. 2016.
- [10] T. Vilaro, C. Colin, and J. D. Bartout, “As-Fabricated and Heat-Treated Microstructures of the Ti-6Al-4V Alloy Processed by Selective Laser Melting,” *Metall. Mater. Trans. A*, vol. 42, no. 10, pp. 3190–3199, Oct. 2011.
- [11] M. Shunmugavel, A. Polishetty, M. Goldberg, R. Singh, and G. Littlefair, “A comparative study of mechanical properties and machinability of wrought and additive manufactured (selective laser melting) titanium alloy - Ti-6Al-4V,” *Rapid Prototyp. J.*, 2017.
- [12] P. Mercelis and J.-P. Kruth, “Residual stresses in selective laser sintering and selective laser melting,” *Rapid Prototyp. J.*, vol. 12, no. 5, pp. 254–265, 2006.
- [13] G. Kasperovich, J. Haubrich, J. Gussone, and G. Requena, “Correlation between porosity and processing parameters in TiAl6V4 produced by selective laser melting,” *Mater. Des.*, vol. 105, pp. 160–170, 2016.
- [14] G. Yu, D. Gu, D. Dai, M. Xia, C. Ma, and K. Chang, “Influence of processing parameters on laser penetration depth and melting/re-melting densification during selective laser melting of aluminum alloy,” *Appl. Phys. A Mater. Sci. Process.*, 2016.
- [15] Y. J. Liu *et al.*, “Microstructure, defects and mechanical behavior of beta-type titanium porous structures manufactured by electron beam melting and selective laser melting,” *Acta Mater.*, vol. 113, pp. 56–67, 2016.
- [16] P. Krakhmalev and I. Yadroitsev, “Microstructure and properties of intermetallic composite coatings fabricated by selective laser melting of Ti–SiC powder mixtures,” *Intermetallics*, vol. 46, pp. 147–155, 2014.
- [17] H. Attar, M. Bönisch, M. Calin, L.-C. Zhang, S. Scudino, and J. Eckert, “Selective laser melting of in situ titanium–titanium boride composites: Processing, microstructure and mechanical properties,” *Acta Mater.*, vol. 76, pp. 13–22, 2014.
- [18] C. Luo, J. Qiu, Y. Yan, J. Yang, C. Uher, and X. Tang, “Finite element analysis of temperature and stress fields during the selective laser melting process of thermoelectric SnTe,” *J. Mater. Process. Technol.*, 2018.
- [19] C. Zopp, S. Blümer, F. Schubert, and L. Kroll, “Processing of a metastable titanium alloy (Ti-5553) by selective laser melting,” *Ain Shams Eng. J.*, vol. 8, no. 3, pp. 475–479, 2017.
- [20] B. Vandenbroucke and J. P. Kruth, “Selective laser melting of biocompatible metals for rapid manufacturing of medical parts,” *Rapid Prototyp. J.*, 2007.
- [21] S. Pal, H. R. Tiyyagura, I. Drstven?ek, and C. S. Kumar, “The effect of post-processing and machining process parameters on properties of stainless steel PH1 product produced by direct metal laser sintering,” in *Procedia Engineering*, 2016.
- [22] M. Geiger, K.-H. Leitz, H. Koch, and A. Otto, *A 3D transient model of keyhole and melt pool dynamics in laser beam welding applied to the joining of zinc coated sheets*, vol. 3. 2009.
- [23] J. Pegues, M. Roach, R. Scott Williamson, and N. Shamsaei, “Surface Roughness Effects on the Fatigue Strength of Additively Manufactured Ti-6Al-4V,” *Int. J. Fatigue*, 2018.
- [24] V. Semak and A. Matsunawa, “The role of recoil pressure in energy balance during laser materials processing,” *J. Phys. D. Appl. Phys.*, vol. 30, no. 18, p. 2541, 1997.
- [25] M. Xia, D. Gu, G. Yu, D. Dai, H. Chen, and Q. Shi, “Porosity evolution and its thermodynamic mechanism of randomly packed powder-bed during selective laser melting of Inconel 718 alloy,” *Int. J. Mach. Tools Manuf.*, vol. 116, pp. 96–106, 2017.
- [26] F. Delannay, D. Pardoën, and C. Colin, “Equilibrium distribution of liquid during liquid phase sintering of composition gradient materials,” *Acta Mater.*, vol. 53, no. 6, pp. 1655–1664, 2005.
- [27] D. Wang *et al.*, “Mechanisms and characteristics of spatter generation in SLM processing and its effect on the properties,” *Mater. Des.*, vol. 117, pp. 121–130, 2017.

The Effect of Machining and Heat Treatment on Cutting Forces of SLM Medical Component

1,2-Amir Mahyar Khorasani*, 1,2-Ian Gibson, 2-Moshe Goldberg, 3-Guy Littlefair

1-School of Engineering, Deakin University, Waurn Ponds, Victoria, Australia

2- Department of Mechanics of Solids, Surfaces & Systems, Faculty of Engineering Technology, University of Twente

3- Faculty of Design and Creative Technologies, Auckland University of Technology

a.khorasani@deakin.edu.au, i.gibson@deakin.edu.au, moshe.goldberg@deakin.edu.au, guy.littlefair@aut.ac.nz

Abstract— Post processing, such as machining, is particularly necessary for metal AM due to the lack of surface quality for as-built parts being a problem when using as a production process. In this paper, a predictive model for cutting forces has been developed by using artificial neural networks (ANNs). The effect of cutting condition, on the generated force during machining of spherical components such as prosthetic acetabular shell was investigated. Different annealing processes have been carried out on the samples to better understand the effect of brittleness, strength and hardness on machining. The results of this study showed that ANN can accurately apply to model cutting force when using ball nose cutters. Scallop height has the highest impact on cutting forces. The results illustrate that using linear tool path and increasing annealing temperature can result in lower cutting force. Higher cutting force was observed with greater scallop height and feed rate whilst for higher finishing allowance, cutting forces decreased. For spindle speed the trend of cutting force was increasing up to a critical point and then decreasing due to thermal softening. **Keywords**-component; formatting; style; styling; insert

1. INTRODUCTION

3D printing, also termed as Additive Manufacturing (AM), is associated with different methods that utilize the coupling of computer-aided design (CAD) and computer aided manufacturing (CAM). In AM, layers are formed and added on top of each other under computer control and almost any shape with complex geometry can be produced directly from 3D CAD models [1-8]. Laser Powder Bed Fusion (L-PBF) systems have different technologies such as selective laser melting (SLM), laser sintered in solid phase, direct metal laser sintering (DMLS) and selective laser sintering (SLS). Metal AM is becoming increasingly popular but applications may often require additional machine finishing.

Different aspects of milling using ball nose cutters have been investigated such as analysing cutting force, vibrations, surface quality, dimensional deviations and tool performance. Analytical models to calculate cutting force for inclined surfaces at the contact point of the cutting tool

by determining chip thickness, with mean and maximum value of cutting force, was carried out by Subrahmanyam et. al. [9].

A mechanistic cutting force model based on edge and cutting/shear coefficients incorporated into a transformation matrix was developed by Altintas [10, 11]. Altintas et al. [12] also analytically modelled axial, radial and tangential components of cutting forces for ball-end cutters in milling by an orthogonal structural mode. They simulated mechanics and dynamics of a ball-end mill by considering the instantaneous regenerative chip load, geometry of ball, local cutting force coefficient and structural transfer matrix. In another study, a general mathematical model of arbitrary milling cutters (including cylindrical, ball-tapered and bull-nose) showed that determining local cutting edge along cutting flute gives accurate results in modelling of cutting force, vibrations, chatter stability lobes and surface roughness [13]. Based on this mechanistic approach different uncut chip formation models, such as static and dynamic, were proposed to increase the accuracy of the model [14]. Gradisek et al. improved the calculation method of cutting and edge coefficients for cutting forces. He also validated the model using simulation and experimental tests [15]. In milling of Inconel 718 using ball-nose cutters, the force values increased by increasing cutting speed, which can be related to strain hardening. Similar increase of this parameter showed that the cutting force decreased in steels due to the dominating influence of thermal softening compared to strain hardening. Higher cutting forces were observed in up-cut milling as well as when using CrN coated tools compared to TiAlN due to the higher value of coefficient of friction for CrN [16].

In this work, spherical components like the prosthetic acetabular shell were printed and post processing on as-built samples (including heat treatment/annealing and machining) have been carried out. Mechanical properties were improved by heat treatment and dimensional tolerances were satisfied by machining. To check the effect of heat treatment on machinability different annealing was

carried out. The effect cutting condition and heat treatment/annealing on the cutting forces were analysed by using Artificial Neural Network (ANN) modelling.

2. EXPERIMENTAL PROCEDURE

2.1. Powder material and SLM operation

Figure 1 (A) shows spherical Ti-6Al-4V powder used in this experiment. To fabricate the samples a Selective Laser Melting machine (SLM 125HL) equipped with a YLR-Faser-Laser with maximum scanning power 200W and minimum spot size 5 μm was used. To obtain fully dense and high quality samples a meander scanning pattern was selected and process parameters are introduced in table 1. In this pattern, the laser has meander movement in each layer and was rotated 670 between subsequent layers (Figure 1 (F)). In this experiment, spherical components were printed as shown in Figure 1 (B-D). To avoid any possible defect in printing process the CAD model was optimized [17] to enable clamping of samples on the milling machine. To match the dynamometer dimensions a base plate with four holes was printed along with samples. The thickness of the samples is 2.45mm (Figure 1 (B and D)). Particle size distribution is shown in Figure 1 (E). Maintaining the Integrity of the Specifications.

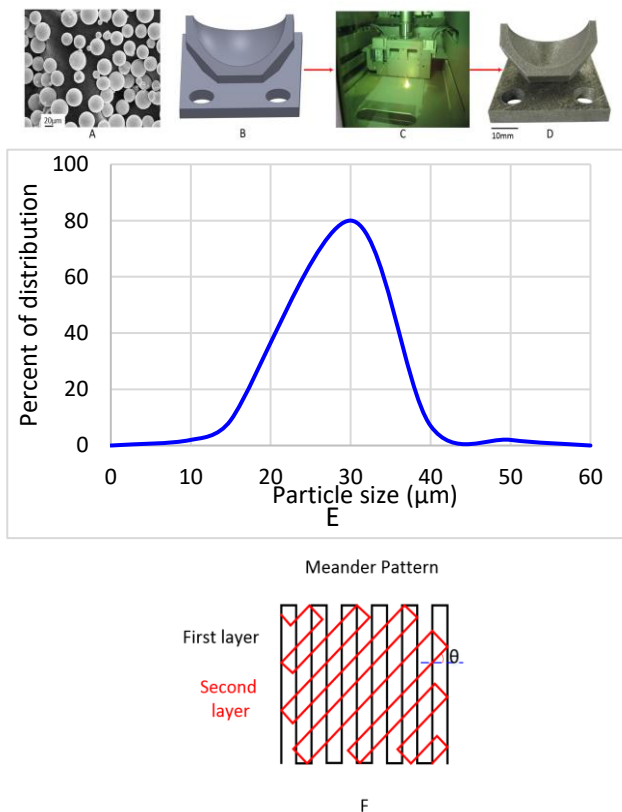


Figure 1 (A) SEM image of powder morphology and size (B, C) CAD-CAM process (D) printed sample (E) particles size distribution (F) Meander pattern
 Table 1 SLM process parameters

System Parameters	Value
Laser Power	100 W, YLR-Faser-Laser
Build Speed	15 ccm/h
Min. Scan Line / Wall Thickness	120 μm
Operational Beam Focus Variable	100 μm
Scan Speed	700 mm/s
Hatch spacing	75 μm
Layer thickness	30 μm
Laser spot diameter	0.2 mm

2.2. Design of experiment (DOE)

To avoid full factorial DOE and decreasing the number of experiments without noticeable loss in accuracy the Taguchi method with orthogonal array was selected. To increase the accuracy, factors in each column should be analysed independently and so if the number of replications in each column is balanced, the design order is called orthogonal.

Based on ASM standard for Ti-6Al-4V annealing has been carried out at four different temperatures that are called, stress relieving, mill annealing, recrystallization annealing and beta annealing to improve the ductility. The increasing and decreasing time, as well as resident time, were each 2 hours [18-20].

Table 2 Cutting condition levels

Tool Path*	Feed rate (mm/min)	Spindle speed (rpm)	Scallop Height (mm)	Finishing Allowance (mm)	Heat treatment Temperature C
1	232	2387	0.0015	0.06	20
1	250	2785	0.003	0.12	600
2	266	3183	0.0045	0.18	750
2	284	3581	0.006	0.24	1050

*Note: tool path 1 is helical and 2 is linear

2.3. Milling operation

The surface quality of as-built SLM samples are inferior and therefore, post processing, such as machining, is needed to improve the surface quality for printed prototypes. A Spinner U 620 machining centre with 5 axes and maximum 20000 rpm was utilized for post processing. The size of the cutter was selected based on component radius and tool manufacturer recommendations. Thus a 8 mm solid carbide ball end-mill was selected for milling and cutter specifications are shown in table 3. In this research, coolant fluid with different nozzles including one nozzle for spindle and four symmetric nozzles for workpiece were used.

As-received SLM samples have low ductility (around 3%) so during machining an engraving effect on the surface is expected. To solve this problem, and enhance mechanical properties, heat treatment was recommended [21-24].

Table 3 Cutter specifications

Diameter mm	Helix angle	Radial relief angle	Radial clearance angle	Elastic modulus GPa	Poisson's ratio	Density g/cm ³	Yield strength MPa	Hardness HV
8	30	11	25	550	0.23	14	4650	1700

To obtain cutting force signals in Cartesian coordinates a Kistler 9257B piezoelectric dynamometer with amplifier was utilized. To avoid Aliasing noise and according to the highest spindle speed and the number of flutes on the cutter, sampling frequency was selected to be 300Hz. In machining of spherical components by moving the cutting tool from the edges to the centre of the work-piece, the cutting area also moves from the highest point on edges toward tool tip at the centre. Cutting speed becomes zero in the centre of workpiece due to the sphericity and therefore, surface quality in this area is decreased. It is highly important to maintain the surface quality in the centre of spherical components, such as in human prosthetic hips, and to avoid losing this surface quality, samples were rotated by 450 according to Figure 2 (A-B) and 5 axis machining was carried out. (The movement of the cutter is shown in Figure 3 (A and B)).

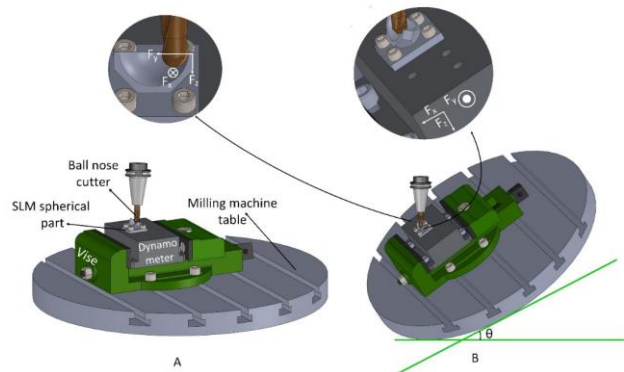


Figure 2 experimental set up

3. ANN Modeling

3.1. Artificial Neural Networks (ANNs)

A statistical learning algorithm based on understanding of the biological neurons is generally referred to as an ANN. This application has been extensively used in modelling and prediction of different industrial operations; such as machining [25-27]. Multi-layer perceptron (MLP) ANN is a suitable application that can be used to predict the behaviour of procedures such as milling or turning, especially when the outputs are not a linearly separable combination of inputs. The mentioned network works on a supervised learning method stated “backpropagation” in the training process. This network has a good capability in functional approximation provided that appropriate selection of hidden layers is made.

In these experiments to obtain an accurate model for functional (force) approximation, tool path, feed rate, spindle speed, scallop height, finishing allowance and heat treatment temperature were selected as inputs and three Cartesian components of cutting force (F_x , F_y and F_z) as outputs. The most efficient network structure was obtained as $6 \times 5 \times 4 \times 3 \times 3$ and Sigmoid transfer function was chosen with a total number of iterations of 5000. In order to train the network 21 samples were used and a validation/test was carried out using three samples to evaluate the accuracy of training and to avoid falling into local extremum during the operation of the model. Also, to verify the accuracy of the designed network eight samples were utilized.

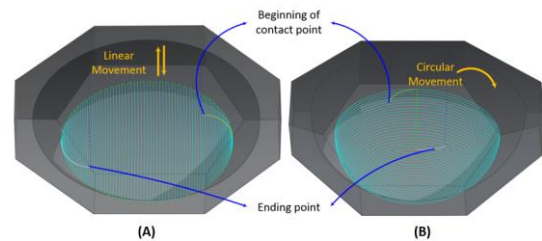


Figure 3 RMS error for (A) Linear movement (B) Circular movement of cutter

3.2. Cross-validation (rotation estimation) and recall procedure

Cross validation/rotation estimation is a model verification approach for evaluating how the results of the statistical computation will generalize to an independent data set. To assess the generality of our model, cross validation was undertaken four times. In each cross-validation 8 samples were used from a DOE list with equal dispersion so all of the experiments were used in both (train+test) and recall procedures to offer a general comprehensive model for cutting force prediction. As indicated in Table 4 the correlation of the training, test/validation and recall for all cross validations were found to be higher than 92% to demonstrate that the designed network is applicable for function approximation in this study.

Table 4 Correlation results for cutting force in cross validations

Force direction	Correlation train %			Correlation test %			Correlation recall %		
	F _x	F _y	F _z	F _x	F _y	F _z	F _x	F _y	F _z
Cross validation									
1 st	99.03	98.92	98.75	91.87	93.26	86.12	87.12	94.54	89.33
2 nd	98.80	99.07	99.06	96.23	89.45	98.32	91.59	93.80	92.06
3 rd	98.57	99.09	99.21	94.98	94.27	99.85	95.31	95.76	96.70
4 th	97.77	98.42	98.65	98.86	98.39	97.50	93.99	93.98	94.56
Averages	98.54	98.88	98.92	95.48	93.84	95.45	92.00	94.52	93.16

4. RESULTS AND DISCUSSION

4.1. Average Contribution of Input Nodes on Outputs

In this section, in order to determine the most influential parameter on cutting force, an interrogator analysis using the proposed ANN was carried out. Interrogator analysis is a specific form of analysis that shows the impact of each parameter by its percentage correlation on the outputs. The average contribution of input nodes on outputs provided a ranking of the most effective parameters on cutting forces from highest to lowest: scallop height > spindle speed > finishing allowance > tool path > heat treatment/annealing temperature > feed rate (Figure 4). Scallop height was found as the most important factor in agreement with the literature. Therefore in the next step interaction analysis for scallop height versus other factors has been carried out.

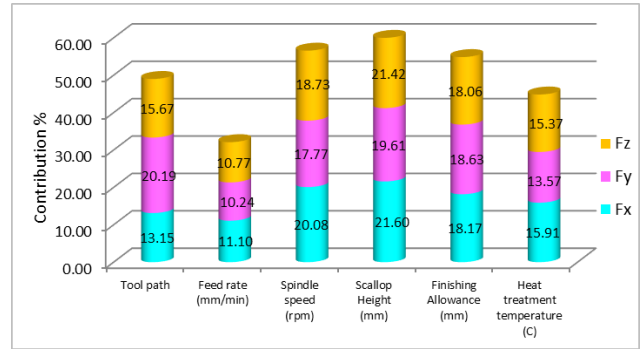


Figure 4 Percentage of input contribution on cutting forces

4.2. The interaction of scallop height versus tool path and feed rate

Figure 5 (A, C and E) also shows that scallop height is the more influential parameter compared to tool path. Also, this Figure depicts that the value of cutting force greatly increased when a helical tool path was used. This is related to the nature of the 5-axis machining. In this research, as stated in section 2.3, in order to obtain better surface quality in the centre of the spherical part, the milling table was rotated about 45° (Figure 5(A)). At the start of the machining with helical tool path, the contact area as shown in Figure 5(B) is the cutting edge which has the highest efficiency. This area is shown by location number 1 in Figure 5(D) and this surface has radial rake angle (Figure 5(C)) to send chips into the helix slot. When cutter moves to the lowest point of the cutter (Figure 5(E)) contact area is changed from point 1 to point 2 in Figure 5(D) and as it is shown this area doesn't have radial rake angle (Figure 5(F)). Therefore, by taking into account of constant radial relief and clearance angles for cutter in both points 1 and 2, wedge angle is increasing and the rake angle is zero.

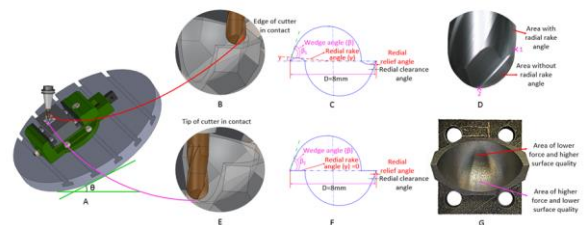


Figure 5 (A) Milling operation (B) material removing by cutter edge (C) cross section of tool in flute area (D) head of the cutter (E) material removing by tip of the cutter (F) cross section of tool in ball head area (G) machined part by helical tool path

The contact edge of cutter will change from Figure 5(C) to 6(F) and this phenomenon is the same as when using a worn tool so the cutting force in this area increased. Another reason for increasing cutting force in helical tool path is shown by moving the cutting area from point 1 to point 2. In Figure 6(D) where the diameter of cutting tool decreases and the contacting/hitting frequency significantly increases (when point 2 in Figure 5(D) is in contact with the workpiece, the dynamic of milling is the same as

turning), taking into account the low elastic modulus for titanium, relatively high levels of spring back and subsequently vibrations were observed. The result is increasing cutting force and an engraving effect, Figure 6 (A, C, E) and Figure 5(G), also shows that this is related to the brittle nature of the SLM process [20, 28, 29]. In the linear tool path, the tip of the cutter in a very tiny area acts as a cutting/contact edge. Therefore lower surface roughness and cutting forces were observed.

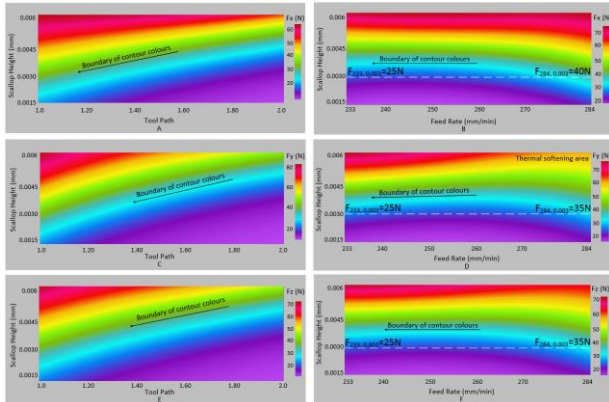


Figure 6 (A, C, E) The interaction of scallop height versus tool path for different force components (B, D, F) The interaction of scallop height versus feed rate for different force components

Figure 6 (B, D and F) show scallop height has higher impact than feed rate on the value of cutting force. By taking into account the force in the cutter as a distributed force [30], it has been mentioned that increasing scallop height leads to increasing contact surfaces and this has direct relation to cutting forces. In this experiment, cutting force increases as a function of increasing feed rate in agreement with the literature. This is a key factor in selection of cutting parameters to avoid workpiece damage and tool wear [9, 25, 26, 31].

4.3. The interaction of scallop height versus heat treatment/annealing temperature

Figure 7 (A-C) shows the interaction of scallop height versus heat treatment/annealing temperature on cutting forces. Analysing this figure shows that scallop height has higher impact on the value of cutting forces compared to heat treatment/annealing temperature. Increasing heat treatment/annealing temperature results in decreasing cutting forces that can be related to the four main issues; microstructure, tensile strength, breaking elongation and macro hardness.

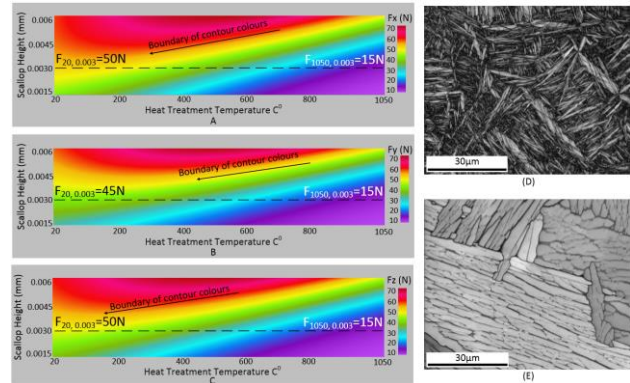


Figure 7 (A, C, E) The interaction of scallop height versus heat treatment temperature for different force components (D) EBSD images for untreated samples (E) β annealing

a) Microstructure of SLM samples

The microstructure of as-built SLM samples has smaller grain size compared to conventional wrought parts related to high cooling rate in the printing process [20, 32-34]. In this investigation, a meander scanning pattern has been used to achieve higher strength and density and due to a temperature elevation and high cooling rate, α' martensitic was observed, increasing tensile strength up to 1.35Gpa and decreasing breaking elongation to 3% [35-37]. Heat treatment procedure below transus temperature is called “ α annealing” including stress relieving and mill annealing. This heat treatment on Ti-6Al-4V alloys results in increasing grain sizes in a fraction of the β phase and relaxation of internal stresses [38]. It is reported that high internal stresses in SLM is released in α annealing by diffusion and dislocation motion [39]. Based on previous research [20] the volume fraction of β in recrystallization annealing (annealing in 900-1000°C) increases to 17.5% and β boundaries becomes a suitable place for nucleation of secondary α so total fraction of α phase increases. Fabrication process in SLM is under controlled atmosphere, but small values of oxygen and nitrogen has been reported in the bulk of printed materials. Ti has high affinity with the mentioned elements in local melting zones. These elements act as a α stabilizer and their existence is a factor of temperature. Thus, bigger grains with α phase were found in β annealing [39-41].

b) Tensile strength

High stability of the lamellar microstructure was found after annealing of printed samples [42, 43]. Due to precipitations in α' -phase, the strength of as-built samples is much higher than wrought parts (about 30%). In mill annealing and stress relieving, due to increase in the grain size, tensile strength decreased slightly. However, in β annealing slow cooling rate causes transformation of β to secondary α and results in significant increase in the α size and formation of coarse α phase and consequently the value of tensile strength decreased to 980Mpa (Figure 8 (A)) [52, 58].

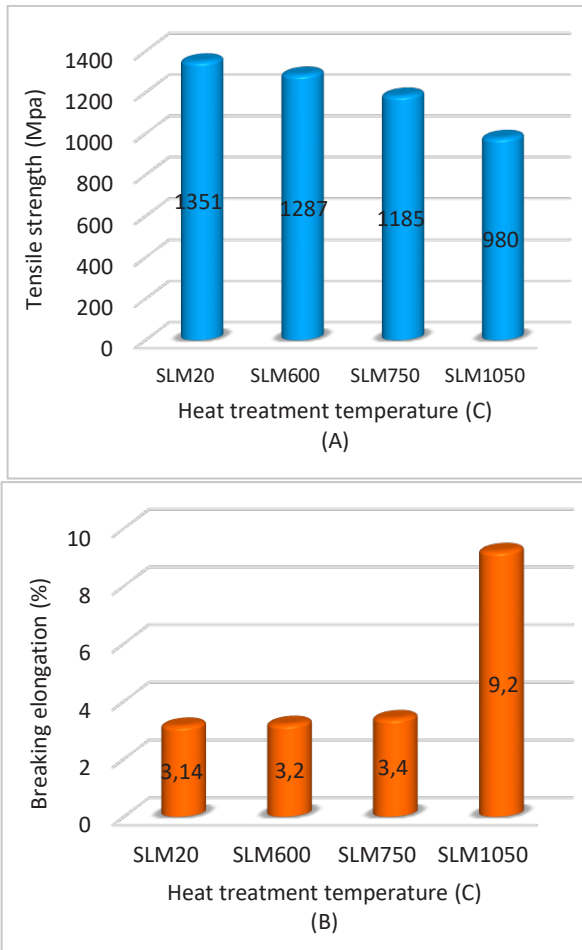


Figure 8 (A) Breaking elongation for various heat treated samples (B) Tensile strength for different annealed samples
Note: 20 means ambient temperature (no heat treatment)

c) Breaking elongation

Small increasing behaviour in the value of elongation was observed in stress relieving and mill annealing. In β annealing, beta growth in residence time then precipitates on α' martensite and because of low cooling rate primary α retains itself and transformation of β to secondary α was observed. This transformation is more significant compared to stress relieving and mill annealing because higher value of β is generated in residence time during beta annealing [19, 37, 42-45].

d) Macro-hardness

In SLM, process parameters, heat affected zones and temperature distribution affect the degree of martensite decomposition which determines the value of hardness. The hardness of as-built Ti-6Al-4V was obtained around 500 HV [46, 47]. This value is about 25% higher than wrought samples that is related to high cooling rate and precipitation of α' martensitic.

Consequently, Figure 7 (D, E), 11 and-12 demonstrate that by increasing annealing temperature the value of

hardness decreased which can explain the falling trend in the value of cutting forces in Figure 7 A-C.

4.4. Cutting force in different directions

Table 5 shows the average value of cutting force in each direction for helical and linear tool paths.

Table 5 The average value of cutting force for each tool path

Helical tool path X (N)	Helical tool path Y (N)	Helical tool path Z (N)	Linear tool path X (N)	Linear tool path Y (N)	Linear tool path Z (N)
44.13	64.04	52.06	52.99	49.05	48.81

This table demonstrates that in helical tool path, due to the longest cutter movement being in the Y direction, the cutting force has the highest value, while for linear tool path the longest movement and force were obtained in X direction.

5. CONCLUSION

In this research characterizing cutting parameters and heat treatment on the generated cutting force in milling of SLM fabricated spherical components have been analysed using numerical application. ANNs appear to possess superior capability to model a variety of parameters such as tool path, feed rate, spindle speed, scallop height, finishing allowance and heat treatment/annealing temperature on both value and trend in cutting force in 5axis machining. Results showed that the most influential parameter on the fluctuation of cutting force is scallop height followed by spindle speed, finishing allowance, tool path, heat treatment temperature and feed rate. Linear tool path produces lower cutting force compared to helical tool path. Increasing feed rate results in a small rising trend in the value of cutting forces, while increasing spindle speed has higher impact in increasing the value of cutting force and mainly is related to raising the value of momentum and strain hardening. Likewise, increasing finishing allowance results in decreasing cutting force which is mainly associated with decreasing cutting pressure and heat affected zones and the minimal contact edge of the cutter. Finally, higher annealing temperature leads to lower hardness and subsequently cutting forces in this study.

6. REFERENCES

- Gibson, I., D.W. Rosen, and B. Stucker, *Additive manufacturing technologies*. 2015: Springer.
- Bourell, D.L., *Perspectives on Additive Manufacturing*. Annual Review of Materials Research, 2016(0).
- Safronov, V., et al., *Distortions and Residual Stresses at Layer-by-Layer Additive Manufacturing by Fusion*. Journal of Manufacturing Science and Engineering, 2017. **139**(3): p. 031017.
- O'Donnell, J., M. Kim, and H.-S. Yoon, *A review on electromechanical devices fabricated by additive*

manufacturing. Journal of Manufacturing Science and Engineering, 2017. **139**(1): p. 010801.

5. Laureijs, R.E., et al., *Metal Additive Manufacturing: Cost Competitive Beyond Low Volumes*. Journal of Manufacturing Science and Engineering, 2017. **139**(8): p. 081010.

6. Chen, C., Y. Shen, and H.-L. Tsai, *A foil-based additive manufacturing technology for metal parts*. Journal of Manufacturing Science and Engineering, 2017. **139**(2): p. 024501.

7. Song, B., et al., *Fabrication and microstructure characterization of selective laser-melted FeAl intermetallic parts*. Surface and Coatings Technology, 2012. **206**(22): p. 4704-4709.

8. Song, B., S. Dong, and C. Coddet, *Rapid in situ fabrication of Fe/SiC bulk nanocomposites by selective laser melting directly from a mixed powder of micro-sized Fe and SiC*. Scripta Materialia, 2014. **75**: p. 90-93.

9. Subrahmanyam, K., et al., *Cutting force prediction for ball nose milling of inclined surface*. The International Journal of Advanced Manufacturing Technology, 2010. **48**(1-4): p. 23-32.

10. Altintas, Y., *Analytical Prediction of Three Dimensional Chatter Stability in Milling*. JSME International Journal Series C Mechanical Systems, Machine Elements and Manufacturing, 2001. **44**(3): p. 717-723.

11. Altintas, Y., *Manufacturing automation: metal cutting mechanics, machine tool vibrations, and CNC design*. 2012: Cambridge university press.

12. Altintas, Y. and P. Lee, *Mechanics and dynamics of ball end milling*. Journal of Manufacturing Science and Engineering, 1998. **120**(4): p. 684-692.

13. Engin, S. and Y. Altintas, *Generalized modeling of milling mechanics and dynamics: Part I—Helical end Mills*. Am. Soc. Mech. Eng. Manuf. Eng. Div.(MED), 1999. **10**: p. 345-352.

14. Tunç, L.T., O.M. Ozkirimli, and E. Budak, *Machining strategy development and parameter selection in 5-axis milling based on process simulations*. The International Journal of Advanced Manufacturing Technology, 2015: p. 1-18.

15. Gradišek, J., M. Kalveram, and K. Weinert, *Mechanistic identification of specific force coefficients for a general end mill*. International Journal of Machine Tools and Manufacture, 2004. **44**(4): p. 401-414.

16. Ng, E.-G., et al., *High speed ball nose end milling of Inconel 718*. CIRP Annals-Manufacturing Technology, 2000. **49**(1): p. 41-46.

17. Amir Mahyar Khorasani, I.G., Moshe Goldberg, Guy Littlefair, *Production of Ti-6Al-4V acetabular shell using selective laser melting: possible limitations in fabrication*. Rapid Prototyping Journal, 2016. **In press**.

18. Joshi, V.A., *Titanium alloys: an atlas of structures and fracture features*. 2006: CRC Press.

19. *ASM Handbooks online Volume 2, Properties and Selection: Nonferrous and specialpurpose Materials, Titanium and Titanium Alloy Castings Product Application Vol. 2*. 2010, America: ASTM international.

20. Amir Mahyar Khorasani, I.G., Moshe Goldberg, Guy Littlefair, *On The Role of Different Annealing Heat Treatments on Mechanical Properties and Microstructure of Selective Laser Melted and Conventional Wrought Ti-6Al-4V* Rapid Prototyping Journal, 2016. **In press**.

21. Mark, A., Y. Xu, and J. Gou, *Deposition Thickness Modeling and Parameter Identification for a Spray-Assisted Vacuum Filtration Process in Additive Manufacturing*. Journal of Manufacturing Science and Engineering, 2017. **139**(4): p. 041002.

22. Wolcott, P.J., et al., *Seam Welding of Aluminum Sheet Using Ultrasonic Additive Manufacturing System*. Journal of Manufacturing Science and Engineering, 2017. **139**(1): p. 011010.

23. Korani, M. and R. Goshe, *Tool selection in machining of selective laser melting based on artificial neural networks and regression models*. Journal of Manufacturing Technology, 2016. **14**(6): p. 60-69.

24. Korani, M. and A. Lotfi, *Heat treatment of titanium alloys produced by selective laser melting*. Journal of Manufacturing Technology, 2015. **13**(2): p. 70-76.

25. Khorasani, A. and M.R. Soleymani Yazdi, *Development of a dynamic surface roughness monitoring system based on artificial neural networks (ANN) in milling operation*. The International Journal of Advanced Manufacturing Technology, 2015: p. 1-11.

26. Khorasani, A.M., et al., *Investigation on the effect of cutting fluid pressure on surface quality measurement in high speed thread milling of brass alloy (C3600) and aluminium alloy (5083)*. Measurement, 2016. **82**: p. 55-63.

27. Khorasani, A.M., M.R. Soleymani Yazdi, and M.S. Safizadeh, *Tool Life Prediction in Face Milling Machining of 7075 Al by Using Artificial Neural Networks (ANN) and Taguchi Design of Experiment (DOE)*. International Journal of Engineering and Technology, 2011. **3**(1): p. 30.

28. Ezugwu, E. and Z. Wang, *Titanium alloys and their machinability—a review*. Journal of materials processing technology, 1997. **68**(3): p. 262-274.

29. Li, C., et al., *Hot Deformation of Ti-5Al-5Mo-5 V-1Cr-1Fe Near β Titanium Alloys Containing Thin and*

Thick Lamellar α Phase. Materials Science and Engineering: A, 2013. **573**: p. 75-83.

30. Khorasani, A.M., et al., *An Improved Static Model for Tool Deflection in Machining of Ti-6Al-4V Acetabular Shell Produced by Selective Laser Melting*. Measurement.

31. Khorasani, A.M., M.R.S. Yazdi, and M.S. Safizadeh, *Analysis of machining parameters effects on surface roughness: a review*. International Journal of Computational Materials Science and Surface Engineering, 2012. **5**(1): p. 68-84.

32. Attar, H., et al., *Manufacture by selective laser melting and mechanical behavior of commercially pure titanium*. Materials Science and Engineering: A, 2014. **593**: p. 170-177.

33. Murr, L., et al., *Microstructure and mechanical behavior of Ti-6Al-4V produced by rapid-layer manufacturing, for biomedical applications*. Journal of the mechanical behavior of biomedical materials, 2009. **2**(1): p. 20-32.

34. Vrancken, B., et al., *Heat treatment of Ti6Al4V produced by Selective Laser Melting: Microstructure and mechanical properties*. Journal of Alloys and Compounds, 2012. **541**: p. 177-185.

35. Gu, D., et al., *Densification behavior, microstructure evolution, and wear performance of selective laser melting processed commercially pure titanium*. Acta Materialia, 2012. **60**(9): p. 3849-3860.

36. Weingarten, C., et al., *Formation and reduction of hydrogen porosity during selective laser melting of AlSi10Mg*. Journal of Materials Processing Technology, 2015. **221**: p. 112-120.

37. Sieniawski, J., et al., *Microstructure and mechanical properties of high strength two-phase titanium alloys*. Titanium Alloys-Advances in Properties Control, 2013: p. 69-80.

38. Baufeld, B., E. Brandl, and O. van der Biest, *Wire based additive layer manufacturing: Comparison of microstructure and mechanical properties of Ti-6Al-4V components fabricated by laser-beam deposition and*

shaped metal deposition. Journal of Materials Processing Technology, 2011. **211**(6): p. 1146-1158.

39. Gorny, B., et al., *In situ characterization of the deformation and failure behavior of non-stochastic porous structures processed by selective laser melting*. Materials Science and Engineering: A, 2011. **528**(27): p. 7962-7967.

40. Baufeld, B., O.V.d. Biest, and R. Gault, *Additive manufacturing of Ti-6Al-4V components by shaped metal deposition: Microstructure and mechanical properties*. Materials & Design, 2010. **31**, Supplement 1: p. S106-S111.

41. Santos, E., et al., *Mechanical properties of pure titanium models processed by selective laser melting*. Proceedings of the Solid, 2002.

42. Welsch, G., R. Boyer, and E. Collings, *Materials properties handbook: titanium alloys*. 1993: ASM international.

43. Yadroitsev, I., P. Krakhmalev, and I. Yadroitsava, *Selective laser melting of Ti6Al4V alloy for biomedical applications: Temperature monitoring and microstructural evolution*. Journal of Alloys and Compounds, 2014. **583**: p. 404-409.

44. Li, X., et al., *Effect of substrate temperature on the interface bond between support and substrate during selective laser melting of Al-Ni-Y-Co-La metallic glass*. Materials & Design, 2015. **65**: p. 1-6.

45. Jovanović, M., et al., *The effect of annealing temperatures and cooling rates on microstructure and mechanical properties of investment cast Ti-6Al-4V alloy*. Materials & design, 2006. **27**(3): p. 192-199.

46. Thijs, L., et al., *A study of the microstructural evolution during selective laser melting of Ti-6Al-4V*. Acta Materialia, 2010. **58**(9): p. 3303-3312.

47. Chlebus, E., et al., *Microstructure and mechanical behaviour of Ti-6Al-7Nb alloy produced by selective laser melting*. Materials Characterization, 2011. **62**(5): p. 488-495.

Study on manufacturing implants of biocomposite materials by water jet cutting

Ioan Alexandru Popan, Technical University of Cluj-Napoca, B-dul. Muncii, 400641, No. 103-105, Cluj-Napoca, Romania, ioan.popan@tcm.utcluj.ro

Nicolae Balc, Technical University of Cluj-Napoca, B-dul. Muncii, 400641, No. 103-105, Cluj-Napoca, Romania, nicolae.balc@tcm.utcluj.ro

Alina Ioana Popan, Technical University of Cluj-Napoca, B-dul. Muncii, 400641, No. 103-105, Cluj-Napoca, Romania, alina.luca@tcm.utcluj.ro

Abstract—This paper presents a case study on processing with abrasive water jet cutting the external contour of the implants made by biocomposite materials. A new biocomposite material, E-glass fiber reinforced composites, is used for manufacturing a personalized implant. It was developed to serve cranio-facial bone reconstruction. Abrasive water jet cutting was proved to be a proper solution for this application. A good surface quality and a high dimensional accuracy was obtained.

Keywords- Water jet cutting, Composite materials, Implant

1. INTRODUCTION

Composite materials are wide used in automotive and aerospace industries, medical fields, etc [1]. The most important characteristics of this materials are: corrosion and thermal resistance, high strength and low weight ratio [2].

In medical field this type of material is known as biocomposite material. The biocomposite material is composed from a matrix reinforced with fibers [3]. The research in this field is focused onto development of new biodegradable and biocompatible composite materials. To manufacture a complex part, as an implant, a custom mould is needed. To obtain the final shape a contour cutting is required [4].

Abrasive water jet cutting (AWJC) process could be a proper solution for cutting complex shapes in composite materials [5, 6]. The main characteristics are: high surface quality, good dimensional accuracy, no thermal stresses and low cost [7].

This paper presents the possibilities to process, using water jet cutting, a personalized implant made from a new biocomposite material, E-glass fiber reinforced composites. It was developed to serve cranio-facial bone reconstruction [3, 4].

2. EXPERIMENTAL PROCEDURE

The 3D model of the implant (Fig. 1) was made using Mimics Research software application. The model was designed starting from the 3D model of the scanned bone.

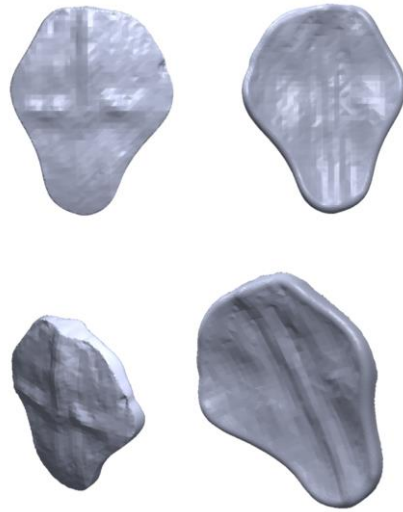


Figure 1. The 3D model of the implant.

Using the 3D model was generated the 2D sketch of the external contour of the implant (Fig. 2), on normal direction. This operation was made using SolidWorks software.

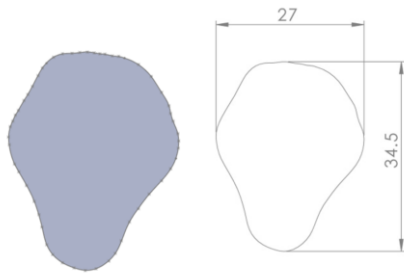


Figure 2. The 2D sketch of the external contour of the implant.

The 2D sketch was imported in Omax Layout software. For processing this 2D complex contour, it was converted as a DXF file (Fig. 3).

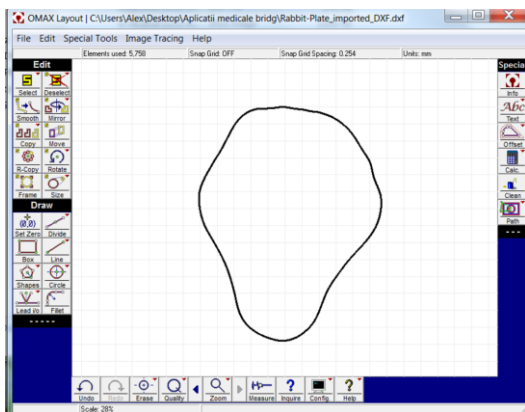


Figure 3. The 2D sketch opened in Omax Software.

Because we have to cut a very small part (27 x 34.5 mm), it must be clamped on the table with tiny bridges. To obtain this bridges the sketch was modified like in figure 4.

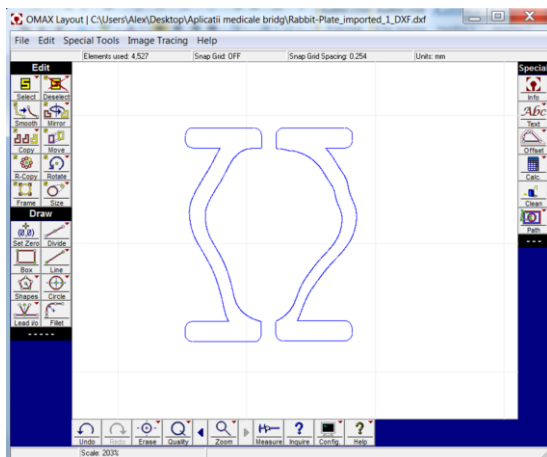


Figure 4. The cutting path.

To control the equipment and to setup the parameters Omax Make - CAM software is used (fig. 5).

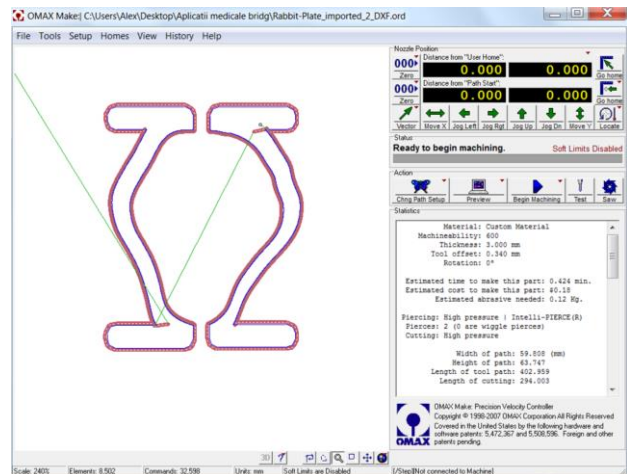


Figure 5. Omax Make - CAM software.

For this experimental research an abrasive waterjet center, Omax 2626 was used. The machine has an OMAX high pressure pump (max.400 MPa) and the cutting head is moved simultaneously on the 3 axes. The cutting parameters used are: sample thickness of 3 mm, pressure 350 MPa, feed rate 1000, mm/min, abrasive type / size Australian Garnet / 80 mesh, abrasive mass flow 0.440 kg/min, nozzle diameter 0.76 mm, orifice diameter (diamond) 0.35 mm, standoff distance 1 mm.



Figure 6. The workpiece.

The sample is a 3 mm thickness 3D part made from biocomposite material. The workpiece is presented in figure 6.



Figure 7. The processed implant.

The final implant was removed from the workpiece, in a manually way. The last step was the deburring and manual polishing. The implant is presented in figure 8.



Figure 8. The impland made by E-glass fiber reinforced composites.

3. RESULTS AND DISCUSSIONS

To evaluate the possibility of using the abrasive water jet cutting process for implant processing, the cut surface quality was studied. To make this measurement was used a Mitutoyo SJ-210 equipment.

The surface was measure in three zones: 1 mm under the top of the surface (Ra 5.1 μm), in the middle of the surface (Ra 2.9 μm) and 1 mm over the bottom of the surface (Ra 6.3 μm).

To evaluate the dimensional accuracy a microscope, type PG 2000 was used. On the kerf geometry a taper angle of 0.5° and a top edge radius of 0.25 mm were obtained. Analyzing the dimensional accuracy of the cut contour, the deviation is between -0.01 up to -0.08 mm.

4. CONCLUSIONS

A new biocomposite material, E-glass fiber reinforced composites was proceeced by abrasive water jet cutting. Cutting the external shape of the implant, a good surface quality and high dimensional accuracy was obtained. The maximum surface roughnes, Ra 6.3 μm , on the bottom zone of the cut surface was obtain. In the case of dimensional accuracy of the cut contour, the deviation is between -0.01 up to -0.08 mm. Must be noted that, the kerf has 0.5° taper angle and the top edge radius is 0.25 mm.

ACKNOWLEDGEMENT

This work was supported by a grant of the Romanian National Authority for Scientific Research and Innovation, CNCS/CCCDI-UEFISCDI, project number PN-III-P2-2.1-BG-2016-0216, within PNCDI III, Internal Competition CICDI-2017 and the H2020 AMaTUC project (GA 691787).

REFERENCES

- [1] Vitale P., Francucci G., Rapp H., Stocchi A., 2018, 'Manufacturing and compressive response of ultra-lightweight CFRP cores', *Composite Structures*, 194, pp. 188-198.
- [2] Popescu A., Hancu L., Bere P., 2013, 'Research concerning the optimum extrusion temperature for reinforced polyamide', *Applied Mechanics and Materials*, 371, pp. 394-398.
- [3] Lazăr MA, Prejmerean C, Prodan D, Roman CR, Bere P, Armencea G, Rotaru H, Crişan B, Bran S, Băciuş M, Băciuş G, Băbţan AM, Câmpian RS., 2018, 'Investigation of the morphology and structure of E-glass fiber-reinforced composites for cranio-facial custom-made implants'. Zilele Universităţii de Medicină şi Farmacie „Iuliu Haţieganu”, Cluj-Napoca, România, 201
- [4] Vitale P., Francucci G., Rapp H., Stocchi A.: Manufacturing and compressive response of ultra-lightweight CFRP cores, *Composite Structures*, 194, pp. 188-198.
- [4] Lazăr M.A., Rotaru H., Roman R., Armencea G., Bosca B., Berce C., Prejmerean C., Prodan D., Balc N, Bere P., 2017, 'Biological behavior of new E-glass fiber reinforced composite for craniofacial bone reconstruction'. COST MP1301 NEWGEN *Biomaterials for Dental and Orthopedic Applications*, Cluj-Napoca, România.
- [5] Shanmugam D.K., 2008, 'A study of delamination on graphite/epoxy composites in abrasive waterjet machining', *Composites: Part A*, 39, pp. 923-929.
- [6] Popan I.A., Balc N., Carean A., Luca A., Ceclan V., 2015 'Developing a new program to calculate the optimum water jet cutting parameters', *Academic journal of manufacturing engineering* 9 (3)
- [7] Popan I.A., Contiu G., Campbell I., 2017, 'Investigation on standoff distance influence on kerf characteristics in abrasive water jet cutting of composite materials', *MATEC Web of Conferences* 137, 01009.

Design for Additive Manufacturing of a Sweat Gland Simulator

Ioan Turcin, CAMPUS 02 University of Applied Sciences, Graz, Austria, ioan.turcin@campus02.at

Cosmin Cosma, Technical University of Cluj-Napoca, Romania, cosmin.cosma@tcm.utcluj.ro

Ali Abdallah, CAMPUS 02 University of Applied Sciences, Graz, Austria, ali.abdallah@campus02.at

Nicolae Balc, Technical University of Cluj-Napoca, Romania, nicolae.balc@tcm.utcluj.ro

Abstract: This paper presents our current efforts to develop a system able to simulate the human body sweating process in various conditions. We designed a human torso and a sweat gland simulator. The parts were designed for Additive Manufacturing (AM), which represents an efficient method to directly produce complex parts. The main purpose of this study was to design the sweat gland simulator according to AM requirements, in order to avoid support structures inside the model's holes and channels. The support structures inside these narrow parts are difficult to remove after fabrication. Moreover, the orientation of parts on the AM working platform was taken into consideration. To test and validate the design, the sweat gland device was SLA printed. The dimensional deviations were determined.

Keywords: virtual model; human torso; sweat gland simulator; fused deposition modelling; stereolithography; sweating

1. INTRODUCTION

Explored by many researchers, the simulation of the human body sweating has become over the years a major area of interest for many industries within the field of textile, protective garments, aeronautics, automotive industries, and sports [1]. Nowadays, there is various software solutions used for the design of different parts for prototyping, which are very flexible and allows a wider range of opportunities to develop very useful components. The available infrastructure offers us a good opportunity to produce prototypes via Additive Manufacturing (AM). A variety of studies showed that AM technologies are proper to manufacture prototypes, moulds, complex parts, and anatomical implants [2], [3], [4], [5], [6].

From the area of AM, the Fused Deposition Modelling (FDM) is certainly one of the well-known. The components are generated sequential, layer-by-layer, by melting thermoplastic filaments. Previous work explored the high importance of the determination of the optimal values of melting temperatures of thermoplastic materials and the quality of the exterior surfaces of the parts obtained

by these technologies [7], [8]. The melting temperature of the plastic and the thermal conditioning in the installation space of the printer can also influence the quality of produced parts.

On the other hand, Stereolithography (SLA) is not only the oldest but also a process, which delivers parts with good surface quality and fine details, created by a local polymerization of the initially liquid monomers [9]. It involves scanning with an ultraviolet beam of a liquid photo-polymer resin [10]. The resin polymerized layer by layer in a similar manner to FDM. These AM technologies could allow a flexible, modular and customized production of parts. However, these parts are anchored to AM platform by supports structures and cleaning those structures is time consuming.

The main objective of this experimental study was to design a virtual model of sweat gland simulator according to AM requirements, in order to avoid supports structures inside the holes and channels, where support structure are difficult to remove. Furthermore, our design was develop considering the proper orientation of the part on the AM working platform. To develop an efficient device, firstly we design a human torso shell to simulate the fixation of the sweating device. Both models were designed to be printed using available AM systems (FDM for human torso and SLA for sweat gland simulator device). These components will be parts of a sweating system.

For the designing and analysing the 3D models, the following software tools were used:

- Creo Parametric and SolidWorks to design the anatomical surfaces.
- Realizer, Meshmixer and RDesigner to optimize the orientation of the part on the FDM/SLA platform, to slice the model and to simulate the AM processes.
- SolidWorks and Meshmixer to analyze the outer boundary thickness and the surface normal.

- Blender and Meshmixer to correct the defects in STL files.

2. HUMAN TORSO DESIGN

In this study, we designed a virtual human torso respecting the anatomy of the human body. Moreover, we limited the structure of human torso to a shell with 5 mm thickness, which contains a solid outer boundary.

Initially, we analyse the following areas: neck and nuchal area, shoulder, thorax, axilla, abdomen, back, navel, hip, pelvis and arms [11], [12]. Based on the human muscles system, the following muscle groups were modelled: trapezium, large pectoral muscle, deltoid muscle, oblique abdominal muscle, the large dorsal and fessler (detailed in Figure 1). Also, open sources have been considered (e.g. www.grabcad.com). The design of the human torso is based on anatomy of a 25 - 35 years old male, clinically healthy, and with athletic constitution. Initially, to develop the outer profile of the torso, Bezier curves were drawn. Based on these curves, the 3D model with anatomical surfaces was designed (Figure 2).

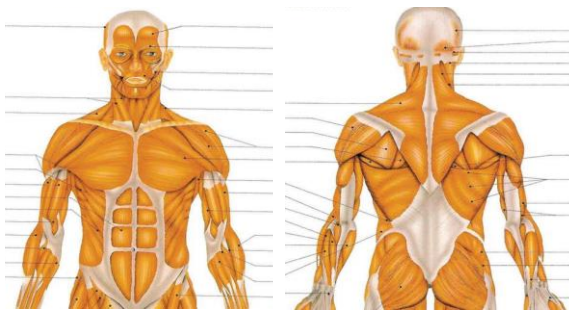


Figure 1. Man’s torso-muscles: front and dorsal view [17]

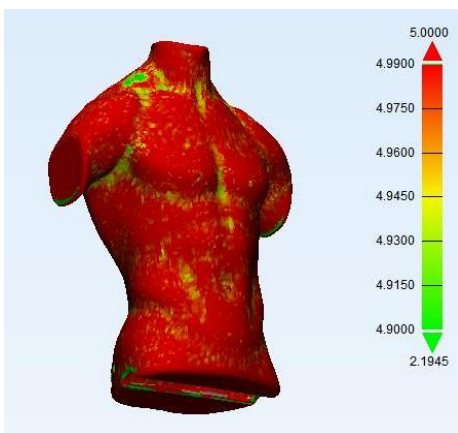


Figure 2. Thickness analysis of virtual male torso (isometric view)

In order to be FDM-manufactured, the 3D model was reduced with more than 50% compare to a real body (the final overall dimensions are 220 mm x 120 mm x 300 mm). Initially, the classic method of exporting the “.STL” format was used, but major deficiencies were found in the exported model (above 1800 errors). To correct the defects, we used Blender and Meshmixer software. Next, we analysed the outer boundary thickness and 97% of the surfaces possess a depth between 4.9 - 5.0 mm (see Figure 2).

Based on the recommendations of the German VDI 3405 standard, regarding the orientation of parts on AM equipment’s, we simulated the FDM processing using Optimaker 2+ Extended and Makerbot Replicator Z18 systems. These simulations undertaken suggest the fact that this human torso could be manufactured vertical without supports structures inside of it or with limited supports in external areas. Moreover, the consumption of PLA material was estimated at 748 g, because the FDM process will fabricate just a shell of the human torso.

3. SWEAT GLAND SIMULATOR DESIGN

As mentioned in the introduction, the human torso is considered as a basic framework for the sweat gland simulator system (including sensors), which could be mountable at chosen location of the human body. The basic concept of the sweating system is illustrated in Figure 3, sensors to measure the humidity and temperature could be integrated.

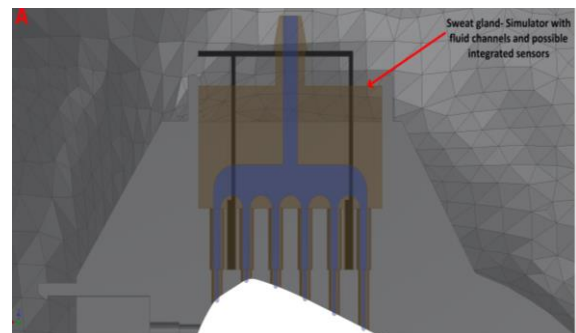
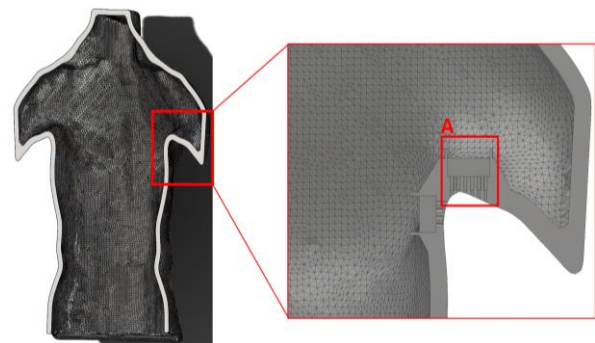


Figure 3. The concept of sweating system contains a human torso and a sweat gland simulator

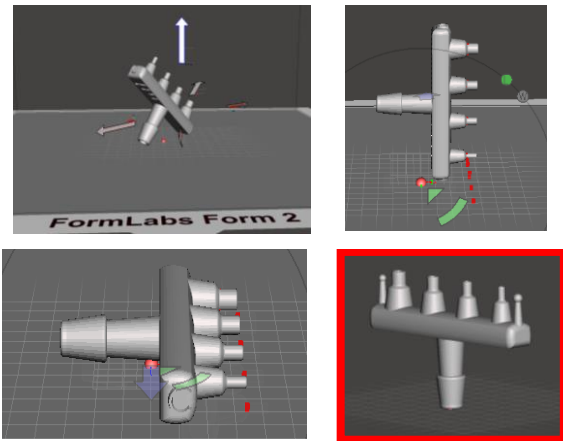


Figure 4. Simulation regarding the orientation of sweat gland simulator device on SLA platform

In order to control and to measure the sweating process, we design a prototype for SLA manufacturing. Since is challenging to remove the supports structures from channels, in the present study we developed channel profiles that do not requires support structures. In addition, we considered the orientation of the part on the SLA platform. Figure 4 shows the result of simulation regarding the orientation of sweat gland simulator on SLA platform. The vertical orientation has been chosen as the proper one because the supports structures are limited on outside surfaces where are easy-to-clean (Figure 4, the picture from red square). Thus, taking into account this orientation on the SLA platform, the device was designed (see Figure 5). Some details regarding the cross sections of channels are presented in Figure 6.

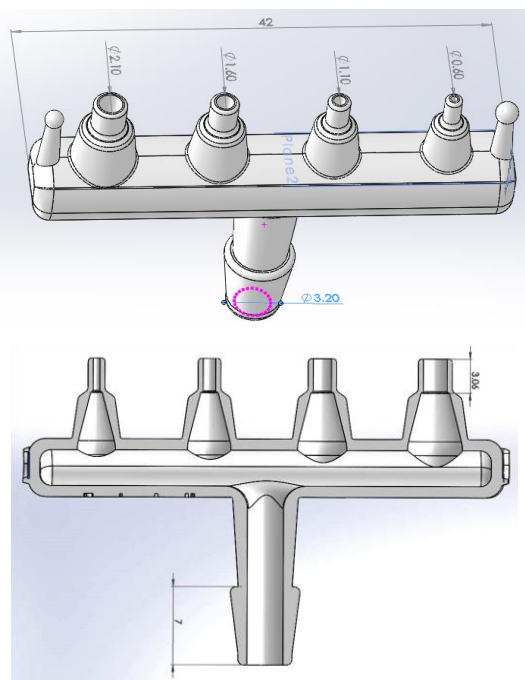


Figure 5. The design of sweat gland simulator

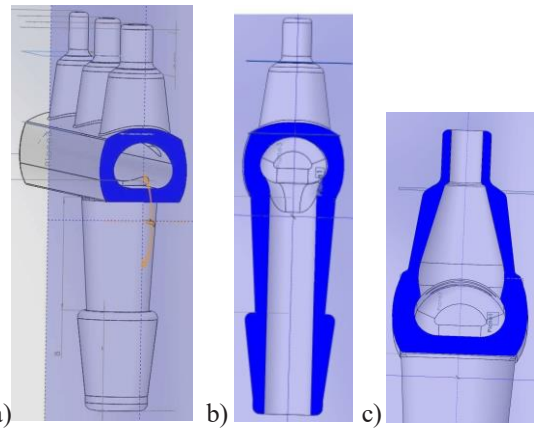


Figure 6. Cross sections of sweat gland device: a) The distribution channel, b) The main channel for liquid access, c) The evacuating channel

The sweat gland device contains a main liquid supply channel, which distributes the liquid through four holes (Figure 6b). The main channel can facilitate the connectivity to various pump equipment's, having 3.2 mm diameter (Figure 6b). The cross section of the distribution channel is illustrated in Figure 6a and possesses maximum 4.63 mm and 3.20 mm height. The evacuation channels have the diameters between 0.6 - 2.1 mm (see Figure 5 and Figure 6c), and they were designed larger with +0.1mm because it is known that the accuracy of SLA manufactured parts is ± 0.1 mm. With this design, we suppose that the final diameter of holes will be between 0.5 - 2.0 mm. After CAD design, the 3D model was exported in STL format. To avoid the surface defects, the STL file was exported with a fine resolution, a nominal tolerance of 0.0124 mm and an angular surface tolerance of 10° .

The analysis of the projected surfaces was performed using the Mesh query function. This tool visualizes pre-defined quantities over the entire mesh, and it reports numeric values for metrics on individual triangles and vertices. The method shows a colour map of the surface normal over the object. Red, green, and blue values correspond to absolute values of the X, Y, and Z components of the surface normal vector at a point on the mesh (see Figure 7a, vertical orientation on SLA platform).

To estimate the volume and the mass of the sweat gland device, clear standard resin was considered. This material carries proper mechanical properties for prototypes, similar with other plastics used in AM [13]. The simulation of SLA manufacturing was elaborate using Formlabs Form 2 equipment. It results that one part will consume up to 3 g of resin, less compared to conventional manufacturing [14], [15]. In order to have a fast and efficient SLA process, the wall thickness of part was reduced throughout the design process. The average wall thickness is between 0.8 - 1.6 mm in 69.5% of the analysed surfaces (detailed in Figure 7b).

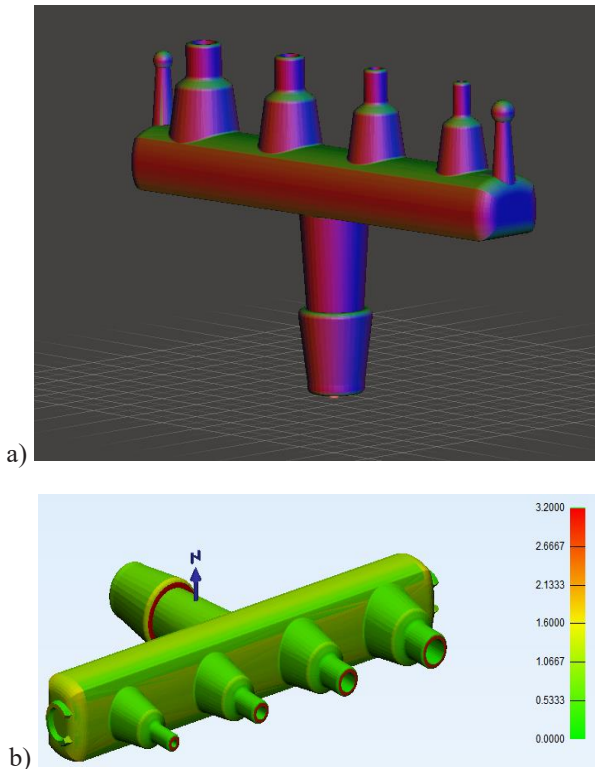


Figure 7. Design evaluation: a) Mesh query (surface normal), b) Thickness analysis

In order to test and validate the design of the sweat gland simulator, we printed 4 prototypes via SLA. The fabrication was done by Formlabs Form 2 system. This SLA equipment has a 405nm violet laser (250mW) and 140 microns the spot size. The clear photoreactive resin was used. This liquid resin is a mixture of methacrylic acid esters and photoinitiator standard resin. The layer thickness was set up at 0.05 mm and it resulted 623 layer with support structures. The supports were added just on outside surfaces where were easy-to-clean, due to vertical orientation of parts on SLA platform (Figure 8a). The SLA process lasted 2 hours 44 minutes and we printed 4 parts illustrated in Figure 8b. After SLA processing, the parts were clean with isopropanol in a ultrasonic bath, clean with compressed air and irradiated with UV for curing. The post-processed parts are shown in Figure 9.

Using the design detailed previous, we printed good sweat gland simulators avoiding the support structures into channels. All the channels were manufactured, even the evacuation channels with minimum diameter. Also, we measured the diameters obtained on the main channel and on the evacuating holes. The results are listed in Table 1. The dimensional deviations determined were between -0.03 mm and -0.07 mm, as we expected.

TABLE 1. DIMENSIONAL ACCURACY OBTAINED ON SLA MANUFACTURED SWEAT GLAND SIMULATOR

Characteristic	Designed diameter [mm]	SLA-manufactured diameter [mm]	Dimensional deviations [mm]
Main channel hole	3.20	3.14	-0.06
Evacuating hole 1	2.10	2.07	-0.03
Evacuating hole 2	1.60	1.57	-0.03
Evacuating hole 3	1.10	1.03	-0.07
Evacuating hole 4	0.60	0.55	-0.05

In this study, we analysed four different diameters of evacuating holes to test the minimum diameter, which can be produced by SLA in this condition and orientation. The sweat gland simulator developed will be used in future studies to analyse and simulate the sweating process and will allow us to decide the optimal profile of the evacuating channel. More studies will be elaborate to create a sweating device completed with various sensors or fluidic micro-electro-mechanical systems. It is known that the fluidic micro-electro-mechanical systems are designed to interact with fluid-based system as micro-pumps or micro-valves [16].

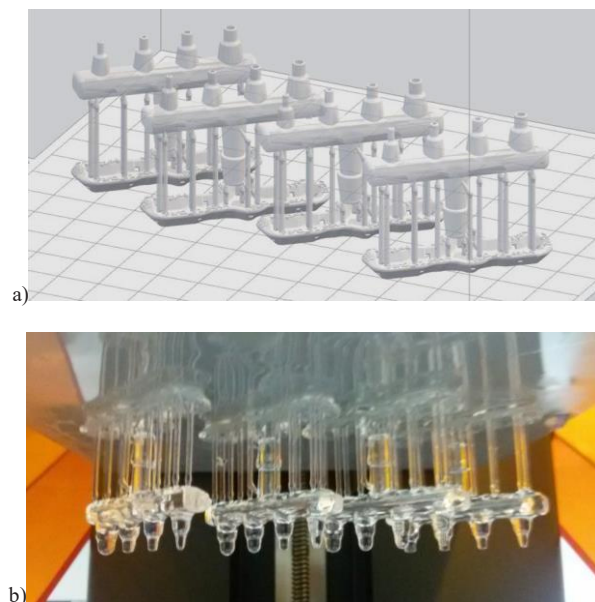


Figure 8. Sweat gland simulator: a) The virtual model orientated vertical on SLA platform and the supports structures were sustained just the outer surfaces, b) SLA-manufactured parts

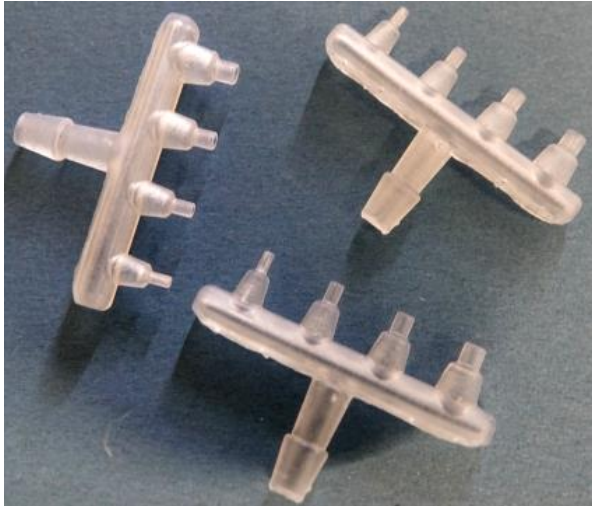


Figure 9. Sweat gland simulators after post-processing

In order to implement the modularity of the sweat gland simulator, we designed and FDM manufactured a plate with four holes and four snap joints (Figure 10). To print the plate, we used an Ultimaker S5 equipment and PLA filament. The snap-fit cantilevered lug, will allow us to couple these devices in various locations on the human torso. After the joining operation, the snap-fit features should return to a stress-free condition. Figure 11 shows the assembly of a sweat gland simulator on the plate.

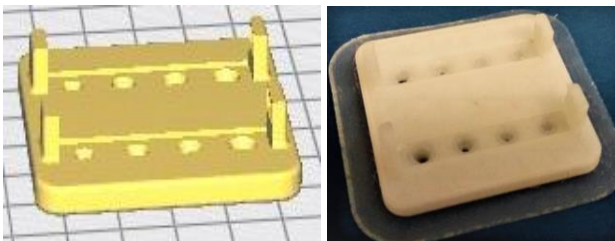


Figure 10. Plate with snap joints: a) 3D model, b) FDM-manufactured



Figure 11. Sweat gland simulator on modular plate

4. CONCLUSIONS AND OUTLOOK

The current case study describes the design for AM process of a human torso and a sweat gland simulator. These parts should be the main components of a sweating system. To test and validate the design developed, which was focused on channel shapes, the sweat gland simulator was manufactured via SLA process without supports inside of channels. Using an optimal orientation on SLA platform, we manufactured a few sweat gland simulator devices with dimensional deviations between -0.03 mm and -0.07 mm. Moreover, to implement the modularity of the sweat gland simulator, we designed and FDM manufactured a special plate with snap joints, which will allow us to couple these devices in various locations on the human torso.

Considerably more work will need to be done, to develop a modular sweating system, in which could integrate sensors to measure the humidity and temperature. This paper provides the main steps developed to design for AM some prototypes parts, focused on avoiding the support structures in channels where are hard to remove. The framework for future development of a feasible system to simulate the sweating process with different parameters was established.

ACKNOWLEDGMENT

The OpTi-DeP Project supported this paper (no. BG101/2016) financed from the UEFISCDI by the Romanian Government, and within the H2020 AMaTUC project (GA 691787).

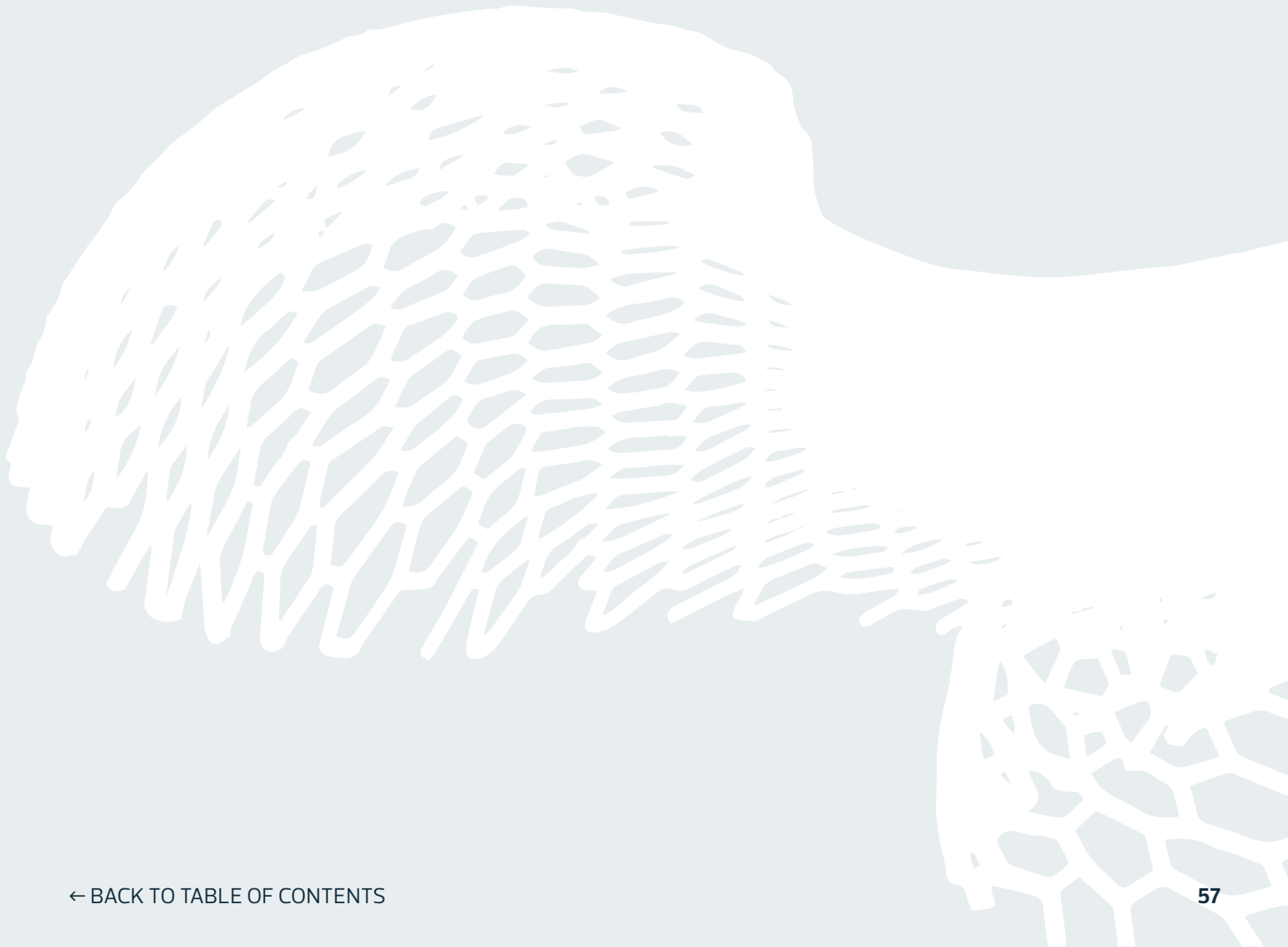
REFERENCES

- [1] Turcin, I., Softic, S., Traussnigg, U., Trif, A., Initial Study on the State of the Art Solutions for the Simulation of the Thermoregulatory Sweating Conditions, *MATEC Web Conf.*, 01016 (137), p. 1-8, 2017.
- [2] Ligon, S., C., Liska, R., Stampfl, J., Gurr, M., Mülhaupt, R., Polymers for 3D Printing and Customized Additive Manufacturing, *Chem. Rev.*, 2017, 117 (15), p. 10212–10290, DOI: 10.1021/acs.chemrev.7b00074.
- [3] Cosma, C., Balc, N., Berce, P., Popan, A., Cosma, A., Burde, A., Direct manufacturing of customized implants from biometals, by 3D printing, *Academic Journal of Manufacturing Engineering*, Vol. 15, Issue 4, p. 42-49, 2017.
- [4] Armencea, G., Berce, C., Rotaru H., Bran, S., Leordean D., Lazar M., Baciut G., et all, Titanium alloys with hydroxyapatite or SiO₂+TiO₂ coatings used in bone reconstruction, *Optoelectron. Adv. Mat.*, vol. 9(5), p.865-868, 2015.
- [5] Doicin, C.V., Ulmeanu, M.E., Neagu, C., Popa, L., Designing and prototyping a bespoke spinal implant using additive technologies, *Revista Materiale Plastice*, vol.53(1), p. 139-143, 2016.
- [6] Pacurar, R., Berce, P., Research on the durability of injection molding tools made by selective laser sintering technology *Romanian Academy Series A - Mathematics Physics Technical Sciences Information Science*, vol.14 (3), p. 234-241, 2013.
- [7] Popescu, A., Contribuții privind îmbunătățirea procesului de extrudare a materialelor compozite polimerice armate cu fibre scurte, Teză de doctorat, Cluj-Napoca, 2011.
- [8] Sever, A. R., Popescu, A. C., Balc, N., Panc, N., Experimental determination of surface roughness of parts obtained by rapid

- prototyping, Proceedings in *ARSA-Advanced Research in Scientific Areas*, Vol. I, 2014/12.
- [9] Gebhardt, A., Understanding Additive Manufacturing, *Rapid prototyping, Rapid tooling, Rapid manufacturing*, ISBN 978-3-446-42552-1, Carl Hanser Verlag, Munich, p. 34, 2012.
- [10] Moldovan, C., Cosma, C., Berce, P., Balc, N., Theoretical analysis and practical case studies of sla, polyjet and fdm manufacturing techniques, *ACTA TECHNICA NAPOCENSIS, Series: Applied Mathematics, Mechanics, and Engineering*, Vol. 61, 2018.
- [11] Benea H., d'Astorg H., Klouche S., Bauer T., Tomoaia G., Hardy P., Pain evaluation after all-inside anterior cruciate ligament reconstruction and short term functional results of a prospective randomized study, *Knee Journal*, vol.21(1), p. 102-106, 2014, doi: 10.1016/j.knee.2013.09.006.
- [12] Burde, A., Gasparik, C., Moldovan, M., Baci, S., Cosma, C., In vitro evaluation of accuracy of single dies captured by two intraoral digital scanners, *Revista Materiale Plastice*, vol. 55 (2), p. 176-178, 2018.
- [13] Borzan, C., Dulescu, C., Ceclan, V., Trif, A., Ridzon, M., Berce, P., PA 2200 vs. PMMA: Comparison Between the Mechanical Properties Obtained for the 2 Biocompatible Materials, *Revista Materiale Plastice*, vol. 53(1), 2016.
- [14] Popan, I.A., Carean, A., Luca, A., Ceclan, V., Balc, N., Research on 3D metal sculpturing by water jet cutting versus CNC machining, *Academic Journal of Manufacturing Engineering*, vol. 11(4), p. 74-79, 2013.
- [15] Soporan, S. V., Crișan, M., Lehene, T., Pop, A. L., Methodology for appreciation the manufacturing castings from perspective of circular economy, *IOP Conf. Series: Materials Science and Engineering*, vol. 133, Article number 012063, 2016.
- [16] Pustan, M., Birleanu, C., Rusu, F., Haragas, S., Dynamic Behavior of MEMS Resonators, *Applied Mechanics and Materials*, Vol. 658, p. 694-699, 2014, doi.org/10.4028/www.scientific.net/AMM.658.694 .
- [17] www.taekwondowtf.ro/wp-content/uploads/2015/09/anatomie_instructori_2015.pdf .

CHAPTER 2.

AM Process - Metals



Electron beam melting of Ti6Al4V alloy: thin-wall samples fabrication, microstructure, and properties evaluation

Igor Shishkovsky, Skolkovo Institute of Science and Technology, I.Shishkovsky@skoltech.ru
Pavel Peretyagin, Moscow State University of Technologies — STANKIN, Moscow, Russia

Abstract — In the present report, the additive manufacturing process of electron beam melting (EBM) was considered with the purpose to produce functional thin-wall samples from Ti6Al4V. After preparing and characterization of the powder, samples consisting of them were melted using various selected parameters: power and velocity of the electron beam. The process window was pointed out earlier. We investigated microstructure, microhardness, XRD pattern data, surface roughness and linear wearing of the fabricated 3D samples. The effect of geometrical disposition on the variability in the grain structure and texture, martensite transformation during crystallization, thin-wall curvature seen in Ti6Al4V alloy components produced by EBM was studied. The final microstructure was determined by its thermal history and also mechanical properties, especially the grain size and morphology were tested.

Keywords - electron beam melting (EBM); Ti6Al4V alloy; thin-wall process optimization; tribological testing

1. INTRODUCTION

Fabrication of thin wall structures of complex shape and without support is one of the main advantages of additive manufacturing because this cannot be realized through traditional milling, turning, gridding or machining techniques and welding. Such thin-walled structures from titanium alloys are widespread in the aerospace industry or medical applications as cooling impellers, blades, honeycomb structures or tissue engineering scaffolds [1-4].

It is known that electron beam melting (EBM) is characterized by the relation of electron beam diameter to its power. Dependence between electron beam impact on geometrical characteristics of the thin-walled samples obtained during a single pass of the beam and different applied linear energy imparted to a single layer has been determined in [2].

Meanwhile, up to the present time, there are no exact laws on the relationship between technological

parameters and the geometric dimensions and properties of thin walls obtained by the EBM. Therefore, the EBM optimization in fabrication of thin topological structures from reacting titanium alloys of given geometry and evaluation of their mechanical properties is an actual task and constitutes the goal of this study.

2. MATERIALS AND METHODS

The thin-wall samples were fabricated using the Arcam A2 EBM machine (Arcam AB, Sweden), with a fixed thickness of 400 μm oriented vertically to the substrate. Titanium based alloy powder material VT6 (equivalent Ti6Al4V alloy) was used; it had spherical particle shape. Granulometric analysis showed the presence of 50 to 100 μm diameter particles, with the average diameter of 75 μm .

The beam diameter depended on the unit's power and constantly changed within the range of 200 to 1000 μm . We varied power (from 100 to 400 W) and travelling speed of the electron beam (from 200 to 1600 mm/s). The travelling speed was chosen in order to ensure the linear energy (from 0.25 to 1.25 J/mm) of the electron beam imparted to a thin wall. As a result (Fig. 1), the EBM optimal regimes were determined in a range of 0.75 - 1.1 J/mm that ensured the thickness of the thin wall from 0.4 to 0.9 mm [2, 3]. Moreover, thin walls made at the preheating temperature ~ 750 °C had a greater uniformity than the walls made at the preheating temperature ~ 450 °C.

After the etching, cross sections of the multi-layered melting samples were subjected to metallurgical analysis with the optical microscope (Neophot 30M, Carl Zeiss) equipped with a digital camera. The 3D samples obtained under the optimized regimes were analyzed by PMT-3M (OKB SPECTR Ltd., St. Petersburg, Russia), microhardness testing and scan electron microscopy LEO 1450 (Carl Zeiss Company) equipped with an energy-dispersive x-ray microanalyzer (INCA Energy 300, Oxford Instruments). The phase composition of the SLM

parts was determined by XRD using a DRON-3M (Bourestnik Inc., St. Petersburg, Russia) diffractometer in Co- K_{α} radiation.

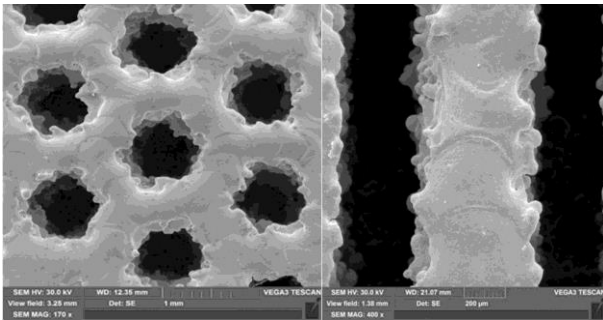


Figure 1. SEM of a scaffold and a separate thin-wall after EBM [2].

The universal complex Universal-1B was used for tribotechnical tests of the thin-wall samples, in order to collect and display the process of friction the data on the normal contact load, self-heating temperature of the friction unit and frictional moment M_{tr} (N·m). For assessment of the sample microgeometry after the EBM process, the profilograph -profilometer Mikron-01 was used (both units are produced by Samara-Balance Ltd., Russia).

3. RESULTS AND DISCUSSION

The fig. 2 shows the metallographic structure of the Ti6Al4V alloy after EBM. Closer to the edge of the thin-wall sample (fig. 2a), the basket-shaped character of the forming structure is clearly visible. The structure resembles the classic Widmanstätten one, which is characteristic of $\alpha + \beta$ titanium alloys. On the borders of α - grain, resulting from speed cooling from the melt, the dark rims of β - phase are recognizable, and then the α - phase disintegrates into α и β crystals of equilibrium content, intertwining into a basket-shape structure. On the outer edge of the thin plate, they are notched and stretched toward the heat removal (fig. 1). According to the martensitic phase transformation occurring in the EBM processing, wavy β grains formed from melt Ti6Al4V and transformed into the dominant twinned α' plates with some retained β phase [5-7].

In the center (fig. 2b) there is a more uniform alloyed structure of titanium α - phase, which has a grain of larger size. The grain size increased due to the change (lowering) of the cooling speed in the center of the thin wall.

The microhardness measurements in the thin-wall gave an average value of $\sim 345 \text{ HV}_{0.1}$ with a variation from 299 ± 30 to $386 \pm 10 \text{ HV}_{0.1}$. It can be concluded that the obtained values of microhardness are the upper limit for the alloy in hardened and tempered condition.

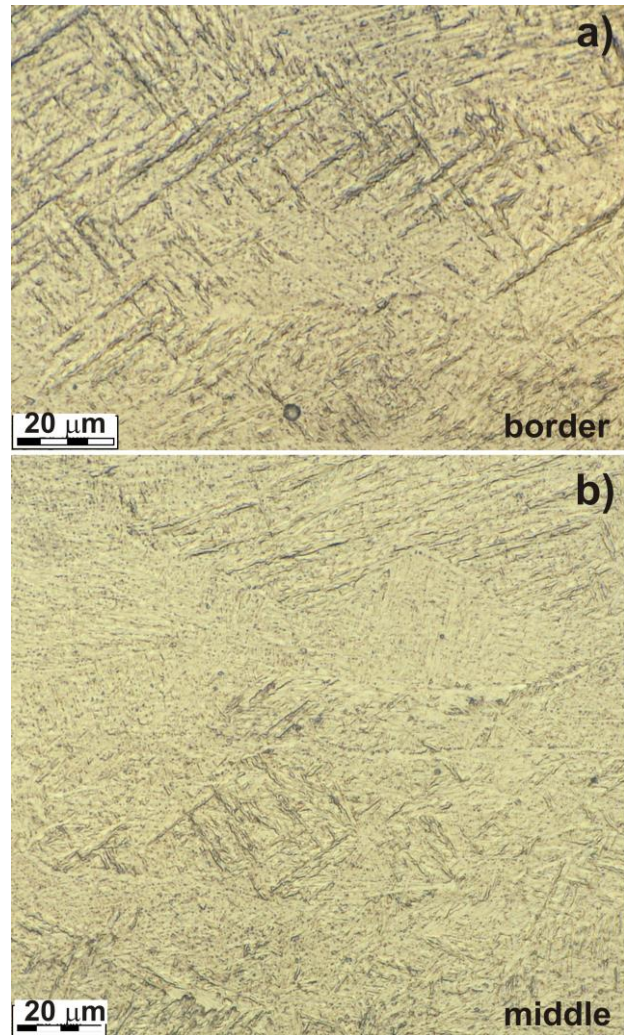


Figure 2. Optical microscopy of the thin-wall sample after the EBM of Ti6Al4V alloy: (a) border of the wall; (b) center of the wall.

XRD analysis was performed on the lateral surface of the thin wall (fig. 3). Presence of α and, possibly, β phases in the structure of the alloy was confirmed. We fixed the hexagonal α -Ti (JCPDS file #01-1198) and some peaks overlap with the cubic phase β -Ti (JCPDS file #44-1288). The β phase is clearly characterized by the (110), (200) and (211) reflections, with $d = 0.23375$, 0.16532 and 0.13496 nm, respectively. Parameters of the grid (the hexagonal and close-packed one) were also counted: for α - phase $a = 2.9225$ Å, $c = 4.6712$ Å, tetragonality c/a for α - phase was 1,6. For β - phase, the parameter of the bcc lattice was $a = 3,3065$ Å. According to the X-ray analysis data, the volume ratio of α and β -phases was 95 and 5 %, respectively.

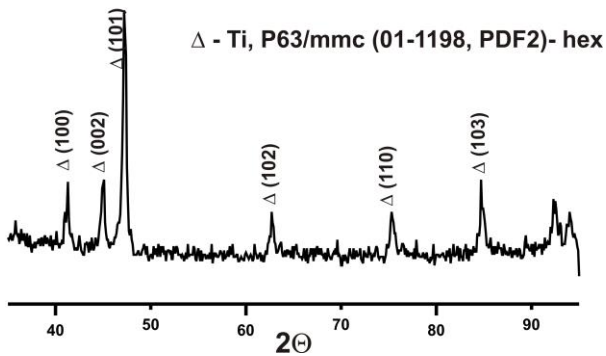


Figure 3. X-ray diffraction pattern of the Ti6Al4V alloy after EBM.

Profilogram of the sample surface after EBM of the Ti6Al4V alloy is shown in the Fig. 4. It can be noted that after the high-speed crystallization from the melt, a rather high surface roughness of R_{max} , often exceeding 59 μm , and $R_a \sim 16.3 \mu\text{m}$ are formed. The rough surface facilitates the future scaffold osteointegration in case of medical applications of our sample [4] and this is a favourable factor. A characteristic wavy surface profile (wave step $S_b \sim 300 \mu\text{m}$) can be seen in the profilogram, also reflecting the conditions of the e-beam remelting of the powder. Use of the thin-wall samples with high values of the parameter $R_{vk} \sim 12.2 \mu\text{m}$, characterizing the surface oil consumption, provides good conditions for retaining the lubricant in the cracking zone.

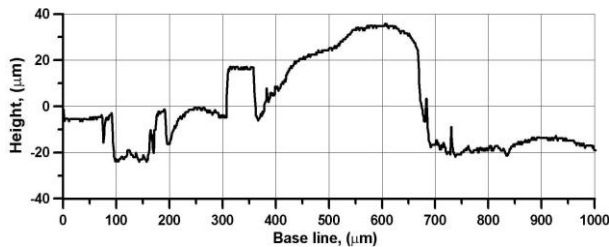


Figure 4. Profilogram from the lateral surface of the thin-wall sample

An example of experimental measurement of a normal load diagram, the average temperature in the friction zone, and frictional moment in the wear test for the Ti6Al4V sample is shown in the Fig. 6. A disk of tempered steel with a hardness of 40 HRC was used as a counterbody. Intensiveness of wearing was determined by measuring the linear wearing from the surface of the thin plate in every cycle of the test, with the load of 20 kgf. The frictional moment is characteristic of periodic changes, which indicates that fatigue mechanism for the Ti6Al4V realizes through thermo fluctuation. Each frictional moment jump corresponds with the kinetic cycle "damage accumulation - material destruction". Visual and microstructural analyses of the thin-wall sample were carried out after the friction tests and tensile

fracture. The OM of the thin-wall edge after the wear test is shown in the Fig. 5. It is visible that dynamic load on the sample caused no detachment of the alloyed metal. There was only gliding fracture at the temperature of 100 °C in the place of contact (fig. 6, green curve).

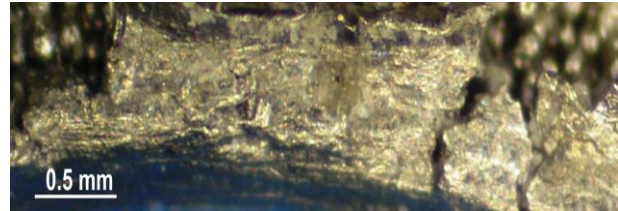


Figure 5. The OM of the thin-wall edge after wear testing.

The calculation shows that the linear wearing h was equal to 0.9 mm, the wearing rate was 16.1 mm/h, the wearing intensity - J was determined as 2.87×10^{-5} , the frictional torque was equal 0.275 N·m and the frictional coefficient was 0.55.

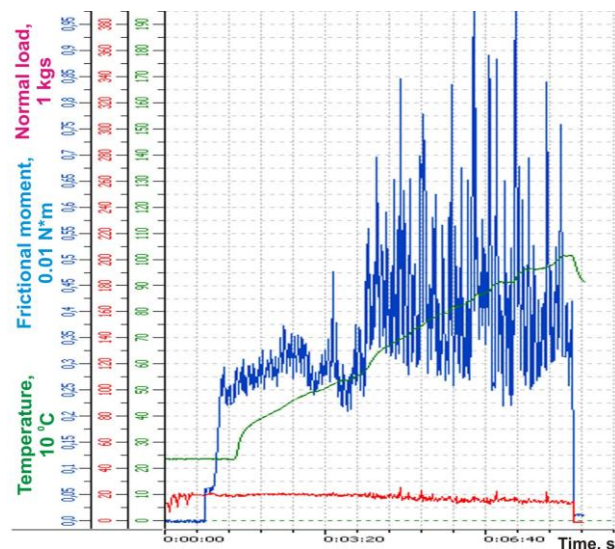


Figure 6. Tribotechnical diagram from the lateral side of the thin-wall sample

As it is clear from the graph (fig. 5), the amplitude of friction moment grew with the time of wearing. Forming a strengthened structure after EBM process can be recommended. The results of the friction testing certify that tribotechnical properties significantly improve at the optimally chosen regime.

4. CONCLUSION

Thus, in the present work, the Ti6Al4V alloy morphology and martensite transformation during high-speed cooling from the melt were studied. It was found, that structural diversities appear in sizes, structural

components of the α -phase and come from the different cooling speed of the layers.

Application of thin-wall Ti6Al4V are considerably restricted by their low tribotechnical properties. The surface roughness of $R_a \sim 16.3 \mu\text{m}$ are obtained, coefficient of friction was 0.55 and the self-heating temperature up to 100 °C was registered. The conducted mechanical and tribological testing allowed to obtain new data on strength, linear wear, wearing profilometry, fracture rupture for the thin-wall samples after the EBM process which can be useful, for example, in the future medical application of such materials.

ACKNOWLEDGEMENT

This study was supported by the Russian Foundation of Basis Researches (grant No 17-48-630290 Povolzh'ye_a).

REFERENCES

- [1] Cormier, D., West, H., Harrysson, O., Knowlson, K. 2004, 'Characterization of Thin Walled Ti-6Al-4V Components Reduced via Electron Beam Welding', *Solid Freeform Fabrication Symposium*, Austin, TX, pp. 440-447.
- [2] Peretyagin, P.Y., Bolbukov, V.P., Cherkasova, N.Y., Kabanov, A.V. 2015, 'Main technological parameters influence of selective electron beam melting on properties of thin-walled titanium alloy samples', *Materials Science Forum*, vol. 834, pp. 13-20.
- [3] Isaev, A., Grechishnikov, V., Pivkin, P., Ilyukhin, Y., Kozochkin, M., Peretyagin, P. 2016, 'Structure and machinability of thin-walled parts made of titanium alloy powder using electron beam melting technology', *Journal of Silicate Based and Composite Materials*, vol. 68(2), pp. 46-50.
- [4] Shishkovskii, I.V., Morozov, Yu.G., Fokeev, S.V., Volova, L.T. 2012, 'Laser synthesis and comparative testing of a three-dimensional porous matrix of titanium and titanium nickelide as a repository for stem cells', *Powder Metallurgy and Metal Ceramics*, vol. 50(9/10), pp. 606-618.
- [5] Zakiev, S.E., Kholpanov, L.P., Shishkovsky, I.V., Parkin, I.P., Kuznetsov, M.V., Morozov, Yu.G. 2006, 'Modeling of the thermal processes that occur in the laser sintering of reacting powder compositions', *Applied Physics A*, vol. 84(1-2), pp. 123 – 129.
- [6] Shishkovsky, I. 2017, 'Heat transfer and the dendrite growth kinetics into the titanium alloys during the electron beam melting', *JSPM Inter. Conf. on Powder and Powder Metallurgy (~60 Anniversary~ JSPMIC 2017)*, Kyoto, Japan, Nov. 6-9, p. 35.
- [7] Wang, P., Nai, M.L.S., Tan, X., Vastola, G., Raghavan, S., Sin, W.J., Tor, S.B., Pei, Q.X., Wei, J. 2016, 'Recent Progress of Additive Manufactured Ti-6Al-4V by Electron Beam. Melting', *Solid Freeform Fabrication Symposium*, Austin, TX, pp. 691-704.

Influence of additional heating on phase structure and resistivity of intermetallic SMA manufactured by PBF process

Igor Shishkovsky, Skolkovo Institute of Science and Technology, I.Shishkovsky@skoltech.ru
Vladimir Sherbakoff, Lebedev Physics Institute of RAS, Moscow, Russia

Abstract — In the present work, we demonstrated how powder bed fusion (PBF) technology can contribute to a better understanding of functional and structural properties of shape memory alloys (SMAs) in Ni-Ti systems. Correlation of specific resistance and phase structure in porous nickel-titanium intermetallic phases after PBF was experimentally observed. The electrical resistivity of the phases studied (austenite, R-phase, martensite) was shown to increase with temperature but the slopes are quite different. The intermediate R-phase in nitinol (NiTi – intermetallic phase) shows generally higher electrical resistivity than the austenite phase, but its value grows with a decrease of temperature for the laser fused samples. We explained this fact by the accumulation of dislocation with the continuous increase of the R-phase with the temperature decrease. Hysteresis loop of the electrical resistivity is more remarkable in the laser sintered samples than in the laser melted ones due to different 3D part's porosity and is a lot higher than that of solid material having a similar composition.

Keywords - nitinol; shape memory alloy (SMA); powder bed fusion (PBF); shape memory effect (SME); specific electrical resistivity (SER); laser thermocycling

1. INTRODUCTION

From the large class of metals and alloys undergoing phase transitions, one can single out a special series of materials in which thermoelastic martensite transformations are observed. These alloys have a high potential in terms of their application in different areas: from micro-technology and aerospace technology to medicine and robotics. In these materials, called shape-memory alloys (SMA), thermoelastic martensite transformation is responsible not only for changing physical and mechanical properties but also is the cause of the manifestation of specific functional properties. Among the most well-known we should name nitinol (intermetallic phase - NiTi) alloy with the unique ability to restore significant inelastic deformations (up to 10-12%) with heating (i.e., shape memory effect (SME)) or

unloading (pseudoelasticity effect) and create high reactive stresses (up to 1000 MPa) (the effect of generating reactive voltages) [1].

According to computer models, laser powder bed fusion (LPBF) allows the making of nitinol both porous and practically cast functional products [2, 3]. However, high heating and cooling rates with selective laser sintering/melting (SLS/M) lead to an essential structural heterogeneity of this alloy [3].

Earlier [2, 4] parameters of martensitic transformations and SME were shown to be determined by structural inhomogeneity of the NiTi alloy, namely, by different nickel concentrations in different regions of the NiTi phase and volume fraction of these regions. Varying structural heterogeneity by changing composition of the mixture, also in combination of SLS/M and self-propagated high-temperature synthesis (SHS) processes [2], and heat treatment, makes it possible to obtain materials with various functional properties. It can be used, on the one hand, in medicine, at temperatures close to the temperature of the human body (for example, as implants) and on the other hand at temperatures above room temperature (for example, as dampers).

It is also known [5, 6] that during the thermal cycling of the TiNi alloy, the numbers of heat release and absorption peaks change. This happens because different volumes of material undergo different sequences of martensite transformations at different temperatures. Since the temperature and the type of the martensite transition are determined by the density of the defects [5, 6], it was concluded that, while thermal cycling in the TiNi alloy, the defect density increases and is distributed nonuniformly in volume, resulting in regions with high and low defect density. This agrees well with the transmission electron microscopy data presented in [6]. In regions with high defect density, direct transition sequence changes from B2 (austenite) → B19 (martensite) to B2 → R (rhombohedral

phase) → B19, and in regions with lower defect density the sequence B2 → B19 remains.

In order to analyze the processes responsible for the accumulation of irreversible deformation during thermal cycling, it is useful to measure electrical resistivity (ER) as a function of temperature [4, 7], which indicates a change in the defect density. Therefore, the aim of the present work was to study the effect of thermal cycling on the structural-phase state of nitinol obtained with SLS/M and to assess the possibilities for controlling the temperature range of direct and shaped austenite-martensite transformations by changing the regimes of laser influence (LI) and additional heating.

2. MATERIALS AND METHODS

For the experiments, a nitinol powder containing 99.76 wt. % intermetallic phase NiTi, produced by Polema (Tula, RF) was used. The NiTi powder was represented by a fraction with a particle size of 60 μm. The pre-alloyed NiTi phase was obtained by gas-phase atomization. The stoichiometry of the NiTi phase had a composition of 45 wt% Ti and the remainder Ni.

Granulometric analysis of the particles was carried out using the ALPAGA 500 NANO optical granulometer, which is a real-time screening system equipped with the CALLISTO image processing software (OCCHIO s.a.).

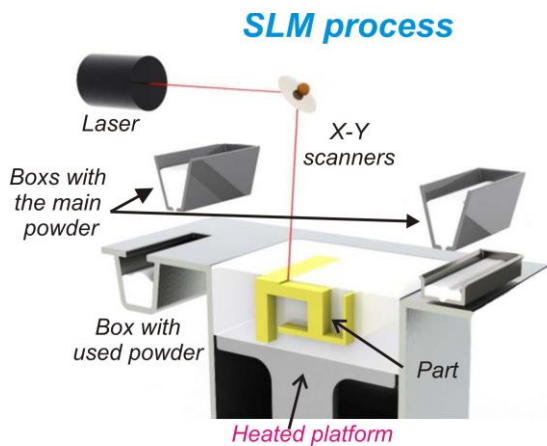


Figure 1. Scheme of SLS/M process with additive heating

The experiments were performed at the SLS/M stand in the Samara branch of the LPI [2, 7]. The source of radiation in it is a continuous YLR-100 ytterbium laser. IPG Photonics, operating at a wavelength of 1075 nm. The sintering process in the chamber could be carried out in presence of a shielding gas. Heaters situated from the platform side allow to raising the temperature in the chamber to $T_{max} = 300$ °C with layered synthesis. The heating temperature was controlled by thermocouples. Fig. 1 shows the scheme of the stand for the SLS/M with heating of the powder mixture from below by nichrome spiral mounted in the base platform.

In our work [3], the parameters of the SLS/M were optimized, the power of the LI was 20-50 W, the spot diameter on the powder surface was 70 μm. The SLM was carried out in an argon atmosphere. The thickness of the applied layers was 60 μm. The SLM technique with the rotation of 90 degrees for each layer was used at distances between Sh - 60-100 μm passages and scan rates of $v - 30-220$ mm/s. We compared the results of the structure formation of nitinol after SLS/M conducted at 20 °C or 300 °C and took laser thermal cycling into account. We used the possibility of SLS/M with heating and without one for creating monolayers and volumetric products (Fig. 2). As we can see in Fig. 2b, heating significantly affects the porosity and strength of the product after the SLS/M.

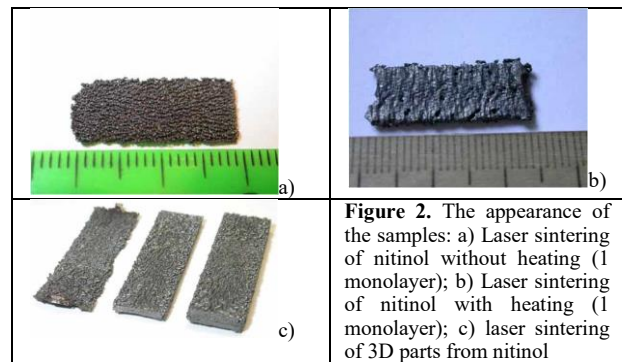


Figure 2. The appearance of the samples: a) Laser sintering of nitinol without heating (1 monolayer); b) Laser sintering of nitinol with heating (1 monolayer); c) laser sintering of 3D parts from nitinol

Since the multilayered SLS/M (Fig. 2c) is actually a repeated LI for the powder volume and the underlying layers (i.e., additional heating), then the effect of such laser thermal cycling for the previous layers should be significant. Thus, to study the effect of additional heating both during platform heating and laser thermal cycling in the layer-by-layer synthesis of bulk products from nitinol on the structural-phase composition of the material and manifestation of the shape-memory effect in the porous state was the aim of our investigations.

Macrostructures of the 3D samples (Fig. 2) were studied on a Neophot 30M optical microscope with a digital camera. Structural and phase composition of the synthesized articles was studied on a DRON-3 diffractometer in Cu-K_α radiation. Phase composition of the samples was determined using the X-ray database PDF2, 1999 release and the computer program - SearchMatch ver. 3.010. The quantitative analysis of the diffractograms was carried out using the Rietveld program PowderCell 2.0.

The measurement of specific electrical resistivity (SER) as a function of temperature was carried out according to a 4-point scheme and described in detail in [4, 7]. We have perfected this technique by including the Lcard-E440 in the A/D converter and digitizing the measurement data on the computer.

3. RESULTS AND DISCUSSION

Earlier, we showed [3] that additional heating of the

laser exposure zone is a useful tool for controlling the strength properties of the porous nitinol products created, their structural-phase composition and, as a consequence, the range of temperatures for SME development.

As is known from the literature, direct and inverse austenite-martensite transformations in nitinol are accompanied by release or absorption of the phase transition latent heat [8, 9]. Earlier it was shown [9] that during the SME intermediate (rhombohedral - R) phase appears in the cooling stage.

We carried out an X-ray structural and phase analysis of the samples (see Fig. 2) from porous nitinol in search for the presence of the corresponding phases. Fig. 3 shows the XRD results of the porous volumetric samples (1-5-10 layers) of nitinol after the SLS/M both with and without heating. As we can see, the rhombohedral phase (intensity peak 1-10) was detected in all the analyzed SLS/M regimes, and with additional heating, the line (210) of this phase is more clearly expressed.

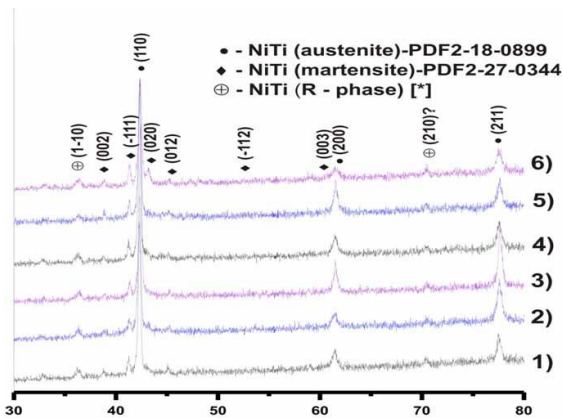


Figure 3. The XRD of 3D samples: 1.4) - two layers; 2.5) - five layers; 3.6) - ten layers. P = 22 W, V = 3.7 cm / s, D = Sh = 100 μm. 1,2,3) SLS/M without heating the mixture; 4,5,6) - SLS/M with heating of the mixture to 300 °C.

Measurements of the SER were carried out in the range from -150 °C to 150 °C. Fig. 4 shows the results of the measurements for individual monolayers and Fig. 5 shows ones for volumetric parts (2-5-10 layers, or in other words, the effect of laser thermal cycling). As we can see in Fig. 4a, additional heating significantly affects the value of resistivity. According to the absolute value, the SER $\rho = \rho(T)$ in porous bulk products from nitinol turned out to be almost twice as high as one of the porous monolayers obtained by the SLS/M method and ten times higher than that of the cast nitinol. Moreover, heating from the bottom of the platform side of the powder volume during the SLS/M significantly changes the value of $\rho(T)$. Fig. 4b shows the XRD data from which we can conclude that the rhombohedral phase (1-10) (i.e., the precursor of the SME) takes place. However, additional heating (~ 300 °C), leading to a reduction of the sample porosity, increases the intensity of the line (1-10) but practically negates the line

(210) of this phase.

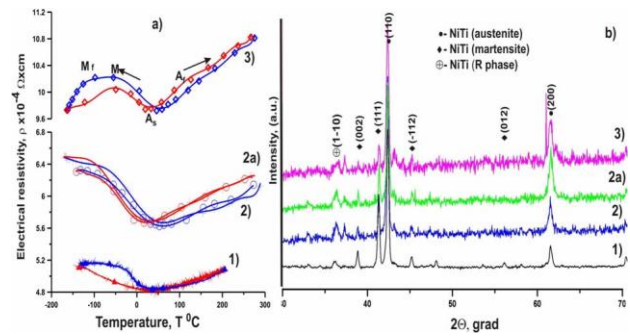


Figure 4. Influence of additional heating of the powder and thermocycling (regime of the LI - v = 2.5 cm/s, P = 21.5 W, A = 8.6 J/mm²): 1) without additional heating; 2) additional heating of the powder surface ~ 200 °C, / 2a - five cycles of heating + cooling when SER measuring; 3) additional heating of the powder volume ~ 300 °C.

As it is visible in Fig. 5, in a three-dimensional product, i.e. of the layered SLS/M, electrical resistivity increases by a factor of 2-3 in absolute values, and the more layers (ie, the thermal cycles) were deposited by the LI, the more likely the SME manifested at the cooling stage (see mode 3).

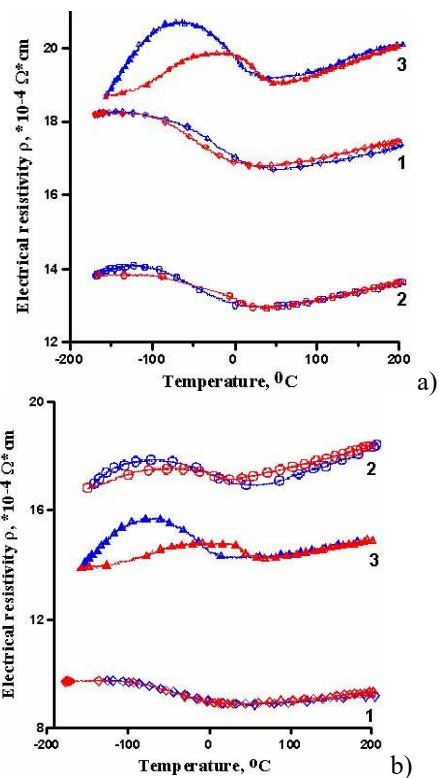


Figure 5. Influence of additional heating of the powder and laser thermal cycling (the LI regime - v = 3.7 cm/s, P = 22 W): a) without additional heating; b) additional heating of the powder surface; 1) - two layers; 2) five layers; 3) ten layers.

According to [10], the change in the electrical resistivity is proportional to the change in the dislocation

density. As it is shown in [11], plastic deformation develops in strictly defined crystallographic directions. In our opinion, the results of thermal cycling of nitinol in an incomplete temperature range of the martensitic transformations show that upon cooling, the growth of martensite sites is accompanied by plastic accommodation, due to the accumulation of defects both in the converting regions and in the austenitic volumes of the alloy that does not undergo the phase transition.

With accelerated heating, which takes place during SLS/M, softening occurs in the "converting" volumes, which contributes to change and redistribution of the defect density, and influences the change in the temperatures of the reverse transition. The degree of softening depends on the volume fraction of the alloy undergoing the reverse martensite transformation, the maximum temperature in the cycle and the rate of thermal cycling. Comparison of our data obtained from thermal cycling of nitinol in the temperature range of incomplete forward and reverse transformations allows us to conclude that the stresses created by growing martensitic plates during cooling initiate dislocation sliding in the austenitic phase, while in martensitic phase they cause reorientation of the martensitic plates. This happens due to the difference in dislocation slip limit the austenite phase and limits of reorientation and dislocation slip in the martensitic phase. We believe that the formation of thermocycling regions with high and low defect densities is due to hardening that occurs during cooling and softening that occurs during heating. It is established that the degree of structural heterogeneity that is formed during thermal cycling of nitinol depends on how completely softening was realized during heating.

4. CONCLUSIONS

In the present work, the influence of additional heating and laser thermal cycling on the structural-phase state of nitinol after SLS/M was studied and the following effects were shown:

- The absolute value of specific electrical resistance (SER) $\rho = \rho(T)$ in porous bulk products from nitinol (intermetallic phase - NiTi) is almost twice as high as that of porous monolayers obtained by the SLS / P method and orders of magnitude higher than that of lithium nitinol.
- The change $\rho = \rho(T)$ is a convenient and effective experimental technique for identifying various phases in materials with shape memory and nitinol and for determining the temperature range of the ESR in porous nitinol after the SLS/M. In 3D parts, an intermediate rhombohedral R- phase was observed.
- An increase in the number of layers (laser thermal

cycles) in volume SLS/M leads to a more pronounced manifestation of the R phase. Laser thermal cycling has a more significant effect on the results of $\rho = \rho(T)$, and therefore on the interval of operating temperatures for the realization of the SME.

Thus, the results showed that the processes of hardening and softening lead to structural inhomogeneity of the alloy during high-speed laser thermal cycling, determine the parameters of the martensite transformations, affect the stability of physical properties and accumulation of irreversible plastic deformation. The more regions with high defect density are there in the alloy, the less is the magnitude of irreversible deformation and stable properties of the alloy during thermal cycling.

ACKNOWLEDGMENT

This study was supported by the Russian Foundation of Basic Researches (grant No 17-48-630290 Povolzh'ye_a).

REFERENCES

- [1] Gureev, D.M., Petrov, A.L., Shishkovsky, I.V. 1999, 'Formation of intermetallics phases under laser sintering of powdered SHS compositions', *Proc. SPIE*, vol. 3688-36, pp. 237-242.
- [2] Zakiev, S.E., Kholpanov, L.P., Shishkovskii, I.V., Parkin, I.P., Kuznetsov, M.V., Morozov, Yu.G. 2006, 'Modeling of the thermal processes that occur in the laser sintering of reacting powder compositions', *Applied Physics A*, vol. 84 (1-2), pp. 123 - 129.
- [3] Shishkovsky, I., Sherbakoff, V., Yadroitsev, I., Smurov, I. 2012, 'Particularities of electrical resistivity and phase structure in the 3D porous nitinol after SLS/SLM', *Proc. Inst. Mech. Eng., Part C: J. of Mech. Eng. Science*, vol. 226 (12), pp. 2982-2989.
- [4] Miyazaki, S., Igo, Y., Otsuka, K. 1986, 'Effect of thermal cycling on the transformation temperatures of TiNi alloys', *Acta Metallurgica*, vol. 34, pp. 2045–2051.
- [5] Pelton, A.R., Huang, G.H., Moine, P., Sinclair, R. 2012, 'Effects of thermal cycling on microstructure and properties in Nitinol', *Materials Science and Engineering A*, vol. 532, pp. 130–138.
- [6] Shishkovsky, I.V. 2005, 'Shape memory effect in porous volume NiTi articles fabricated by selective laser sintering', *Technical Physics Letters*, vol. 31 (3), pp. 186-188.
- [7] Uchil, J., Mahesh, K.K., Kumara, K.G. 2001, 'Calorimetric study of the effect of linear strain on the shape memory properties of Nitinol', *Physica B*, vol. 305, pp. 1–9.
- [8] Uchil, J., Mahesh, K.K., Kumara, K.G. 2002, 'Electrical resistivity and strain recovery studies on the effect of thermal cycling under constant stress on R-phase in NiTi shape memory alloy', *Physica B*, vol. 324, pp. 419–428.
- [9] Basinski, Z.S., Dugdale, J.S., Howie, A. 1963, 'The electrical resistivity of dislocations', *Philosophical Magazine*, vol. 8, pp. 1989 – 1997.
- [10] Simon, T., Kroeger, A., Somsen, C., Dlouhy, A., Eggeler, G. 2010, 'On the multiplication of dislocations during martensitic transformations in NiTi shape memory alloys', *Acta Materialia*, vol. 58, pp. 1850–1860.

Influence of the Process Gas on the Laser Beam Melting Process

Andreas Wimmer[†], Christian Zeller[†], Fabian Bayerlein[†], Dominik Scherer[†], Michael F. Zaeh[†], Pierre Forêt[‡], and Jürgen Scholz[‡]

[†]Technical University of Munich, TUM Department of Mechanical Engineering, Institute for Machine Tools and Industrial Management, Boltzmannstr. 15, 85748 Garching, Germany, andreas.wimmer@iwb.mw.tum.de

[‡]Linde AG, Carl-von-Linde-Str. 25, 85716 Unterschleissheim, Germany

Abstract—Optical high-speed monitoring provides insights into the process dynamics of laser beam melting (LBM) on a microsecond-scale. This study presents investigations on the transient behavior of particles emitted from the process zone during LBM. Evaluation of the data by particle tracking velocimetry yields numbers for particle spots, tracks, and velocities. The number of particles and tracks decreases with increasing helium concentration, while no deviation in either of the quantity could be observed for argon and nitrogen.

Keywords: Additive Manufacturing; laser beam melting; process gases; high-speed monitoring; particle tracking.

1. INTRODUCTION

High costs of product developments often pose major challenges for companies. Additive Manufacturing (AM) in general and LBM in particular streamlines and expedites the product development process. In order to reduce the time-to-market and improve the product quality, AM is becoming increasingly important as a tool for rapid product development [1].

The quality of additively manufactured parts is influenced by various process parameters, whereby the process gas has only been considered in isolated cases [2]. However, the respective influence in related processes such as welding is considered significant for both, the process stability and the weld quality. This leads to the assumption that the influence of the process gas used during LBM may also be important.

The aim of this paper is to investigate and quantify the influence of the process gas employed during LBM. Specifically, the influence on the process dynamics and the related stability in the process zone was surveyed. The quality of workpieces produced through LBM is usually evaluated post process using metallography. This method does not allow for conclusions regarding the dynamics of the process zone. Therefore, high-speed recordings were made to analyze the influence of the process gas on the process stability.

The data was evaluated using particle tracking velocimetry. The influence of various argon-helium and argon-oxygen mixtures as well as of pure nitrogen on the manufacturing process with AlSi10Mg was studied. A Concept Laser Mlab was employed due to a well-defined flow of the process gas. Recordings were made at three different scanning directions to investigate its influence on the results.

2. STATE OF THE ART

2.1. Process gases in laser manufacturing

Argon and nitrogen are the most common process gases for the LBM process [3]. In other laser material processes (e.g. laser beam welding or laser cutting) also gas mixtures and helium are employed [4]. The most important task of the process gas in laser material processing is to shield the melt pool from the atmosphere. Otherwise oxidations are likely to occur, which lead to component imperfections that in the worst case scenario cause a part failure. Furthermore, the process gas is used as a cross jet that prevents the laser optics from soiling with spatter particles [5].

The high temperature of the melt pool as well as the high tendency of the powder to react with the atmosphere are additional reasons to employ process gases during LBM [6, 7]. The use of inert gases protects the powder material from environmental influences. Moreover, the circulation of the process gas in the process chamber reduces the deposition of spatter particles on the powder bed or on already processed components significantly. These particles can lead to defects in the produced parts that alter their mechanical properties [8]. Inert gases are also used to suppress the formation of plasma during LBM. This plasma potentially destabilizes the laser beam and causes additional attenuation of the laser energy reaching the surface of the melted component [9].

Additionally, Jahn et al. [2] observed a correlation between chemical properties of the process gas and the quality of parts produced by LBM. Such chemical

properties are the density, the heat conductivity and the ionization energy. Furthermore, the authors analyzed the correlation between the type of the process gas and the resulting mechanical properties. They found that the use of nitrogen increased the mechanical properties of the nickel alloys Inconel 625 and Hastelloy X. This effect was attributed to the nitration of the titanium contained in these alloys. Regarding normal aluminum alloys, this change in mechanical properties is not expected for varying process gases.

When it comes to laser beam welding, process gases are specifically used to protect the melting pool from moisture absorption. With aluminum alloys, this can lead to the so-called hydrogen porosity and weaken the mechanical properties such as the stiffness and strength of the component [10]. The active gas CO₂ calm the melt pool, which leads to a decreased spatter formation [11]. Moreover, these gases ensure a high welding penetration depth [12]. And finally, similar to the LBM process, process gases are used in laser welding to suppress the plasma owing to the high temperatures during the process. The plasma absorbs the laser energy, leading to insufficient melting of the joining partners [13].

2.2. Use of high-speed monitoring in laser manufacturing

The benefits of high-speed camera systems, e.g. to visualize very fast movements, offer great opportunity for quality control in laser material processes [14, 15]. High-speed cameras are not only used to observe laser welding and laser cutting processes, but also in powder-based processes such as LBM. Liu et al. [16] analyzed the size, the scattering and maximal height of spatter particles using a high-speed camera.

With respect to the laser beam welding process, high-speed camera systems are employed to study the capillary geometry and the dynamics of melting [17]. Moreover, the resulting vapor plume fluctuations can be analyzed employing camera based monitoring. With this characterization, the welding penetration depth can be estimated and possible defects can be detected [18].

As for laser cutting or drilling processes, high-speed camera systems are used to analyze the melt pool and to track spatters, which are forced out of the melt pool [19, 20].

3. METHODOLOGY

Due to the short exposure times of high-speed cameras, an additional light source is required. In this paper, an illumination laser with a wavelength of 810 nm was used. Although this does not correspond to the wavelength of 1070 nm of the processing laser, it is nevertheless absorbed by the laser protection glass. The installation of the illumination laser inside the process chamber was not an option since the process gas flow should not be influenced

and the high-speed camera must be placed outside the LBM-machine. Two possibilities arose to enable the illumination of the process chamber. The first was an exchange of the protection glass with an interference filter, which transmits the radiation of the illumination laser (wavelength 810 nm) and absorbs the radiation from the process laser (wavelength 1070 nm). The second was a replacement of the protection glass with a borosilicate glass that possesses excellent optical properties and transmits both the radiation of the process laser and the illumination laser. Although the second possibility required an additional housing of the LBM-machine, it was more feasible.

3.1. High-speed monitoring set-up

An adapter with slots for the high-speed camera as well as for the illumination laser and a webcam was designed. The webcam is required to monitor the complete process since the high-speed camera only shows a very small image detail of the chamber. The complete set-up is shown in Fig. 1.

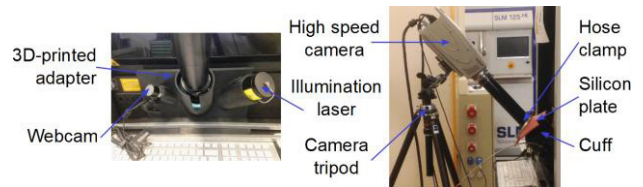


Figure 1. Experimental set-up for high-speed recordings with the Concept Laser Mlab

The adapter was built using Fused Deposition Modeling and consisted of the amorphous as well as temperature-resistant plastic acrylonitrile-butadiene-styrene. The safety concept was validated by the responsible trade association through a measurement of the scattered radiation.

3.2. Experimental procedure

During all experiments, the 'fill' or 'flood' state of the circulation system was activated to ensure the required concentration of inert gas in the process zone at all times. The only exceptions were the experiments with pure helium.

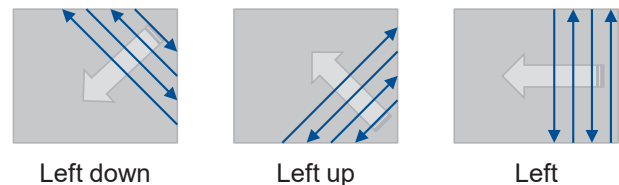


Figure 2. Different scanning direction for statistical assurance

During initial flooding of the process chamber, a rapid enrichment of helium around the oxygen sensor hindered further flooding of the chamber so that only the flow rate in

the 'hold' state was used. Investigations into the influence of the scanning directions were conducted according to Fig. 2.

The process gases argon, various argon-helium-mixtures, argon-oxygen mixtures and pure nitrogen were used. Table 1 lists the gases and their exact chemical composition.

Table 1. Process gases that were used in the experiment with corresponding concentration.

Process gas	Concentration in %
Argon	100
Argon/oxygen	99.5/0.5
Argon/helium	80/20
Argon/helium	40/60
Argon/helium	20/80
Helium	100
Nitrogen	100

In addition to the investigation of various process gases, the influence of the fan setting (5 % and 30 %) was considered for argon and the left down direction. The standard fan setting was set to 20 %. Further details of the experimental set-up are summarized in Table 2.

Table 2. Experiment set-up

Item	Term/Value
Manufacturing system	Concept Laser Mlab
High-speed camera	Olympus i-SPEED 3
Illumination system	Cavilux HF
Frames per second	7,500
Exposure time	2.66 μ s
Shutter speed	50x
Aperture	22
Focal length	150
Tubes	5

3.3. Data processing

The image sequences were truncated to 2000 frames each to provide a sufficiently long clip with multiple passages of the laser beam focus spot, but reasonable processing effort. The spatial calibration was performed by comparing the real and the picture width of the weld seams for multiple tracks. This resulted in approximately 5.6 μ m/pixel. The temporal calibration is determined by the

recording frequency, resulting in approx. 0.13 ms/frame at 7500 frames/s.

The sequences were processed with a probabilistic temporal median filter [21] with a time window of nine frames to separate foreground from the background. The foreground was defined as being two standard deviations above the median of the background. Sample results for this process are shown in Fig. 3. Subsequently, the image sequences were processed using the ImageJ Plugin TrackMate [22]. The Laplacian of Gaussian segmentation algorithm was used for blob detection, with an estimated blob size of 100 μ m (cf. Fig 4). After initial thresholding based on a combined quality feature reported from the segmentation algorithm, no further spot filtering criteria were applied.

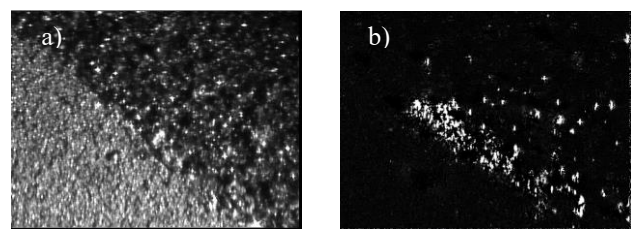


Figure 3. Exemplary result of the temporal filtering process. The distinction between moving foreground and background is significantly increased from the original image a) to the filtered one b).

The simple Linear Assignment Problem (LAP)-Tracker was used for particle tracking. TrackMate therefore implemented the framework suggested in Jaqaman et al. [23] and used the algorithm described in Munkres [24] to solve the LAP. The maximum linking distance as well as the gap-closing distance was set to 200 μ m and the maximum frame gap was set to 3 frames in order to avoid spurious linking.

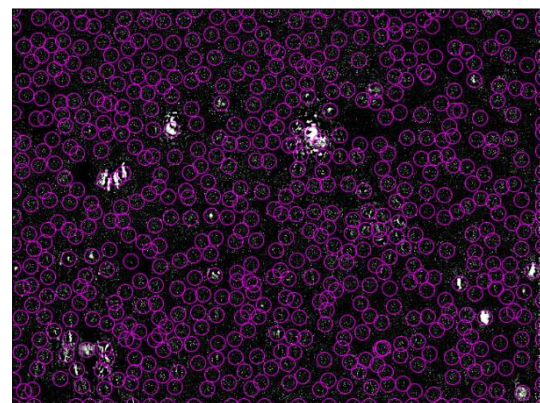


Figure 4. Result of the spot detection algorithm

Finally, the tracks were filtered by velocity standard deviation and length of the track (i.e. track displacement) to avoid tracking the reflections of the melt pool

(cf. Fig. 5). Since real sputters travel over relatively long distances and have relatively constant velocities, they were easily distinguishable from the stochastic and chaotic tracking results of the melt pool reflections. The variability in the image sequences did not allow a uniform setting of the respective thresholds; a manual selection of parameters was necessary to determine the appropriate trade-off in terms of signal-to-noise-ratio.

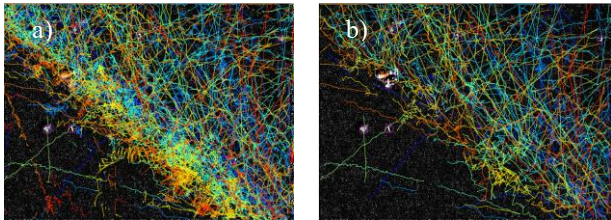


Figure 5. Initial tracking result a) and the result after applying an upper bound to velocity standard deviation and a lower bound to total track displacement b). The color represents the medium velocity of the particle on the respective track.

4. RESULTS AND DISCUSSION

4.1. Quantity of tracked spots

As shown in Fig. 6, the total number of particles decreases with an increasing helium concentration. A deviation of the monotonous decrease is observed for the direction ‘left’. The number of particles are nearly equal for different fan settings. Deviations between argon and nitrogen could not be observed. What’s more, an increased number of particles was not detected by the addition of small amounts of oxygen to argon.

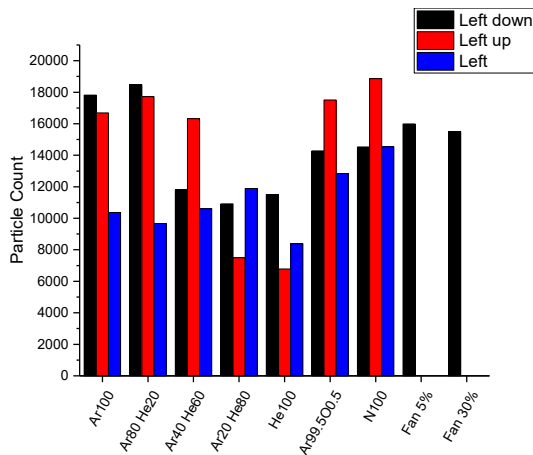


Figure 6. Sum of tracked spots per gas with respective scanning direction

4.2. Quantity of tracks

Fig. 7 shows a decrease in the number of tracks with an increasing helium concentration. It is assumed that the differences in the tracks, which were recorded at different fan settings were caused by the reduced removal of particles from the process zone.

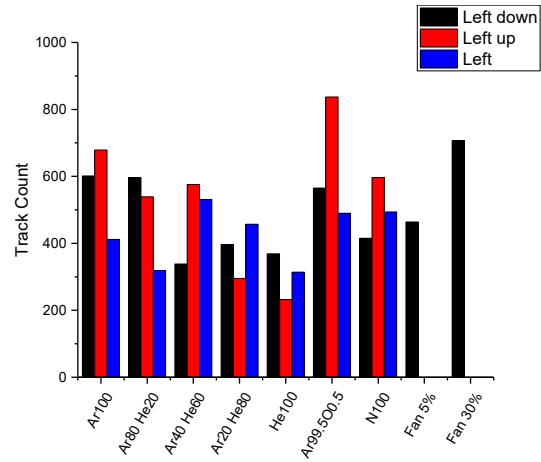


Figure 7. Sum of tracks per gas with respective scanning direction

4.3. Tracked velocity of particles

An initial decrease in the average velocity with a low admixture of helium can be observed in Fig. 8. Higher helium concentrations lead to the cancellation of this effect. The average velocity of the tracked particles with nitrogen is in the same range of the process gas argon with a low admixture of helium. The extreme values are obtained by varying the fan settings. The effect of the decrease and subsequent increase of the average velocity with an increasing helium concentration can be attributed to the altered flow rate, which results from the density reduction of the process gas.

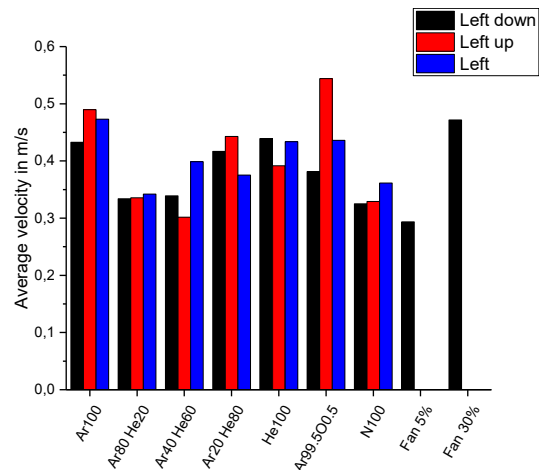


Figure 8. Average velocity of tracks per gas and per scanning direction

5. CONCLUSION

High-speed recordings of the process zone with subsequent evaluation procedures gave quantities for tracked particle spots, tracks and velocities. According to the presented data, the influence of the process gas on the process dynamics in LBM is not negligible. In particular, the number of particles and tracks decreases with increasing helium concentration. Remarkably, the velocity of the particles is independent from the quantity of the particles. The possibility of controlling the spatter formation in LBM processes with the help of the process gas is a fundamental finding for the AM industry.

Further research is necessary to determine the exact influence of the flow rate sensor on the process dynamics. Additional investigations, e.g. metallography and tensile testing, of the samples may provide a deeper insight into the influence of the process gas on material parameters.

REFERENCES

- [1] I. Wohlers Associates, *Wohlers Report 2017: 3D printing and Additive Manufacturing state of the industry*. Annual Worldwide Progress Report: Wohlers Associates, Inc., 2017.
- [2] S. Jahn, C. Straube, S. Matthes, R. Kahlenberg, and S. Sändig, "Einfluss der Prozessgase beim Laserstrahlschmelzen," *Schweißen und Schneiden*, vol. 67, no. 7, pp. 372–377, 2015.
- [3] G. Witt, A. Wegner, and J. T. Sehr, *Neue Entwicklungen in der Additiven Fertigung*. Berlin, Heidelberg: Springer Berlin Heidelberg, 2015.
- [4] J. Fieret and J. Herrmann, "Innovative Prozessgase zum Laserschweißen," *Laser Magazin*, no. 3, pp. 33–34, 2014.
- [5] BOC-Member of the Linde Group, Ed., "Laser Welding. Laserline Technical," 2009.
- [6] C. Wagner, "Untersuchungen zum Selektiven Lasersintern von Metallen," Dissertation, RWTH Aachen, Aachen, 2003.
- [7] I. Gibson, D. W. Rosen, and B. Stucker, *Additive Manufacturing Technologies*. Boston, MA: Springer US, 2010.
- [8] B. Ferrar, L. Mullen, E. Jones, R. Stamp, and C. J. Sutcliffe, "Gas flow effects on selective laser melting (SLM) manufacturing performance," *Journal of Materials Processing Technology*, vol. 212, no. 2, pp. 355–364, 2012.
- [9] B. Zhang, L. Dembinski, and C. Coddet, "The study of the laser parameters and environment variables effect on mechanical properties of high compact parts elaborated by selective laser melting 316L powder," *Materials Science and Engineering: A*, vol. 584, pp. 21–31, 2013.
- [10] J. Herrmann, "The role of process gases in laser welding," *LTJ*, vol. 8, no. 5, pp. 24–27, 2011.
- [11] T. Ammann, "Schutzgasschweißen und Formieren von hochlegierten Werkstoffen," 2004.
- [12] B. G. Chung, S. Rhee, and C. H. Lee, "The effect of shielding gas types on CO2 laser tailored blank weldability of low carbon automotive galvanized steel," *Materials Science and Engineering: A*, no. 272, pp. 357–362, 1999.
- [13] L. Kvasna, P. Remenova, M. Turna, J. Härtl, and M. F. Záh, "Angepasste Prozessgase für das Schweißen mit Hochleistungsdiolenlasern," in *CO-MAT-TECH*, Trnava, 2003.
- [14] R. Poprawe, H. Weber, and G. Herziger, *Laser Applications*. Berlin/Heidelberg: Springer-Verlag, 2004.
- [15] S. Berumen, F. Bechmann, S. Lindner, J.-P. Kruth, and T. Craeghs, "Quality control of laser- and powder bed-based Additive Manufacturing (AM) technologies," *Physics Procedia*, vol. 5, pp. 617–622, 2010.
- [16] Y. Liu, Y. Yang, S. Mai, Di Wang, and C. Song, "Investigation into spatter behavior during selective laser melting of AISI 316L stainless steel powder," *Materials & Design*, vol. 87, pp. 797–806, 2015.
- [17] M. G. Müller, "Prozessüberwachung beim Laserstrahlschweißen durch Auswertung der reflektierten Leistung," Dissertation, Universität Stuttgart, Stuttgart, 2002.
- [18] C. Brock, F. Tenner, F. Klämpfl, R. Hohenstein, and M. Schmidt, "Detection of weld defects by high speed imaging of the vapor plume," *Physics Procedia*, vol. 41, pp. 539–543, 2013.
- [19] J. Pocorni, D. Petring, J. Powell, E. Deichsel, and A. F. H. Kaplan, "Measuring the melt flow on the laser cut front," *Physics Procedia*, vol. 78, pp. 99–109, 2015.
- [20] K. T. Voisey, S. S. Kudesia, W. S. O. Rodden, D. P. Hand, J. D. C. Jones, and T. W. Clyne, "Melt ejection during laser drilling of metals," *Materials Science and Engineering: A*, vol. 356, no. 1–2, pp. 414–424, 2003.
- [21] R. M. Parton, R. S. Hamilton, G. Ball, L. Yang, C. F. Cullen, W. Lu, H. Ohkura, and I. Davis, "A PAR-1 orientation gradient of dynamic microtubules directs posterior cargo transport in the *Drosophila* oocyte," *The Journal of Cell Biology*, vol. 194, no. 1, pp. 121–135, <http://jcb.rupress.org/content/194/1/121>, 2011.
- [22] J.-Y. Tinevez, N. Perry, J. Schindelin, G. M. Hoopes, G. D. Reynolds, E. Laplantine, S. Y. Bednarek, S. P. Shorte, and K. W. Eliceiri, "TrackMate: An open and extensible platform for single-particle tracking," *Methods*, vol. 115, pp. 80–90, 2017.
- [23] K. Jaqaman, D. Loerke, M. Mettlen, H. Kuwata, S. Grinstein, S. L. Schmid, and G. Danuser, "Robust single-particle tracking in live-cell time-lapse sequences," *Nature Methods*, vol. 5, no. 8, pp. 695–702, 2008.
- [24] J. Munkres, "Algorithms for the assignment and transportation Problems," *Journal of the Society for Industrial and Applied Mathematics*, vol. 5, no. 1, pp. 32–38, 1957.

Defect formation and influence on metallurgical structure due to powder cross-contaminations in laser-based powder bed fusion

Copper alloy particles in Aluminum alloy feedstock

Max Horn^{a,*}, Dr.-Ing. Georg Schlick^a, Felix Wegner^a, Dr.-Ing. Christian Seidel^{a,b}, Christine Anstaett^a, Prof. Dr.-Ing. Gunther Reinhart^{a,b}

(a) Fraunhofer Research Institution for Casting, Composite and Processing Technology IGCV,
Beim Glaspalast 5, 86153 Augsburg, Germany

(b) Institute for Machine Tools and Industrial Management of Technical University of Munich,
Boltzmannstr. 15, 85748 Garching b. München, Germany

* Corresponding author: max.horn@igcv.fraunhofer.de

Abstract—This study elaborates the influence of metal powder cross-contamination of CuCr1Zr in AlSi10Mg occurring during the multi-material laser-based powder bed fusion (LBPF) process chain. Four different alloy mixing grades ranging from 0.5 to 5.0 weight percent (wt.%) CuCr1Zr were processed and their effect on the metallurgical structure of AlSi10Mg was examined. The contaminations lead to an even distribution of characteristic Cu-rich enclosures in an overall heterogeneous structure. The intermetallic compound Al₂Cu was found to be the predominant phase appearing in transition zones from Cu-rich areas to the overall AlSi10Mg structure. From described investigations, a model was derived to explain the formation of defects caused by powder cross-contaminations.

Keywords – Additive Manufacturing; Laser Beam Melting; Laser-based Powder Bed Fusion; multi-material; metal powder; cross-contamination; CuCr1Zr; AlSi10Mg; Al₂Cu

1. INTRODUCTION

Increasing Copper (Cu) prices and a rising desire for more energy efficient lightweight structures in the mobility industries, demand to substitute more and more Cu components in electrical systems with cheaper, less dense materials [1, 2]. Aluminum (Al) alloys are key substitutes for this purpose, hence joining the two materials is an ongoing research topic, of which references [1, 3–6] give examples and overviews. Friction stir welding is among the most promising joining technologies. However, it is quite limited in terms of processible geometries and material configurations. In contrast to that, the freedom of design in

3D multi-material additive manufacturing (AM), combined with its capability of arbitrary material arrangement makes the production technology predestined to manufacture electrical components from Cu and Al [7]. One single-step AM technology that is promising to achieve high quality final parts in this context is multi-material (MM) laser-based powder bed fusion (LPBF) as described by Anstaett et al. [8–12]. Apart from the question of general processability of desired material combination via this novel production technology, cross-contaminations currently occurring during the MM LPBF in- and post-process can weaken the structural Al parts [13]. Thus, influence and criticality of Cu particles on metallurgical structure of an Al alloy need to be investigated to gain information about achievable mechanical properties of final parts and thus overall applicability of MM LPBF.

2. LITERATURE REVIEW

In this chapter, literature from three research areas is reviewed. First, the status of MM LPBF is summarized. Second, general processability of Cu and Al alloys using named production technology is reviewed. Third, current research about metal powder cross-contaminations and their significance for the processability of previously mentioned material combination is added to the review.

2.1. Multi-material laser-based powder bed fusion

Processing more than one material during a build job is nothing new in AM. Some process categories [14], such as Material Jetting, already offer commercially available

systems with full 3D multi-material capabilities [13]. Recent research aims at enabling the same evolution in LPBF. One main task to do so, is to enhance and refine currently available powder deposition systems [13]. Following the classification of Anstaett et al. [10] as depicted in Fig. 1, all multi-material activities can be categorized in 2D hybrid, 2D multi-material or 3D multi-material AM, depending on the possibility to create material transitions between substrate plate and part, between layers (horizontal transition) and/or within layers (vertical transition). References [8, 15–17], show examples of 2D multi-material systems based on different deposition systems. In contrast, references [9–11, 18] showcase 3D multi-material capabilities in LPBF. Both facilitate a vacuum system to either remove an entire powder layer [9–11] or create a local cavity in the powder bed [18] before depositing the second or third material. As pointed out by Vaezi et al. [13] a second inhibitor to further multi-material LPBF adaption are unintentional cross-contaminations that can occur during material deposition as well as powder removal. The system introduced by Anstaett et al. [10, 11] demands to separate processed materials in the post-process as they get mixed during the build job [12]. The same might be true for powders removed by the vacuum unit applied by Wei et al. [18], but the information is not provided. Even if deposition systems evolve, e.g. by implementing advanced local deposition systems as suggested by Ott [19] or Muguruza et al. [20], the fact that at least two different materials are processed within a single build job and build space will always carry the danger of cross-contaminations. Criticality of these defects and their influence on final part properties depends on the combination of mixed materials and has to be investigated on a single case basis. In order to better understand and evaluate occurring cross-contamination defects for the material combination of Al and Cu, literature about material interaction, processability and joining behavior was reviewed.

2.2. Laser-based powder bed fusion of Aluminum and Copper

For Cu, Al is used as an alloying element up to 15 wt.% in order to increase tensile strength, fracture elongation and hardness [21]. Cu in turn is used as main alloying element in the 2xxx-series of Al wrought and cast alloys below its maximum solubility of 5.65 wt.% in order to enable precipitation hardening by creating α -Al solid solution [22]. At 53.5 wt.% Cu the hard and brittle θ (Al_2Cu) intermetallic compound occurs. The Al- Al_2Cu system has an eutectic at 32.7 wt.% Cu [23]. At concentrations between 53.5 wt.% and 87.2 wt.% Cu in Al, a number of brittle intermetallic compounds form, of which references [23–25] give detailed information. In addition to different physical and mechanical properties, the formation of these intermetallic phases makes joining the two materials technically challenging [4, 6]. General practicability of MM LPBF of Al and Cu was already

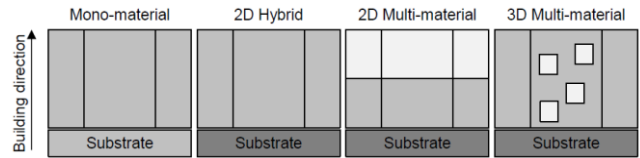


Figure 1: Categorization of multi-material AM [10]

showcased by Sing et al. [26] who created 2D multi-material bimetallic laminates with good inter-metal bonding. The interface between AlSi10Mg and Cu alloy C18400 however showed high Al_2Cu contents, which lead to decreased mechanical properties of the Al part. Reference [27] used LPBF to process mixed Al and Cu powders in five steps between 4.5 and 40 wt.% Cu to in-situ fabricate Al-xCu alloys. Al_2Cu content rose from 10 wt.% to 77 wt.% and was found to be responsible for increased material strength. Due to selective melting and the occurrence of different cooling rate zones with varying material diffusion, the overall material structure resulted to be inhomogeneous. In 3D MM LPBF however, local concentrations of foreign material can be below 1 wt.%, e.g., due to technical limits of mixed powder separation [12]. Thus results of Sing et al. [26] and Wang et al. [27] are only partially applicable. In order to find what is transferable from previously elaborated research and to understand contamination-induced defect formation, relevant literature of this field was reviewed.

2.3. Cross-contaminations in laser-based powder bed fusion

Lutter-Guenther et al. [28] conducted a Failure Mode and Effect Analysis (FMEA) for powder material along the LPBF process chain. They found cross-contaminations to be a defect type with low probability and medium impact on part properties for the mono-material process. A contamination level of 1 wt.% Ni-base alloy Inconel 718 in AlSi10Mg lead to characteristic swirl-like defects in the metallurgical structure but not to part failure. Their study shows that Ni-base alloy particles are fully molten during the process despite the difference in melting temperatures of the two materials. For the same material combination, at an unknown contamination level however, Kilburn [29] observed cracking and thus part failure. Reference [29] suggests brittle $NiAl_3$ and $AlNi_3$ phases that occur due to high local concentrations as reasons for appearing cracks. Another study found Tungsten particles in Ti6Al4V specimen to be responsible for a larger variation in yield strength and tensile strength as well as decreased fracture elongation [30]. In contrast to Lutter-Guenther et al. [28] and Kilburn [29] the foreign particles did not melt but appeared as spherical defects in the Ti6Al4V structure. The same applies to Tungsten particles applied to Ni-base alloy Inconel 625 by Jamshidinia et al. [31]. Depending on the degree of contamination however, the foreign particles caused delamination in the final parts. Thus, it can be found that cross-contaminations do have critical negative effects on material structure and properties in LPBF. Defect

formation, appearance and impact on final parts however varies between different material combinations and has to be further investigated on a single case basis. Therefore, the formation of defects and their influence on metallurgical structures during the multi-material LPBF process chain for Al and Cu was explored and corresponding results are described within the next chapters.

3. MATERIAL AND METHODOLOGY

For previously listed applications in electro mobility, Cu serves as conductor whereas Al mainly serves as load-bearing structural material. Thus, mechanical properties of contaminated Al are at the center of this investigation. In order to secure comparability with Al-Cu wrought alloys, the maximum Cu concentration in Al should remain below the maximum solubility of Cu in Al and was determined to be 5 wt.%. Based on findings from Seidel et al. [12] about general separability of mixed LPBF powder materials, the lower contamination level was chosen to be 0.5 wt.% Cu. In addition, 1 and 3 wt.% Cu were chosen as intermediate steps. The processed Al alloy was AlSi10Mg with a particle size distribution $d_{10,3} - d_{90,3}$ of 20 – 63 μm from SLM Solutions GmbH. Powder material of Cu alloy CuCr1Zr [32] with a particle size distribution $d_{10,3} - d_{90,3}$ of 20 – 45 μm from Schmelzmetall GmbH was used as contamination material. Fifteen minutes of manual tumbling in adjusted powder containers mixed the powders which were then processed using a SLM 250^{HL} LPBF machine from SLM Solutions GmbH to create 10 x 10 x 10 mm³ cubic specimen. Referring to the z-axis as build direction, the test bodies were cut in xy- and yz-planes to obtain metallurgical cross sections. A Hitachi TM3030Plus Scanning Electron Microscope (SEM) with and Energy-dispersive X-ray Spectroscopy (EDS) module from Bruker Nano as well as an Olympus BX53M upright metallurgical light microscope were used for qualitative and quantitative analysis of the specimen.

4. RESULTS AND DISCUSSION

In order to describe and characterize occurring defects, AlSi10Mg specimen contaminated with 0.5 wt.% CuCr1Zr were investigated first. Afterwards the influence of an increased degree of contamination was explored. Cross sections depicted in Fig. 2 show random, yet all over homogenous distribution of coppery enclosures in the Al

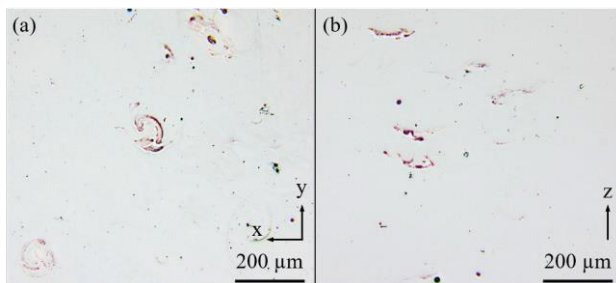


Figure 2: Cross sections of AlSi10Mg parts showing homogenous distribution of coppery defects

structure. In the xy-plane (a) the defects have a swirly shape as already shown by Lutter-Guenther et al. [28]. In the yz-plane (b) however, the coppery conspicuities seem to only appear on the bottom of the melt pools. In contrast to findings from Kilburn [29], no increased accumulations of pores or cracks were found close to the defects. Dark field images also show melt track borders and positions of Cu enclosures within them. It is considered that single particles are responsible for the coppery abnormalities in the xy-plane as Fig. 3 indicates. The bright conspicuities also do not reach beyond melt pool borders. For the yz-plane however, partial remelting of the defects and in this way lifting of mixed material onto the next layer of material at decreased concentrations is possible. SEM and EDS images, also depicted in Fig. 3, show Al and Cu material distribution. In order to further investigate the different material compositions within the enclosures and explore the influences of varying levels of contamination, magnified SEM and EDS images are shown in Fig. 4.

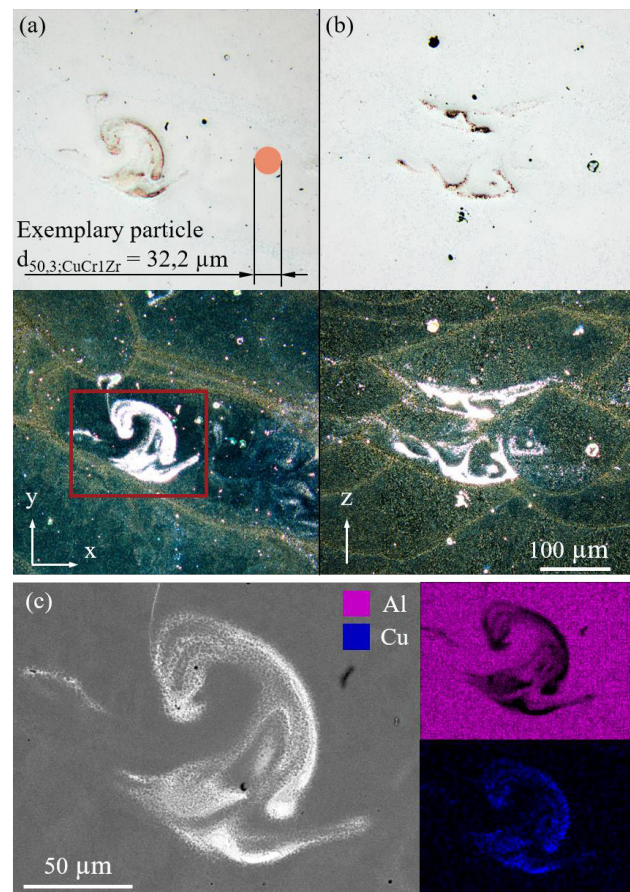


Figure 3: Bright field (BF, top) and dark field (DF, middle) images of AlSi10Mg cross sections in xy-plane including an exemplary CuCr1Zr particle for comparison (a), yz-plane (b) and SEM EDS detail of the highlighted defect in the xy-plane, including element mapping (c).

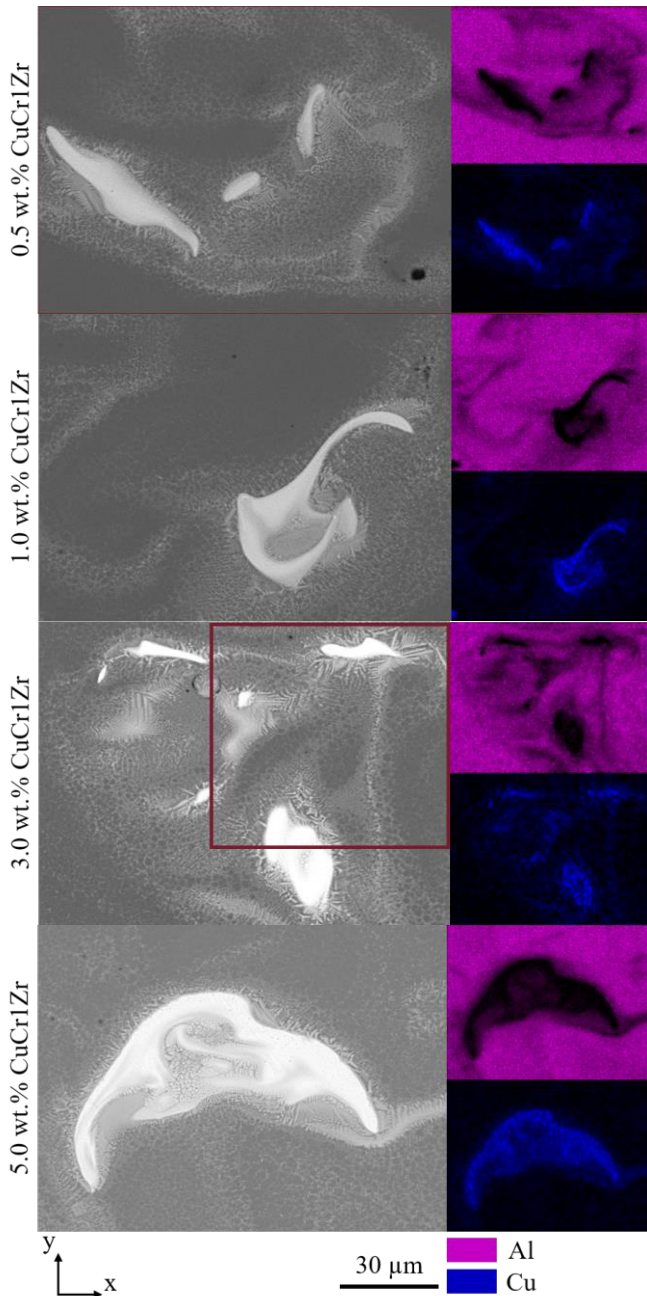


Figure 4: Selected SEM EDS detail images of defects caused by 0.5, 1.0, 3.0 and 5.0 wt.% CuCr1Zr in AlSi10Mg. See Fig. 5 for enlarged detail of 3.0 wt.% CuCr1Zr.

First, despite the different shapes, it appears the general structure of the defects does not change significantly. All material variations contain homogenous Cu-rich zones with maximum Cu contents around 60 wt.%, depicted in white on the SEM image and blue on the EDS picture. The appearance of named areas was explained due to low solute diffusivity of Cu in Al and high cooling rates of the melt pool by Wang et al. [27]. On a more macroscopic level, Cu enclosures are surrounded by α -Al rich zones with purities beyond 90 wt.% Al, shown in black (SEM) and pink (EDS).

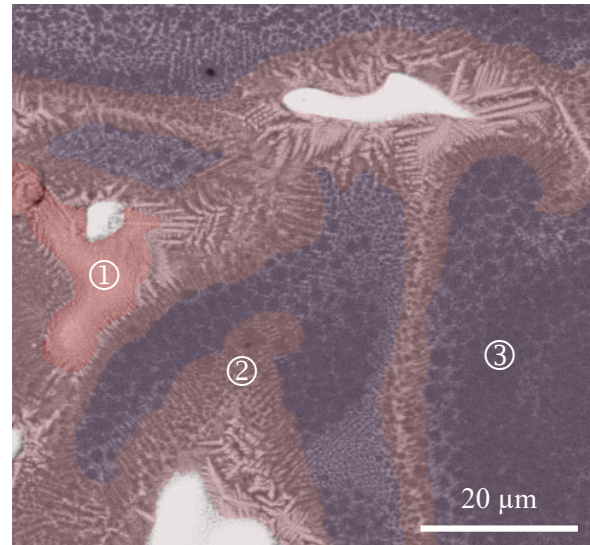


Figure 5: Transition zones ① - ③ with different metallurgical structure exemplary depicted for the highlighted area (Fig. 4) of 3 wt.% CuCr1Zr in AlSi10Mg, xy-plane

Between both single-material-rich zones, three transition zones were identified for all degrees of contamination (Fig. 5). Following the logic of [27], the zones are formed by different cooling rates in the melt pool, which again are explained by varying material compositions due to partial Cu diffusion into the Al matrix. Zone 1 shows a homogenous structure that appears darker than the bright Cu-rich zones it usually verges on. Quantitative wt.% Cu values as depicted in Fig. 6 were obtained by six randomly distributed SEM EDS point measurements per respective zone for each contamination grade. Every single SEM EDS measurement spot was five micrometer in diameter and the chart (Fig. 6) shows arithmetic means as well as standard deviations for said six point measurements. Cu wt.% of zone 1 vary from 30 to 40 thus indicate mainly Al_2Cu -rich hypereutectic material. Verging on zone 1 and high CuCr1Zr content areas, acicular, needle-like structure with

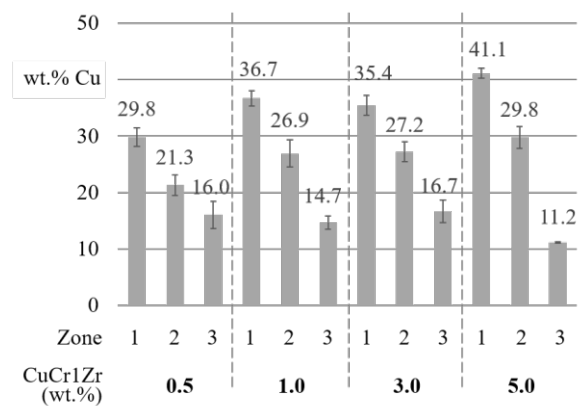


Figure 6: Quantitative SEM EDS Analysis of weight percent Cu in Al for given structural regions

Cu wt.% between 21 and 30 can be found. The appearance leads to the assumption that zone 2 consists of hypoeutectic material which mainly contains lamellar eutectic structure in primary Al matrix. With decreasing Cu content, the microstructure changes to honeycombed Al₂Cu-lattice with floe-like α -Al enclosures in zone 3. The lower the Cu content gets, the coarser the appearance of the honeycombed structure becomes. Cu wt.% between 11 and 16 again indicate hypoeutectic structure which transitions towards α -Al-rich areas further away from the conspicuities. Despite the on average increasing Cu content between different levels of contamination, the defects do not change their overall appearance and all three transition zones can be found for all material composition variations.

Although the types of CuCr1Zr-caused defects in the AlSi10Mg material do not change with increased degree of contamination, the overall structure does. Fig. 7 shows images for all variations that indicate a transition from mostly isolated single abnormalities at 0.5 and 1.0 wt.% CuCr1Zr towards an Al₂Cu-enriched mixed metal structure at 3 and 5 wt.%. The latter is similar to low Cu wt.% in-situ alloying investigations from Wang et al. [27] in terms of heterogeneous structural appearance and even distribution of Al₂Cu enclosures. The influence of

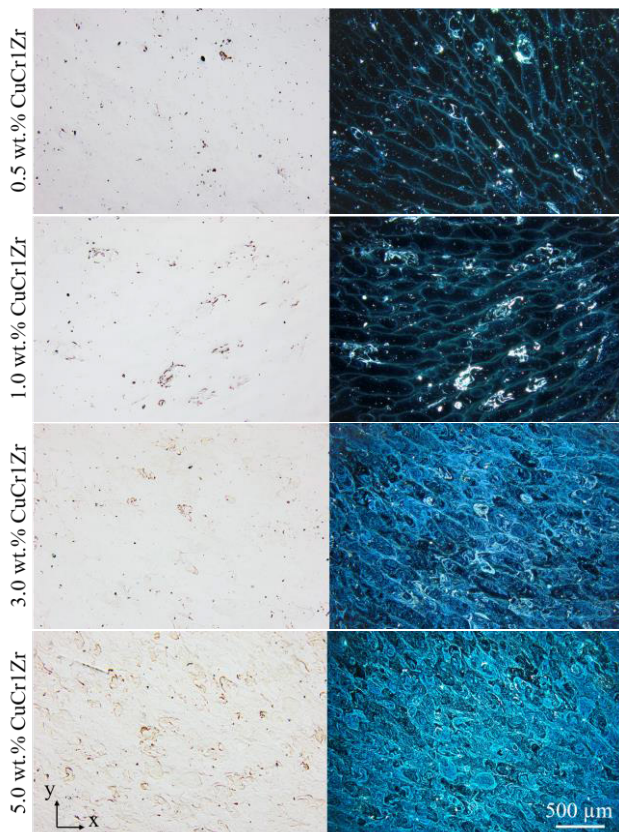


Figure 7: Bright field (left) and dark field (right) overview images of xy-plane cross sections for 0.5, 1.0, 3.0 and 5.0 wt.% CuCr1Zr in AlSi10Mg

increased Al₂Cu creation on material properties (as built), such as hardness, part strength or fracture elongation, for given degrees of contamination should be explored in further investigations. Findings by Sing et al. [26] and Wang et al. [27] however give first indications. Increasing presence of Al₂Cu leads to material embrittlement and higher compressive strength, compared to pure Al alloy cast parts. Maximum bearable compressive stresses rose 20% from 4.5 wt.% Cu to 6.0 wt.% Cu at constant true strains. Findings by Sing et al. [26] support an overall trend towards decreased plasticity and increased part strength for increased Al₂Cu concentration. However, the possibility of material homogenization by thermal treatment has not yet been examined for the underlying material mixtures. Remaining cross-contaminations can be used for in-situ alloying during laser-based powder bed fusion, as suggested by e.g., Wang et al. [27]. Further diffusion of Cu into the Al matrix during optimized thermal treatment could yield material properties similar to precipitation hardened standard Al-Cu alloys.

5. DEFECT FORMATION MODEL

From results of the metallurgical analysis as described in the previous sub-chapter a schematic model to explain defect formation was derived. Fig. 8 illustrates the approach and serves as reference for the following explanation. Image ① of Fig. 8 shows a newly deposited powder layer containing a foreign particle on previously solidified material. Laser energy is used to solidify the powder and in this way to build the part (image ②). Once the laser induced melt pool reaches the foreign particle, two main scenarios can occur. Firstly, the energy input is not high enough to melt the foreign particle due to differences in melting temperature. It then remains unaffected in the final part as described by [30, 31]. Depending on the material combination however, some diffusion between accompanied elements can take place at the edge layer of the foreign particle. This has not yet been studied and should be part of further investigations. In case no diffusion takes place, the defect can be equated to a pore with the volume similar to the enclosed particle. The second scenario, in which the foreign particle is partially or fully melted, was observed and described in the previous sub-chapter. In this scenario, induced laser energy and occurring melt pool dynamics, such as Marangoni convection or natural convections [33, 34], create characteristic swirls of foreign material (image ③). Depending on material solubility, solute diffusivity, mixing grade, melt pool size and temperature as well as cooling rate and material composition in the melt pool, metallurgical reactions take place on the fringe of the foreign material. After solidification, defects as shown in image ④ remain in the metallurgical structure. During solidification of consecutive layers, the defect can be partially remolten, as implied in image ⑤. This can take

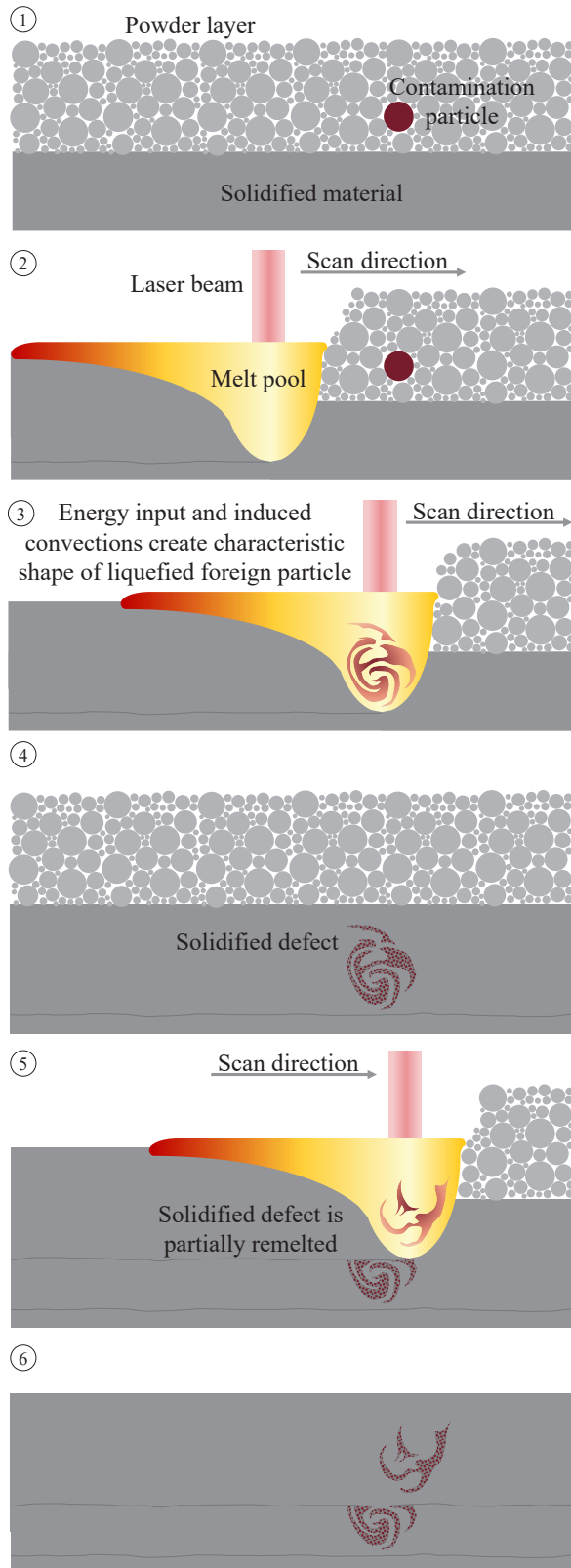


Figure 8: Schematic representation of defect formation due to a single foreign particle

place multiple times and results in structural anomalies as shown in Fig. 3 as well as reflected in image © of Fig. 8. If no additional contamination particle is added to the melt pool at this step, foreign material concentration decreases from layer to layer in build direction.

6. CONCLUSION AND OUTLOOK

In this paper, the relevance of joining Cu and Al alloys to create cost-effective electronic lightweight components via MM LPBF was elaborated. These novel production technologies currently face two challenges: precise material deposition and cross-contaminations occurring at certain stages along the process chain. Regarding the latter, influence of 0.5, 1.0, 3.0 and 5.0 wt.% CuCr1Zr contamination in AlSi10Mg during LPBF was explored. Foreign particles were found to form characteristic swirls in the melt pool due to occurring convections. Because of fast cooling rates, only partial diffusion can take place, which leads to different transition zones from Cu-rich enclosures towards Al-rich structures. General shape of CuCr1Zr induced defects and prevalence of described transition zones are similar for all contamination grades. Repeated remelting of named swirls however leads to wider Cu distribution in the final structure as well as a general Al₂Cu enrichment. Previous research indicates a general trend towards decreased plasticity and elevated compressive strength as well as general material embrittlement for rising Cu concentrations due to Al₂Cu enrichment [26, 27]. Influence of increased Al₂Cu appearance in the AlSi10Mg matrix at given concentrations less than 5 wt.% Cu, on mechanical properties – foremost on tensile and fatigue strength – should be part of upcoming investigations. Initial findings for named material combination however, lead to the assumption that cross-contaminations occurring in MM LPBF might turn out noncritical up to specific levels or could even improve certain part properties via in-situ alloying. From described learnings, a model to delineate defects occurring from metal powder cross-contaminations was derived. Upcoming research needs to verify the postulated model and should further extend it by adding information about e.g., supplementary material combinations.

7. ACKNOWLEDGMENT

The authors express their sincere thanks to the Freistaat Bayern and its Bavarian Ministry of Economic Affairs, Energy and Technology for funding the "MULTIMATERIALZENTRUM Augsburg" (English: "Multi-material Center Augsburg").

8. REFERENCES

- [1] K. Hofmann, M. Holzer, F. Hugger, S. Roth, and M. Schmidt, "Reliable Copper and Aluminum Connections for High Power Applications in Electromobility," *Physics Procedia*, vol. 56, pp. 601–609, 2014.

- [2] German Copper Alliance, “Schweißen von Kupfer und Kupferlegierungen,” *Informationsdruck i.12*, 2009.
- [3] J. P. Bergmann, F. Petzoldt, R. Schürer, and S. Schneider, “Solid-state welding of aluminum to copper—case studies,” *Weld World*, vol. 57, no. 4, pp. 541–550, 2013.
- [4] I. Galvão, J. C. Oliveira, A. Loureiro, and D. M. Rodrigues, “Formation and distribution of brittle structures in friction stir welding of aluminium and copper: influence of process parameters,” *Science and Technology of Welding and Joining*, vol. 16, no. 8, pp. 681–689, 2011.
- [5] T. A. Mai and A. C. Spowage, “Characterisation of dissimilar joints in laser welding of steel–kovar, copper–steel and copper–aluminium,” *Materials Science and Engineering: A*, vol. 374, no. 1–2, pp. 224–233, 2004.
- [6] J. Kaspar *et al.*, “Challenges in Joining Aluminium with Copper for Applications in Electro Mobility,” *MSF*, vol. 783–786, pp. 1747–1752, 2014.
- [7] R. Werner, J. Rudolph, and F. Lorenz, *Manufacturing complete electric engines in a 3D printer*. [Online] Available: <https://www.maschinenmarkt.international/manufacturing-complete-electric-engines-in-a-3d-printer-a-699051/>. Accessed on: May 25 2018.
- [8] C. Anstaett and C. Seidel, “Next Step in Laser-Based Powder Bed Fusion - Multi Material Processing,” *LTI*, vol. 13, no. 3, p. 21, 2016.
- [9] C. Anstaett, C. Seidel, and G. Reinhart, “Multi-Material Processing in Laser Beam Melting,” *DDMC 2016: Fraunhofer Direct Digital Manufacturing Conference*, 2016.
- [10] C. Anstaett, C. Seidel, and G. Reinhart, “Fabrication of 3D Multi-material Parts Using Laser-based Powder Bed Fusion,” *Proceedings of the 28th Annual International Solid Freeform Fabrication Symposium*, 2017.
- [11] C. Anstaett, C. Seidel, and G. Reinhart, “Multi-Material Fabrication of Copper-Chrome-Zirconia and Tool Steel 1.2709 by Powder Bed Based Laser Beam Melting,” *DDMC 2018: Fraunhofer Direct Digital Manufacturing Conference*, 2018.
- [12] C. Seidel, C. Anstaett, M. Horn, and M. Binder, “Status-quo der metallischen Multimaterialverarbeitung mittels Laserstrahlschmelzen,” *DGM-Fachtagung Werkstoffe und Additive Fertigung - Conference Presentation*, 2018.
- [13] M. Vaezi, S. Chianrabutra, B. Mellor, and S. Yang, “Multiple material additive manufacturing – Part 1: a review,” *Virtual and Physical Prototyping*, vol. 8, no. 1, pp. 19–50, 2013.
- [14] *DIN EN ISO ASTM 52900:2015, Additive Manufacturing - General Principles - Terminology*.
- [15] T. Laumer, M. Karg, and M. Schmidt, “Laser Beam Melting of Multi-Material Components,” *Physics Procedia*, vol. 39, pp. 518–525, 2012.
- [16] A. G. Demir and B. Previtali, “Multi-material selective laser melting of Fe/Al-12Si components,” *Manufacturing Letters*, vol. 11, pp. 8–11, 2017.
- [17] Y. Chivel, “New Approach to Multi-material Processing in Selective Laser Melting,” *Physics Procedia*, vol. 83, pp. 891–898, 2016.
- [18] C. Wei, L. Li, X. Zhang, and Y.-H. Chueh, “3D printing of multiple metallic materials via modified selective laser melting,” *CIRP Annals*, 2018.
- [19] M. Ott, “Laser beam and powder bed based multi-material additive manufacturing process,” Dissertation, Technical University of Munich, Munich, 2012.
- [20] A. Muguruza *et al.*, “Development of a multi-material additive manufacturing process for electronic devices,” *Procedia Manufacturing*, vol. 13, pp. 746–753, 2017.
- [21] German Copper Alliance, “Cu Al Alloys (3rd Edition),” *Informationsdruck i.6*, 2010.
- [22] E. Macherauch and H.-W. Zoch, Eds., *Praktikum in Werkstoffkunde: 91 ausführliche Versuche aus wichtigen Gebieten der Werkstofftechnik*, 11th ed. Wiesbaden: Vieweg+Teubner Verlag / Springer Fachmedien Wiesbaden GmbH Wiesbaden, 2011.
- [23] J. L. Murray, “The aluminium-copper system,” *International Metals Reviews*, vol. 30, no. 1, pp. 211–234, 1985.
- [24] D. M. Rabkin, V. R. Ryabov, A. V. Lozovskaya, and V. A. Dovzhenko, “Preparation and properties of copper-aluminum intermetallic compounds,” *Powder Metall Met Ceram*, vol. 9, no. 8, pp. 695–700, 1970.
- [25] N. Ponweiser, C. L. Lengauer, and K. W. Richter, “Re-investigation of phase equilibria in the system Al-Cu and structural analysis of the high-temperature phase η 1-Al11- δ Cu,” (eng), *Intermetallics*, vol. 19, no. 11, pp. 1737–1746, 2011.
- [26] S. L. Sing, L. P. Lam, D. Q. Zhang, Z. H. Liu, and C. K. Chua, “Interfacial characterization of SLM parts in multi-material processing: Intermetallic phase formation between AlSi10Mg and C18400 copper alloy,” *Materials Characterization*, vol. 107, pp. 220–227, 2015.
- [27] P. Wang *et al.*, “Microstructure and mechanical properties of Al-Cu alloys fabricated by selective laser melting of powder mixtures,” *Journal of Alloys and Compounds*, vol. 735, pp. 2263–2266, 2018.
- [28] M. Lutter-Günther, F. Schwer, C. Seidel, and G. Reinhart, “Effects on Properties of Metal Powders for Laser Beam Melting Along the Powder Process Chain,” *DDMC 2016: Fraunhofer Direct Digital Manufacturing Conference*, 2016.
- [29] P. Kilburn, “LPW Technology – Intelligence in Metal,” *Company Presentation*, http://www.advantageaustria.org/gb/events/LPWTechnologies_PhilKilburn_3011_2.pdf, 2016.
- [30] A. D. Brandão *et al.*, “Challenges in Additive Manufacturing of Space Parts: Powder Feedstock Cross-Contamination and Its Impact on End Products,” (eng), *Materials*, vol. 10, no. 5, 2017.
- [31] M. Jamshidinia, P. Boulware, J. Marchal, H. Mendoza, L. Cronley, S. Kelly, S. Newhouse, “In-Process Monitoring of Cross Contamination in Laser Powder Bed Fusion (L-PBF) Additive Manufacturing (AM),” *Proceedings of the 27th Annual International Solid Freeform Fabrication Symposium*, 2016.
- [32] German Copper Alliance, “Material data sheet CuCr1Zr,”
- [33] C. L. A. Leung *et al.*, “In situ X-ray imaging of defect and molten pool dynamics in laser additive manufacturing,” *Nature Communications*, vol. 9, no. 1, p. 1355, 2018.
- [34] P. Yuan, D. Gu, and D. Dai, “Particulate migration behavior and its mechanism during selective laser melting of TiC reinforced Al matrix nanocomposites,” *Materials & Design*, vol. 82, pp. 46–55, 2015.

Parameter study on laser beam melting of WC-Co at 800°C pre-heating temperature

Tobias Schwanekamp, iWFT Institute of Manufacturing and Tooling Technology,
University of Applied Sciences Cologne (RFH), Germany, tobias.schwanekamp@rfh-koeln.de

Martin Reuber, iWFT Institute of Manufacturing and Tooling Technology,
University of Applied Sciences Cologne (RFH), Germany, reuber@rfh-koeln.de

Abstract— In contrast to the classical sintering of WC-Co, the Laser Beam Melting (LBM) process is subject to a highly localized energy input and thermal exposure times in the order of microseconds. As a result, laser molten WC-Co is characterized by a heterogeneous microstructure inclosing pores, cracks, brittle material phases and WC grain growth. To reduce the thermal gradients during the process and thereby improve the mechanical properties of the material, a high temperature pre-heating module is applied. The effectiveness of 800°C pre-heating is demonstrated in an initial test by generating fully crack free specimens from WC-Co composite powder materials. Based on the results, the present study focuses on the optimization of the main process parameters at an elevated base plate temperature of 800°C. A response surface-based Design of Experiments is applied to determine the impact of the LBM parameters on the mechanical and microstructural material properties.

Keywords— Laser Beam Melting; Selective Laser Melting; LBM; SLM; Additive Manufacturing; Tungsten Carbide; WC-Co; High Temperature Pre-Heating; Parameter Optimization; Design of Experiments; Cutting Tools; PraeziGen

1. INTRODUCTION

Industrial applications of Laser Beam Melting (LBM) in cutting tool manufacturing are hitherto limited to the processing of a few steel alloys. A sufficient quality for carbide materials, such as WC-Co, is not yet achieved. Laser molten WC-Co is still characterized by a heterogeneous microstructure inclosing pores, cracks, brittle material phases and WC grain growth. An overview of studies on LBM of WC-Co, conducted since 2010 by different research institutions, was published by [1]. A conflict between reducing the relative porosity and preventing the material from cobalt evaporation during the LBM process was pointed out. The induction of a high laser energy causes an increased amount of liquid phase inside the melting pool, which leads

to an improved wetting behavior and a reduction of porosity. In contrast, a high energy input causes a significant evaporation of cobalt, a reduction of fracture toughness and, in combination with the high temperature gradients, thermal cracking. Even an evaporation of carbon was detected, which leads to a formation of brittle W₂C- and η -carbides. This conflict was also confirmed by the authors [2] and is illustrated in Figure 1 for three different specific energies E_V . The conflict cannot solely be solved by an optimization of the main LBM parameters such as laser power P , scan speed v , hatch distance h and layer thickness Δs . Hence, additional measures must be applied to improve the material quality.

A significant reduction of residual stresses and thermal cracking in laser molten high-speed steel parts was achieved by pre-heating of the build platform up to 200°C [3]. A study conducted in preparation of this paper indicated, that pre-heating temperatures around 800°C are promising for LBM of WC-Co due to the following expected effects.

- The laser energy input, which is required for consolidation of the powder, can be reduced.
- Thermal gradients between the process zone, respectively the melt pool and the surrounding area are reduced.
- The fracture toughness of WC-Co is significantly increased at temperatures around 800°C [4].
- According to [5], the formation of brittle W₂C in the W-Co-C system is inhibited.

Hence, an 800°C pre-heating module was developed and the effectiveness was demonstrated in an initial test by generation of crack- and W₂C-free specimens from WC-Co powder materials with Co mass fractions of 12% and 17% [6] as illustrated in Figure 2.

The presented work is conducted in the framework of the project “PraeziGen” and supported by the Federal Ministry of Education and Research (BMBF) under the topic of “Photonische Prozessketten”, support code: 03XP0012H.

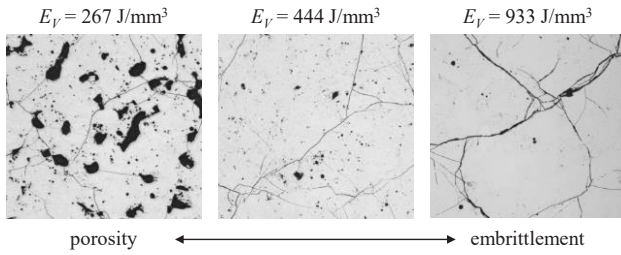


Figure 1. Conflict of objectives in the parameter optimization for SLM of WC-Co, porosity for low energy input, embrittlement for high energy input

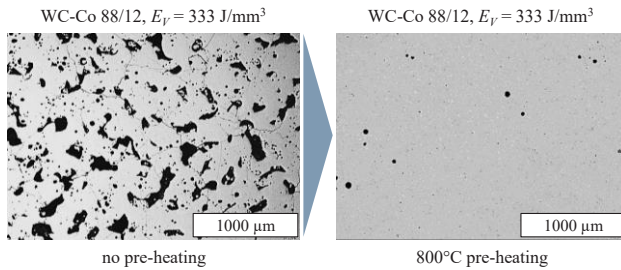


Figure 2. Impact of 800°C pre-heating on the material structure of WC-Co specimens, generated with identical powder and laser parameters

A parallel study, published by Schubert et al. indicated, that a positive effect can already be observed at pre-heating temperatures of 650°C [7]. Based on these positive results, a response surface-based Design of Experiments (DoE) is applied in the present paper to determine the impact of the LBM parameters on the mechanical and microstructural material properties and to optimize the main process parameters at 800°C pre-heating temperature.

2. EXPERIMENTAL PROCEDURE

2.1. Material

For the present study, agglomerated and pre-sintered WC-Co thermal spray powders are used. Table 1 gives an overview of the powder specifications as provided by the factory certification test report from DURUM VERSCHLEISS-SCHUTZ GMBH. Two different cobalt mass fractions of 17% and 12% with different particle size distributions and carbide grain sizes are investigated. SEM images of the powders and particle cross-sections are shown in Figure 3. The particles are compact and largely spherical by approximation, ensuring a sufficient flow capability for the LBM process. The porosity inside the 88/12 particles is significantly lower in comparison to the 83/17 particles, resulting in an increased bulk density and a better hall flow.

TABLE 1. MATERIAL DATA OF THE PROCESSED POWDER TYPES PROVIDED BY DURUM

DURMAT	111.008	102.007
WC/Co	88/12	83/17
Co [wt-%]	12.0	17.04
C [wt-%]	5.4	5.46
W [wt-%]	82.5	77.5
Bal. [wt-%]	0.1 (Fe)	-
Particle size	-45+10 µm	-45+22 µm
WC-grain size	1.3 µm	2.5 µm
Bulk density	6.1 g/cm ³	4.9 g/cm ³
Hall flow (50 g)	10.1 s	15.0 s

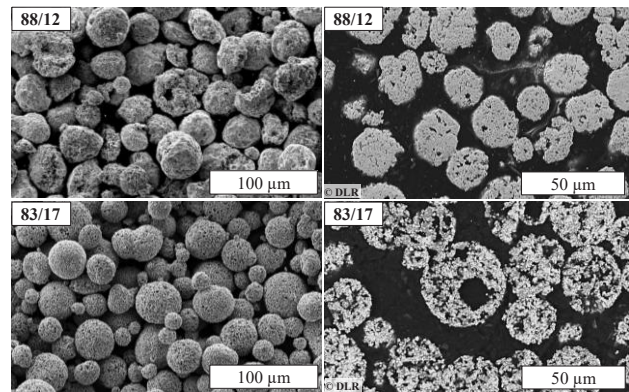


Figure 3. SEM image of 88/12 (top) and 83/17 (bottom) powder particles, top view (left) and cross-section polish (right)

2.2. LBM process

All experiments are conducted on a Renishaw AM 250 system under inert gas atmosphere (nitrogen 5.0) at an elevated base plate temperature of 800°C. A standard meander scan pattern is applied using a 200 W fiber laser with a focal diameter of $d_f = 75 \mu\text{m}$ (Gaussian mode, TEM₀₀). The layer thickness is kept on a constant value of $\Delta s = 30 \mu\text{m}$. The impact of variations in the laser power P , the scan velocity v and the hatch distance h on the porosity, the occurrence of thermal cracks, the Vickers hardness, and the cobalt evaporation is investigated. Furthermore, the flexural strength is determined for WC-Co 83/17. To reduce the experimental effort, a central composite DoE is implemented, which enables to consider second order response models (Figure 4). DoE is widely used in research and statistics and a comprehensive description of the applied methodology can e.g. be found in [8]. For this paper, the statistical software Minitab 17 is utilized. The applied DoE setup consists of 15 different parameter settings, eight cube points, six axial points and one center point. Four specimens are generated for each cube and axial point and 24 specimens are generated for the center point to consider process-related fluctuations.

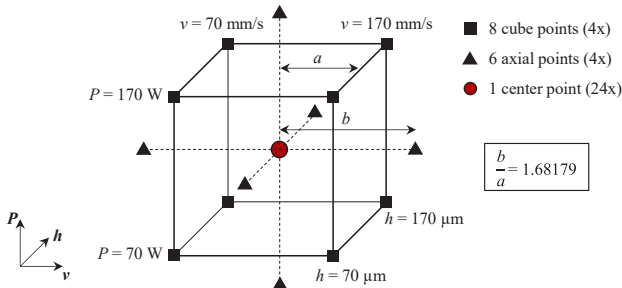


Figure 4. Central composite DoE, applied for the present study

3. RESULTS AND DISCUSSION

3.1. Porosity

The porosity ϕ_{rel} is defined as the percentaged volume of voids respectively pores in relation to the total volume of a porous medium. Main effects plots are used to visualize the qualitative changes in the average porosity ϕ_{rel} of the laser molten specimens, caused by variations of the input parameters P , v and h (Figure 5). The correlation between the input parameters and the response is approximated by a second order regression model. An example of such a model is given in equation (1) for the response ϕ_{rel} . The coefficients c_0 to c_9 are fitted to the results of the porosity measurements using the least squares method (Table 2).

$$\phi_{rel} = c_0 + \underbrace{c_1 P + c_2 v + c_3 h}_{\text{linear effects of } P, v \text{ and } h} + \underbrace{c_4 P^2 + c_5 v^2 - c_6 h^2}_{\text{quadratic effects of } P, v \text{ and } h} + \underbrace{c_7 P v + c_8 P h + c_9 v h}_{\text{2-factor interactions between } P, v \text{ and } h} \quad (1)$$

TABLE 2. FITTED COEFFICIENTS FOR THE REGRESSION EQUATION OF THE POROSITY ϕ_{rel} AS A FUNCTION OF P , v AND h

c_i	WC-Co 83/17	WC-Co 88/12
c_0	3.91	7.28
c_1	- 0.1197 W ⁻¹	- 0.2835 W ⁻¹
c_2	0.0528 s/mm	0.1279 s/mm
c_3	31.5 mm ⁻¹	79.8 mm ⁻¹
c_4	0.000678 W ⁻²	0.001689 W ⁻²
c_5	0.00008 s ² /mm ²	- 0.000072 s ² /mm ²
c_6	- 49.0 mm ⁻²	- 55.0 mm ⁻²
c_7	- 0.000533 W ⁻¹ s/mm	- 0.001073 W ⁻¹ s/mm
c_8	- 0.1961 W ⁻¹ mm ⁻¹	- 0.797 W ⁻¹ mm ⁻¹
c_9	0.1156 s/mm ²	0.532 s/mm ²

A strong impact on the porosity is exerted by the laser power P , whereas the main effect of the scan velocity v and the hatch distance h is less distinct. It must be noted, that negative values for ϕ_{rel} are occurring in consequence of the statistical model and can be considered as physically irrelevant.

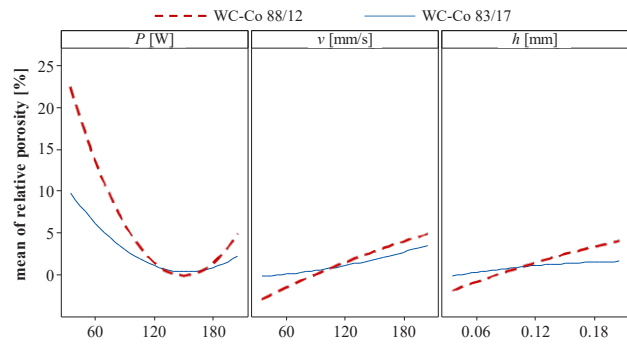


Figure 5. Main effects plot for the mean of the porosity ϕ_{rel}

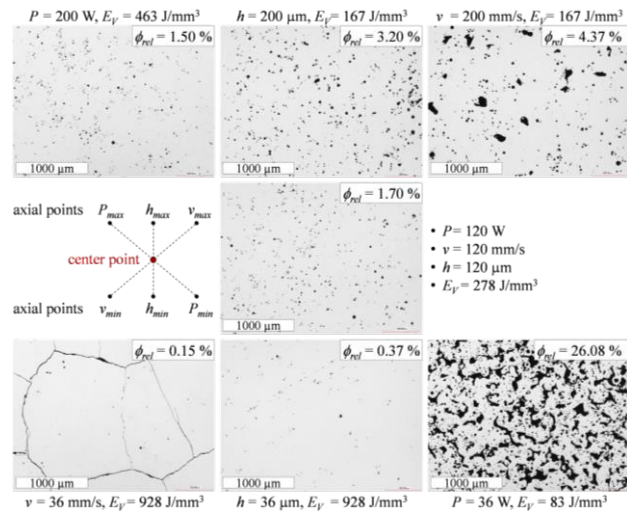


Figure 6. Polished cross sections of the specimens generated from WC-Co 88/12 with parameter settings of the DoE center point and axial points

In summary, a more significant impact of P , v and h on the porosity is detected for the powder with the lower initial cobalt content. Taking this into account, the polished cross sections of the specimens, made from WC-Co 88/12 with the parameter settings of the axial points and the center point are compared in Figure 6. The lowest measured porosities of $\phi_{rel} = 0.15\%$ and $\phi_{rel} = 0.37\%$ are achieved for the minimum values of v and h . However, for WC-Co 88/12, thermal cracking cannot reliably be prevented for these parameter settings. The lowest mean porosities in the overall DoE without any occurrence of cracks are determined by $\phi_{rel} = 0.8\%$ (WC-Co 88/12) and $\phi_{rel} = 0.6\%$ (WC-Co 83/17).

3.2. Cobalt evaporation

Energy dispersive X-ray spectroscopy (EDX) is applied to determine the remaining Co fraction inside the specimens in comparison to the initial powder material. The measurement results are used for the approximation of a second order regression model, similar to equation (1). A considerable loss of Co is detected for all the specimens (Figure 7).

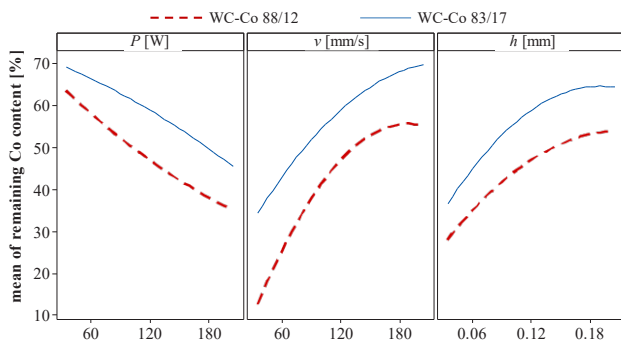


Figure 7. Main effects plot for the mean of remaining Co content in the specimens in percentage of the Co content of the original powder material

Significant impact of P , v and h is observed as well as an influence of the overall specific energy E_V . Parameter settings leading to an increase in E_V result in an increased Co evaporation by trend. The relative loss in Co is basically more severe for the lower initial Co content (88/12). It must be noted that at least 35% for 88/12 respectively 25% for 83/17 of the initial Co of the powder are evaporated during the LBM process, even for the lowest energy inputs. This must be considered for the choice of a suitable powder material. For future studies, increased initial Co contents could hence be used in combination with a suited application of laser energy to reproducibly create parts with tailored Co fractions and mechanical properties.

3.3. Cracks

The occurrence of thermal cracking can significantly be reduced by 800°C pre-heating. All specimens made from WC-Co 83/17 are completely free of cracks. For WC-Co 88/12, cracking is only detected for parameter settings with high specific energy inputs above 900 J/mm³ (Figure 8). For $E_{V,max}$ and v_{min} cracking is always observed, whereas for h_{min} cracking is detected rather sporadically. A possible correlation to the Co depletion in the specimen can be assumed, since for $E_{V,max}$ and v_{min} an average Co evaporation by approx. 90% compared to the powder composition is detected. This means that only about 1.2 wt.-% of Co are left in the material. For h_{min} , the average evaporation of 75% is lower than for $E_{V,max}$ and v_{min} . A significant impact of the position order on the base plate as well as the laser power P on the formation of cracks is not detected. The impact of v and h is found to be much stronger.

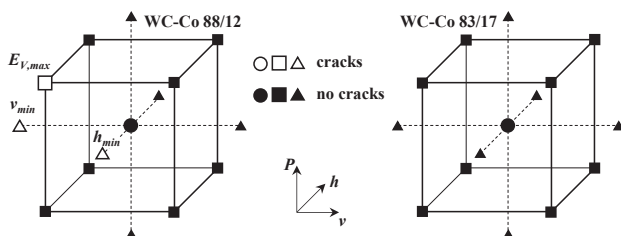


Figure 8. Critical parameter settings in terms of cracking

3.4. Vickers hardness

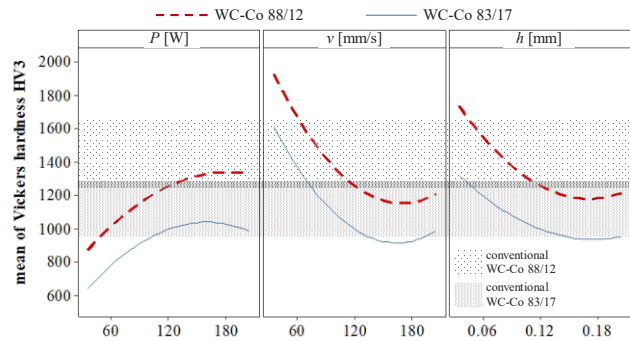


Figure 9. Main effects plot for the mean of Vickers hardness HV3

The determined regression models revealed significant effects of the factors P , v and h on the mean Vickers hardness HV3 (Figure 9). The Vickers hardness range of conventionally manufactured WC-Co 88/12 and 83/17 is not only dependent on the Co content but also on the WC grain size and is illustrated in the figure, too. Higher HV3 values of the laser molten specimens are an indicator for Co evaporation and embrittlement, whereas lower values can be attributed to an increase of material defects such as pores and Co agglomerations.

3.5. Flexural strength

Due to the experimental effort, the flexural strength σ_f is only measured for the specimens made from WC-Co 83/17 in a three-point flexural test according to ISO 3327:2009. Figure 10 shows the main effects of P , v and h on the mean of σ_f . A significant impact of P and v is evident. Parameter settings leading to a high specific energy E_V result in an increased Co evaporation and therefore in a reduction of σ_f , caused by embrittlement or even by thermal cracking. On the other hand, a significant reduction of E_V causes a decrease in σ_f due to an increased porosity and a corresponding reduction of the effective cross-section. Furthermore, a significant positive interaction between P and v as well as between P and h is detected based on the regression model. This means that increased factor levels of v or h lead to an intensification of the effect of P . The maximum flexural strength of all tested specimens is measured by $\sigma_f = 1320$ MPa.

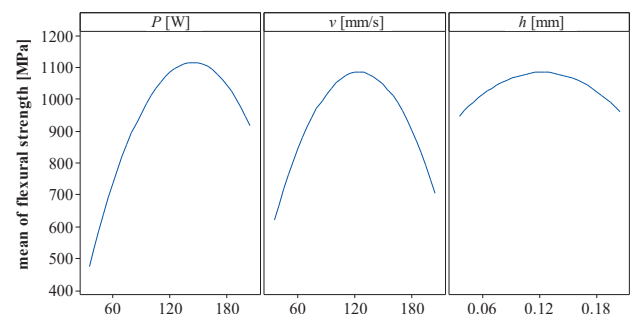


Figure 10. Main effects plot for the mean of σ_f (WC-Co 83/17)

3.6. Response optimization

Based on the results of the DoE, optimized factor level combinations for P , v and h are determined for WC-Co 83/17 by means of the derived regression equations. It is found, that the achieved results are sensitive to the number of optimization goals. Hence, three different optimization steps with an increasing number of optimization goals are conducted. In a first step (Opt. 1), a maximization of σ_f is chosen as a single optimization goal. The response optimization provides the factor levels $P_1 = 200$ W, $v_1 = 177$ mm/s and $h_1 = 194$ μ m. The relatively high values of the factor levels compared to Figure 10 can be attributed to the significant positive interactions between P and v respectively h . In a second step (Opt. 2), the porosity ϕ_{rel} as well as the Co evaporation should be minimized. The response optimization provides the factor levels $P_2 = 193$ W, $v_2 = 204$ mm/s and $h_2 = 204$ μ m. In the third step (Opt. 3), the minimization of the standard deviation in the Vickers hardness S_{HV3} is taken as an optimization goal, in addition to the minimization of ϕ_{rel} and the Co evaporation. The standard deviation in the repeatedly measured Vickers hardness HV3 is affected by material defects such as pores, Co agglomerations and the WC grain size and can therefore be referred to as a qualitative indicator for the homogeneity of the material microstructure. For the determination of S_{HV3} , six measurements of HV3 are taken on each specimen. The third response optimization step provides the factor levels $P_3 = 200$ W, $v_3 = 204$ mm/s and $h_3 = 180$ μ m. The additional optimization goal does not have a major effect on the optimized factor levels, since the lowest values of S_{HV3} can be achieved in a parameter range very similar to Opt. 1 and Opt. 2 (Figure 11). The factor levels of the three optimization steps are inserted into the regression equations to obtain the predicted values of flexural strength, relative porosity, Co evaporation and Vickers hardness. Beyond that, the upper and lower limits of the 95% confidence intervals are determined for each combination of factor level and response variable. To validate the results, five specimens are built for each of the three factor levels and their flexural strength, the relative porosity, the Co evaporation and the Vickers hardness is measured. The average results and the standard deviations are shown in Figure 12 in comparison to the 95% confidence interval and the predicted response values. All response variables are inside of the confidence interval and hence, flexural strength, relative porosity, Co evaporation and Vickers hardness can be assumed to be sufficiently approximated by the regression equations. The highest values of flexural strength with the lowest standard deviations are achieved with the parameter setting (P_1 , v_1 , h_1) of optimization Opt. 1. This is in line with the expectations, since the objective of Opt. 1 was the maximization of σ_f . However, for all optimized factor levels Opt. 1, Opt. 2 and Opt. 3, the achieved flexural strength is still below the predicted response value. A correlation to the porosity and the Co evaporation is apparent here. Both are above the predicted values, which negatively affects the flexural strength.

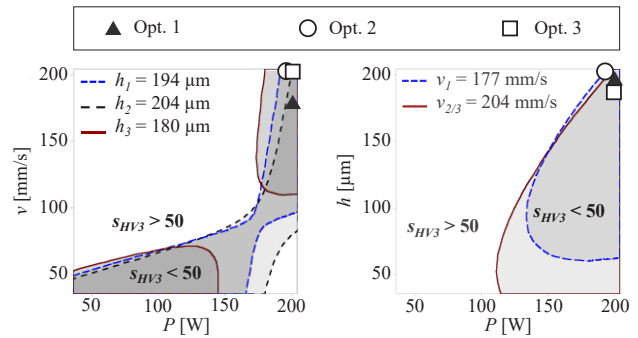


Figure 11. Contour plots of the effect of interacting factors P , v and h on S_{HV3}

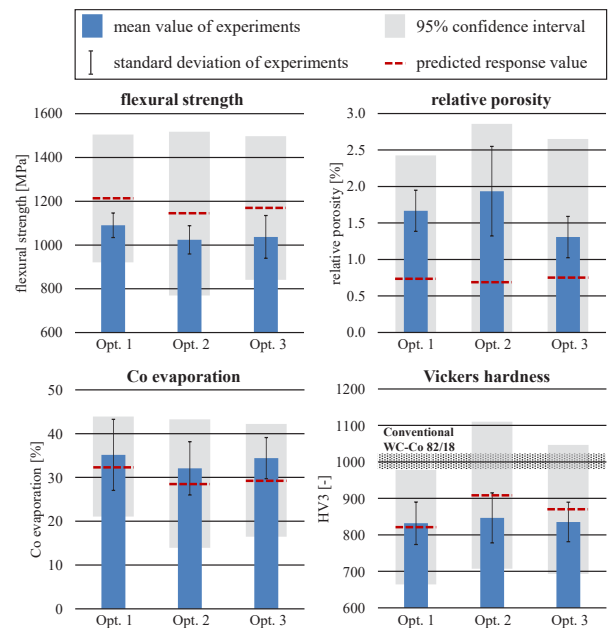


Figure 12. Comparison of σ_f , ϕ_{rel} , Co evaporation and Vickers hardness of the optimized specimens with the 95% confidence interval

Looking into the Vickers hardness, it can be noted, that all values are significantly below the hardness of conventionally sintered material, which can be attributed to the remaining material defects such as pores, WC grain growth and cobalt agglomerations. This is also underlined by the higher standard deviations of the LBM processed samples in comparison to the conventionally sintered material. It can be noted, that a reference measurement on a conventional WC-Co 82/18 (grade G40) results in a Vickers hardness HV3 of 998 (and a standard deviation of $S_{HV3} = 22$). In contrast, the minimum standard deviation of the response optimization is achieved for the parameter set of Opt. 3 by $S_{HV3} = 54$. This can be considered as an indicator for a more heterogeneous microstructure.

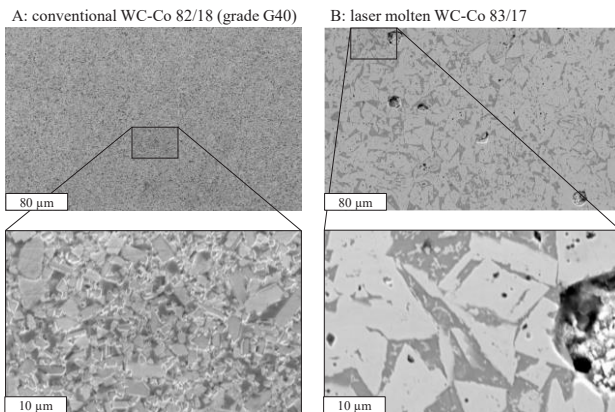


Figure 13. SEM images of polished cross sections, conventionally sintered WC-Co 82/18 (left) and laser molten from WC-Co 83/17 powder (right)

The remaining defects in the LBM samples causing the inferior mechanical properties compared to conventionally sintered WC-Co are visible in Figure 13. Besides the large entrapped gas pores (Figure 13 B, top), there are also small pores inside the large WC particles (Figure 13 B, bottom), most likely caused during recrystallization and grain growth. An SEM/EDX analysis of the Co binder between the WC-particles showed filamentary structures, rich in tungsten. According to the literature those structures are caused by metastable solidification of WC, dissolved in the Co phase due to very high melt pool temperatures [7].

3.7. Continuative approaches

Beyond the parameter optimization at 800°C, continuative approaches are followed to further improve the homogeneity and thereby the mechanical properties of the material. The positive impact of a multiple scan strategy was already described by Schwaneckamp and Reuber for a base plate temperature up to 170°C [2]. A first test with WC-Co 83/17 also reveals a significant effect at 800°C. For the main laser exposure, a laser power of $P = 60 \text{ W}$ ($E_V = 167 \text{ J/mm}^3$) is chosen. A triple post exposure is conducted with $P = 30 \text{ W}$. Figure 14 shows the polished cross sections of a specimen, generated only with one main laser exposure (left) and a specimen generated with an additional triple post exposure (right). A reduction of the relative porosity by more than 50% is achieved. Furthermore, the standard deviation in the Vickers hardness is reduced from $SHV_3 = 134$ to $SHV_3 = 40$. Hence, this approach seems to be promising for the further optimization of the material quality and will be investigated by systematic studies in the future. However, the drastically increased processing time of this method must be considered as a serious disadvantage in terms of economic efficiency.

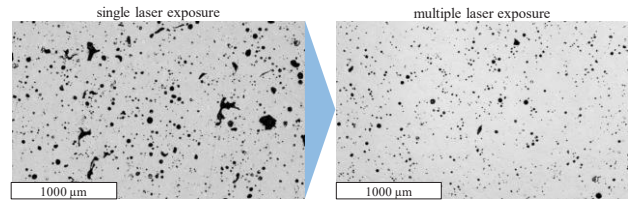


Figure 14. Cross section of specimens, generated with a single laser exposure (left) and with a triple laser post exposure at 800°C pre-heating

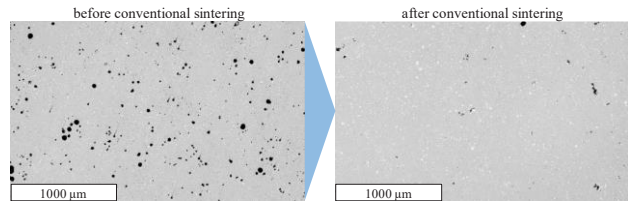


Figure 15. Cross section of a WC-Co specimen generated at 800°C pre-heating before (left) and after (right) conventional sintering post-process

Alternatively, it was shown by [9] and [10] that thermal post-processing is a suitable approach to reduce thermal stresses in laser molten metal parts. To investigate, whether this approach is effective for WC-Co specimens generated with 800°C pre-heating, some initial tests are carried out with samples made from WC-Co 83/17. They are post-processed with a conventional sintering process under vacuum with a maximum sintering temperature of 1400°C. Figure 15 shows the cross section of a specimen before and after the sintering process. A significant reduction of the relative porosity from 2.1% to 0.35% can be measured. It was found, that the effect of thermal post-processing significantly increases with decreasing the size of the pores and an increasing Co content inside the material.

4. SUMMARY AND OUTLOOK

The presented results on LBM of WC-Co indicate that the fundamental conflict of objectives in the simultaneous minimization of ϕ_{rel} and the prevention of embrittlement and Co evaporation also exists at 800°C pre-heating temperature. However, beyond a sole optimization of the main process parameters P , h and v , high temperature pre-heating offers the possibility to significantly expand the boundaries of the achievable optimization results compared to the previous state of technology and research. Thermal gradients can be reduced as well as the required laser energy input for densification of the material. Another positive effect of the high temperature is given by the increase of fracture toughness through thermal softening and the inhibition of W_2C formation. In consequence, a prevention of thermal cracking and thereby a significant increase of the material strength can be achieved for a wide range of parameters. Even though an identification of optimized LBM parameter sets using DoE is possible, limiting factors such as residual

pores, WC grain growth and Co-agglomerations, are still present. Those deficits degrade the mechanical properties in comparison to the predicted values and, much more, in comparison to conventionally sintered WC-Co. The defects can be attributed to the fundamental characteristics of the LBM process, mainly the heterogeneous energy input. Based on the findings of this study, it must be supposed, that residual defects can only be eliminated by a further homogenization of the energy input and thereby a further expansion of the optimization boundaries. The following potentially promising approaches for this purpose are recommended:

- An increase in the prediction accuracy of optimized parameters by means of DoE can be expected, if fundamental microstructural defects, such as WC grain growth, are also implemented into the regression model.
- A further homogenization of the energy input in addition to pre-heating, e.g. by multiple scan strategies, is promising for the reduction of residual porosity and heterogeneity.
- Dependent on the Co-content and the pore sizes, a significant reduction of porosity can be expected by thermal post-processing (re-sintering).

ACKNOWLEDGEMENT

The authors gratefully acknowledge the contribution of the associated project partners in “PraeziGen”. A great debt of gratitude is owed to Mr. Andreas Müller and Mr. Daniel Poddig, student researchers at the iWFT, for their significant contribution to the materials testing.

REFERENCES

- [1] Uhlmann, E., Bergmann, A., and Gridin, W. (2015) Investigation on Additive Manufacturing of Tungsten Carbide-cobalt by Selective Laser Melting. *Procedia CIRP*. 35, pp. 8–15.
- [2] Schwaneckamp, T. and Reuber, M. (2016) Additive Manufacturing of application optimized tungsten carbide precision tools. in: *Proceedings of the 6th International Conference on Additive Technologies*, Nürnberg.
- [3] Kempen, K., Vrancken, B., Buls, S., Thijs, L., Van Humbeeck, J., and Kruth, J.-P. (2014) Selective Laser Melting of Crack-Free High Density M2 High Speed Steel Parts by Baseplate Preheating. *Journal of Manufacturing Science and Engineering*. 136 (6), 061026.
- [4] Teppernegg, T., Klünsner, T., Kremsner, C., Tritremmel, C., Czettl, C., Puchegger, S., et al. (2016) High temperature mechanical properties of WC-Co hard metals. *International Journal of Refractory Metals and Hard Materials*. 56, pp. 139–144.
- [5] Kurlov, A.S. and Rempel, A.A. (2007) Effect of Sintering Temperature on the Phase Composition and Microhardness of WC-8 wt % Co Cemented Carbide. *Inorganic Materials*. Vol. 43, No.6, pp. 602–607.
- [6] Reuber, M. and Schwaneckamp, T. (2018) Vollhartmetallwerkzeuge additiv herstellen. *Technische Rundschau*, pp. 68–70.
- [7] Schubert, T., Breninek, A., Bernthaler, T., Sellmer, D., Schneider, M., and Schneider, G. (2017) Investigations on Additive Manufacturing of WCCo Hard Metals by Laser Beam Melting. *Practical Metallography*. 54 (9), pp. 577–595.
- [8] Myers, R.H., Montgomery, D.C., and Anderson-Cook, C.M. (2016) Response Surface Methodology: Process and Product Optimization Using Designed Experiments. 4th Edition Wiley, .
- [9] Shiomi, M., Osakada, K., Nakamura, K., Yamashita, T., and Abe, F. (2004) Residual Stress within Metallic Model Made by Selective Laser Melting Process. *CIRP Annals - Manufacturing Technology*. 53 (1), pp. 195–198.
- [10] Mercelis, P. and Kruth, J. (2006) Residual stresses in selective laser sintering and selective laser melting. *Rapid Prototyping Journal*. 12 (5), pp. 254–265.

Effect of scan strategy, re-melting and exposure time on the microstructure of stainless steel 17 - 4 PH fabricated by laser powder bed fusion of metals

Platt, Sebastian; Wegner, Jan; Kleszczynski, Stefan; Witt, Gerd, University of Duisburg-Essen, Lehrstuhl Fertigungstechnik, Duisburg, Germany, sebastian.platt@uni-due.de

Abstract—One advantage of laser powder bed fusion is the possibility to locally influence the emerging microstructure by a local variation of scan strategies and process parameters and thereby affect the mechanical properties. This paper presents the effects of different process strategies on the microstructure of additively manufactured 17-4 PH (X5CrNiCuNb16-4) stainless steel. Within this investigation specimens of different scan strategies, like stripe, chess or re-melting strategies, were fabricated. In addition, the effect of various exposure strategies at specific exposure times was validated. The specimens were systematically analyzed by X-ray powder diffraction, scanning electron microscopy and hardness indentation. It turned out, that an appropriate process strategy influences solidification conditions by means of the martensitic and austenitic phase fraction and grain size which can lead to a local modification of the mechanical properties. As the results demonstrate, an increase in hardness of 36 % is achieved by a subsequent exposure strategy at short exposure times.

L-PBF-M; 17-4 PH; exposure strategy; tailored materials

1. INTRODUCTION

Over the last few years laser powder bed fusion of metals (L-PBF-M) established in a wide range of industrial applications such as automotive, aerospace or medical engineering [1]. L-PBF-M, as an important and most emerging member of Additive Manufacturing (AM) technologies, combines the possibility of fabricating high geometrical complexity with a high resource efficiency [2].

During L-PBF-M process, metal powder is locally molten by a focused laser beam, whereupon a new metal powder layer is applied. Finally, a dense functional part is created in a layer by layer process. Its unique mechanical properties, like high tensile strength at rather low ductility, are defined by its typical small-grained microstructure

which is caused by process inherent high thermal gradients and extremely high cooling rates of up to 10^6 K/s. [3][4]

The layer-wise process as well as the locally and temporally controllable laser energy input, which generates small melt pools, allows to create targeted and selectively designed microstructures [5][6]. Currently, various publications focus on influencing microstructure through the variation of process parameters. Niendorf et al. observed a strict microstructural borderline between sample areas of different process parameters, resulting in locally altered mechanical properties [7]. Within his investigation he spatially increased laser energy input by means of a very high laser power leading to different microstructures, fine-grained, columnar grained and columnar coarse-grained. Beside the variation of process parameters Yadollahi et al. also demonstrated, that the exposure time also has a clear influence on the microstructure [8]. Yadollahi et al. investigated that a longer exposure time increases cooling rates which finally leads to a finer microstructure together with higher yield and tensile strength.

For this reason, this paper discusses the effects of different exposure strategies at comparatively high (160 s) and low (20 s) exposure times. However, another possibility to influence the microstructure is to adjust exposure strategies allowing a reduction of the scanning vector length which, among other parameters, reduces thermal stresses and leads to varying thermal histories and heat affection in the surrounding material [9]. Through changing the thermal conditions, the exposure strategy can also cause different solidification morphologies i.e. phase states. The microstructural evolution of additively manufactured parts could therefore be influenced by a targeted process control towards a functional targeted material behavior. The aim of this paper is to investigate

the possibilities of influencing the microstructural formation of additive manufactured samples made of 17-4 PH stainless steel by applying different process strategies such as re-melting, enhanced cycle time and various scanning strategies. By this approach it might be possible to locally vary the strength of the components through microstructural modifications, making it attainable to optimize the mechanical properties of components not only by a macroscopic design but also by locally influencing the microstructure.

2. EXPERIMENTAL METHODS AND TECHNOLOGIES

Within these investigations 17-4 PH stainless steel (X5CrNiCuNb16-4) by EOS was used and processed via L-PBF-M. The experimental methods can be divided into two steps. The first step was the manufacturing of the specimens with an industrial M290 L-PBF-M machine by eos GmbH. The machine is equipped with a 400 W Yb-fibre laser with a maximum scan speed of 7000 mm/s and a laser beam diameter of about 0.1 mm. Cubical specimens (10 mm x 10 mm x 10 mm) were manufactured with different exposure strategies. All specimens were built-up with 20 µm layer heights and a hatch spacing of 0.09 mm. To determine the exposure time of each layer the total scan vector length for all specimens were calculated and divided by its respective scan speed. The increased exposure time of 160 s was achieved by additional "virtual samples", processed with a laser power of 0 W. Two exposure strategies were investigated. Beside the standard stripe exposure (stripe width 5 mm), a chessboard exposure with a square size of 1 mm² was applied. For both exposure strategies the same parameters of 190 W and 1150 mm/s were used. Re-melting was realized through additional subsequent stripe exposure. The process parameters for the re-melting strategy were evaluated in a previous investigation (50 W and 100 mm/s). For a better understanding of the exposure strategies used, these are shown in Figure 1 with the corresponding encodings.

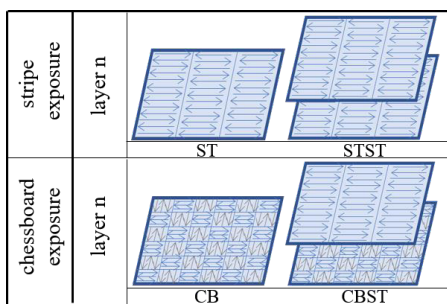


Figure 1: Schematic illustration of the exposure strategies used. ST: stripe exposure; STST: stripe with additional stripe exposure; CB: chessboard exposure; CBST: chessboard with additional stripe exposure.

After specimen built-up, the second step within the carried out experimental methods and technologies was the

analysis of the microstructure. Specimens were cut, embedded and polished separately for hardness indentation and scanning electron microscope (SEM) analysis, where the grain size was determined graphically by measuring the individual grains. Hardness indentation was executed on a Zwick small load Vickers hardness tester equipped with a BX41 Microscope by Olympus GmbH and performed according to DIN EN ISO 6507-1 [10]. SEM analysis was carried out by a Gemini Leo 1530 scanning electron microscope. To evaluate the grain size and structure, the specimens were etched with a mixture of 100 cm³ HCl, 100 cm³ H₂O and 10 cm³ HNO₃ (V2A etchant) prior to the SEM validation. Afterwards, the specimens were analysed by X-ray powder diffraction. To reduce the sample quantity, all investigations were performed perpendicular to the build direction.

3. RESULTS AND DISCUSSION

Hardness indentation tests

The results of the hardness indentation tests can be seen in **Napaka! Vira sklicevanja ni bilo mogoče najti.** The hardness values of the samples generated with ST exposure and an exposure time of 20 s conforms very precisely to the value given by the system manufacturer eos of 230 ± 20 HV [11]. The low standard deviation therefore indicates good reproducibility.

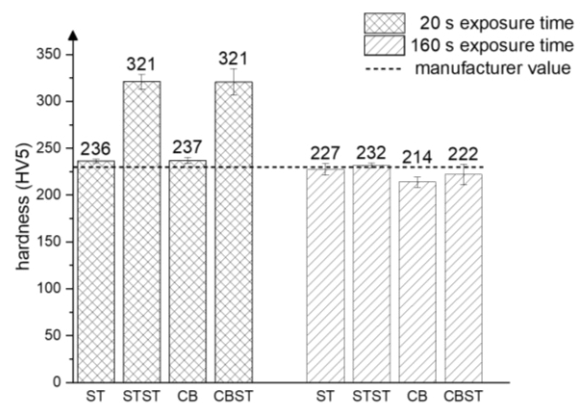


Figure 2: Hardness measurements (HV5)

The same applies, at 20 s exposure time, for the CB strategy, which has an almost identical hardness value compared to the ST strategy. Contrary to the single exposure ST, the hardness increases significant due to subsequent additional exposure relating to the 20 s exposure time. The hardness increases from 236 HV by around 36 % to 321 HV. Which also applies for the CBST exposure strategy at 20 s exposure time. The results of the hardness measurements for a significantly increased exposure time of 160 s exhibit a changed material behavior. Though, the values of the single-exposed samples (ST and CB) are still in the range of the manufacturer's specifications, they are all slightly lower than the values of the shorter exposure time. The lowest hardness value of

214 HV is generated by the CB strategy. In general, the specimens built-up by chessboard exposure exhibit lower hardness values than those built-up by stripe exposure. Contrary to the samples with short cycle times, the re-melted specimen processed with long cycle times do not exhibit a significant increase in the hardness values. The hardness properties of the samples were only negligibly affected by the additional energy input during longer exposure times. Again, the low standard deviation indicates good reproducibility. To gain further information about the cause of the changed hardness value, a detailed investigation of the microstructure is required. It can be assumed that the temperature level of the specimen rises as a result of subsequent exposure, resulting in hardening effects such as an increased amount of precipitates, grain refinement or the formation of different phase fractions. Due to the small deviation in the hardness values between the stripes and the chessboard strategies, the exposure types ST and STST at both 20 s and 160 s exposure time were selected for further SEM analysis.

Microstructural investigation by SEM

The exemplary evaluation of the SEM images (**Napaka! Vira sklicevanja ni bilo mogoče najti.**) taken from the ST respectively the STST strategy at 20 s exposure time clarifies that the significant increase in hardness, which occurred during additional exposure of the samples, was apparently not caused by a grain refinement. As the graphical evaluation of the SEM images reveals, the average grain size is 0.61 μm for the ST exposure and 0.7 μm for the STST exposure specimens. Along the grain boundaries, nanoscale precipitates can be assumed, as they are characteristic for this material [12]. As the size of the precipitates was limited, it was rather difficult to determine the elements using an EDX measurement and therefore no clear results were obtained. Anyhow, a significant difference in size, shape or quantity of the precipitates is not quantifiable.

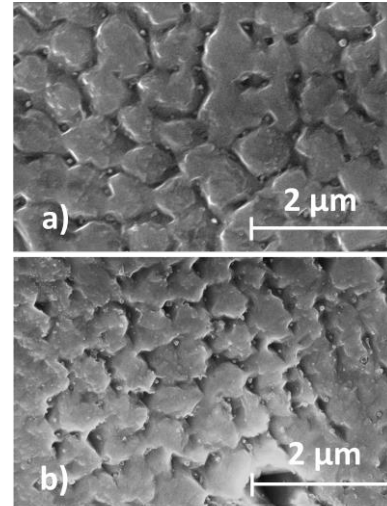


Figure 3: SEM images of the grain structure for a) STST and b) ST strategy at 20 s exposure time

A summary of the grain size determination is illustrated in Figure 4. It can be observed that even for a longer exposure time of 160 s no substantial grain refinement occurred so that a hardness increases through a grain refinement mechanism seem unlikely. Remarkable is the unusually high standard deviation for the STST strategy at 160 s exposure time which may be caused by an inhomogeneous grain size distribution. In summary, the determination of the grain size does not provide an explicit explanation for the differences in hardness that were observed. Therefore, further investigations are required to explain the effects of the different exposure strategies on the emerging microstructure. It should be noted that samples produced in the L-PBF-M process generally have both cellular and columnar dendritic grain structures [3]. The cellular dendritic grains are usually graded in an orientation perpendicular to the build-up direction, whereas the columnar dendritic grains are evaluated longitudinally to the build-up direction. Since during these examinations the alignment was limited to a perpendicular orientation to the build-up direction, a detailed evaluation of the columnar dendritic grains is not possible. Though it may provide further information about the origin of the different hardness values. However, additional information about the resulting hardness values could be provided by the observation of the columnar grain structures.

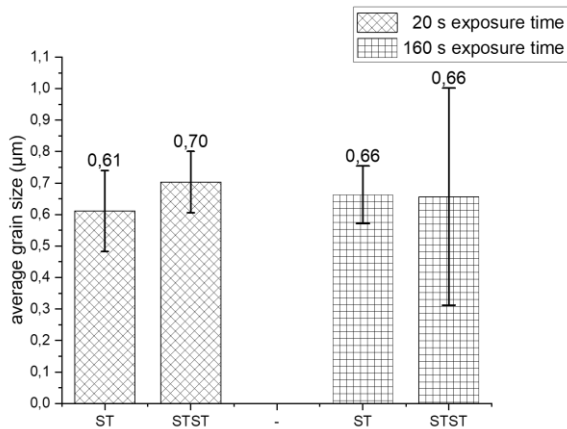


Figure 4: Average grain size for 20 s and 160 s exposure time

X-Ray powder diffraction is another suitable possibility to characterize microstructural phenomena, since it can provide valuable indications of different phase fractions that possibly describe the hardness variations.

XRD Measurement

The XRD spectra were measured from 30° - 80° to reduce the measurement time and since the most significant phase changes are to be expected in this range. As the results for the 20-s exposure time demonstrate in Figure 5, the microstructure of the standard exposure strategy ST shows predominantly austenitic phases.

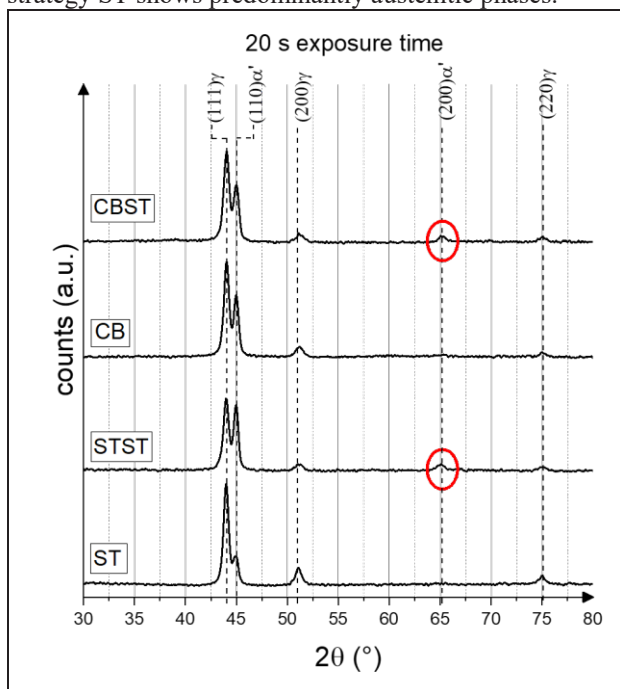


Figure 5: X-Ray powder diffraction of different exposure strategies at a 20 s exposure time. Red circles marking (200)α' phases which appeared after double exposure strategies.

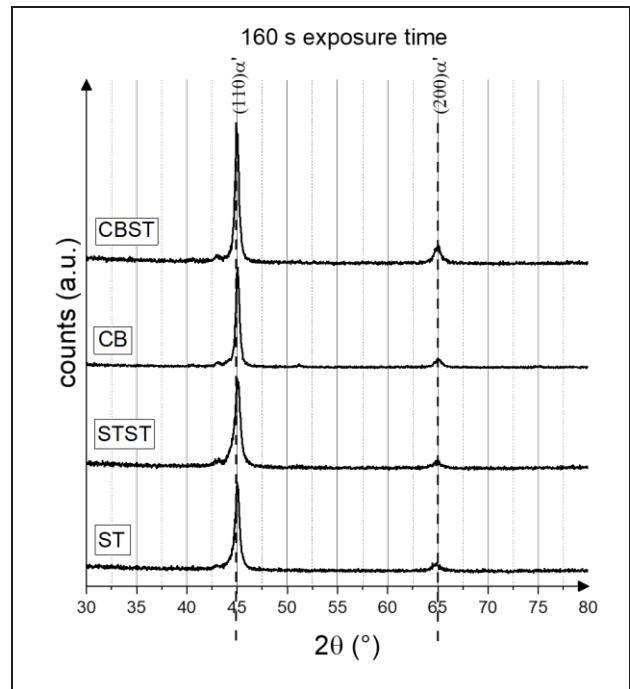


Figure 6: X-Ray powder diffraction of different exposure strategies at a 160 s exposure time.

Where the preferred orientation is the (111)γ phase. Only one orientation of the body-centred cubic (bcc) α-Fe phase [(110)α'], is recognizable within the measured spectrum. Since most of the publications assign martensitic phases to the bcc α-Fe peaks, such phases are also described as martensitic in the further course of this paper, although a clear evaluation without further investigations is not doubtlessly possible [13] [14]. Due to the generally high proportion of austenite, a comparatively ductile material behaviour can be concluded. Comparing the ST samples to the specimens with subsequent double exposure (STST), it is apparent that the austenitic content has been reduced and as a result the martensitic content within these specimens has been increased. Within the STST strategy at the 20 s exposure time the ratio of (111)γ and (110)α' phase is approximately the same. Furthermore, the previously visible austenitic (200)γ and (220)γ peaks inhere small intensities which are strongly overlapped by the noise signal. Instead, “martensitic” (200)α' and (211)α' phases, were observed after the STST exposure strategy. Therefore, it can be assumed that the additional laser exposure caused a phase transformation or change in the solidification mode towards an increased “martensitic” phase fraction. In contrary to the ST strategy, the CB strategy already demonstrates a comparatively higher “martensitic” content without subsequent double exposure due to the presence of (110)α and in minor form (211)α' phases. However, a “martensitic” (200)α' phase isn't visible in the SB strategy specimen. Comparable to the STST strategy this (200)α'

phase is induced by the subsequent double exposure. But, unlike the STST strategy, the preferred (111) γ and (110) α' phases induced by CBST strategy have almost identical intensities to the exposure strategy without subsequent double exposure (CB). This implies, that the origin of this phase can be found in the subsequent exposure. Looking at the XRD analysis for the significantly increased exposure time of 160 s (Figure 6), it is evident that there is no discernible difference regarding phase formation for different exposure strategies. Furthermore, unlike during build-up with a low exposure time, no austenitic (111) γ or (200) γ phases are formed. The preferred orientations are limited to the (110) α' and (200) α' martensitic phases. Only a slight difference in an increase of intensity may be suspected, in the CBST exposure strategy. Which may explain the slight difference in the hardness values but can not be clearly proven. From the results of the XRD analysis it can be deduced, that with shorter exposure times a subsequent double exposure causes the formation of the martensitic (200) α' phase. In contrast, the formation of the (200) α' phase for longer exposure times seems to be independent from the exposure strategy.

An explanation might be found in the process parameters of the subsequent exposure as well as in the resulting different temperature levels of the samples with different exposure times during production. As the XRD results demonstrate, the phase fractions caused by the different exposure strategies for short exposure times are significantly varying. The generally high austenite content in the ST exposure with short cycle time is probably caused by the assumable higher temperature level within the sample during the build-up. Figure 7 schematically illustrates the exemplary temperature levels for the 20 s and 160 s exposure times. Due to the short exposure times, the sample has shorter cooling cycles resulting in an increased global sample temperature.

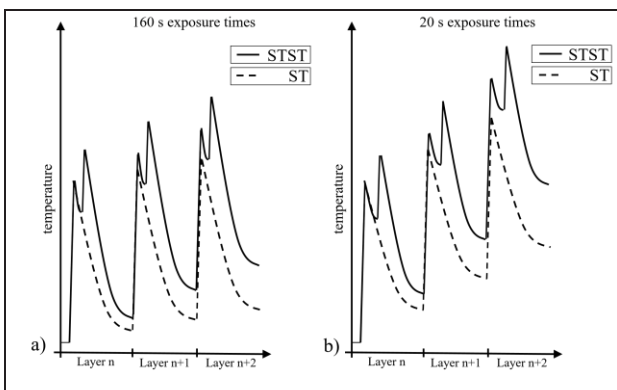


Figure 7: Schematic illustration of the temperature level within one specimen for a) 160 s and b) 20s exposure time during ST and STST exposure.

As a result, a smaller amount of material in the heat affected zone reaches the martensite start temperature, leading to a lower fraction of martensitic grain structures

[15]. With STST exposure, however, the re-melting seems to increase the martensitic phase fraction and introduces the usually in L-PBF-M uncommon grain orientation (200) α' . Which might result from the very low scanning speed of the re-melting (100 mm/s). This scan speed may generate a temperature level and melt pool formation/shape which promotes the formation of martensite phases, whereby the formation of the (110) α' martensite would be explained. Furthermore, the increased thermal conductivity of the already melted material in comparison to the previous powder layer could promote the formation of martensite. The creation of the (110) α' phase in the CB strategy could also be explained by the increased re-melting in the transition areas of the single square units. However, a doubtless explanation for the formation of this phase is not possible at this stage of the investigations and certainly requires further examinations. The cause of the formation of (200) α' martensite in both the STST and CBST strategies could be described by the process parameters used for the subsequent exposure. It is known that very slow scanning speeds form comparatively wide melting zones [16]. Combined with the fact that grain growth generally takes place in the direction of the energy source, grain growth in this case would take place in a horizontal direction [17]. It is generally known that (200) α' martensite grows perpendicular to the building direction [12]. Thus the explanation of the measured (200) α' phases would lie in the formation of comparatively wide melt pools, caused by the low scanning speed of the subsequent exposure. The significant increase of the hardness values of the specimens with additional subsequent exposure (Figure 2) could therefore be partly explained by the resulting martensite phases and the reduction of the austenite. Although as already mentioned above, further investigations are essential.

As the observation of the XRD analysis for longer exposure times pointed out, there is a clear difference to the examined short exposure times. For longer exposure cycles, only (110) α' and (200) α' phases can be measured. This phenomenon could again be caused by the martensite start temperature or the general temperature level in the built-up samples (Figure 6). As already mentioned above, the conversion to form martensite is only possible when the temperature falls below the martensite start temperature. Thus a longer cooling time favours the formation of this phase, which could explain the high proportion of (110) α' martensite at longer exposure times. Additionally, a longer cooling time may promote the formation of different martensitic phases, which could explain the presence of (200) α' phase without subsequent exposure. A multidirectional grain growth would become possible or at least favourable, especially with an increased overall height and reduced heat transport via the build platform [18]. The almost identical intensities of the (200) α' phases of all considered exposure strategies suggests that the pool size of the subsequent exposure had no significant influence on the measured phases. The comparison of the hardness

values shown in Figure 2 also reveal a value distribution independent of the exposure strategy, though due to the high martensite content a general increase in hardness could have been expected. The results imply that primary other mechanisms are responsible for the significant increased hardness. It appears that the overall temperature level in the sample during the thermal cycling are accountable for the observed strengthening (Figure 6). Due to the numerous influencing factors the reason for this unfortunately cannot be clearly identified at this point of the investigations. It may be possible to cite over-ageing phenomena or the unexamined formation of columnar grain structures as possible reasons.

4. CONCLUSION

Within this publication, the influence of different exposure strategies at both short and long exposure times was investigated. As the results exposed, a significant increase in hardness can be achieved within the short exposure time by using an additional subsequent exposure. This was valid for both STST and CBST exposure strategy. The hardness increased to approx. 36 % to 321 HV10. As the XRD analyses could reveal, this increase in hardness may be caused by the conversion of austenite to martensite. Remarkable were the measured (200) α' phases which occurred for short exposure times only with a subsequent exposure. The formation of this phase is presumably due to the process parameters of the subsequent exposure. The combination of comparatively low scanning speed and laser power within the subsequent exposure may led to the formation of a wide and flat melt pool. Due to the grain growth directed to the energy source, (200) α' phases could have developed perpendicular to the build-up direction. The origin of the (110) α' phases in the STST, CB and CBST strategies could not be unequivocally verified. Furthermore, it should be mentioned that the graphic determination of the grain size only represents a local and comparatively inaccurate evaluation and only provided information about the cellular dendritic grains within the observed orientation. An examination of the columnar grain structures could provide additional evidence. A further and more detailed method of assessing the microstructure would be to carry out an EBSD analysis to determine grain size and orientation. As the results of the hardness measurements for longer exposure times pointed out, no significant increase in hardness could be detected. Neither through a change in the exposure strategy nor through a subsequent exposure. The hardness values achieved were even consistently lower than with all exposure strategies of the shorter exposure time. The origin of these hardness values was not evident when looking at the XRD results. The measurements only indicated martensitic phases ((110) α' and (200) α'). The origin of these phases could be assumed both in the global temperature level and the expansion of the subsequent exposure melt pool, but not proven. Side effects such as an over-ageing phenomenon may have occurred. Again, an

EBSD study could also provide additional evidence here. As the results of this publication have illustrated, the resulting temperature level during build-up can have a significant effect on the material properties. Taking this into account, a suitable simulation of these temperature levels would be sensible to be able to estimate the resulting mechanical properties better.

ACKNOWLEDGEMENT

This work was kindly supported by the German Research Foundation (DFG) under the project number WI 2118/9-1. We also thank Prof. Fischer, Prof. Winterer and Prof. Farle from the University of Duisburg-Essen and their teams for the utilization of analysis devices and support regarding sample preparation, etching, hardness measurements, XRD analysis and SEM investigations. Furthermore, the authors thank Hanna Schönrrath for the execution of the SEM analysis.

REFERENCES

- [1] Yap, C. Y. ; Chua, C. K. ; Dong, Z. L. ; Liu, Z. H. ; Zhang, D. Q. ; Loh, L. E. ; Sing, S. L.: Review of selective laser melting: Materials and applications, In: Applied Physics Reviews , 2 (2015), Heft 4, S. 41101.
- [2] Ford, S. ; Despeisse, M.: Additive manufacturing and sustainability: an exploratory study of the advantages and challenges, In: Journal of Cleaner Production , 137 (2016), S. 1573–1587.
- [3] Bourell, D. ; Kruth, J. P. ; Leu, M. ; Levy, G. ; Rosen, D. ; Beese, A. M. ; Clare, A.: Materials for additive manufacturing, In: CIRP Annals , 66 (2017), Heft 2, S. 659–681.
- [4] Herzog, D. ; Seyda, V. ; Wycisk, E. ; Emmelmann, C.: Additive manufacturing of metals, In: Acta Materialia , 117 (2016), S. 371–392.
- [5] Kruth, J.-P. ; Badrossamay, M. ; Yasa, E. ; Deckers, J. ; Thijs, L. ; van Humbeeck, J.: Part and material properties in selective laser melting of metals, In: Proceedings of the 16th International Symposium on Electromachining , 2010.
- [6] Martin, J. H. ; Yahata, B. D. ; Hundley, J. M. ; Mayer, J. A. ; Schaedler, T. A. ; Pollock, T. M.: 3D printing of high-strength aluminium alloys, In: Nature , 549 (2017), 365-369.
- [7] Niendorf, T. ; Leuders, S. ; Riemer, A. ; Brenne, F. ; Tröster, T. ; Richard, H. A. ; Schwarze, D.: Functionally Graded Alloys Obtained by Additive Manufacturing, In: Advanced Engineering Materials , 16 (2014), Heft 7, S. 857–861.
- [8] Yadollahi, A. ; Shamsaei, N. ; Thompson, S. M. ; Seely, D. W.: Effects of process time interval and heat treatment on the mechanical and microstructural properties of direct laser deposited 316L stainless steel, In: Materials Science and Engineering: A , 644 (2015), S. 171–183.
- [9] Mercelis, P. ; Kruth, J.-P.: Residual stresses in selective laser sintering and selective laser melting, In: Rapid Prototyping Journal , 12 (2006), Heft 5, S. 254–265.
- [10] DIN EN ISO, 2018-07-00: DIN EN ISO 6507-1.

- [11] eos GmbH: EOS StainlessSteel GP1: SS-GP1-M270_Material_data_sheet_04-09_de.doc.
- [12] Murr, L. E. ; Martinez, E. ; Hernandez, J. ; Collins, S. ; Amato, K. N. ; Gaytan, S. M. ; Shindo, P. W.: Microstructures and Properties of 17-4 PH Stainless Steel Fabricated by Selective Laser Melting, In: Journal of Materials Research and Technology , 1 (2012), Heft 3, S. 167–177.
- [13] Rafi, H. K. ; Pal, D. ; Patil, N. ; Starr, T. L. ; Stucker, B. E.: Microstructure and Mechanical Behavior of 17-4 Precipitation Hardenable Steel Processed by Selective Laser Melting, In: Journal of Materials Engineering and Performance , 23 (2014), Heft 12, S. 4421–4428.
- [14] Mahmoudi, M. ; Elwany, A. ; Yadollahi, A. ; Thompson, S. M. ; Bian, L. ; Shamsaei, N.: Mechanical properties and microstructural characterization of selective laser melted 17-4 PH stainless steel, In: Rapid Prototyping Journal , 23 (2017), Heft 2, S. 280–294.
- [15] Costa, L. ; Reti, T. ; Deus, A. M. ; Vilar, R.: SIMULATION OF LAYER OVERLAP TEMPERING KINETICS IN STEEL PARTS DEPOSITED BY LASER CLADDING, In: 2002 Int. Conference on Metal Powder Deposition for Rapid manufacturing (2002).
- [16] Gusarov, A. V. ; Yadroitsev, I. ; Bertrand, P. ; Smurov, I.: Heat transfer modelling and stability analysis of selective laser melting, In: Applied Surface Science , 254 (2007), Heft 4, S. 975–979.
- [17] Zhong, Y.: Sub-grain structure in additive manufactured stainless steel 316L, Dissertation, Stockholm, Stockholm University, 2017.
- [18] Yadollahi, A. ; Shamsaei, N. ; Thompson, S. M. ; Elwany, A. ; Bian, L.: Mechanical and Microstructural Properties of Selective Laser Melted 17-4 PH Stainless Steel, In: ASME 2015 International Mechanical Engineering Congress and Exposition: November 13-19, 2015, Houston, Texas, USA, New York, N.Y., American Society of Mechanical Engineers, 2016, V02AT02A014.

Nano- Micro- Macro- Hardness of LPBF 316L Austenitic Stainless Steel

Massimo Lorusso, Istituto Italiano di Tecnologia, Torino, Italy, massimo.lorusso@iit.it

Diego Manfredi, Istituto Italiano di Tecnologia, Torino, Italy, diego.manfredi@iit.it

Flaviana Calignano, Politecnico di Torino DIGEP, Torino, Italy flaviana.calgiano@polito.it

Marco Actis Grande, Politecnico di Torino DISAT, Torino, Italy marco.actis@polito.it

Abstract — Laser Powder Bed Fusion (LPBF) is an additive manufacturing (AM) technique for the fabrication of near net-shape parts directly from computer-aided design data by melting together different layers of metallic powders with a laser source. LPBF is very attractive thanks to its extremely high melting and solidification rates, that make possible to obtain materials with hardness values higher than those by traditional manufacturing routes.

Aim of this study is first to investigate the hardness at macro, micro- and nano scale, of 316L austenitic stainless steel processed by LPBF. After the LPBF process, these alloys exhibit sub-micrometric grains with precipitates at the nano-scale, and therefore their effect could be detected only characterizing at this length scale. 316L austenitic stainless steel was investigated before and after a solubilization heat treatment (1050°C for 1 h and quenching).

LPBF, 316L Austenitic Stainless Steel, Macro- Micro- Nano- Hardness

1. INTRODUCTION

Laser Powder Bed Fusion (LPBF) is an Additive Manufacturing (AM) technique for the fabrication of near net shape parts directly from computer –aided design data by melting together different layers of metallic powders with a laser source. LPBF is a very attractive thanks to its extremely high melting and solidification rates, that make possible to obtain materials with hardness values higher than those by traditional manufacturing routes. [1-4].

The 316L austenitic stainless steel is one of most important material processed by LPBF. 316L austenitic stainless steel has many application in different fields for its very good resistance at corrosion and oxidation. The main applications are in oil and gas, marine, nuclear and bio medical industry [5-6].

Aim of this study is first to investigate the hardness at macro-, micro- and nano- scale of 316L austenitic stainless steel processed by LPBF in as-built condition and after heat treatment. Second aim was to investigate the microstructure of 316L austenitic stainless steel before and after heat treatment.

2. MATERIALS AND METHODS

316L austenitic stainless steel samples were manufactured by LPBF with an EOSINT M 270 Dual Mode version. This machine uses a powerful ytterbium fiber laser system in an argon atmosphere to melt powders. The laser is in continuous mode with power up to 200 W and a minimum spot size of 100 μm . The 316L austenitic stainless steel powder used is a gas atomized one produced by EOS GmbH, the nominal composition in weight is: C \leq 0.03%, Mn \leq 2.0%, Si \leq 0.75%, Ni = 12-14%, Cr = 16-18%, Mo = 2-3%, S \leq 0.03% , P \leq 0.045% and Fe= bal [7]. The 90% of particles of 316L stainless steel powder have a diameter minor than 42 μm . The Fig. 1 shows the result of laser granulometry analysis on 316L stainless steel powder.

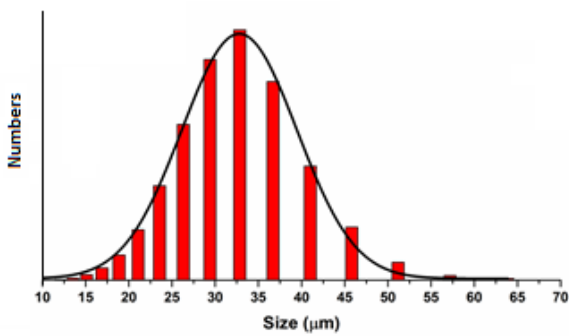


Figure 1. Laser granulometry analysis

As can be seen in Fig. 2, through a field emission scanning microscopy (FESEM, Zeiss Supra TM 40), the powders are spherical, ensuring a good flowability on the building platform fundamental aspect in the LPBF process.

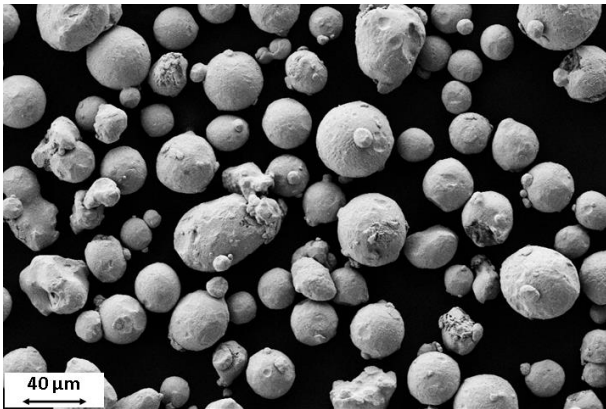


Figure 2. FESEM analysis (Mag. = 1000x) 316L austenitic stainless steel powder

Table 1 shows the parameters used to process the 316L austenitic stainless steel. The samples used for this investigation were cubes with side of 10 mm. The surface of the cubes was polished down to a roughness of 0.03 µm.

TABLE I. BUILDING PARAMETERS

Power	Scanspeed	Hatching distance
[W]	[mm/s]	[mm]
190	800	0,20

Half of all produced samples were subjected at solution treatment for 1h at 1050°C and then quenching in pure water. Solution treatment changes the content of ferrite to ensure good properties on corrosion for 316L stainless steel.

The morphological characterization of the sample surface was carried in top view configuration using optical microscopy (Leica DMI5000 M).

Before the morphological characterization the samples are etched with Kalling’s solution for 90 s. Kalling’s solution is an etching reagent for developing the microstructure of chromium steels with more than 5% of chromium. It contains 5 g copper chloride, 100 mL hydrochloric acid, 100 mL alcohol, and 100 mL water.

Hardness was evaluated in three different scales, macro-, micro- and nano-.

- Macrohardness was evaluated using a Brinell indenter with a steel ball of 2,5 mm diameter and a load of 62.5 N. The load was applied for 15 s. Five different indentations were realized for each sample and then the average was calculated together with the standard deviation.
- Microhardness was evaluated using a microVickers indenter with a load of 300 g applied for 15 s (ISO 6507). Nine different indentations were realized for each sample and then the average and standard deviation were calculated. All indentations were then observed using optical microscopy to evaluate the symmetry of indentation.
- Nanohardness [H] and elastic modulus [Er] measurements were carried out using the NanoIndenter TI950 (Hysitron). The most common method to analyze the hardness and modulus values from an indentation curve is the Oliver-Pharr method [8]. The Oliver-Pharr method requires no imaging of indentation, instead it is based on contact mechanics solutions developed by Sneddon [9]. The test is performed by applying and removing a controlled load to the specimens using a geometrically well-defined probe, producing traditional force versus displacement curves. The analysis of these curves provides information regarding the mechanical properties of the sample. The used indenter was a Berkovich tip, that is a 3-sided diamond pyramid with an included angle of 142.3°, where the angle from normal to a face is 65.35°. An indentation grid with 21 indentations per side, distant 5 µm from each other (for a total of 441 indentations), were realized for every sample. The load of 2.5 mN was applied with a rate of 0.25 mN/S, with a permanence time at maximum load of 5 s.

3. RESULTS AND DISCUSSION

3.1 Morphological characterization

Studying the microstructure of LPBF 316L austenitic stainless steel help to understand melting process. The optical microscopy (Fig. 3a) shows a dense structure of well overlapped melt pool characterized by semicircular shape in a plane parallel to the building direction. The overlapping nature of the melt pool means a good fusion and solidification of powder particles and a strong bonding within layers [10].

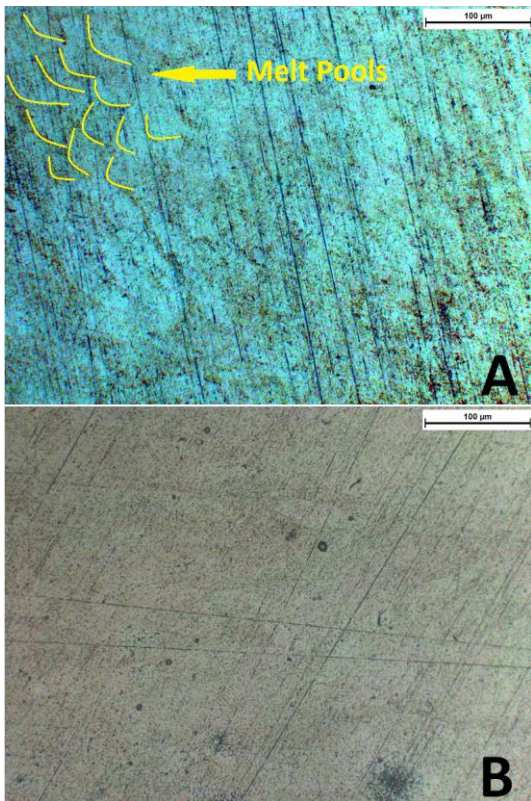


Figure 3. Optical microscopy (Mag. = 200x) of etched 316L austenitic stainless steel obtained by LPBF before (A) and after (B) heat treatment.

After heat treatment the microstructure is different, the melt pools are less evident and the grains have not preferential directions. It is know that solution treatment can cause the grain coarsening, but it also can decrease the ferrite content some extent [12].

3.2 Micro and Macro Hardness

In table II are reported the results and standard deviation of macroindentation tests (5 indentations for each

sample). It could be stated that the hardness value of as built 316L austenitic stainless steel (316L ASS AB) is higher than the hardness value of heat treated 316L austenitic stainless steel (316L ASS HT). The results of microindentation tests (9 indentation for each sample) reported in table III shows similar results.

TABLE II. MACRO HARDNESS BRINELL

	Hardness [HB10]	St.Dev. [HB10]
316L ASS AB	187.3	2.2
316L ASS HT	166.2	4.5

TABLE III. MICRO HARDNESS VICKERS

	Hardness [HV_{0.3}]	St.Dev. [HV_{0.3}]
316L ASS AB	212.3	4.5
316L ASS HT	202.1	11.3

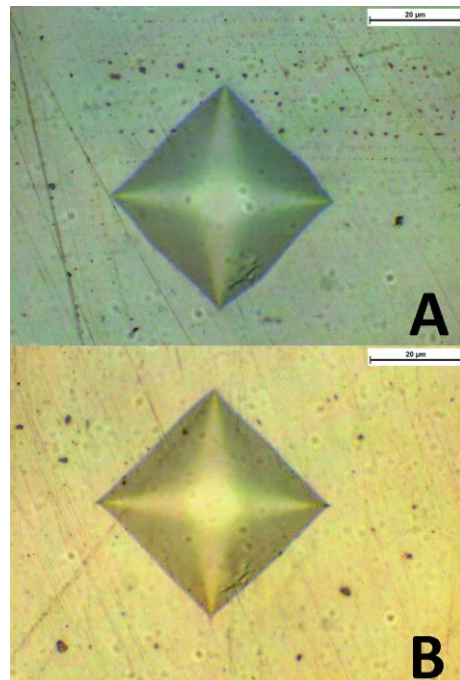


Figure 4. Optical microscopy (Mag. = 200x) of microVickers indentation on 316L stainless steel obtained by LPBF before (A) and after (B) heat treatment.

In Fig.4 single microindentation are on each material considered is shown. In the as built 316L austenitic stainless steel is possible to observe the influence of residual stress on the indentation symmetry. In fact, the rhombohedral indentation on as built 316L austenitic stainless steel has the border that are not so well define like the indentation on heat treated 316L austenitic stainless steel. The study of micro indentation projected contact area is a well-known method to have an evaluation of residual stress on the sample [11].

3.3 Nanohardness

Nano indentation tests on 316L austenitic stainless steel are shown in Fig.5. It is possible to note how the nanohardness is homogenous for 316L austenitic stainless steel. This could be ascribe to the extreme fine grains. On the other side 316L HT has a different behavior with different hardness region.

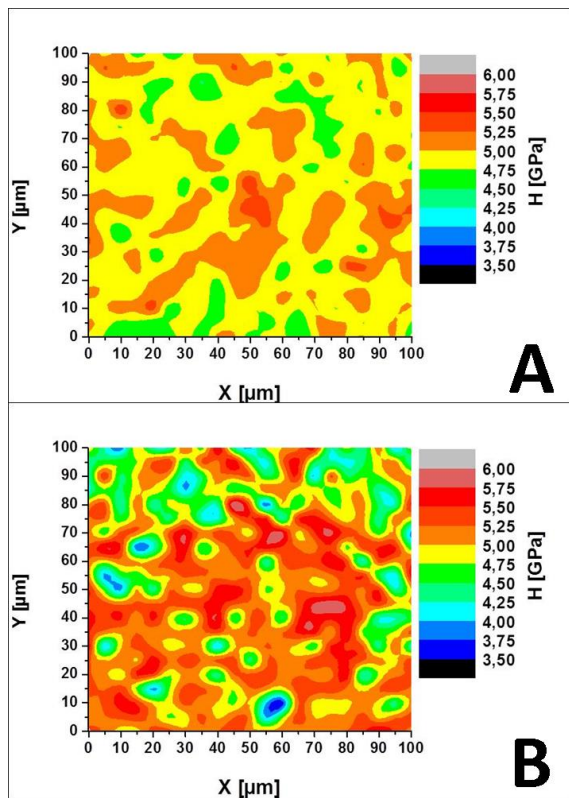


Figure 5. Maps of nanohardness tests of the 316L austenitic stainless steel before (A) and after (B) heat treatment .

The average nanohardness is similar (5.0 GPa for the as built 316L austenitic stainless steel and 4,9 GPa for the

heat treated 316L austenitic stainless steel), but the distribution of hardness is different because the microstructure is different.

4. CONCLUSIONS

This paper describes the hardness at macro, micro- and nano scale of 316L austenitic stainless steel processed by LPBF. 316L austenitic stainless steel are investigated in as built condition and after solution heat treatment. The main result are the following:

- The macro and micro hardness values show that the very fine microstructure (typical of LPBF) of as built 316L austenitic stainless steel guarantees higher performance in terms of hardness respect the heat treated 316L stainless steel.
- The optical microscopy of microVickers indentations shows the presence of residual stresses in as built 316L austenitic stainless steel. The well define borders of microindentation on heat treated 316L stainless steel show that residual stresses are less than in as built 316L austenitic stainless steel.
- Nanohardness shows that the hardness distribution on as built 316L austenitic stainless steel is more homogenous than the hardness on heat treated 316L austenitic stainless steel. This is a confirm that the microstructure of material processed by LPBF is very fine with peculiar and innovative characteristics.

REFERENCES

- [1] B. Vayre, F. Vignat, F. Villeneuve; *Metallic additive manufacturing: state-of-the-art review and prospects*, Mech. Ind. 13 (2012) 89–96.
- [2] Y. Zhai, D.A. Lados, J.L. LaGo; *Additive manufacturing: making imagination the major limitation*, JOM 66 (2014) 808–816.
- [3] Y.M. Wang, T. Voisin, J.T. Mc Keown, J. Ye, N.P. Calta, Z. Li, Z. Zeng, Y. Zhang, W. Chen, T.T. Roehilling, R.T. Ott, M.K. Santala, P.J. Depond, M.J. Matthews, A.V. Hanza, T. Zhu; *Additively manufactured hierarchical stainless steels with high strength and ductility*; Nature Materials, volume 17, pages 63–71 (2018).
- [4] W.E. Frazier, Metal additive manufacturing: a review, Mat. Eng. Perfor. 23 (6) (2014) 1917e1928.
- [5] International Stainless Steel Forum, Rue Colonel Bourg 120 B-1140 Brussels Belgium, <http://www.worldstainless.org/Files/issf/non-image-files/PDF/Marineapplications.pdf> sited 08-10-17).
- [6] M.M. Dewidar, K.A. Khalil, J.K. Lim, *Processing and mechanical properties of porous 316L stainless steel for biomedical*

- applications*, Trans. Nonferrous Met. Soc. China 17 (2007) 468-473.
- [7] EOS data sheet 316L stainless steel (2016).
- [8] W.C. Oliver and G.M. Pharr; An Improved Technique for Determining Hardness and Elastic Modulus Using Load and Displacement Sensing; Indentation Experiments, J. Mater. Res., 1992, 7, p 1564–1583.
- [9] I.N. Sneddon, *The Relation Between Load and Penetration in the Axisymmetric Boussinesq Problem for a Punch of Arbitrary Profile*, Int. J. Eng. Sci., 1965, 3, p 47–57.
- [10] W.T. Tucho, V.H. Lysne, H. Austbo, A. Sjolyst-Kverneland, v. Hansen; *Investigation of effects of process parameters on microstructure and hardness of SLM manufactured SS316L*; Journal of Alloys and Compounds 740 (2018) 910e925.
- [11] F. Liu, X. Lin, G. Yang, M. Song, J. Chen, W. Huang; Microstructure and residual stress of laser rapid formed Inconel 718 nickel-base superalloy; Optics & Laser Technology 43 (2011) 208-213.
- [12] R Song, J. Xiang, D. Hou; Characteristics of Mechanical Properties and Microstructure for 316L Austenitic Stainless Steel; Journal Of Iron And Steel Research, International. 2011, 18(11): 53-5

CHAPTER 3.

CAE and Testing



Tensile testing of 3D printed continuous carbon fibre-reinforced PLA composites

Marius Rimašauskas, Department of Production Engineering, Kaunas University of Technology, Kaunas, Lithuania, marius.rimasauskas@ktu.lt

Tomas Kuncius, Department of Production Engineering, Kaunas University of Technology, Kaunas, Lithuania, tomas.kuncius@ktu.lt

Abstract—Additive manufacturing technologies are very well known for their abilities to produce products of complex shape. However, there are limitations too, such as limited variety of materials and lower mechanical properties. This research paper is dedicated to the analysis of mechanical properties of 3D printed composite materials. The experimental results showed that tensile strength of composite material is about twice higher than 3D printed poly lactic acid (PLA). Analytical calculations showed that carbon fibre content in the samples was about 6.9%.

Keywords—3D printing, continuous fibre reinforced polymers, fused deposition modelling

1. INTRODUCTION

Additive manufacturing is widely used in various industries because of its main advantages like design flexibility, possibility to produce high complexity parts, reduction of product waste and shorter delivery time to the market. However, there are many limitations that currently exist in the field of 3D printing of polymer materials. Moreover, these limitations come from both sides: material and technology. Lack of new materials, relatively high cost and other limitations motivate for new technology developments or improvement of the existing technologies. On the other hand, there is high demand for new technologies which could be used for the production of high-performance structural parts. These types of the parts can be produced from composite materials by using traditional technologies, however, the production of structural parts by using 3D printing technologies could offer a lot of advantages. Moreover, there are some existing technologies (PolyJet, SLS and other) which could be perfectly used for production of composite materials. One of them is fused deposition modelling (FDM) or fused filament fabrication (FFF), leading RP technology for production of parts layer by layer. Due to

its simplicity and flexibility, this technology can be used for the production of composite parts. FDM is usually used for production of parts and products of thermoplastic materials such as ABS, PLA, PC, etc. Moreover, to the market offers the aforementioned plastics mixed with reinforcement materials. According to the performed tests, short fibre reinforced polymer (SFRP) materials and carbon nano tubes reinforced materials showed much better mechanical characteristics as compared with thermoplastic parts [1, 2]. Limited improvement of mechanical performance, for example, up to 20% of tensile strength, has been achieved by adding short fibre into the plastic feedstock due to the limitations in the reinforcement of short fibre [3]. Nevertheless, the properties of SFRP materials are worse than properties of composites produced with traditional technologies. Historically, fibre reinforced polymer composites have been considered as high-strength, light-weight materials that are composed of strong load carrying fibres (e.g. carbon/glass fibres, ~5-6 μm in diameter and tens of centimetres in length) held together by an epoxy matrix [4]. FDM technology could also be used for production of above-mentioned structures when continuous carbon fibre is inserted into printing head and extruded together with molten thermoplastic. However, many printing parameters, extrusion nozzle and heater must be changed as well [5]. Moreover, there are few possible solutions how FDM technology could be used for continuous fibre-reinforced polymer materials CFRP printing:

- Embedding the fibre directly in the component.
- Embedding the fibre in the injector. In this case, the fibre and the resin are mixed in the injector, just before the injection stage.
- Embedding the fibre before the injection [6].

This research was funded by a grant (No S-M-ERA.NET-17-4) (project acronym: '3D-CFRP') from the Research Council of Lithuania.

Other studies have shown that the above-mentioned FDM printing process could be used for printing free-hanging lattice structures [7].

In this study, continuous carbon fibre-reinforced PLA composite samples were prepared by using FDM technology. Mechanical properties were tested and microstructural analysis was performed. The achieved results are promising and could be used as a background for the future research.

2. METHODOLOGY

During the research, thermoplastic material – poly lactic acid (PLA) of the diameter of 1.75 mm from DR3D Filament was used. As reinforcement material, carbon fibre yarn T300B 1k (1,000 fibres in a tow untwisted) from Toray was selected. T300B is a high-performance carbon fibre made of polyacrylonitrile. Tensile strength of the material is 3,530 MPa, modulus of elongation – 230 GPa and density – 1.76 g/cm³. FDM technology for the 3D printing was selected because of its flexibility and ease of control. Easy to control and simple to modify open source 3D printer Mecreator 2 was selected and the printing head was changed to allow printing of continuous carbon fibre. The diameter of printing nozzle was changed to 1.5 mm to allow leaking of molten plastic and continuous fibre. Distance between the lines was set manually to 0.75 mm. It was decided to print unidirectional samples of composites and test their mechanical properties. Printing head temperature was set to 200 °C, while build plate temperature was 70 °C. It is important to mention that during printing borosilicate bed and Dimafix spray were used to increase adhesion between the first printed layer and the printing bed. Infill percentage was set to 100% and printing speed was set to 1 mm/s while the layer height was set to 1 mm for all layers and the extrusion width was adjusted to 0.75 mm. Schematic representation of printing process parameters is presented in Fig. 1.

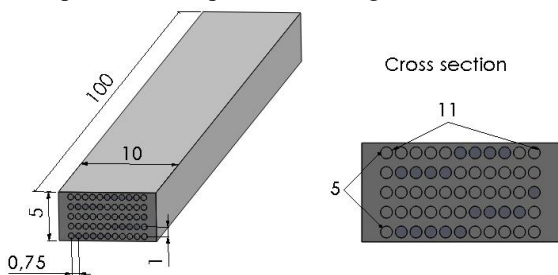


Figure 1. Schematic view of the specimen

It can be seen that 11 yarns per width and 5 yarns per thickness were embedded.

2.1 Mechanical testing

For tensile test it was decided to use ASTM D3039 (Method for tensile properties of polymer matrix

composite materials) standard because it is recommended for highly oriented or high tensile modulus fibre-reinforced polymer composites. According to the above-mentioned standard, at least five specimens must be used to determine the material properties. Therefore, it was decided to prepare 5 specimens in absolutely the same printing conditions and by using the same materials. Geometry of samples is not strictly regulated, however, there are requirements for tensile specimens' geometry and these requirements were taken into account during preparation stage. Thus, it was decided to use rectangular cross-section shape specimens with dimensions 100x10x5 mm. It is clearly known that the accuracy of FDM technology is still a big challenge especially when new materials and new printing parameters are used. Consequently, all specimens were measured and more detailed results can be seen in Table 1 and Table 2.

TABLE 1. RESULTS BEFORE SANDING

Specimen No	Length, mm	Before sanding		
		Weight, g	Width, mm	Thickness, mm
1	100.06	5.26	10.21	5.41
2	100.02	5.28	10.20	5.45
3	100.18	5.26	10.27	5.52
4	100.4	5.29	10.41	5.45
5	99.97	5.25	10.23	5.46

It can be seen that the specimens were analysed before and after sanding. Manual sanding was used to equalize measurement results. It is important to mention that the length of specimens was measured one time and no sanding was used on both ends. However, the width and thickness of each specimen were measured in three different positions (at every end and in the middle of the sample) and average of the measurement is presented in Table 1. Measurements were performed with digital calliper and samples were weighed with precision scales GR-200.

TABLE 2. RESULTS AFTER MANUAL SANDING

Specimen No	Length, mm	After sanding		
		Weight, g	Width, mm	Thickness, mm
1	100.06	5.19	9.65	5.31
2	100.02	5.16	9.65	5.38
3	100.18	5.21	9.67	5.36
4	100.4	5.16	9.91	5.44
5	99.97	5.12	9.43	5.28

According to ASTM D3039 standard, specimens do not require having tabs, however, the usage of the tabs can have a considerable effect on failure mode and location. It is well known that the material of the tabs could also affect the above-mentioned parameters, however, it was decided to use 3D printed PLA tabs with dimensions 25x10x2 mm.

Tabs bevel angle was left at 45°. Before gluing the tabs, specimens were sanded and cleaned with isopropyl alcohol (99.8%). Tabs were glued with cyanoacrylate glue and contact places were pressed for 24 hours. Prepared samples are presented in Fig. 2.

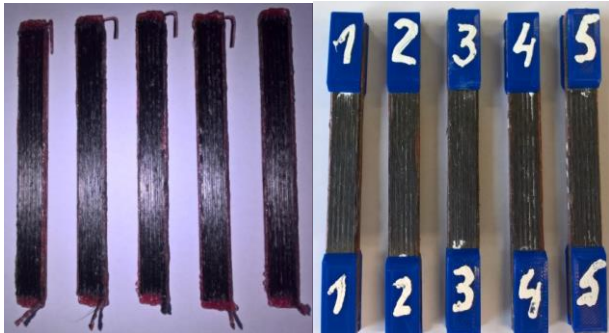


Figure 2. Printed samples

Standard head displacement rate of 2 mm/min was used during the tensile tests. Dual column tensile machine Tinius Olsen H25KT (capacity 25kN) was used to perform the experimental part.

2.2 Microstructural analysis

The microstructural analysis of surface and morphology of 3D printed composite specimens were tested by using Nikon Eclipse LV100ND motorised microscope and high-definition colour camera DS-Ri2. Maximum permissible sample size for the microscopic analysis is 150x150 mm and maximum image resolution of camera is 4908x3264 pixels. For image analysis microscope imaging software NIS Elements D was used which allows preparing and processing of the data.

3 RESULTS

As mentioned before in the methodology, tensile testing was performed by using universal machine Tinius Olsen H25KT (Fig. 3) and universal mechanical wedge action grips. In order to receive reliable results, 5 specimens were used and tests were performed in the same testing conditions. The tensile strength of samples can be simply calculated as a ratio between the stretching force (N) and cross-section area of the sample (mm²). As shown in the Fig. 4, the results can be accepted as reliable because of insignificant variation of results. The average stretching force was 4,398 N and the average displacement until break was 2.87 mm. Following results are presented in Table 3. As can be seen from Table 3, tensile strength variation is insignificant and about twice higher than PLA tensile strength. However, the received results can be much higher and it is important to mention that carbon fibre content in composite material must be considered. Preliminary content of carbon fibre can be calculated according to the printing strategy and toolpath.



Figure 3. Test of tensile strength of 3D printed composite material

As it was mentioned before, 55 carbon fibre yarns were embedded into the specimen. Considering that the length of specimen was 100 mm, the approximate total length of embedded carbon fibre yarn should be about 5,500 mm.

TABLE 3. TENSILE STRENGTH RESULTS

Specimen No	Area, mm ²	Force, N	Tensile strength, MPa
1	51.34	4300	83.7
2	51,95	4450	85.6
3	51,84	4380	84.4
4	53,92	4460	82.7
5	49,82	4400	88.3

According to the properties of T300B-1000, linear density is 66 tex. Thus, can be said preliminary that each sample had about 0.36 g of carbon fibre and that is about 6.9%.

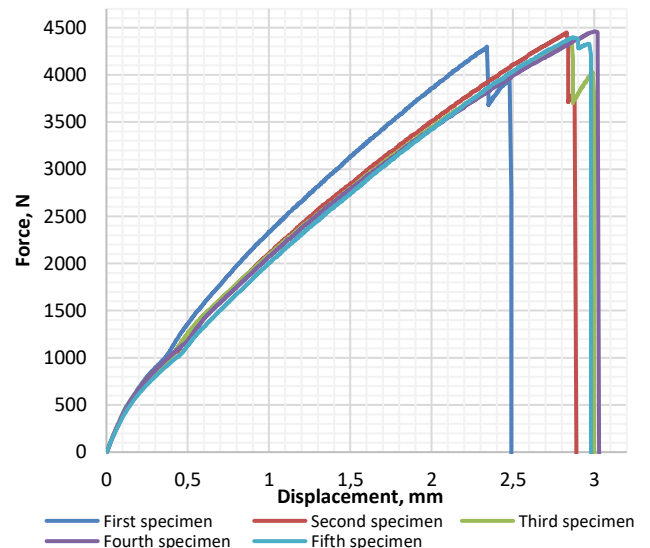


Figure 4. Mechanical properties of tested specimens

It is a very small percentage of carbon fibre, therefore, it results that the increased amount of carbon fibre can significantly improve tensile strength. On the other hand, during experiments the adhesion between layers was perceived to be insufficient. It can be clearly seen from Fig. 4 (for specimens No 1-3). After reaching the maximum, the force falls down sharply then slightly increases and decreases down to 0. It was determined that the above-mentioned material behaviour resulted from delamination between the layers. Specimens after test and failure mode can be seen in Fig. 5.



Figure 5. Printed samples

It is known that failure of composite material can occur because of breaking of fibre, micro cracks in matrix, debonding between the matrix and reinforcement and delamination between the layers. It is possible to conclude that the main reason of fracture in printed samples was delamination. Moreover, it is possible to predict that, if delamination problem is solved, tensile strength will increase.

To determine how well carbon fibre is embedded into matrix material, microstructural analysis was performed. It was found that carbon fibre is inserted in the upper part of the each layer. Meanwhile, on the upper part of the layer, matrix material is not sufficient. This effect can be easily seen in the Fig. 6.

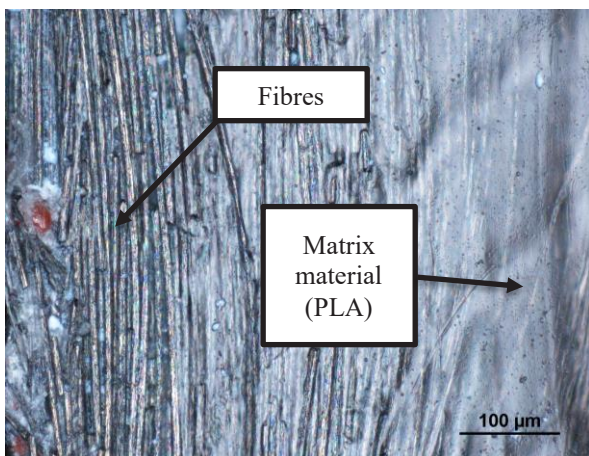


Figure 6. Surface morphology of the printed sample

Delamination of layers also can be the main reason of the above-mentioned behaviour. Therefore, it can be said

that despite a relatively high volume of matrix, distribution of material inside composite is poor. These problems can be solved by changing printing parameters, especially printing speed and layer height. Even more changes of extrusion device and nozzle may be needed.

4 CONCLUSIONS

Additive layer manufacturing technology of continuous carbon fibre-reinforced poly lactic acid composite was presented. The mechanical strength and surface morphological testing were performed and the following conclusions were made:

- 4.1 Five specimens were prepared for tensile tests according to standard (ASTM D3039). The average tensile strength was found to be 84.9 MPa.
- 4.2 Carbon fibre content in composite material was analytically calculated. Each sample was found to contain about 6.9% of carbon fibre. In order to improve the mechanical properties, the amount of carbon fibre must be increased.
- 4.3 It was found that the fracture of specimens was caused mainly by the delamination of layers. Delamination of layers may result from uneven distribution of matrix material in the specimen.

5 ACKNOWLEDGEMENT

This research was funded by a grant (No S-M-ERA.NET-17-4) (project acronym: '3D-CFRP') from the Research Council of Lithuania.

REFERENCES

- [1] Zhang, W., Cotton, C., Sun, J., Heider, D., Gu, B., Sun, B., Chou, T., 2018, 'Interfacial bonding strength of short fiber/acrylonitrile-butadiene-styrene composites fabricated by using fused deposition modeling', *Composites Part B: Engineering*, vol. 137, pp. 51-59.
- [2] Wang, X., Jiang, M., Zhou, Z., Gou, J., Hui, D., 2017, '3D printing of polymer matrix composites: A review and perspective', *Composites Part B*, vol. 110, pp. 442-458.
- [3] Tain, X., Liu, T., Yang, C., Wang, Q., Li, D., 2016, 'Interface and performance of 3D printed continuous carbon fiber reinforced PLA composites', *Composites: Part A*, vol. 88, pp. 198-205.
- [4] Spackman, C. C., Frank, C. R., Picha, K. C., Samuel, J., 2016, '3D printing of fiber-reinforced soft composites: Process study and material characterization', *Journal of Manufacturing Processes*, vol. 23, pp. 296-305.
- [5] Li, N., Li, Y., Liu, S., 2016, 'Rapid prototyping of continuous carbon fiber reinforced poly lactic acid composites by 3D printing', *Journal of Materials Processing Technology*, vol. 238, pp. 218-225.
- [6] Justo, J., Távora, L., Garcia-Guzman, L., Paris, F., 2018, 'Characterisation of 3D printed long fibre reinforced composites', *Composite Structures*, vol. 238, no. 1, pp. 537-548.
- [7] Liu, S., Li, Y., Li, N., 2018, 'A novel free-hanging 3D printing method for continuous carbon fiber reinforced thermoplastic lattice truss core structures', *Materials & Design*, vol. 137, pp. 235-244.

Topology Optimization in Additive Manufacturing Considering the Grain Structure of Inconel 718 using Numerical Homogenization

D. Hübner*, Mathematical Optimization, daniel.huebner@fau.de

M. R. Gotterbarm*, Chair of Materials Science and Engineering for Metals, martin.gotterbarm@fau.de

A. Kergaßner*, Chair of Applied Mechanics, andreas.kergassner@fau.de

J. Köpf*, Chair of Materials Science and Engineering for Metals, johannes.koepf@fau.de

C. Pobel*, Chair of Materials Science and Engineering for Metals, christoph.pobel@fau.de

M. Markl*, Chair of Materials Science and Engineering for Metals, matthias.markl@fau.de

J. Mergheim*, Chair of Applied Mechanics, julia.mergheim@fau.de

P. Steinmann*, Chair of Applied Mechanics, paul.steinmann@fau.de

C. Körner*, Chair of Materials Science and Engineering for Metals, carolin.koerner@fau.de

M. Stingl*, Mathematical Optimization, michael.stingl@fau.de

*Collaborative Research Centre 814 – Additive Manufacturing,
Friedrich-Alexander-Universität Erlangen-Nürnberg, Germany

Abstract—This paper introduces a new manufacturing aware design approach that exploits the possibilities of additive manufacturing processes to generate arbitrary geometries and simultaneously adjust the grain structure of the materials by choosing particular scan strategies. A combined experimental-simulative approach is developed which experimentally analyses the producible grain structures in the selective electron beam process, computes macroscopic material properties for these grain structures and employs these material properties in an optimization procedure in which the topology of a part and the orientation of the grains are optimized. In one example, the stiffness of a designed part can be increased by 30% when the grain orientation is taken into account.

Keywords: selective electron beam melting, optimization, grain structure

1. INTRODUCTION

One major advantage of additive manufacturing (AM) processes is their flexibility regarding the geometry of the manufactured parts. Mathematical optimization can be applied to compute the optimal part geometry for various loading conditions and AM processes offer the possibility to build these parts. However, the fabrication of arbitrary

geometries is only one of the advantages of AM processes. Another one is the potential to adapt the microstructure of the produced metals. The size, shape and orientation of the grains are influenced by means of specific scan strategies during the process and determine the macroscopic mechanical properties of the manufactured part. To exploit the full potential of AM processes a combination of topology and grain structure optimization, in combination with process simulations and homogenization approaches to obtain the relation between microstructure and macroscopic properties is required. The present paper introduces a combined experimental-simulative approach, which represents a first step in this direction: An experimental study is conducted, supported by process simulations, to understand which grain orientations can be realized by varying the scan strategy in the selective electron beam melting (SEBM) process. In the next step, the macroscopic properties of the materials with these grain structures are computed by means of numerical homogenization. These material properties are then applied as input parameters in an optimization process of additively manufactured parts, in which the topology and simultaneously the orientation of grains (via the homogenized properties) are varied. As a result, the

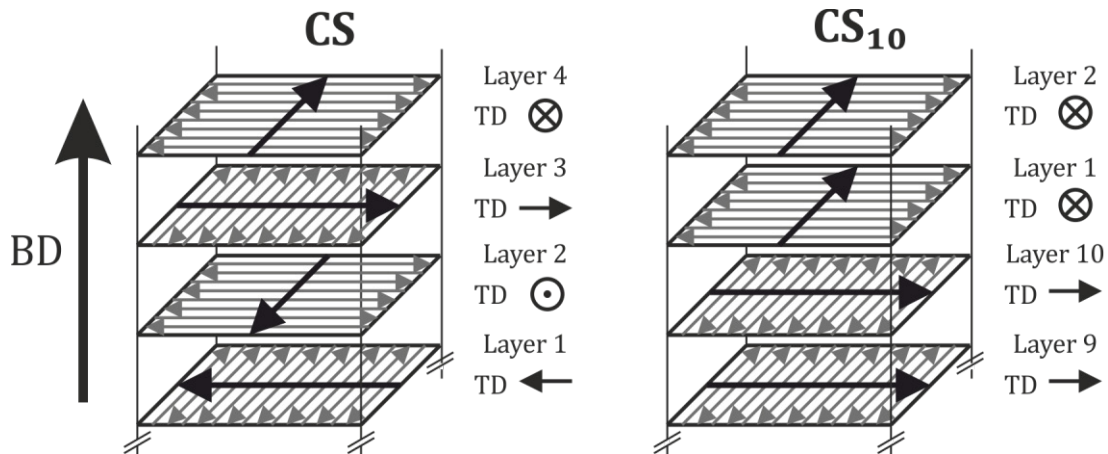


Figure 1. Schematic illustration of the standard cross snake hatching strategy and the employed scan strategy CS10.

optimal geometry of a part for a certain load case is obtained, together with the scan strategy to manufacture this part to obtain the desired mechanical properties in particular regions.

The standard scan strategy for SEBM is cross snake hatching (CS). It is schematically illustrated in Fig. 1 on the left hand side. In CS, the beam scans the surface in a snake like manner, as depicted by the grey arrows, and thus moves along the travelling direction. The scan pattern is rotated by 90° after each layer. The resulting grain structure of CS consists of columnar grains exhibiting a strong <001> fiber texture parallel to the building direction. This results in an anisotropic mechanical behavior [11,1,15].

In order to fully understand the grain structure evolution in SEBM one has to take the solidification conditions during the process into account. We have shown in prior publications that our self-developed numerical simulation tool SAMPLE^{2D} (Simulation of Additive Manufacturing on the Powder scale using a Laser or Electron beam) can accurately model the SEBM process [13,14,18,19]. Our investigations especially highlighted the great importance of the orientation of the thermal gradient during solidification for the resulting grain structure and its texture [13,15,16].

Körner et al. [16] and Helmer et al. [10] introduced the idea of manipulating the scan strategy in order to tailor the orientation of the columnar grains in SEBM (“tilted grains”). The studies showed that the thermal gradient is in fact slightly misaligned with the building direction in every layer, and that the degree of misalignment can be tailored by tightly controlling the beam parameters during melting. It is the nature of the commonly used scan strategy of cross snake hatching that causes the thermal gradient to be aligned parallel to the building direction on average. As can be seen in Fig. 1 the scan pattern is rotated by 90° after every layer. This leads to an averaging effect of the misalignment in the thermal gradient with respect to the building direction, and is thus responsible for the well-

known <001> fiber texture parallel to the building direction. To introduce a defined misalignment into the columnar grains, the scan strategy is altered, in order to eliminate the averaging effect of the scan pattern rotation on the thermal gradient in classic cross snake hatching. For this purpose, a CS_n scan strategy was introduced, where *n* stands for the number of layers after which the scan pattern is rotated. On the right hand side of Fig. 1 this strategy is schematically depicted for *n* = 10, which was also used for this study. This is the starting point for a feasibility study, in the framework of which it is investigated, to which extent the columnar grain structure can be controlled in the SEBM studies, see section 2.

The macroscopic elastic properties of the manufactured materials depend on the orientation of the columnar grains, i.e. the stiffest material response is obtained at a 45° angle to the orientations of the columnar grains [11]. The resulting elastic properties can be obtained by means of numerical homogenization, see e.g. [7]. Based on the experimental results, a representative cutout of the microstructure is geometrically modelled, the so-called Representative Volume Element (RVE). The shape and orientations of the grains can be chosen freely, in accordance with the experimental observations. Certain load cases are simulated for the RVEs and the microscopic results are averaged to obtain the macroscopic material parameters. The precise numerical procedure is outlined in section 3.

The obtained material model is then used to set up an optimization model, which allows for the concurrent optimization of grain orientation and the topological layout of components; the model is based on an extension of the well-known SIMP model [3] and allows for the numerical solution by standard nonlinear optimization software [8]. Using this, we investigate two test cases: in the first test case the topology as well as the orientation of the grain structure is optimized with respect to a given loading scenario. The result is compared to the pure topological solution, i.e. with standard orientation of the grains. In a

second test case, only the orientation is subject to optimization to demonstrate the potential of exploiting the anisotropic mechanical behavior of the grain structure itself. Details about the optimization model as well as an in-depth discussion of the numerical results are presented in section 4.

Finally, we give our conclusion as well as a short outlook in section 5.

2. MESOSCOPIC GRAINSTRUCTURE

2.1. Setup

In order to assess the possibilities of grain structure tailoring in SEBM by means of a defined misalignment of the <001> directions of the columnar grains from the build direction, an experimental feasibility study was conducted. As first step a large range of parameter settings was numerically simulated by the SAMPLE^{2D} suite, which is described in detail elsewhere [13,14,18,19], in order to identify a number of promising parameter sets which were subsequently manufactured by SEBM. The selection criterion was a maximum deviation of the thermal gradient during solidification from the building direction as suggested by Körner et al. [16] and Helmer et al. [10], as well as a relative density of > 99.5%.

The samples were fabricated on an Arcam A2 machine (Arcam AB, Mölndal, Sweden) which was modified to meet specifications of an Arcam A1. Build jobs were conducted at 950°C start plate temperature and a building chamber pressure of 2x10⁻³ mbar under Helium atmosphere. As raw material Inconel 718 powder with a size distribution of 45 – 105 µm was used, provided by TLS Technik GmbH & Co. Spezialpulver, Bitterfeld, Germany. The powder particles showed spherical morphology with few satellites and moderate residual porosity. The chemical composition is given in Table 2.

Specimens to verify the simulated parameters were built as 15x15x20 mm³ cuboids on 5 mm cylindrical supports. Polycrystalline IN718 discs with a thickness of 16 mm were used as start plates.

Scan strategy CS₁₀ was used (see Fig. 1) in order to depict the possibilities of grain alignment with respect to all four possible travelling directions, i.e. +/- X and +/- Y. The manufactured samples were metallographically prepared as longitudinal microsections and subsequently macro etched using 5% H₂O₂ in a 32% HCl solution. The sample that was found to exhibit the most significant grain tilting was manufactured with the parameters listed in Table 1.

TABLE 1. PARAMETER SETTINGS FOR THE EXAMINED CS10 SPECIMEN.

Scan strategy	Layer thickness (10 ⁻⁶ m)	Power (W)	Scan speed (ms ⁻¹)	Scan line spacing (10 ⁻⁶ m)
CS ₁₀	50	220	2	50

In order to gain further insights about the grain orientation, electron backscatter diffraction (EBSD) measurements were performed on this sample. The data was collected in the center of the sample, close to the top surface with an area of 1.73 x 2.65 mm² and a step size of 2.5 µm. The measurements and post processing were performed on a Helios NanoLab DualBeam 600 FIB/SEM (FEI Company, Hillsboro, USA) equipped with a NordlysNano EBSD detector using the AZtecHKL and the HKL CHANNEL5 software (Oxford Instruments, Abingdon, GB). The pole figures were created with a half width of 10° and a cluster size of 10°.

2.2. Results

The possibilities of the CS_n scan strategy for grain structure tailoring can be estimated by examining the grain structure of a sample that was built up using the scan strategy CS₁₀. Fig. 2 shows an IPF-Map (color-coding corresponding to the build direction) derived from an EBSD mapping. The dashed lines mark the layers at which the scan pattern was rotated, i.e. the travelling direction was constant in between these. The corresponding {100} pole figures are displayed on the right hand side for each marked section, as well as the travelling direction. It is evident that most grains appear strongly elongated and misaligned with the build direction. From the IPF map a significant grain tilting away from the build direction is noticeable for travelling direction +/- Y. Prior to the EBSD measurements, a rough estimation of the tilt angle was performed by means of image analysis of an etched microsection. This yielded a value of about 19° deviation of the grain orientation from the build direction. It is interesting to note, that the EBSD measurements confirm this straightforward approach: The peak intensity in the pole figures lies at a deviation from the build direction of around 20° for all travelling directions. The EBSD measurement can also help with the interpretation of the grains in the layers where the travelling direction corresponds to +/- X, as the grain structure appears to be rather equiaxed when just considering the longitudinal section. The pole figures however reveal that the grains are actually tilted according to the travelling direction (i.e. out

TABLE 2. ELEMENT CONTENT (WT.-%) IN INCONEL 718 POWDER.

Fe	Ni	Cr	Nb	Mo	Ti	Al	Co	C
bal.	53.07	19.33	5.20	2.99	0.96	0.50	0.29	0.03

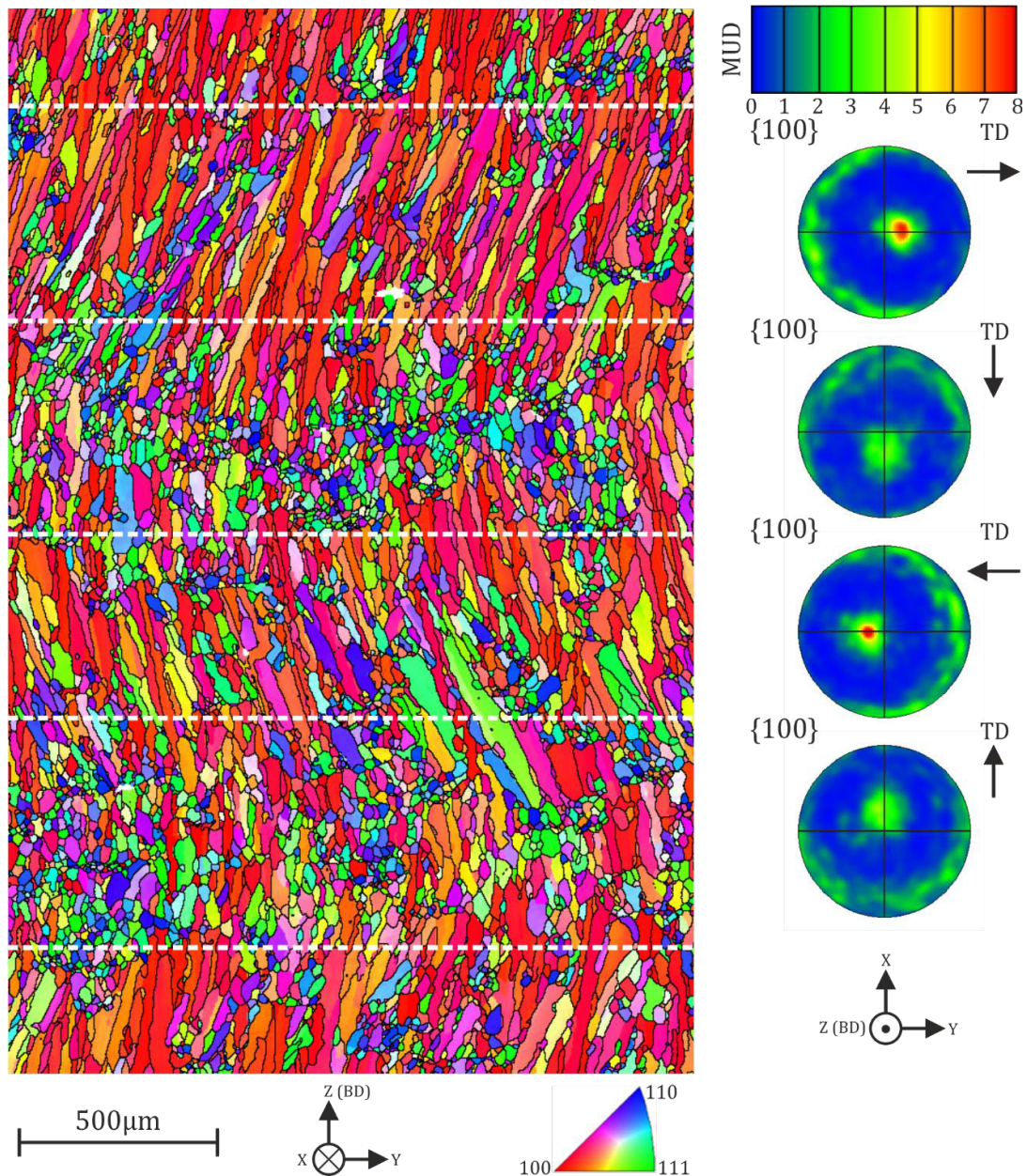


Figure 2. Results of a large area EBSD mapping. The IPF coloring was with respect to the building direction. The dashed lines mark the layers at which the scan pattern was rotated. The corresponding pole figures and travelling directions of the beam are shown on the right hand side.

of the sectioning plane). Thus, it is the nature of the longitudinal section that causes the false interpretation of the in fact strongly elongated grains. What is also interesting to note, is that the change in grain orientation is carried out over the course of just one or two layers (i.e. 50-100 µm).

This feasibility study shows the potential of controlling the grain orientation of columnar grains within the SEBM process. A misalignment of the grains' <100> directions relative to the build direction of about 20° can be obtained

by employing the CS_n strategy. It was shown that the grains can be tilted according to the travelling direction, and can thus be tilted in virtually any direction, as long as the travelling direction can be controlled unfettered. This opens up new possibilities for topology optimization, as grain orientation now becomes a new variable.

In addition to the experimental tests, numerical simulations with the same setup were performed with SAMPLE^{3D} [13], see Fig. 3. Since a nucleation model is currently under development, new grains could not be

initiated when the scan pattern rotates after ten layers. Therefore, a continuous selection process of the grains with an orientation along the build direction occurs. Nevertheless, especially in the first section the tilt angle of the grain structure is clearly visible.

3. MACROSCOPIC CONSTITUTIVE LAW

The macroscopic material behavior of the columnar-grained Inconel 718 is identified by means of microscopic simulations using the finite element method and computational homogenization. Based on measured grain size distributions and textures representative volume elements (RVE) are generated using a Voronoi tessellation based method and numerical homogenization is applied to determine a macroscopic elastic constitutive law. The columnar grain structure results in transversal isotropic material behavior on the macroscale, in which the direction of the plane of symmetry can be manipulated by means of the scanning strategy during the process as discussed in the previous section.

3.1. Governing equations on the microscale

The presented theory is restricted to geometrically linear problems. The displacement field is denoted by $\mathbf{u}(\mathbf{x}, t)$ and the strain $\boldsymbol{\varepsilon}$ is defined as the symmetric gradient of the displacement field and considered fully elastic

$$\nabla \mathbf{u}^{sym} = \boldsymbol{\varepsilon} = \boldsymbol{\varepsilon}^e. \quad (1)$$

The usual balance of linear momentum is defined in terms of the stress tensor $\boldsymbol{\sigma}$

$$\text{div}(\boldsymbol{\sigma}) = 0. \quad (2)$$

Body forces are neglected and the boundary conditions on the RVE follow from the homogenization procedure.

The microscopic elastic behavior in each grain is assumed to be cubic symmetric since the considered Inconel 718 has a face centered cubic (fcc) crystal structure. The stresses and strains are related by the constitutive relation

$$\boldsymbol{\sigma} = \mathbb{C} : \boldsymbol{\varepsilon}. \quad (3)$$

The components of the fourth order elasticity tensor \mathbb{C} are defined in terms of the parameters Young's modulus E , Poisson's ratio ν and shear modulus μ as

$$\begin{aligned} C_{ijkl} &= C_{12} \delta_{ij} \delta_{kl} + C_{44} [\delta_{ik} \delta_{jl} + \delta_{il} \delta_{jk}] \\ &\quad + \bar{C} \delta_{ij} \delta_{kl} \delta_{jk}. \\ \bar{C} &= C_{11} - C_{12} - 2C_{44} \\ C_{11} &= \frac{E\nu}{(1+\nu)(1-2\nu)}, \\ C_{12} &= \frac{E(1-\nu)}{(1+\nu)(1-2\nu)}, \quad C_{44} = \mu. \end{aligned} \quad (4)$$

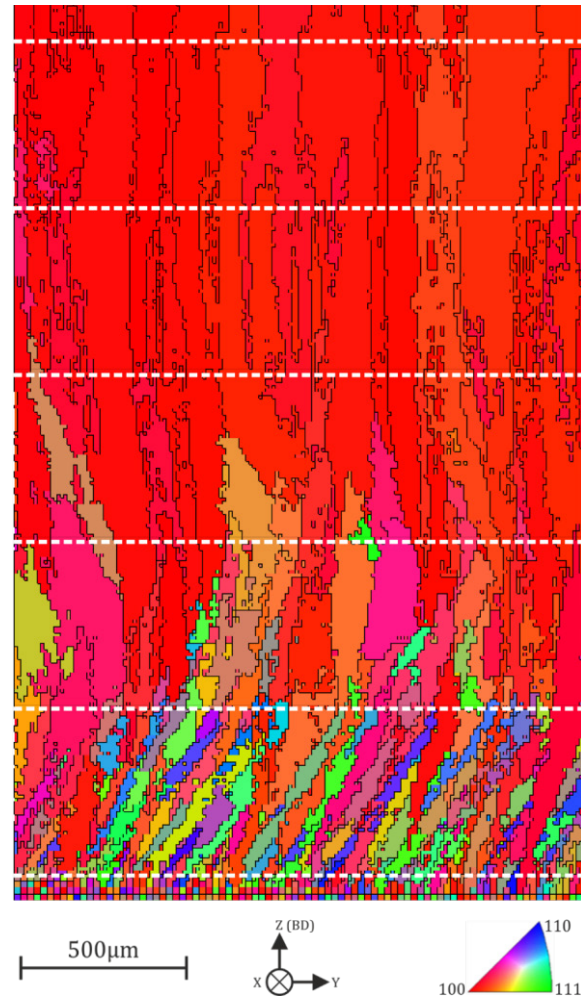


Figure 3. Results of a numerical simulation with the same IPF coloring as the experiment. The dashed lines mark the layers at which the scan pattern was rotated.

The microscopic material parameters are identified by means of inverse parameter identification using macroscopic uniaxial tensile test in three different orientations to building direction. A detailed description of the identification procedure is given in [12]. The identified microscopic constants are $E = 121344 \text{ MPa}$, $\nu = 0.3858$ and $\mu = 107212 \text{ MPa}$.

3.2. Computational Homogenization

The balance of linear momentum (2) is solved for a representative grain structure, the RVE. For topology optimization, the material behavior on the scale of manufactured parts – the macroscale – is needed and derived by means of numerical homogenization. Here, a short summary of computational homogenization is given, a detailed overview can be found in e.g. [20].

In the following, macroscopic quantities are denoted by an overbar ($\bar{\square}$). The macroscopic displacement field for a first-order strain driven homogenization ansatz reads

$$\bar{\mathbf{u}} = \bar{\boldsymbol{\varepsilon}} \cdot \mathbf{x} + \tilde{\mathbf{u}}, \quad (5)$$

whereby ($\tilde{\square}$) describes the fluctuations. Macroscopic strains and stresses are derived as volume averages of their microscopic counterparts

$$\begin{aligned} \bar{\boldsymbol{\varepsilon}} &= \frac{1}{V} \int_{\mathbb{B}} \boldsymbol{\varepsilon} \, dV = \frac{1}{V} \int_{\partial\mathbb{B}} [\mathbf{u} \otimes \mathbf{n}]^{sym} \, dA \\ \bar{\boldsymbol{\sigma}} &= \frac{1}{V} \int_{\mathbb{B}} \boldsymbol{\sigma} \, dV = \frac{1}{V} \int_{\partial\mathbb{B}} [\mathbf{t} \otimes \mathbf{x}]^{sym} \, dA, \end{aligned} \quad (6)$$

with V denoting the volume of the RVE. The Hill-Mandel condition – equivalence of microscopic and macroscopic stress power – has to be satisfied:

$$\bar{\boldsymbol{\sigma}} : \dot{\bar{\boldsymbol{\varepsilon}}} = \frac{1}{V} \int_{\partial\mathbb{B}} \mathbf{t} \cdot \dot{\mathbf{u}} \, dA. \quad (7)$$

The traction vector \mathbf{t} is derived from the stress tensor with the normal vector to the boundary of the RVE as $\mathbf{t} = \boldsymbol{\sigma} \cdot \mathbf{n}$ and the over-dot denotes the time derivative. Using eqs. (5-7) and some reformulations it comes out that the integral of the power due to the fluctuations must vanish on the boundary

$$\frac{1}{V} \int_{\partial\mathbb{B}} \mathbf{t} \cdot \dot{\tilde{\mathbf{u}}} \, dA = 0. \quad (8)$$

This is satisfied automatically for periodic – antiperiodic boundary conditions, in which the displacement fluctuations are prescribed to be periodic and the tractions are antiperiodic.

Periodic RVEs of columnar-grained Inconel 718 are generated using the Voronoi tessellation based method described in [6], see Fig. 4. Due to the periodic boundary conditions the grains are modelled as being infinitely long in building direction. The unit cells are randomly rotated around the crystallographic $\langle 100 \rangle$ axis which is tilted up to 5° against the building direction to render the experimental texture in [9].

The macroscopic elasticity tensor $\bar{\mathbb{C}}$ is calculated from averaging the homogenized behaviour of 100 RVEs with different orientation sets of unit cells using the macroscopic relation

$$\bar{\boldsymbol{\sigma}} = \bar{\mathbb{C}} : \bar{\boldsymbol{\varepsilon}}. \quad (9)$$

Six different unit load cases are simulated to derive the components of the macroscopic tensor. The resulting macroscopic tensor is, as expected, very close to a transversal isotropic tensor and is projected into the transversal isotropic tensor space using the eighth order projection tensor given in [17]. The macroscopic transversal isotropic elasticity tensor can also be represented as an elasticity matrix with five parameters

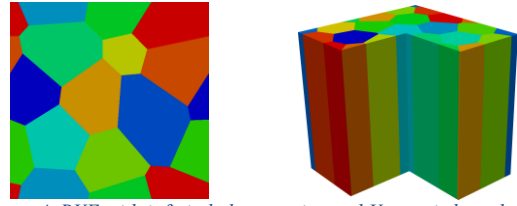


Figure 4. RVE with infinitely long grains and Voronoi shaped cross sections, compare [1].

$$\bar{\mathbb{C}} = \begin{pmatrix} \lambda + 2G_{\perp} & \lambda & 2\nu(\lambda + G_{\perp}) & 0 & 0 & 0 \\ \lambda & \lambda + 2G_{\perp} & 2\nu(\lambda + G_{\perp}) & 0 & 0 & 0 \\ 2\nu(\lambda + G_{\perp}) & 2\nu(\lambda + G_{\perp}) & C_{1111} & 0 & 0 & 0 \\ 0 & 0 & 0 & G_{\parallel} & 0 & 0 \\ 0 & 0 & 0 & 0 & G_{\parallel} & 0 \\ 0 & 0 & 0 & 0 & 0 & G_{\perp} \end{pmatrix}$$

$$\lambda = \frac{-\left(1 - \frac{E_{\perp}}{2G_{\perp}} - \nu^2 \frac{E_{\perp}}{E_{\parallel}}\right) G_{\perp}}{1 - \frac{E_{\perp}}{4G_{\perp}} - \nu^2 \frac{E_{\perp}}{E_{\parallel}}},$$

$$C_{1111} = \frac{\left(1 - \frac{E_{\perp}}{4G_{\perp}}\right) E_{\parallel}}{1 - \frac{E_{\perp}}{4G_{\perp}} - \nu^2 \frac{E_{\perp}}{E_{\parallel}}}.$$

The elastic parameters of the considered Inconel 718, resulting from the homogenization procedure and applied in the optimization process, are summarized in Table 3. Additionally the stiffness for tensile loading in all directions is visualized in Fig. 5.

4. OPTIMIZATION

For numerical demonstrations, we solve two different two-scale optimization problems, for both of which the upscaling is done by the homogenization technique outlined in section 3.

4.1. Problem formulation

We conduct a SIMP approach (cf. e.g. [3]) on the macroscopic level with density variable $\rho \in [0.01, 1]$ and penalization parameter $p = 3$. The rotation of the grain structure is realized by rotation of the homogenized stiffness tensor $\bar{\mathbb{C}}$ by an angle α around the X-axis and an angle β around the Z-axis. Thus, the material law for the resulting macroscopic elasticity matrix $\tilde{\mathbb{C}}$ is given by

$$\tilde{\mathbb{C}} = \rho^3 \mathbf{R}(\alpha, \beta) \bar{\mathbb{C}} \mathbf{R}^T(\alpha, \beta). \quad (10)$$

This results in the following optimization problem:

TABLE 3. PARAMETERS OF THE HOMOGENIZED MACROSCOPIC STIFFNESS TENSOR.

E_{\parallel}	E_{\perp}	ν	G_{\parallel}	G_{\perp}
121517 MPa	160171 MPa	0.3856	107120 MPa	67290 MPa

$$\min_{\substack{\rho \in \mathbb{R}^m \\ (\alpha, \beta) \in \mathbb{R}^{2m} \cap S}} f^T u \quad (11)$$

$$\mathbf{K}(\rho, \alpha, \beta) u = f \quad (12)$$

$$\frac{1}{m} \sum_{i=1}^m \rho_i \leq \bar{V} \quad (13)$$

Here m is the number of finite element cells in the macroscopic domain, f is the nodal force vector, u the macroscopic displacement vector and $\mathbf{K}(\rho, \alpha, \beta)$ is the global stiffness matrix given by the formula

$$\sum_{i=1}^m \sum_{k=1}^8 \tilde{\rho}_i^3 \mathbf{B}_{i,k} \mathbf{R}(\tilde{\alpha}_i, \tilde{\beta}_j) \bar{\mathbf{C}} \mathbf{R}^T(\tilde{\alpha}_i, \tilde{\beta}_j) \mathbf{B}_{i,k}^T, \quad (14)$$

where $\mathbf{B}_{i,k}$ denote macroscopic strain-displacement matrices evaluated at Gaussian points for each element. The symbol $\tilde{\cdot}$ means that the design variables are filtered by a standard density filter [4,5]. The set S encodes both bound constraints for the rotation angles as well as further restrictions saying, e.g., that the orientation has to be constant on a fixed subdomain, see section 4.2. Finally the objective (11) is the well-known compliance functional, (12) the linear elasticity state equation and (13) a resource condition. For both settings discussed in Section 4.2 and 4.3 the optimization problems are solved using the SQP algorithm SNOPT [8].

4.2. First test case

First, we seek to solve problem (11-13) for the loading scenario given in Fig. 6 and Fig. 7 with a prescribed material volume of 25%, $V=0.25$ in (13). The design space is clamped at patches in the lower four corners and a force is applied to a patch at the upper boundary. As outlined in section 4.1 we apply density filters for both density as well as rotation variables. This does not only regularize the problem but also provides a coarse model of the transition behavior when changing the grain orientation. In

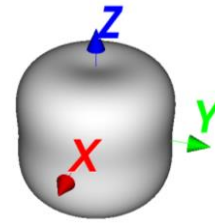


Figure 5. Visualization of the directional stiffness of the considered Inconel 718.

accordance with process conditions the rotational angles are constrained to $\alpha \in [0, 20^\circ]$ and $\beta \in [0, 360^\circ]$.

Varying the grain orientation in each point of the domain is not yet possible in the manufacturing process. Hence, we divide the design domain based on an educated guess into five subdomains with different, but constant grain orientation, see Fig. 6 and Fig. 7. We further introduce an additional design parameter h , which shifts the interface between subdomain 5 and the others in direction +/- Z. We note that for all feasible configurations the resulting components can be printed as one single part without the need of post-processing like bonding or welding. The described approach also drastically reduces the number of design variables to $m + 11$ (m topology variables, 2 angles per subdomain, 1 shifting parameter). It is expected that because of this restriction the number of local optima introduced by the rotational design parameters is drastically reduced.

Although the design complexity is significantly limited, it is still possible that the grain orientation in the optimized component jumps at the interfaces between the individual subdomains. We perform several steps to account for this. First, we choose the filter radius for the design variable ρ large enough to make sure that the optimized component essentially consists of four big “struts” starting from the four corners where the structure is clamped and ending all up at the position where the structure is loaded, see Fig. 8. Second, the shifting parameter h is restricted in such a way

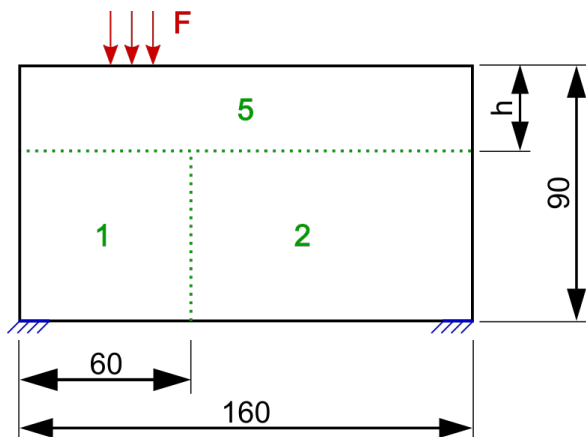


Figure 6. Setting 1, front view, numbers in mm.

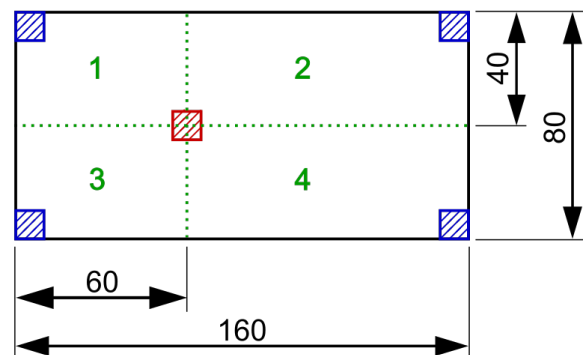


Figure 7. Setting 1, bottom view, numbers in mm.

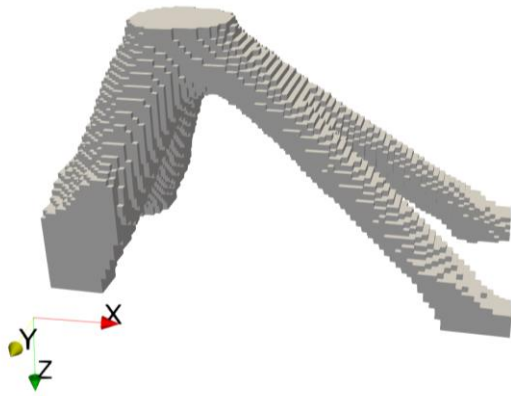


Figure 8. Topological result of the first test case, i.e. $\alpha=0^\circ, \beta=0^\circ$.

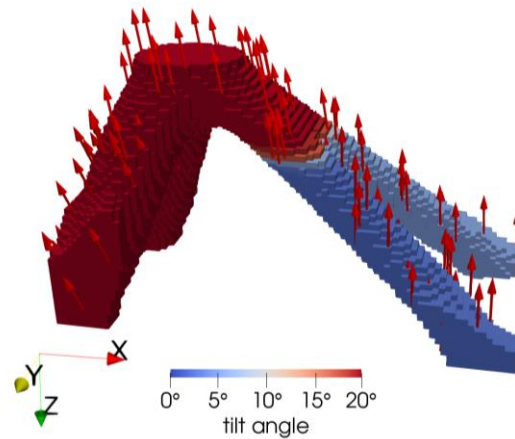


Figure 9. Optimized design of the first test case for $\alpha \in [0^\circ, 20^\circ], \beta \in [0^\circ, 360^\circ]$. The color encodes values of α and the arrows indicate the direction of growth of the grains.

that the hyperplane separating subdomain 5 from subdomains 1 to 4 (horizontal dotted line in Fig. 6) intersects the optimized structure at a vertical position where the four struts are still separated. Doing so, the optimized structure does not intersect interfaces among subdomains 1, 2, 3 and 4. The purpose of this restriction is to minimize the total transition area, as the precise grain structure there is yet unknown. Third, the filter radius for the rotation variables is set to $615 \mu\text{m}$ constituting a conservative guess for the real diameter of the transition zone. We note that this filter has only an effect at the transition areas, as the rotation angles are constant in the interior of each subdomain.

In the following, we discuss the results for this first scenario. As a reference, we first compute the topological solution for fixed $\alpha = 0^\circ, \beta = 0^\circ$ in all five subdomains (cf. Fig. 7). As can be seen in Fig. 5 the columnar grain structure has its highest stiffness at an angle of approximately 45° from the Z-axis. Because the load paths in the optimized structure are also roughly aligned in the same angle to the Z-axis, the component is already rather stiff without rotating the grains. The compliance value in this case is 0.319. The optimized structure with rotation, i.e. $\alpha \in [0, 20^\circ]$ and $\beta \in [0, 360^\circ]$, is depicted in Fig. 9. The main struts in subdomains 1 and 3 form an angle of 77° to the ones in subdomains 2 and 4, such that the tensor can be easily rotated in a way that the maximal stiffness can be pretty well aligned with the load paths in every strut. For the struts in subdomain 2 and 4 this is easily achieved with an angle of $\alpha = 17^\circ$. However, in subdomains 1 and 3 the maximal admissible value $\alpha = 20^\circ$ prevents optimal rotation and thus the angle is at this bound. In subdomain 5 the orientation is chosen such that the stiffness in direction $\pm Z$ is maximized. The gain compared to the topological solution is 13% for an achieved objective value of 0.279. We again note that the comparison is made to a solution for which the orientation is already approximately in line with the load paths.

4.3. Second test case

We investigate a second test case depicted in Fig. 11. Here we fix the topology to an "L-shape" to understand the impact of the grain structure alone. L-shapes are often investigated in minimum stress design problems. In this article, we are however not interested in stresses, but want to find the optimal rotation of the grain structure in the component for the given boundary conditions.

In the following we discuss the results. The initial compliance value for standard orientation of the grains, i.e. $\alpha = 0^\circ, \beta = 0^\circ$, is 4.75. To investigate the influence of grain orientation on the components performance, first we divide the structure in two subdomains, where again the rotation angles have to be constant in each of those subdomains. Doing this, we end up with only four design variables, i.e. angles α and β in each of the two subdomains. In the optimized result, shown Fig. 12, the grain structure is tilted as much as possible by $\alpha = 20^\circ$ in both subdomains, with $\beta = 136^\circ$ also equal in both subdomains. The achieved objective value of 4.37 shows a gain of 8%. This relatively small improvement is due to the manufacturability constraint of the maximal admissible grain tilting and can be overcome if we admit arbitrary values for α . If we do so, the compliance drops to 3.33, which means a gain of 30%. The optimized angles in subdomain 1 are now $\alpha = 46.3^\circ, \beta = 117^\circ$ and $\alpha = 41.7^\circ, \beta = 167^\circ$ in subdomain 2. This shows that there is still a lot of potential left, and extending the limits of grain structure orientation is much desirable. We also note that the optimal angles leading to this gain may be realized by an alternative orientation of the component in the build chamber. A similar effect can be seen if instead of the subdivision we allow the angles to differ from point to point. We again prevent high oscillations in the orientations by applying a density filter to the rotational angles. The result for a maximal admissible rotation of α by 20° is shown in Fig. 10 and Fig. 13. As expected the achieved

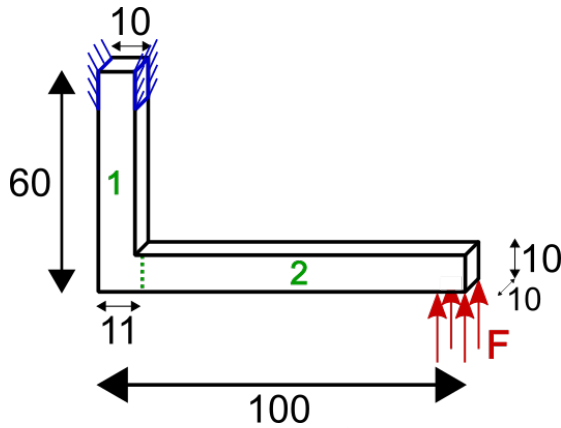


Figure 11. Setting 2, numbers in mm.

compliance value of 4.25 is better than compared to the corresponding result with two subdomains. However, the gain of only 2.7% is relatively small compared to the large increase in the number of design variables. This is also true for the unbounded case. If α is unbounded we obtain an objective value of 3.15, i.e. a gain of 5% compared to the case with 2 subdomains and unbounded rotations. We note that in the latter case we might be stuck in a poor local minimum. In future, we want to prevent such effects by using advanced optimization algorithms as suggested in [21].

5. CONCLUSION

A new manufacturing aware design approach exploiting the controllability of the grain structure in additive manufacturing has been presented. It was demonstrated that in the best cases a gain in the stiffness of the designed components of up to 30% can be obtained. On the other hand, the material model for the transition zones between areas with different orientations was still chosen by a simple averaging approach, technically realized by an appropriate density filter. In future advanced models based on measurements should be used in the interest of predictions that are more accurate. Finally, we have ignored

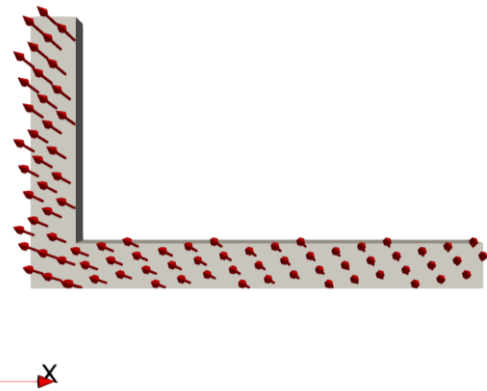


Figure 12. Optimized design of the second scenario for $\alpha \in [0^\circ, 20^\circ], \beta \in [0^\circ, 360^\circ]$. The arrows indicate the direction of growth of the grains.

that the grain orientations close to the outer boundaries are unknown. However, if a post-processing step, like e.g. etching, is applied to the component, these boundary layers might be removed anyway.

ACKNOWLEDGEMENT

We gratefully acknowledge financial support by the German Research Foundation (DFG) within the Collaborative Research Centre 814: Additive Manufacturing (subproject B2, B4, C2, C5).

REFERENCES

- [1] Antonysamy, A.A., Meyer, J., and Prangnell, P.B., 2013, 'Effect of build geometry on the β -grain structure and texture in additive manufacture of Ti6Al4V by selective electron beam melting', *Materials Characterization*, vol. 84, pp. 153–168.
- [2] Bauereiß, A., Scharowsky, T., and Körner, C., 2014, 'Defect generation and propagation mechanism during additive manufacturing by selective beam melting', *Journal of Materials Processing Technology*, vol. 214, no. 11, pp. 2522–2528.

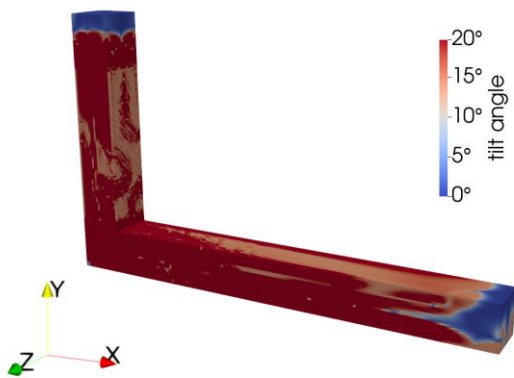


Figure 10. Optimized design of the second scenario for $\alpha \in [0^\circ, 180^\circ], \beta \in [0^\circ, 360^\circ]$. The color encodes the values of α .

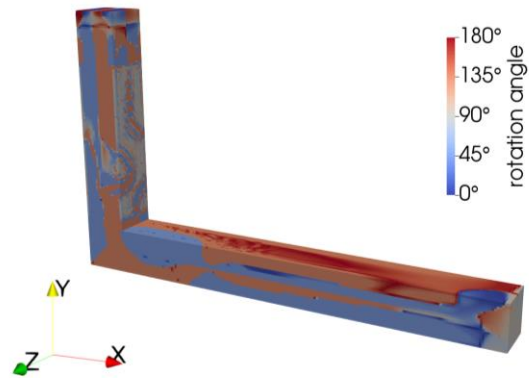


Figure 13. Optimized design of the second scenario for $\alpha \in [0^\circ, 180^\circ], \beta \in [0^\circ, 360^\circ]$. The color encodes values of β .

- [3] Bendsoe, M.P., 1989, 'Optimal shape design as a material distribution problem', *Structural Optimization*, vol. 1, no. 4, pp. 193-202, Springer.
- [4] Bourdin, B., 2001, 'Filters in topology optimization', *International journal for numerical methods in engineering*, vol. 50, no. 9, pp. 2143-2158.
- [5] Bruns, T.E., and Tortorelli, D.A., 2001, 'Topology optimization of non-linear elastic structures and compliant mechanisms', *Computer methods in applied mechanics and engineering*, vol. 190, no. 26-27, pp. 3443-3459.
- [6] Fritzen, F., Böhlke, T., and Schnack, E., 2009, 'Periodic three-dimensional mesh generation for crystalline aggregates based on Voronoi tessellations', vol. 43, no. 5, pp. 701-713.
- [7] Geers, M.G.D., Kouznetsova, V.G., Brekelmans, W.A.M., 2010, Multi-scale computational homogenization: Trends and challenges, *Journal of Computational and Applied Mathematics*, vol. 234, pp. 2175-2182.
- [8] Gill, P.E., Murray, W., and Saunders, M.A., 2005, 'SNOPT: An SQP algorithm for large-scale constrained optimization'. *SIAM review*, vol. 47, no. 1, pp. 99-131.
- [9] Helmer, H.E., 2017, 'Additive Fertigung durch Selektives Elektronenstrahlschmelzen der Nickelbasis Superlegierung IN718: Prozessfenster, Mikrostruktur und mechanische Eigenschaften.'
- [10] Helmer, H.E., Bauereiß, A., Singer, R.F., and Körner, C., 2016, 'Grain structure evolution in Inconel 718 during selective electron beam melting', *Materials Science and Engineering: A*, vol. 668, pp. 180-187.
- [11] Helmer, H.E., Hartmann, N., Körner, C., and Singer, R.F., 2014, 'Relation Between Processing Strategy, Grain Structure and Mechanical Properties in Superalloy Inconel 718 Processed by Selective Electron Beam Melting', *DDMC 2014: Fraunhofer Direct Digital Manufacturing Conference proceedings*, Berlin.
- [12] Kergaßner, A., Mergheim, J., and Steinmann, P., 2018, 'Modelling of additively manufactured materials using gradient-enhanced crystal plasticity', *Computers and Mathematics with Applications*.
- [13] Köpf, J., Gotterbarm, M., Markl, M., Körner, C., 2018, 3D Multi-Layer Grain Structure Simulation of Powder Bed Fusion Additive Manufacturing, *Acta Materialia*, vol. 152, pp. 119-126.
- [14] Köpf, J., Rai, A., Markl, M., Körner, C., 2016, 3D Grain Structure Simulation for Beam-Based Additive Manufacturing. *Proceedings of the 6th International Conference on Additive Technologies (iCAT)*, pp. 215-221.
- [15] Körner, C., 2016, 'Additive manufacturing of metallic components by selective electron beam melting — a review', *International Materials Reviews*, vol. 61, no. 5, pp. 361-377.
- [16] Körner, C., Helmer, H.E., Bauereiß, A., Singer, R.F., 2014, 'Tailoring the grain structure of IN718 during selective electron beam melting', *MATEC web of conferences*, vol. 14, EDP Sciences.
- [17] Moakher, M., and Norris, A. N., 2006, 'The closest elastic tensor of arbitrary symmetry to an elasticity tensor of lower symmetry', *Journal of Elasticity*, vol. 85, no. 3, pp. 215-263.
- [18] Rai, A., Helmer, H., Körner, C., 2017, Simulation of grain structure evolution during powder bed based additive manufacturing. *Additive Manufacturing*, vol. 13, pp. 124-134.
- [19] Rai, A., Markl, M., Körner, C., 2016, A Coupled Cellular Automaton LBM for Grain Structure Simulation during Additive Manufacturing. *Computational Materials Science*, vol. 124, pp. 37-48.
- [20] Saeb, S., Steinmann, P., and Javili, A., 2016, 'Aspects of Computational Homogenization at Finite Deformations: A Unifying Review From Reuss' to Voigt's Bound', *Applied Mechanics Reviews*, vol. 68, no. 5, p. 050801.
- [21] Semmler, J., Pflug, L., and Stingl, M., 2018, 'Material Optimization in Transverse Electromagnetic Scattering Applications', *SIAM Journal on Scientific Computing*, vol. 40, no. 1, pp. B85-B109.

On a combined geometry and multimaterial optimization approach for the design of frame structures in the context of additive manufacturing

D. Hübner, M. Stingl, Mathematical Optimization, Collaborative Research Centre 814 – Additive Manufacturing, Friedrich-Alexander-Universität Erlangen-Nürnberg, daniel.huebner@fau.de,
michael.stingl@fau.de

Abstract – In this article, a novel design method based on the sequential global programming (SGP) method is discussed. The new approach allows to optimize frame structures based on a Timoshenko beam network model simultaneously with respect to continuous as well as combinatorial design variables. Consequently, possible design parameterizations can cover geometric decisions such as positions of nodes (geometry optimization) and sizing of the beams (sizing optimization) as well as decisions on the topology of the frame structure. The latter allow not only answering the question, where in the design space a beam should be placed, but also which material properties should be chosen from a given discrete catalogue (material & topology optimization). The design method is particularly suited for additive manufacturing (AM) as the direct access to geometric quantities in the design space allows to model important manufacturability constraints in a straightforward way. Otherwise, due to the high design flexibility, the full potential of additive manufacturing in terms of design freedom can be exploited. The efficiency of the method is demonstrated by means of a 3D multi-material gripper.

Structural Optimization, Additive Manufacturing, Multi-material design

1. INTRODUCTION

Structural optimization has been successfully applied to academic and industrial applications for a long time; for an overview see the monographs [1, 2, 3] introducing sizing, shape and topology optimization as branches of structural optimization, discussing mathematical solution methods for the same and showing their application to many practical problems from mechanics, acoustics, optics and other areas. Although these publications show that structural optimization is a well-established discipline, the field experienced a new boost when the additive manufacturing technology became available. One of the main reasons is the ability to build complex parts

directly from scratch with minimal restrictions on the complexity of the design. Apart from the high design freedom in terms of shape and topology of a component, AM more recently also offers the possibility to treat multiple materials directly in one manufacturing step [4]. Despite all its opportunities, from the structural optimization perspective, AM comes also with a number of challenges. Of major importance are so called printability constraints ideally leading to self-supporting designs or at least preventing excessive use of support structures, see e.g. [5]. More traditional manufacturing constraints include so called feature size constraints. While in traditional manufacturing processes upper and lower bounds on member sizes may have to be taken into account, in AM mainly the lower bound is crucial. The precise lower bound of course depends on the particular AM technology and can be quite small in certain cases; however, for specific applications this does by no means imply that these constraints can be neglected in the design model. A particular type of application, where smallest feature size constraints are of utmost importance is the design of compliant mechanisms with applications in micro mechanics but also the design of (mechanical) meta materials; for particular examples, see [6] as well as [1] and the references therein. The complexity of modelling feature size constraints depends to a large extent on the chosen type of design variables. In particular when topology optimization problems are studied, this modelling is rather involved and can only be done indirectly. The big break through here came with the so-called robust topology optimization approach [7]. While this technique turned out to be powerful for various types of design problems, it still does not come for free. Some of the implications are that instead of one design problem a full sequence of problems has to be solved. While this is

typically realized by a carefully chosen continuation strategy, in the limit the resulting problems tend to become non-smooth and thus may give rise to numerical instabilities. Moreover, the indirect formulation can have some (unknown) impact on the optimality of the solution. While being already involved for a design with only one type of material, the situation gets even more complicated if multiple materials are used and, e.g., feature size constraints have to be imposed individually on each phase. In the work by Gaynor et al. [8], this problem was mastered using a nested projection method. The results show that the method in principal works quite well for 2D test cases, however a generalization to 3D – to the best knowledge of the authors – has not been presented in literature so far. In addition, the quality of the results in terms of the chosen objective is hard to judge due to the combinatorial and at the same time almost non-smooth character of the design problem.

Otherwise in shape and sizing optimization geometric quantities of the design can be accessed much more directly and thus the formulation of feature size constraints does not impose a major challenge. The downside of this is that - in particular in sizing optimization - the design space is already defined in terms of parameterised elements (e.g. rods, beams, plates) giving rise to a more restrictive model and thus leading to less performant designs. To compensate for this, in the case of truss and frame structures, several authors have tried to combine techniques from topology optimization based on the ground structure approach [9] with sizing and geometry optimization. In [10,11] the different design steps are organized along a sequential design chain.

In this paper we pursue a strategy similar to [10,11], i.e. we combine techniques from sizing, geometry and topology optimization for a frame model based on the ground structure approach. However, in contrast to [10,11], topology, material- and sizing optimization are treated simultaneously using the idea of the sequential global programming approach (SGP) [12]. This design step is alternated in the framework of an alternating directions approach with a second step, in which the member sizes as well as positions of nodes are optimized concurrently. In both design steps, feature size constraints can be treated in a strict sense. The SGP method is not the first method to treat multi-material design problems. A popular alternative is the discrete material optimization (DMO) framework; see, e.g. [13,14]. However, the concurrent treatment of sizing and material variables in combination with feature size constraints leads – even after the typical DMO relaxation – to a disjunctive structure of the feasible set, which cannot be directly handled within a DMO based approach. In principal, the problem addressed in this article could also be approached by using genuine techniques from combinatorial

optimization, see, e.g. [15]. However, for the given number of the design variables the problems studied in this article are still beyond the scope of mixed integer nonlinear programming solvers.

We finally note that the frame model we are using is built on a network of linear elastic Timoshenko beams. For this setting, it has been shown recently in [16] that fully analytic network solutions cannot only be calculated but are also numerically accessible through the employment of appropriate shape functions in a finite element type procedure. Consequently, in a linear elastic regime no discretization along the individual beams is required and thus elastic deformation problems can be solved rapidly even for larger networks. This allows us to solve structural optimization problems including all different types of design variables, as described above, for many starting configurations in reasonable time. In contrast to combinatorial approaches, we do not claim that we can find globally optimal solutions in this way, however we are at least able to avoid poor local optima to a large extent with a significantly lower computational effort.

The remainder of this article is structured as follows: in Section 2 we briefly sketch the idea of the SGP method in a general setting. Then, in Section 3, the Timoshenko beam network model is introduced. It is demonstrated that using the analytic network solutions suggested in [16] the state equation can be rephrased suitable for the generic SGP framework. In Section 4, we briefly sketch the alternating directions approach and finally in Section 5 the whole algorithm is applied to the design of a multi-material gripper, realizable by additive manufacturing technologies.

2. SEQUENTIAL GLOBAL PROGRAMMING

In this section, we recall the idea of the SGP method; for details and convergence analysis we refer to [12].

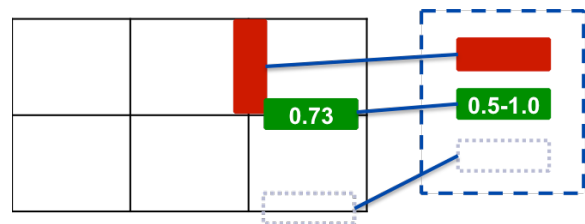


Figure 1: On the left, the design space consisting of a finite number of design elements is displayed. In the general SGP framework, design cells can be, e.g., FE cells in a finite element discretization, or edge elements in a network. In this article, design elements will be potential beams in a given ground structure which is described by a graph. The right side shows the catalogue of admissible materials.

In a combined multi-material and topology optimization setting, the following questions have to be answered for each position X in the design space: “should material be

placed at position X in the design space?” and, in case the answer is yes, “which material Y should be assigned from a catalogue of admissible materials for optimal performance?”. If in addition sizing is allowed for some of the components in the material catalogue, additionally the question arises: “how should material Y at position X be sized”? In an abstract setting, all these questions can be posed in form of an assignment problem. Fig. 1 illustrates this for the case of two different materials where one material (green) is configurable w.r.t. size. Moreover, an artificial “void material” is introduced to cover also the topological decision. In the following a mathematical structure is suggested, which allows to address all these questions concurrently. While classical DMO methods typically work with the convex hull of all catalogue materials, in [12] a more flexible model, based on a graph structure, is suggested. The advantage of the latter is that complex disjunctive constraints can be modeled in a more straightforward way; for a comparison of both models as well as an example, see Fig. 2.

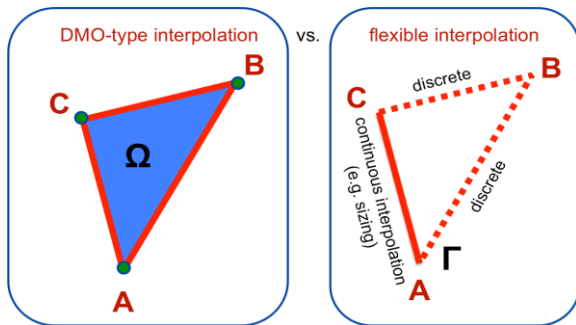


Figure 2: On the left side, the typical DMO interpolation in material space is depicted. Given are materials A , B and C . For the DMO model, a relaxation in the domain Ω are declared feasible; to compensate undesired intermediate materials in the solution (i.e. strict convex combinations of A , B and C) a penalization scheme is used. On the right hand side, a graph-based parameterization is suggested. The SGP algorithm only works with materials on the line connections between A , B and C . Moreover, different interpolation schemes can be applied to the individual edges. For instance, the interpolation between A and C can be given in terms of a sizing variable, while interpolations along the dotted edges can realize a relaxation, which allows the SGP algorithm to move from A to B or B to C throughout the optimization process. Consequently, intermediate values have to be penalized only on edges $[AB]$ and $[BC]$. In both settings, a topological decision can be easily approximated in this framework by modeling A , B or C as a void material (i.e. the stiffness is almost zero).

To formalize this idea, we introduce a parameter space

$$\mathfrak{X} = (\mathfrak{X})^m \quad (1)$$

where m denotes the number of design elements, and \mathfrak{X} consists of tuples $t = (\ell, \alpha) \in \mathbb{N} \times [0; 1]$ with ℓ denoting the index of the edge in the parameterization and α the interpolation parameter; note that the normalization to the parameter interval $[0; 1]$ can be done without loss of generality. Along with the set \mathfrak{X} we introduce so called parameter-to-material functions $C: \mathfrak{X} \rightarrow \mathbb{R}^{d \times d}$ mapping the parameter tuples $t = (\ell, \alpha)$ to a material tensor; we note that the dimension d depends on the particular application (e.g. $d = 6$ for 3D elasticity and $d = 1$ for a truss setting). Moreover, through the dependence of C on the edge index ℓ this formalism allows to prescribe different interpolation laws for the individual edges. Having this, we introduce the overall parameter vector $\mathbf{t} = (t_1, t_2, \dots, t_m) \in \mathfrak{X}$ collecting design parameters for all design elements as well as the overall material vector

$$\mathbf{C}(\mathbf{t}) = (C(t_1), C(t_2), \dots, C(t_m)) \in (\mathbb{R}^{d \times d})^m.$$

We note that in slight abuse of its strict definition, we have used the word ‘vector’ for arrays of tuples and matrices, respectively.

In the following we assume that the physics of our design problem is described by an abstract state problem of the form

$$\mathbf{K}(\mathbf{C}(\mathbf{t}))\mathbf{u} = \mathbf{f}, \quad (2)$$

with n denoting the degrees of freedom of the underlying physical system, $\mathbf{f} \in \mathbb{R}^n$ the right hand side vector (typically containing loads) and the solution vector $\mathbf{u} \in \mathbb{R}^n$. Further, the so called stiffness matrix \mathbf{K} is composed as

$$\mathbf{K}(\mathbf{C}(\mathbf{t})) = \sum_{i=1}^m B_i C(t_i) B_i^T \quad (3)$$

where the matrices $B_i \in \mathbb{R}^{n \times d}$, $i = 1, 2, \dots, m$, typically contain geometric information. To give some examples, in a 3D linear elasticity problem, each matrix B_i would be a strain-to-displacement matrix evaluated at an integration point while in a truss topology design framework B_i would encode the connectivity of the i -th rod in the ground structure as well as its nodal position. In Section 3 we will further concretize formulae (2) and (3) in the case of linear elastic Timoshenko beams using analytical network solutions. For the moment we stick to the abstract setting and just keep in mind that the design vector \mathbf{t} encodes all material, topology and sizing decisions in an appropriate way. To complete the statement of our abstract design problem, a cost function $\mathbf{J}: \mathbb{R}^n \rightarrow \mathbb{R}$ is introduced. We assume that \mathbf{J} depends on the material vector \mathbf{C} only indirectly through the state vector \mathbf{u} . Now, the abstract design problem takes the form

$$\min_{\mathbf{t} \in \mathfrak{X}} \mathbf{J}(\mathbf{u}(\mathbf{C}(\mathbf{t}))) + \mathbf{G}(\mathbf{t}) + \mathbf{V}(\mathbf{t}). \quad (4)$$

Here, by $\mathbf{u}(\mathbf{C}(\mathbf{t}))$ we denote a solution to the state problem (2) for the given design $\mathbf{t} \in \mathfrak{X}$. The function \mathbf{G} is an optional term which can be used to penalize undesired material choices along individual edges (cf. dotted edges in Fig. 2, right) and \mathbf{V} is a term (again optional) which is used to model the volume, weight or more generally the material consumption of the structure. Along with the cost function in (4) we further introduce the reduced cost function

$$\bar{\mathbf{J}}(\mathbf{C}(\mathbf{t})) = \mathbf{J}(\mathbf{u}(\mathbf{C}(\mathbf{t}))).$$

Now in addition to the somewhat extraordinary definition of the feasible set \mathfrak{X} there is a second important ingredient of the SGP recipe. First, problem (4) is substituted by a sequence of optimization problems (indexed by k) in which the reduced cost function $\bar{\mathbf{J}}$ is approximated by computationally significantly cheaper models \mathbf{J}^k , $k = 1, 2, \dots$. While this is a rather conventional idea, which is known from classical optimization algorithms like SQP [17,18] or the MMA [19] method, the way the model \mathbf{J}^k is established in this article differs. While in the classical approaches, first and/ or second order models are directly based on the derivatives of the cost functions w.r.t. the design variables, here the cost function is formulated in the material variable \mathbf{C} and thus also the models \mathbf{J}^k , $k = 1, 2, \dots$ are based on derivatives w.r.t. material variables $(C_1, C_2, \dots, C_m) \subseteq (\mathbb{R}^{d \times d})^m$. This idea was for the first time described in [20] in the context of the free material optimization approach. Instead of giving the precise formula (see [12] for this), here we just describe the most important properties of the model \mathbf{J}^k :

- a) \mathbf{J}^k is a local *first order approximation* of $\bar{\mathbf{J}}$, i.e. the function values as well as all partial derivatives of both functions coincide in the current iterate $\mathbf{C}^k = \mathbf{C}(\mathbf{t}^k)$.
- b) \mathbf{J}^k is a *block separable* function, i.e. \mathbf{J}^k can be written as $\mathbf{J}^k(\mathbf{C}) = \sum_{i=1}^m J_i^k(C_i)$.

Using this, the sub-problem in iteration k becomes:

$$\min_{\mathbf{t} \in \mathfrak{X}} \mathbf{J}^k(\mathbf{C}(\mathbf{t})) + \mathbf{G}(\mathbf{t}) + \mathbf{V}(\mathbf{t}). \quad (5)$$

Next, we exploit property b). Before we do so, we note that for the functions \mathbf{G} and \mathbf{V} it is only natural to assume that these functions can be written separably in terms of the design variables (t_1, t_2, \dots, t_m) , i.e.

$$\mathbf{G}(\mathbf{t}) = \sum_{i=1}^m G_i(t_i) \quad \text{and} \quad \mathbf{V}(\mathbf{t}) = \sum_{i=1}^m V_i(t_i).$$

To again give examples, recall that $t_i = (\ell, \alpha)$. Then, in the simplest case $G_i(\ell, \alpha) = \gamma\alpha(1 - \alpha)$, with a penalty parameter $\gamma > 0$ if ℓ corresponds to an edge on which intermediate values are penalized and $\gamma = 0$ if this is not the case. Analogously the material consumption $V_i(\ell, \alpha)$ can be defined edge-wise through the dependence on ℓ for each design element. With this, the objective function in

(5) is block separable w.r.t. \mathbf{t} and thus the optimization task formulated in (5) can be solved equivalently by the solution of m individual problems of the type:

$$\min_{t_i \in \mathfrak{X}} J_i^k(C(t_i)) + G_i(t_i) + V_i(t_i). \quad (6)$$

Finally, we can get rid of the dependency on the discrete edge parameter ℓ by solving each element problem (6) separately for each edge of the material graph and then accepting the winner as element solution. Each such edge problem can be posed directly in the continuous interpolation variable α :

$$\min_{\alpha \in [0;1]} J_i^k(C(\ell, \alpha)) + G_i(\ell, \alpha) + V_i(\ell, \alpha). \quad (7)$$

Problem (7) is a continuously differentiable univariate optimization problem. However, either of the terms in its objective can depend on the interpolation variable α in a non-convex way. It belongs to the strategy of the SGP method to solve each of the problems (7) to global optimality. This can be done often in a fully analytical way (see [12]) or based on a simple univariate multigrid strategy, which is used for the examples presented in this article. It is important to understand that either of the described procedures provides a globally optimal solution to the model problem (5) in each iteration k . This does not imply that in general globally optimal solutions for the original problem (4) can be computed by the SGP algorithm, but our experience shows that poor local solutions can be avoided to a large extent. The SGP algorithm is completed by a globalization strategy, which is again described in detail in [12] and is inspired by [21]. The simple idea is that the solution of each sub-problem (5) is used as a new trial point for (4). If no sufficient decrease is obtained, a more conservative sub-problem is formulated and solved. This process is repeated until either sufficient decrease is achieved or convergence to a stationary point is obtained; see again [12] for a convergence proof under rather mild assumptions.

3. TIMOSHENKO BEAM NETWORKS IN THE FRAMEWORK OF THE SGP METHOD

In this article, the SGP method outlined in Section 2 shall be applied to the concurrent topology, material and sizing optimization of a Timoshenko beam network, in other words, a frame structure built of linear elastic and straight Timoshenko beams. For the precise definition of the individual beam equations, the continuity conditions on the network as well as the derivation of fully analytic network solutions the interested reader is referred to [16] and the references therein. Here we just stress that the analytic network solutions are numerically accessible through the implementation of so-called analytical shape functions for the beam elements, which are similar to those in [22]. We directly start from the (still exact) algebraic reformulation of the beam network problem in

[16], which is slightly adapted to the notation of this article. We start with the definition of the condensed local stiffness matrix K^{loc} of a beam element formulated in the local coordinate system of the considered beam. We assume that the local degrees of freedom for the considered individual beam are sorted as follows:

$$(u_x^1, u_y^1, u_z^1, \theta_x^1, \theta_y^1, \theta_z^1, u_x^2, u_y^2, u_z^2, \theta_x^2, \theta_y^2, \theta_z^2).$$

Here u and θ refer to the translational and rotational degrees of freedom, respectively. The lower index indicates along or around which local axis the beam is displaced and the upper index specifies if the start or end node of the beam is displaced by the considered entry. We further require a rotation matrix $T \in \mathbb{R}^{12 \times 12}$ which is built as a block diagonal matrix consisting of identical blocks $T_{block} = [e_x, e_y, e_z] \in \mathbb{R}^{3 \times 3}$, where e_x is a normalized vector aligned with the centerline axis of the beam and e_y, e_z are chosen such that T_{block} forms an orthonormal matrix. By T_j in the following we denote the j -th column of T . Moreover we denote by E, k, G the elastic modulus, shear correction factor and shear modulus of the beam, by l its length, and by A, I_y, I_z, I_t its cross sectional area as well as its second moments of inertia, respectively. We note that A, I_y, I_z, I_t depend on the shape of the cross section of the beam and are functions of sizing variables. In Section 5 we will consider beams with a rectangular cross section of fixed width w such that A, I_y, I_z, I_t are described by analytic univariate functions of the height h of the beam. Now, starting from the formulae in [16] the stiffness matrix K^{loc} can be decomposed into the following sum:

$$K^{loc} = K^1 + K^2 + K^3 + K^4 + K^5 + K^6 + K^7 + K^8$$

with $K^j = c^j M^j, j = 1, 2, \dots, 8$ and

$$c^1 = EA/l, \quad c^2 = GI_t/l$$

as well as

$$c^3 = \frac{12EI_y GkA}{12EI_y l + GkAl^3}, \quad c^4 = \frac{E^2 I_y^2}{12EI_y l + GkAl^3}, \quad c^5 = \frac{2EI_y GkAl}{12EI_y + GkAl^2}.$$

Further, c^6, c^7, c^8 are fully analogous to c^3, c^4, c^5 just using I_z instead of I_y , at all occurrences. Finally the matrices M^1, M^2, \dots, M^8 are symmetric and built from the columns of the transformation matrix T . Exemplarily we only show the formula for the first matrix here, which is

$$M^1 = (T_1 - T_7)(T_1 - T_7)^T.$$

Having this, we can rearrange the local stiffness matrix in the following form:

$$K^{loc} = M \text{diag}(c^1, c^2, \dots, c^8) M^T.$$

Here M is composed from the matrices M^1, M^2, \dots, M^8 and the operator ‘diag’ creates a diagonal matrix from c^1, c^2, \dots, c^8 in a straightforward way. Finally, introducing for each beam i a matrix P_i , which maps local

degrees of freedom into global ones and removes degrees of freedom in which Dirichlet conditions are applied, the formula for the global stiffness matrix can be written as:

$$\mathbf{K}(c^1, c^2, \dots, c^8) = \sum_{i=1}^m P_i M_i \text{diag}(c^1, c^2, \dots, c^8) (P_i M_i)^T.$$

This is already almost the form of (3) in Chapter 2, if we define $B_i = P_i M_i, i=1, 2, \dots, m$. The only thing which remains to be done is to write the material matrix $\text{diag}(c^1, c^2, \dots, c^8)$ using the graph structure defined for the SGP model in Chapter 2. We do this directly for the parameterization, which will be utilized in Chapter 5. There, we want to design a gripper made of a weak and a strong polymer. Moreover, a void material is introduced, which is used to remove beams from the ground structure. Finally, if the strong or the weak material is chosen, the beam can be further configured by adjusting the height variable in given bounds. To describe this in mathematical terms, we define a linear graph with 5 nodes (void material V , weak material at lower sizing bound W_l , weak material at upper sizing bound W_u , strong material at lower sizing bound S_l , strong material at upper sizing bound S_u) and 4 edges; for the interpolation properties applied at the individual edges, we refer to Fig. 3.



Figure 3: A linear graph is used for the parameterization of each beam in the network. Dotted lines indicate that a linear interpolation between the material matrices associated with the associated nodes is used. A solid line indicates that the interpolation is realized by writing A, I_y, I_z, I_t as functions of the height variable and inserting these functions into the expressions c^1, c^2, \dots, c^8 using the material parameters E, k, G for the weak (second edge) or the strong material (fourth edge), respectively. Below edges are labeled by $\ell = 1, 2, 3, 4$ from left to right.

Using this parameterization we can now easily define the material function $C(t)$ in terms of the graph variables (ℓ, α) . We finally have to specify the functions $V_i(t)$ and $G_i(t)$ for the case of the Timoshenko beams. Both types of functions have to be defined edge wise: we let $G_i(\ell, \alpha) = \gamma\alpha(1 - \alpha)$ with $\gamma > 0$ for $\ell = 1, 3$ and $G_i(\ell, \alpha) = 0$ for $\ell = 2, 4$; moreover the term $V_i(\ell, \alpha)$, which corresponds to the volume of beam i , linearly interpolates the volume of V and W_l or W_u and S_l on edges 1 and 3, respectively. On edges 2 and 4 it is computed as product of the cross sectional area A (depending on α) and length l of the beam. We finally note that the volume of the void material is simply set to 0. By this we are now ready to write the beam network design problem in the form of (4).

4. AN ALTERNATING DIRECTIONS APPROACH

In order to increase the design flexibility and thus to fully exploit the design possibilities provided by AM we

want to be able to incorporate the positions of the network nodes (see, e.g., Fig. 4) as optimization variables into our design model. As optimization of nodal positions does not fit very well into the separable element oriented construction of the SGP method (cf. Section 2), we come up with an alternative solution. We define a kind of alternating direction approach in which the following alternating steps are iteratively applied: we first fix the positional variables and solve the resulting optimization problem by the specialized SGP approach outlined in Sections 2 and 3. Then we fix the topological and material decision and solve the resulting problem in sizing and positional variables; we refer to this problem as geometry optimization problem in the sequel. We explicitly keep the sizing variables in both problems, which typically results in faster convergence. As no combinatorial decisions have to be made in the geometry optimization problem, we can solve this by the SQP solver SNOPT [18] in a straightforward manner. It is noted that the objective function as well as the constraints are formulated in a fully consistent way for both, the topology/sizing and material optimization as well as the geometry optimization problem. As a consequence, a monotonically decreasing sequence of feasible solutions for the full design problem is obtained. Finally the fact that the sizing variables occur in either of the two design problems solved in each iteration of the alternating directions approach, convergence is typically obtained in very few steps. In particular, the method stops immediately, as soon as no combinatorial decision (i.e. material assignment) is modified in the SGP based problem.

5. NUMERICAL EXPERIMENTS AND RESULTS

Throughout this section we want to apply the alternating direction method outlined in Section 4 to the design of a gripper. We set up the graph parameterization for the SGP sub-problem as suggested in Section 3 with a void material, a weak polymer as well as a strong material. For the strong material we apply the material properties of PA12, while the weak material is chosen to be 8 times weaker than the strong one. Moreover, the height variables are constrained to be between 1 and 1.5 mm for each beam in the ground structure. In the concurrent geometry and sizing optimization, the same bounds for the sizing variables apply. The width in z-direction is fixed to 10 mm. Moreover node 1, 2, ..., 6 as well as 8, 9, 10 (see Fig. 4) are allowed to move in x- and y-direction by 2 mm, node 7 is allowed to move only vertically (i.e. in y-direction) and node 14 is allowed to move only horizontally (i.e. in x-direction) throughout optimization. Nodes 11, 12, 15 and 16 are completely fixed during optimization as they form the contact surface of the gripper, which should stay in its original position; also the loaded node 13 stays fixed. It is further noted that due to a lying position in the build chamber, the design is

self-supporting independent of the particular choice of the design variables. Moreover, the smallest feature size constraints for the individual materials are realized by the lower sizing bounds. For the definition of the boundary conditions applied to the state problem, we refer to Fig. 4. Finally the objective J is defined as the negative sum of the vertical displacements at nodes 11 and 12.

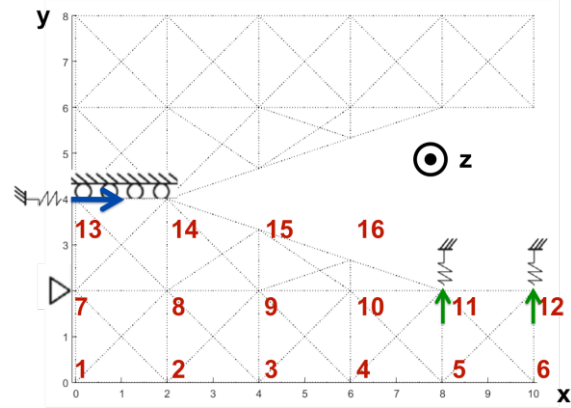


Figure 4: The ground structure is depicted in the x-y-plane (top view on the build chamber). The ground structure has a size of 10 cm in horizontal and 8 cm in vertical direction. In z-direction (build direction; out of plane) all beam elements have a constant size of 1 cm. The red numbers are the node indices. For symmetry reasons only half of the ground structure enters the computational model; thus a symmetry condition is applied at nodes 13 and 14. Moreover a homogeneous Dirichlet conditions is applied to node 7 and a horizontal force acts at the input node 13. Output nodes are nodes 11 and 12, for which the vertical displacement should be maximized. Springs are attached to input and output nodes. The spring at the input node approximates an inhomogeneous Dirichlet condition (the spring constant is chosen such that node 13 is moving 1 mm in horizontal direction when loaded). The springs at the output nodes are an indirect means to control forces at the contact surface when the gripper is catching an object.

Having completed the description of the mechanical setup we now turn to the results. We first started the SGP algorithm in Section 2 from 10.000 randomly generated initial designs. The total computation time was below 1h on a standard Linux workstation with 8 cores running Matlab 2018a. This clearly shows the advantage of the analytic network solutions provided. For the 10 best results we carried out the alternate direction algorithm described in Section 4. In the following, we discuss the results of 2 of these cases in detail; for the other cases it is just noted that the alternate direction method converged without problems. The two cases discussed in more detail have been selected as the results provide a good compromise between used material and amplification of the displacement from the input to the output nodes. In

both cases, no topological/ material changes were performed anymore by the SGP method after the first full SQP run, i.e. the SGP method applied for the concurrent optimization of topology, material choice and sizing variables as well as the SQP method for the concurrent determination of the nodal positions and the sizing variables were executed only once. To be more precise, the SGP algorithm was started for a second round, however it stopped directly accepting the current iterate as an optimal solution, i.e. the alternating directions algorithm converged after just one iteration. The total run time in either of the cases was in the range of a few seconds and is thus not documented in more detail. More interesting is the performance of the two structures. After the first SGP step, structure 1 (with output springs in place) provides an amplification of 9, i.e. the average displacement at the two output nodes is higher than the input displacement by a factor of 9. After the SQP step, which allows to move also the nodal positions the amplification increases to 17.2. Without the output springs (which corresponds to a free movement) the amplification factor is almost 30. The final design is depicted in Fig. 5 in an open, closed and unloaded state. Similar results are obtained for structure 2. After the first SGP step, the amplification factor is 7.8. This time the amplification factor is raised to 17.8 after the concurrent geometry and sizing optimization. On the other hand, the total volume of structure 2 is about 5.5% higher than that of structure 1. The final design is depicted in Fig. 6. To see both grippers in action, we performed several simulations for both optimized structures. The results are visualized in Fig. 7.

6. CONCLUSIONS

A new manufacturing aware structural optimization method for the design of multi-material components has been presented. The efficiency of the method in terms of the chosen objective as well as CPU time was demonstrated by means of an example from the mechanism design field. The resulting design is accessible to additive manufacturing techniques.

In future the calculated design should be realized by an SLM process in the framework of the CRC 814. From computational perspective, a geometrically exact beam model may be employed for validation purposes or even in the optimization process.

ACKNOWLEDGEMENT

We gratefully acknowledge financial support by the German Research Foundation (DFG) within the Collaborative Research Centre 814: Additive Manufacturing (subproject C2).

- [1] Bendsoe MP and Sigmund O., 2003, *Topology Optimization - Theory, Methods, and Applications*, Springer, Berlin Heidelberg.
- [2] W. Christensen, P. and Klarbring, S., 2008, *An Introduction to Structural Optimization*, Springer, Berlin Heidelberg.
- [3] Haslinger, J. and Makinen, R. A. E., 2003, *Introduction to Shape Optimization: Theory, Approximation, and Computation*, Soc. for Industrial and Applied Math., Philadelphia, PA, USA.
- [4] Bandyopadhyay, A. and Heer, B., 2018, 'Additive manufacturing of multi-material structures', *Materials Science and Engineering: R: Reports*, vol. 129, pp. 1-16.
- [5] Langelaar, M., 2016, 'Topology optimization of 3D self-supporting structures for additive manufacturing', *Additive Manufacturing*, vol. 12, part A, pp. 60-70.
- [6] Sigmund, O., 1997, 'On the design of compliant mechanisms using topology optimization'. *Journal of Structural Mechanics*, vol. 25, no. 4, pp. 493-524.
- [7] Wang, F., Lazarov, B.S. and Sigmund, O., 2011, 'On projection methods, convergence and robust formulations in topology optimization', *Struct. Multidiscip. Optim.*, vol. 43, pp. 767-784.
- [8] Gaynor, A., Meisel, N., Williams, C. and Guest, J., 2014, 'Multiple-Material Topology Optimization of Compliant Mechanisms Created Via PolyJet Three-Dimensional Printing', *Journal of Manufacturing Science and Engineering*, vol. 136, pp. 061015-1 – 061015-10.
- [9] Dorn, S., Gomory, R.E. and Greenberg, H.J., 1964, 'Automatic design of optimal structures', *Journal de Mecanique*, vol. 3, no. 1, pp. 25-52.
- [10] Torstenfelt, B. and Klarbring, A., 2006, 'Structural optimization of modular product families with application to car space frame structures', *Struct. Multidiscip. Optim.*, vol. 32, no. 2, pp. 133-140.
- [11] Torstenfelt, B. and Klarbring, A., 2007, 'Conceptual optimal design of modular car product families using simultaneous size, shape and topology optimization', *Finite Elements in Analysis and Design*, vol. 43, no. 14, pp. 1050-1061.
- [12] Semmler, J., Pflug, L. and Stingl, M., 2018, 'Material Optimization in Transverse Electromagnetic Scattering Applications', *SIAM Journal on Scientific Computing*, vol. 40, no. 1, pp. B85-B109.
- [13] Hvejsel, C. F. and Lund, E., 2011, 'Material interpolation schemes for unified topology and multimaterial optimization', *Struct. Multidiscip. Optim.*, vol. 43, pp. 811-825.
- [14] Stegmann, J. and Lund, E., 2009, 'Discrete material optimization of general composite shell structures', *Internat. J. Numer. Methods Engrg.*, vol. 62, pp. 2009-2027.
- [15] Hvejsel, C., Lund, E. and Stolpe, M., 2011, 'Optimization strategies for discrete multi-material stiffness optimization', *Struct. Multidiscip. Optim.*, vol. 44, pp. 149-163, 2011.
- [16] Kufner, T., Leugering, G., Semmler, J., Stingl, M., Strohmeier, C., 2018, 'Mathematical Modelling and Numerical Analysis', in review.
- [17] Nocedal, J. and Wright, S., 2006, *Numerical Optimization*, Springer, New York, NY, USA.
- [18] Gill, P. E., Murray, W., and Saunders, M. A., 2005, 'SNOPT: An SQP algorithm for large-scale constrained optimization'. *SIAM review*, vol. 47, no. 1, pp. 99-131.
- [19] Svanberg, K., 1987, 'The method of moving asymptotes-a new method for structural optimization', *Int. J. Numer. Methods Engrg.*, vol. 24, pp. 359-373.
- [20] Stingl, M. Kocvara, M. and Leugering, G., 2009., 'A Sequential Convex Semidefinite Programming Algorithm with an Application to Multiple-Load Free Material Optimization', *SIAM J. Optim.*, vol. 20, pp. 130-155.
- [21] Svanberg, K., 2002, 'A class of globally convergent optimization methods based on conservative convex separable approximations', *SIAM Journ. on Optim.*, vol. 14, no. 2, pp. 555-573.
- [22] Luo, Y., 2008, An Efficient 3D Timoshenko Beam Element with Consistent Shape Functions. *Advances in Theoretical and Applied Mechanics*, 1(3), pp. 95-106. 2008.

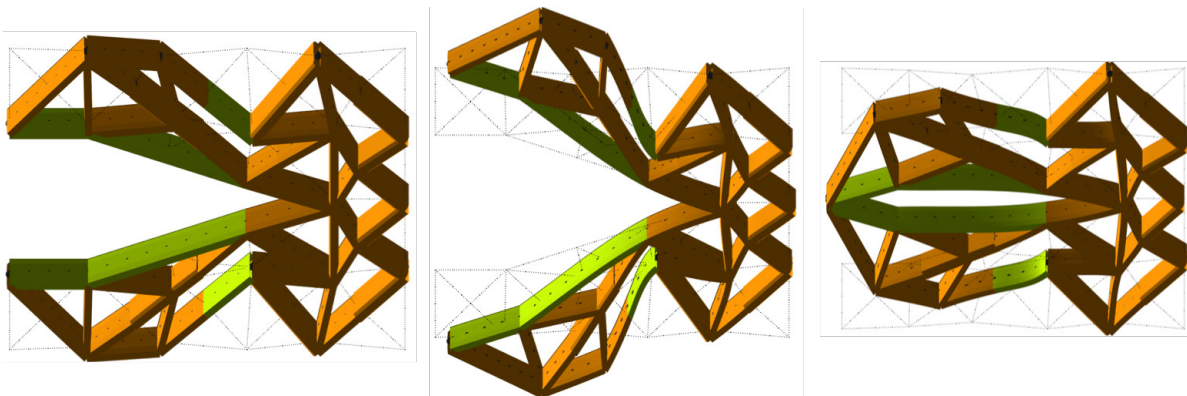


Figure 5: From left to right the optimal design of gripper 1 is depicted in states unloaded, open (i.e. the input force pulls to the right) and closed (input force pushes to the left). The green color indicates beams for which beams the weak material has been used. The dashed black lines in the background show the positions of nodes after geometry optimization.

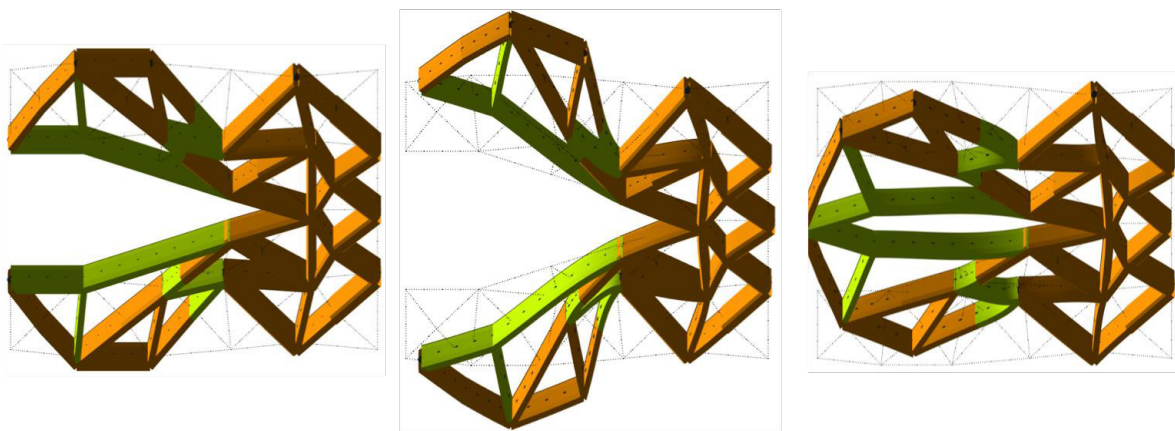


Figure 6: The optimal design of gripper 2 is displayed. Gripper 2 uses more weak material than gripper 1.

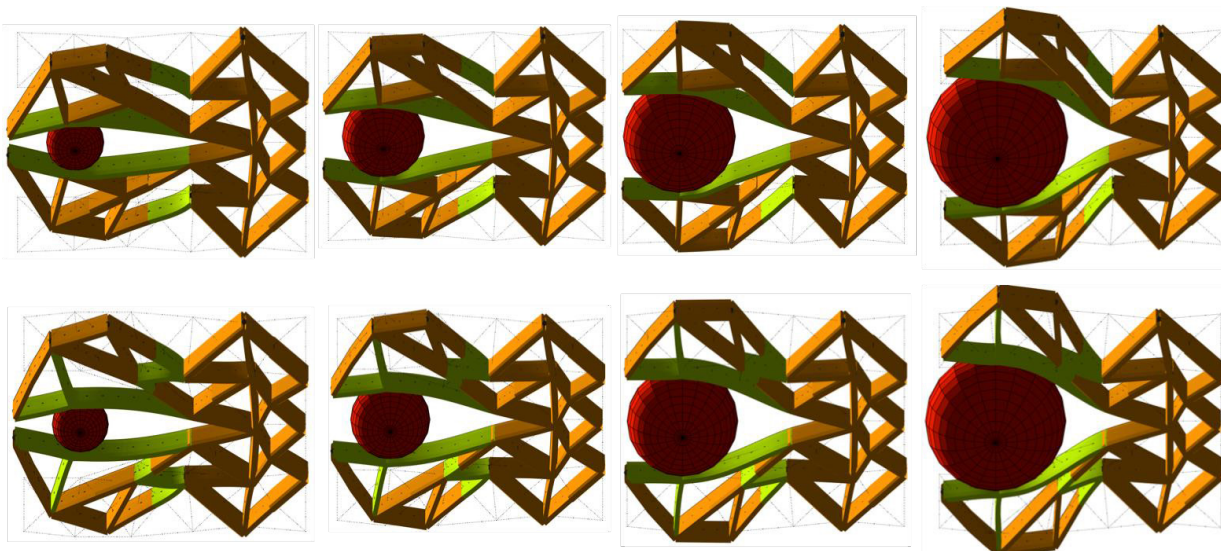


Figure 7: Several contact problems have been solved for gripper 1 (top row) and gripper 2 (bottom row). From left to right both grippers are displayed holding a ball with diameters 2cm, 3cm, 4cm and 5cm.

The Examination of Photopolymer-based 3D Printed Products in the Case of Pinpoint Loading

Luca KOTROCZ, Department of Polymer Engineering, Budapest University of Technology and Economics, Budapest, Hungary, kotrocz.luca@gmail.com

Péter BAKONYI, Department of Polymer Engineering, Budapest University of Technology and Economics, Budapest, Hungary, bakonyi@pt.bme.hu

Abstract— We present a new mounting unit for Dynamic Mechanical Analysis (DMA) equipment, suitable for measuring microhardness and indentation, and its usability on photopolymers. We used a Vickers-type microhardness indenter, and examined the dimensions of the indented area and the loading force.

Keywords—photopolymer, pinpoint load, measurement of indentation, Vickers, DMA

1. INTRODUCTION

Nowadays polymers are more and more widely used in all facets of life. They can replace metals in numerous areas of use, due to their adequate strength, low density, good corrosion resistance and vibration damping ability, but their mechanical behaviour can be considerably different from that of metals. In the case of polymers it is not enough to examine quasi-static mechanical characteristics (tensile and flexural tests) because they react to long-term loading with continuously increasing deformation; this is called creeping. Therefore, it is an important rule for designers that they should design parts not for lifetime but maximal possible deformation. Creep is most widely determined with tensile and flexural tests, but torsion and compression loading is also used. The latter can be loading on area or a pinpoint load [1, 2].

As additive technologies develop, materials and procedures offer more possibilities to designers and users alike. A great advantage of products manufactured this way is that their weight can be easily adjusted with the degree of filling and the product can have almost any geometry. Polymer-based 3D printed products are not only prototypes nowadays but are also used as functional products (e.g. dental implants), therefore it is important that as many technical parameters of these materials are revealed as possible so that their areas of use can be accurately determined [3, 4].

The hardness of materials is an important characteristic that helps designers select the right material. It is defined

as the resistance of a solid material to penetration by a body. Pinpoint compression loading can be examined very well with a hardness test. Depth-sensitive (dynamic) hardness testing (depth sensing indentation – DSI) was developed while the advantages of hardness testing (simplicity, little use of material) retained. This test can characterize mechanical properties dynamically. During this process the measuring body is pushed into the surface at constant speed or with constant force, and then removed. The impression depends on the properties of the material and the geometry of the indenter, and various characteristics can be determined from it, such as dynamic hardness, conventional hardness, modulus of elasticity, and elastoplastic mechanical properties. The geometry of the impression depends on the depth of indentation, which in turn depends on the loading force, and the time of loading, and of course, environmental parameters, such as humidity and temperature [3].

The advantage of depth sensing indentation is that measurements can be made in the millimetre, micrometre and nanometre range as well. This facilitates the testing of various thin films, or new materials produced by nanotechnology (e.g. nanocomposites), even with very little loading forces (in the case of nanohardness testing, it can be 0.01 mN). This procedure may be suitable for the testing of outer, even coated layer of 3D printed polymer-based products. A disadvantage is that the measurement results are always local, and can be very different. Also, there are two important phenomena to be mentioned. Next to the indenter, at the side of the indented area, the surface can sink (sinking-in), or can be raised because material is pushed out (pilling-up), and these can cause inaccuracies (Fig. 1). For this reason, several tests have to be performed for accurate results [2].

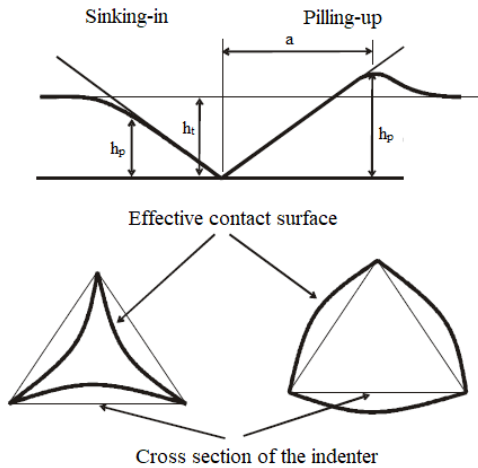


Figure 1. Sinking-in and pilling-up [2]

According to the literature we analysed, [6-8] this procedure, combined with creep tests, is used successful on polymer materials. The geometries of the indenters are the same as used in the case of static hardness tests, but mostly the Vickers and Berkovich types are used. Usually, finite element analysis is performed as well, to support the measurement results.

The literature [6-8] shows that although this method is spreading, tests are performed almost exclusively at room temperature. Objects used in everyday life are exposed to different temperatures and humidity; therefore we decided that tests should be performed in a wide range of temperatures. In order to provide the small loading forces and constant temperature required for the test, we designed a mounting unit suitable for pinpoint loading for a dynamic mechanical analyser (DMA), with which short, long and also cyclical tests can be performed.

2. THE TESTS

2.1. The mounting unit designed

We designed the mounting unit for a TA Instruments (USA) Q800 device. The analyser can perform various tests (tensile, compression, flexural and shear tests) in a wide temperature range (-145 to +600 °C). It has a frequency range of 0.01 Hz to 200 Hz, and the maximum load is 18 N. The device can determine the mechanical and viscoelastic properties of various materials. Both constant and periodic loading can be applied [9].

We designed the mounting unit based on an existing fixture used for compression tests. We tested the two designs we liked best with finite element analysis to see what deformations occur. The two designs were the one where the indenter is fastened in the middle of the fixture, and the “horse race track” design (this allows the positioning of the indenter). Fig. 2 shows that in the case of the horse race track design, in an extreme position, at a load of 18 N, the frame deforms as well, which can destroy the air bearing of the DMA and the mounting unit itself,

especially if deformation resulting from temperature change is also taken into account. Therefore, we selected as the final design the centrally positioned, gripped indenter design.

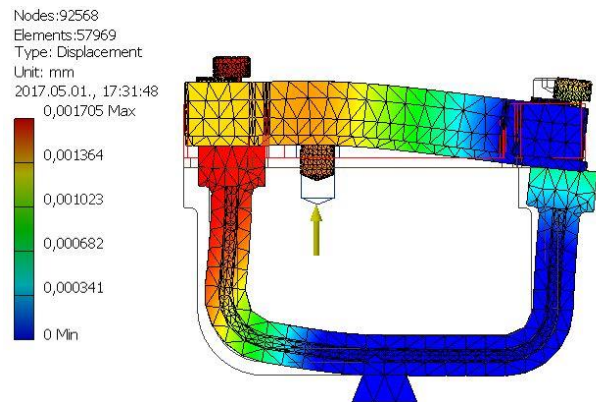


Figure 2. The finite element simulation results of the horse race track in an extreme position

We made the sample holder so that the sample can be positioned. This makes it possible to perform several measurements on a single sample. Thanks to the vice design, the specimen can be tightly gripped and so it does not move during the test. The final design can be seen in Fig. 3.

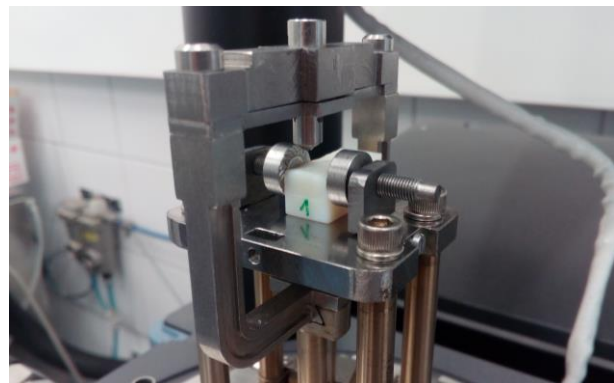


Figure 3. The fixture we designed and the gripped photopolymer specimen

2.2. The test program and the investigated materials

We tested two different kinds of photopolymers in the trial tests: RGD720 (FullCure 720) and RGD835 (Vero White Plus). The dimensions of the specimens were 10 mm x 20 mm x 9 mm. We performed the test on the 10 mm x 20 mm untreated (unpolished) surface, the top layer according to build direction. In the first stage, we increased loading force (F [N]) by 0.5 N in each step to 4 N, then in the second stage we used steps of 1 N and went up to 10 N, and finally we went all the way up to 18 N in steps of 2 N. We repeated all individual steps three times. This way we covered the force range of the DMA. In the tests, we used a Vickers microhardness indenter, which is a

pyramid shape and is made of diamond. The geometry reduces dependence on loading force. The parameters measured on the negative mark of the indenter can be seen in Fig. 4, where a and b are the side length, d_1 and d_2 the diagonals and h the cone-height of the Vickers indenter.

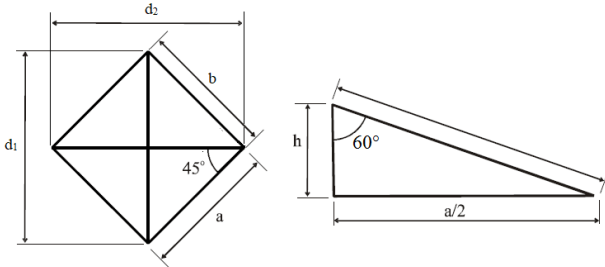


Figure 4. The impression of a Vickers indenter and its geometrical parameters [2]

The testing program consisted of the following steps: we heated the heat chamber to 35 °C, and then held this temperature for 3 minutes. Then we applied the loading force, which we held for 1 minute. After loading ceased, we analysed the indented area with an optical microscope (Olympus BX51M), and measured the diagonals of the indented areas (d_1 , d_2 [μm]).

2.3. Measurement results

As mentioned above, evaluation started with the microscopy examination of the indented areas. At a loading force of 0.5 N, the indented area could not be seen very clearly in the case of both materials. Above 1 N, however, the outlines of the rhombus-shaped indented area were clearly visible. We experienced pilling-up and sinking-in several times during the tests, these are shown by Fig 5.

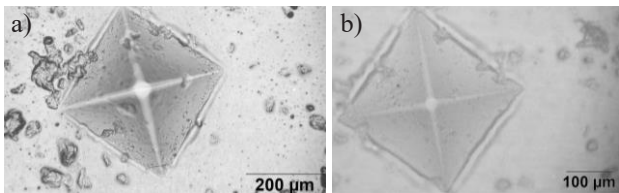


Figure 5. Pilling-up on the RGD720 (a) and sinking-in on the RGD835 material (b)

The microscopic images show (Fig. 6) that an increase in loading force enlarges the diagonals of the impression. The results show that the RGD810 material is softer; at the same load, the indenter left a larger impression on the surface of the specimen.

We examined whether the machine can push the indenter into the sample properly, perpendicularly to the surface. The diagonals of the impressions were averaged separately and displayed in one diagram (Fig 7.).

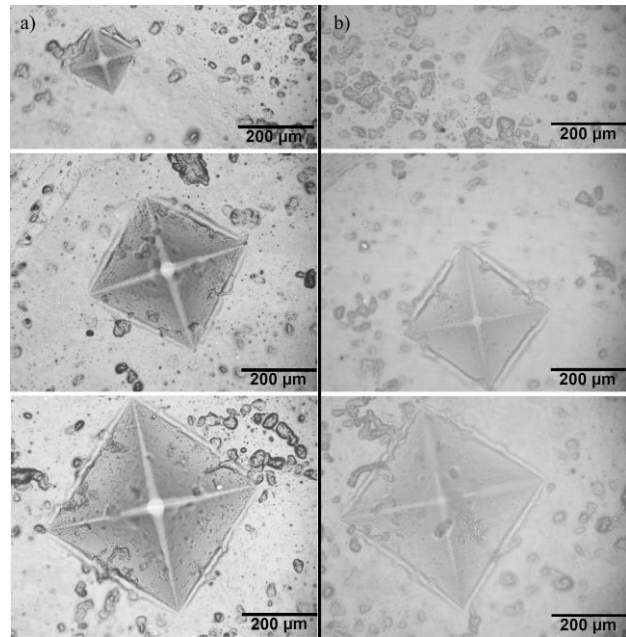


Figure 6. The impression on the RGD720 (a) and the RGD835 (b) materials at a loading force of 1 N (top), 6 N (middle) and 12 N (bottom)

It is visible that the points are on one line with little deviation. This proves that the impressions are symmetrical; therefore, the fixture can be used with indentation tests in a DMA. The largest standard deviation in the case of RGD720 is 18,595 μm , while in the case of RGD835, it is 13,218 μm .

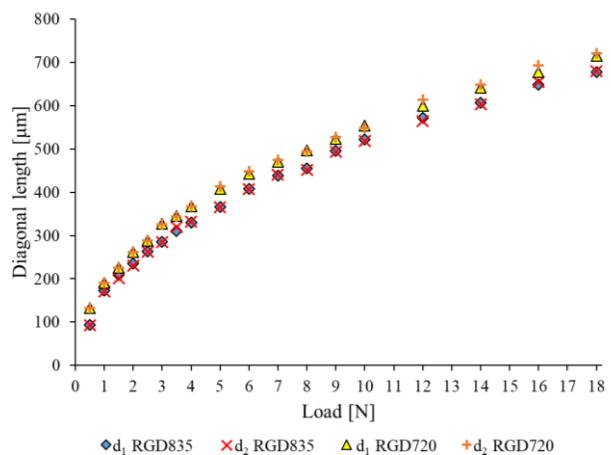


Figure 7. Comparison of the diagonals of impressions in both materials

As previously we proved that the impressions are symmetrical, the diagonals measured with a microscope can be averaged and the values can be displayed in a scatter plot as a function of loading force (Fig. 8). Also, if the diagonals are known, the projected area (A [μm^2]) of the pyramid created by the indenter can be calculated (1), and its change can be plotted as a function of the force (Figure 9).

$$A = \frac{d_1 \cdot d_2}{2} [\mu\text{m}^2] \tag{1}$$

In the case of both diagrams, we fitted a function of the same equation (2) on the points, which produced the highest determination coefficient (R^2). Its coefficients (a , b , c) can be determined with the method of least squares with the help of the measured series of points (Table 1).

$$f(x) = a \cdot (1 - e^{-b \cdot x}) + c \cdot x \tag{2}$$

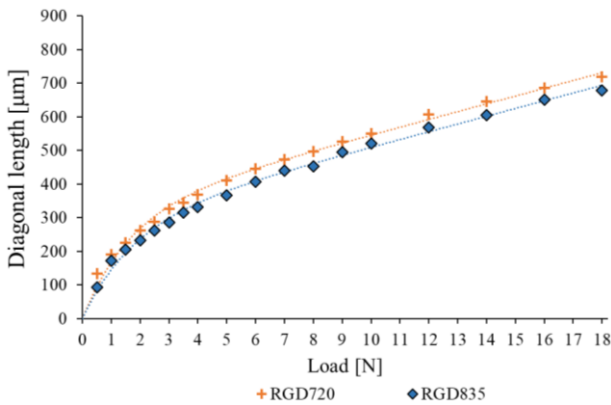


Figure 8. Average diagonals as a function of loading force

TABLE 1. THE COEFFICIENTS OF THE FITTED FUNCTION FOR THE DIAGONAL – FORCE (A) AND THE PROJECTED AREA – FORCE (B) CURVES

		a [μm]	b [$\frac{1}{N}$]	c [$\frac{\mu\text{m}}{N}$]	R ² [-]
A	RGD720	314,74	0,61	23,131	0,994
	RGD835	280	0,57	22,983	0,995
		a [μm ²]	b [$\frac{1}{N}$]	c [$\frac{\mu\text{m}^2}{N}$]	R ² [-]
B	RGD720	13848	0,45	13792	0,999
	RGD835	4504	0,42	12818	0,998

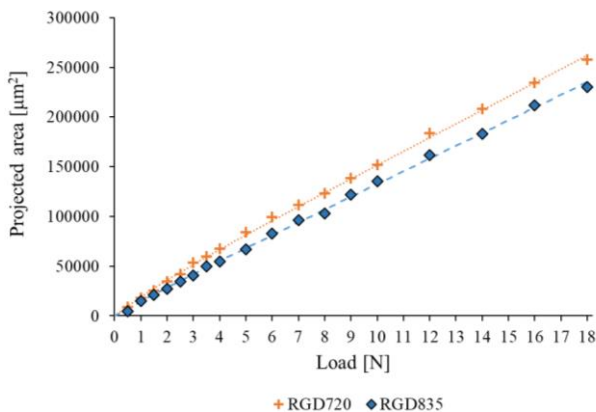


Figure 9. Projected area as a function of loading force

The function can be used well in the case of small forces too. It can be seen that the average diagonal–loading force curve has an initial power-like character, then after 7 N it

increases nearly linearly. This is less visible on the projected area curve but when enlarged (Fig. 10), it shows that the linear character starts after 3 N.

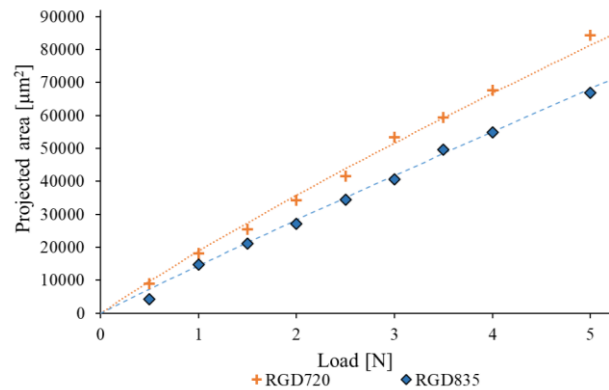


Figure 10. The projected area as a function of loading force, enlarged

CONCLUSIONS

The tests showed that the fixture we designed is suitable for depth sensing indentation tests with DMA equipment. This method can be used for the mechanical testing of the surface of prototypes or even finished products. This procedure can have an especially important role in materials development and in coating development, as important technological parameters can be determined in the case of thin layers, too. The method can also provide accurate information about the mechanical properties of the outer layer.

Thanks to the DMA equipment, the procedure can be used not only for static tests but also dynamic or even cyclic tests. In addition, tests can be performed in a wide range of temperatures.

In the case of longer tests, creep has to be expected, which is characteristic to polymers. In smaller sizes, creep can be more pronounced; therefore more detailed tests could be done in connection with this.

In the future the same series of tests as we did could be performed on specimens with a polished surface, and it could be examined whether any surface hardening occurs due to polishing, and also, what is the influence of the disappearance of surface defects.

ACKNOWLEDGEMENT

The project is funded by the National Research, Development and Innovation (NKFIH) Fund, Project title: "Developing a new generation of customized medical implants and medical aids for additive technologies"; The application ID number: NVKP_16-1-2016-0022. The developers are grateful for the support.

REFERENCES

[1] Urzumtsev J. S. and Maksimov R. D., 1982, *Deformation of plastics. Prognostics on the basis of*

similarity principles (in Hungarian), Műszaki Könyvkiadó, Budapest

[2] Nagy P. M., 2007, *Investigation of block and surface mechanical properties of structural polymers by indentation measurement technologies (in Hungarian)*, PhD-Theses, Eötvös Lóránd University, Budapest

[3] Gebhardt A., 2011, *Understanding additive manufacturing*, Hanser, Munich

[4] Gibson I., Rosen D. and Stucker B., 2010, *Photopolymerization Processes in Additive Manufacturing Technologies*, Springer, London

[5] Gubicza J., 2018, *Measuring the dynamic nano- and mikrohardness (in Hungarian)*, Eötvös Lóránd University Science Books

[6] Wei P. J., Shen W. X. and Lin J. F., 2008, 'Analysis and modeling for time-dependent behavior of polymers exhibited in nanoindentation tests'. *Journal of Non-Crystalline Solids*, vol. 354, no. 33, pp. 3911–3918.

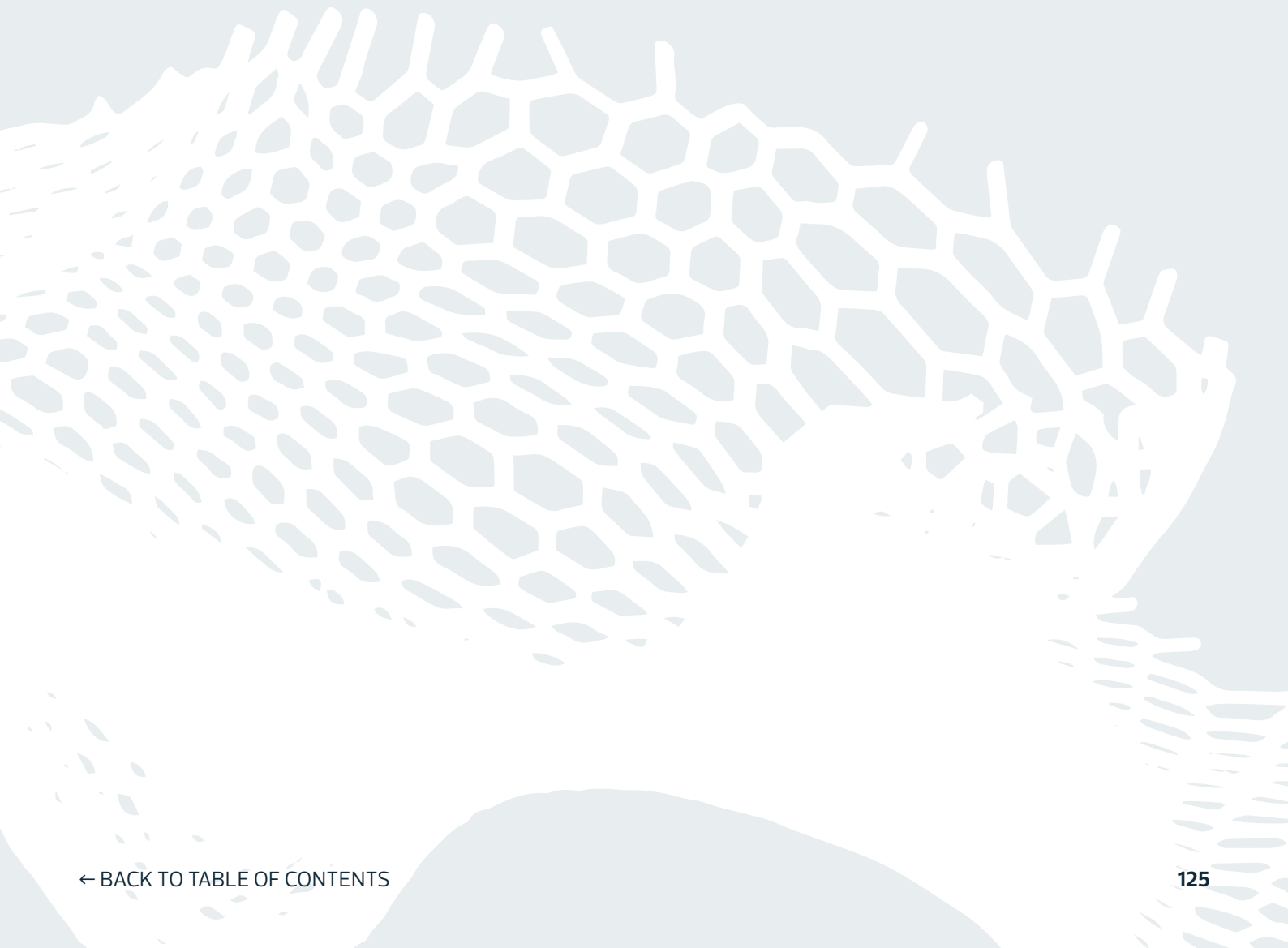
[7] Seltzer R. and Mai Y.-W., 2008, 'Depth sensing indentation of linear viscoelastic-plastic solids: A simple method to determine creep compliance', *Engineering Fracture Mechanics*, vol. 75. no. 17, pp. 4852-4862.

[8] Altaf K., Ashcroft I. A. and Hague R., 2012, 'Modelling the effect of moisture on the depth sensing indentation response of a stereolithography polymer'. *Computational Materials Science*, vol. 52, no. 1, pp. 112-117.

[9] TA Instruments, DMA Q800 user manual

CHAPTER 4.

Education and Arts & Design



Implementation of interdisciplinary student teams in design education for additive manufacturing

Stefan Junk, Department of Business and Industrial Engineering, University of Applied Sciences Offenburg, Campus Gengenbach, Germany, stefan.junk@hs-offenburg.de

Abstract—Additive manufacturing (AM) technologies are becoming increasingly popular in all areas of product development. Therefore, it is imperative that students be taught Design for AM. However, due to the rapid development of new methods and materials for AM, it does not make sense to only teach particular design guidelines, as these can quickly become obsolete. Rather, students should acquire the competence to develop guidelines themselves, that take into account the current state of the art. Thus, they will be able to react to changing processes and new materials in the future. In order to convey the independent development of design guidelines for additive manufacturing by students, a new concept was developed, which is presented in this contribution. In this process, the learning goal is worked out by a group of students on the basis of a practical task. The group consists of an interdisciplinary team in order to combine different competencies and to provide different perspectives on the task. A case study will show the design and manufacture of a miniature aircraft using Fused Layer Modelling. The aim of the development is above all the design for additive manufacturing. In addition, a low use of resources in combination with lightweight construction should be achieved. In the implementation of the task, the students are confronted with challenging aerodynamic design of wings as well as with the economic evaluation of the development process. An examination of the level of knowledge before and after the case study examines the learning success.

Keywords—*Design for Additive manufacturing; Design guidelines; learn by yourself; interdisciplinary teams; Fused Layer Modelling*

1. INTRODUCTION

In recent years, the number of available processes for rapid prototyping (RP) and additive manufacturing (AM) and their fields of application have grown enormously [1]. One important reason for this are the new possibilities offered by additive manufacturing with regard to the design of components, particularly with complex geometries. In order to maximize the potential of the new generative manufacturing processes, the particular requirements of the layer structure must be taken into account in the

development and design of components and products [2]. However, the education and training of students in design engineering nowadays often continues to focus on conventional (that is, formative and subtractive) manufacturing. As a result, the skills and knowledge of AM among many engineers today are very limited [3].

In order to remedy this deficiency, a number of textbooks and design guidelines are now available. In addition, some universities have established lectures and seminars that include design for additive manufacturing [4, 5]. However, in the exercises of such courses, laboratories offered to a huge number of students who often have only limited access to 3D printers [6]. Thus, students are able to use the laboratories, but unfortunately, they often lack a deeper understanding of production technology and its options and limitations in practical application. In addition, they receive limited training how to react to the rapid changes and fast-paced developments in this field of technology.

As such, this contribution introduces a new course, in which students learn to understand AM manufacturing technology and independently develop a structure adapted to it. In this manner, a close and practical cooperation of manufacturing technology and structure is established. In the new Rapid Prototyping Workshop course, students are entrusted with the challenging task of developing a miniature airplane. In doing so, they are to observe boundary conditions with regard to technology and cost-effectiveness. A 3D printer is available for realization. Students are to learn to adhere to the various and sometimes contradictory boundary conditions when designing the miniature airplane. In particular, they are also to learn which guidelines to apply to AM and the post-processing with the use of the 3D printer. In doing so, the guidelines are not defined in the course of a lecture; rather, the students themselves work them out. In this manner, they are to learn how to create design guidelines and adapt them to different requirements and boundary conditions. Thus, they are always able to react appropriately to changing demands in their later professional life.

2. LITERATURE REVIEW

AM technologies have been successfully used in teaching for several years now [7, 8]. In theoretical training of product development, there is a great variety of materials. This is ranging from simple introduction books to detailed works that offer a particular description and evaluation of procedures and processes. In the practical training of students, various studies show that the use of AM ensures the rapid availability of prototypes. This ensures that students have direct feedback regarding, for example, the feasibility of their designs [9-11].

Until recently, the use of AM technologies in teaching was limited, given the fact that, as a rule, only a few devices were available in the laboratories of universities and research centers. In addition, specially trained operating personnel were required for these often highly specialized devices. In order to overcome these limitations, more and more universities are setting up laboratories with a larger number of easy-to-use 3D printers, which have limited installation space [12]. This means that larger groups of students can be guaranteed access to the devices in a short period of time. However, students in such laboratories are only passive users of the technology, without deeper insight into the manufacturing processes and the precise operation of 3D printers.

The use of DIY self-assembly kits represents a further approach for imparting the special requirements for the design of components and products in additive manufacturing. The students first assemble a 3D printer as a kit and put it into operation. This gives them a good understanding of how the 3D printer works. This understanding can be used in the later design of components, e.g. in the form of design guidelines [13].

Unfortunately, however, it has been shown in practice that the assembly of a 3D printer as a DIY kit is highly time-consuming. In addition, the kits are often delivered without detailed instructions, such that students spend a great deal of time on assembly and initial operation. Moreover, support on the part of kit manufacturers is not always optimal and timely. Thus, there is very little time left in the exercise to use the finished printers and to develop design guidelines [14, 15]. As such, a different approach is pursued in this contribution. Students are able to use an industrial printer, thereby fully concentrating on product design and component optimization.

3. STRUCTURE OF THE COURSE

The Rapid Prototyping Workshop course, offered for Master's students from different programs as an elective course, has a time expenditure of 2 semester hours per week; that is, approximately 30 hours in total. Since both technical and economic tasks are considered within the course, interdisciplinary teams consisting of four students from the fields of mechanical engineering, industrial engineering and also business administration are formed.

The task includes the development, design and manufacture of a miniature airplane using 3D printing. A rubber band powers the miniature airplane. This links different requirements with each other. Since the manufacturing is to be additive, a design geared to 3D printing must be created. In addition, low resource consumption and lightweight construction are to be implemented. Furthermore, the aim is to achieve a high degree of performance; that is, high speed and long flight distances.

The timing of the course is structured as follows. After the kick-off meeting, during which the organizational and technical boundary conditions are defined, training phase takes place. This includes the assembly of a balsa plane as an introductory example. In addition, test flights are carried out with the balsa plane and a collection of empirical values are compiled through the balsa plane. An instruction is given on the 3D printer that is used (HP Designjet 3D Color). Fused layering modeling (FLM) is used as an additive manufacturing process, since both printing and material costs are relatively low. In a second work step, the supporting material used for this purpose is washed away with the aid of an alkaline bath.

In the subsequent conception phase, ideas are generated. Such ideas are implemented with the selection of profiles through simulations and the elaboration of the concept for the first prototype. Subsequently, the design is created and 3D printing is carried out. After assembly, test flights are carried out and evaluated. This part of the development process is repeated twice in optimization loops, in an effort to improve results. Finally, in the last phase, the results of the three prototypes developed are compared with each other, and the cost-effectiveness of the developed solutions are analyzed and evaluated.

3.1. Results from the conception phase

The first conclusions could be drawn from the assembly of the kit for an airplane made of balsa wood (see Tab. 1). Initially, all necessary parts for the construction of a plane could be identified. In addition, students developed an understanding of the size ratio of the airplane. Further more, findings regarding the simple assembly and operation of the rubber engine were collected. Learning the throwing technique for the launch of the airplane is also important.

In the technical design of the miniature glider, various simulation tools were used; for example, in order to specify the profile geometry of the wings and to determine the proportions of wings, tail unit and fuselage. For design, the simulation data were transferred to a professional CAD system.

The students learned about the interrelationships of different parameters relevant for the flight, such as the angle of attack of the airfoil to the fuselage or the dimensioning of the weight of the airplane to the glide ratio.

TABLE I. TECHNICAL AND ECONOMIC PARAMETERS OF THE DEVELOPED PROTOTYPES

	<i>Balsa plane</i>	<i>1st prototype</i>	<i>2nd prototype</i>	<i>3rd prototype</i>
Weight [g]	35	110	17	41
Wingspan [cm]	60	60	40	40
Wing load [g/cm ²]	0.09	0.37	0.06	0.146
Set-up time [min]	90	20	175	180
Materials	Balsa wood, glue, rubber, plastics, metal insert	ABS, rubber, instant adhesive	ABS, foil, rubber, instant adhesive plastics, metal insert	ABS, foil, rubber, instant adhesive plastics, metal insert
Materials costs[€]	20	46.55	21.49	37.31
Flight distance [m]	18	8	7	6
Fight time [s]	3	3	3	2
Air speed [m/s]	6	2.66	2.33	3

In addition, the adjustment of a selected profile was carried out in order to achieve a balanced relationship between the airplane's glide ratio, stability measure, flight speed and center of gravity.

3.2. Results of the first prototype phase

For better comparability with the balsa plane, a "replica" was realized in the first approach; that is, the surfaces and the fuselage of the airplane were completely developed and manufactured as shells. Since the construction material used (ABS-plastics) is considerably heavier than balsa wood, the large difference in weight makes it impossible to compare them. In addition, poor flight behavior was also found, because the lightweight design was not taken into account.

As an optimization measure for the next development step, it was determined that the wings were to be covered with foil for the urgently needed lightweight design. The horizontal stabilizers and rudder were also to be covered. Further potentials for improvement by means of suitable adhesive bonds for improved stability were identified. In addition, the ratio of the wingspan and depth of the airfoil was to be changed, in an effort to improve the position of the center of gravity and flight characteristics.

3.3. Results of the second prototype phase

In the second approach, a truss structure with a foil covering was chosen, as this made it possible to achieve a substantial savings in weight by leaving out material in the fuselage, airfoils, horizontal stabilizers and rudder. Through this extreme lightweight construction, the weight of the printed glider could be reduced significantly below the weight of the balsa wood glider. However, this led to a deterioration in flight characteristics. In order to avoid

twisting of the airfoil, a linking of the wings using a screw connection was developed for further development. From the viewpoint of manufacturing and assembly, printed components are able to tolerate only a little heat. For this reason, distortions can easily arise in the filigree components upon the removal of support material and upon covering.

3.4. Results of the third prototype phase

In the third approach, the truss structure with a foil covering from the second approach was optimized. To this end, the cross-sections of the truss members were increased, in order to reduce distortion and to significantly increase stability. This was connected with a slight increase in weight, yet the additive manufacturing and assembly in particular could be significantly improved. In order to be able to adjust the center of gravity of the airplane more easily, a sliding connection between the fuselage and wings with the aid of a slotted hole was also developed.

3.5. Results of the economic evaluation

The evaluation of the time spent on the various prototypes shows that, with each development stage, the amount of time spent on assembly also increased (see Fig. 1). This is mainly due to the fact that the diversity of the used materials used also became greater, thus increasing the complexity of the product.

The material costs for the various prototypes are all higher than the costs of the balsa plane (see also Tab. 1). The reason for this is the relatively high costs for the plastic filament in additive manufacturing using FLM. Moreover, the particularly light prototype 2 results in the lowest material costs. This shows the clear influence of lightweight design on material costs.

The time expenditure of the students on the various tasks within the course shows that 29% of their time was spent on brain storming, design and simulation. Only 11% was spent on additive manufacturing (pre- and post-processing of the print). About 21 % of the available time was spent on assembly and test flights.

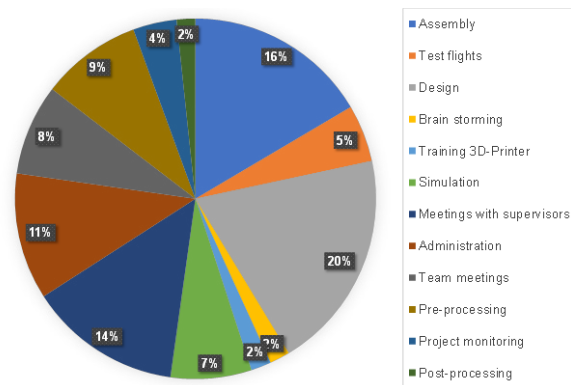


Figure 1. Share of individual activities in the total workload for product development

4. DISCUSSION OF THE COURSE RESULTS

The course provides students with insight into design engineering in airplane construction. In particular, through structuring and simulation in the design of wings, they learn how to apply their knowledge in the modelling of wing profiles. Students independently develop the necessary guidelines for the implementation of the design by means of additive manufacturing. In addition, they are also confronted with the influence of anisotropic material properties in FLM. During the subsequent assembly of the airplane and test flights, students receive direct feedback on their designs. Such feedback can be applied in further development loops by adapting the design guidelines and optimizing the lightweight design.

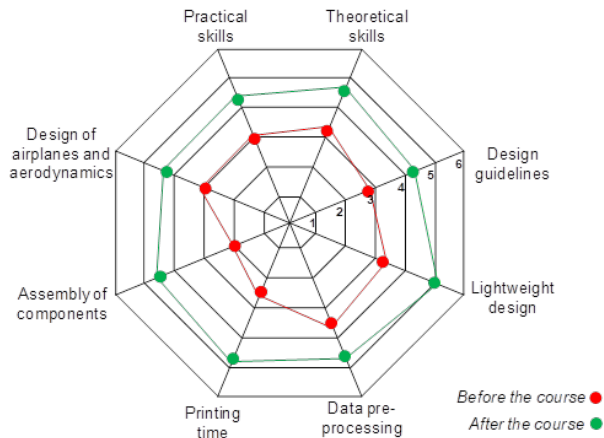


Figure 2. Knowledge of students in specific areas of product development and additive manufacturing before and after the course

A survey of students regarding their knowledge in different areas before and after the course shows that they have been able to achieve significant improvements in their knowledge and skills in all eight areas (see also Fig. 2). The students could rate their skills and knowledge from very poor (1) to very good (6). This result applies in particular to the area of design of airplanes and aerodynamics, but also design guidelines and lightweight design. Particularly strong improvements were also achieved in the areas of additive manufacturing (e.g. forecast of printing times and assembly of printed components).

5. SUMMARY

At this time, there is a large number of different additive manufacturing processes and different materials for the processes currently on the market. In addition, the processes are subject to constant further development, and new materials are being offered. For this reason, this contribution presents a newly developed course, in which students independently learn how to develop and create new products using additive processes. Through the independent approach, students are to be prepared to adapt to changes in processes and materials.

As part of the course, the students independently developed a miniature airplane while working in teams. They have been able to greatly expand their knowledge in many technical areas (aerodynamics, design and additive manufacturing). Different prototypes could be developed within three development cycles. A comparison of these three variants shows a significant improvement in terms of lightweight construction and material savings.

Given the interdisciplinary composition of the teams, different technical and economic requirements could be implemented. The students assessed their own time requirements for different tasks within product development and additive manufacturing. In this manner, they were able to independently determine the interrelationships between lightweight construction, stability and material consumption, and have them introduced into product development.

REFERENCES

- [1] Wohlers T. Campbell R.I. Diegel O. Kowen J. and Caffrey T. "Wohlers Report 2017 - Additive Manufacturing and 3D Printing State of the Industry, Annual Worldwide Progress Report, 2017, Wohlers Associates Inc., Fort Collins, USA
- [2] de Beer N. Additive Manufacturing - Turning Mind into Mater, 2013, Sierra College for Applied Competitive Technologies
- [3] Kriesi C., Steinert M., Meboldt M. and Balters, S. Physiological Data Acquisition for Deeper Insights into Prototyping, In: Laakso, M. and Ekman, K. (Editors): Proceedings of NordDesign 2014 Conference, Aalto Design Factory and Design Society, 2014, pp. 580-589
- [4] Steinar K. Additive Manufacturing: Design, Methods, and Processes, Pan Stanford Publishing, Singapore, 2017
- [5] Gibson I. Rosen D. W. and Stucker B. Additive Manufacturing Technologies: 3D Printing, Rapid Prototyping, and Direct Digital Manufacturing, 2014, Springer
- [6] Chen T. Stoeckli F. and Shea K. Design for Mass Customization using Additive Manufacture: Case-Study of a Balloon-Powered Car, Proceedings of the 20th International Conference on Engineering Design (ICED 15) Vol 4, 2015
- [7] Ertu U. Atkinson P. and Tancock, D. Applying 3D Scanning and Modeling in Transport Design Education, Computer-Aided Design & Applications, Vol. 3, Nos. 1-4, 2006, pp. 41-48
- [8] Celani G. Duarte J. and Pupo R. Introducing rapid prototyping and digital fabrication laboratories in architecture schools: planning and operating, Proceedings of ASCAAD 2010, 2010, pp. 65-74
- [9] Ford P. and Dean, L. Additive manufacturing in product design education: out with the old and in with the new?, Proceedings of E&PDE 2013, the 15th International Conference on Engineering and Product Design Education, Dublin, Ireland, 2013. pp. 611-616
- [10] Mostert-van der Sar M. Mulder I. Remijn L. and Troxler P. Fablabs in design education, Proceedings of E&PDE 2013, the 15th International Conference on Engineering and Product Design Education, Dublin, Ireland, 2013, pp. 629-634
- [11] Widden M. and Gunn K., Design-build-test od model aerofoils for engineering education using FDM, Virtual and Physical Prototyping, Vol.5, No. 4, 2010, pp 189-194
- [12] Chen T. Egan P. Stöckl F. and Shea K. Studying the Impact of Incorporating an Additive Manufacturing Based Design Exercise in a Large, First Year Technical Drawing and CAD Course, Proceedings of the ASME 2015 International Design Engineering Technical Conferences & Computers and Information in Engineering Conference, 2015

- [13] Junk S. New approach in design education using additive manufacturing, In: Marjanovic D. et al. (Ed.): Proceedings of 13th international Design Conference, 2014, pp. 1391-1398
- [14] Junk S. and Matt, R. New Approach to Introduction of 3D Digital Technologies in Design Education, Proceedings of CIRP 25th Design Conference, Procedia CIRP Volume 36, 2015, pp. 35–40
- [15] Junk S. and Schrock S. New Developments in design education for additive manufacturing, Proceedings of the 18th International Conference on Engineering and Product Design Education (E&PDE16), 2016

3D interpretation of Snežnik Castle and its surroundings in a form of a scale model

Tanja Nuša Kočever¹, Aja Knific Košir¹, Eva Razložnik², Luka Dakskobler¹, Matej Pivar¹, Marjeta Čuk¹, Deja Muck¹, Helena Gabrijelčič Tomc¹

¹ University of Ljubljana, Faculty of Natural Sciences and Engineering, Department of Textiles, Graphic Arts and Design, Chair of Information and Graphic Arts Technology, Snežniška 5, 1000 Ljubljana, Slovenija

² University of Ljubljana, Faculty of Architecture, Zoisova cesta 12, 1000 Ljubljana

Corresponding author: helena.gabrijelcic@ntf.uni-lj.si

Abstract—In this research the 3D interpretation of Snežnik Castle is presented. In the introduction the use and the application of 3D technologies in the documentation, the presentation and especially in the interpretation are shortly explained. In the experimental part the workflow is shown and the working phases are presented. The scope of the 3D interpretation is defined with the opportunity of the project that was given from Ars Viva Institute. The conceptualization is presented with the documentation process and prototyping. Production stage was divided in two parts, i.e. the first part that included visualization of the castle and the second that were 3D printing and laser cutting. Last phase was installation and evaluation that resulted in final composition of the scale model and its permanent installation in Hostel Ars Viva.

KeyWords: *Snežnik castle, 3D interpretation, 3D printing, scale model, cultural heritage*

1. INTRODUCTION

1.1. 3D technologies and cultural heritage

3D technologies can serve as an accurate and precise framework of methodologies and tools for documentation, presentation and interpretation of cultural heritage [1]. They are applicable in cultural heritage with the aims of archiving data, providing support for conservation-restoration interventions, support for object reconstructions, management, promotion and popularization, the creation of virtual collections and museums, interpretations of heritage in the form of scale models, visualizations and simulations, spatial installations, presentations in combination with live-acting performances and 3D printed reproduced models intended for education [2].

Even though, they are well established in the science and cultural heritage applications, they are still challenging,

mainly in the documentation fields of acquisition of virtual data and geometric description, organization of data and metadata and supporting professionals in accessing data for research and study [3]. Besides, when it comes to presentation and interpretation as the interchangeability of the data from virtual to physical, the presentation and reproduction of 3D cultural heritage objects, the implementation of interactivity and the digital 3D reconstruction and reproduction, there are also many obstructions that researchers should overcome to produce consistent and reliable representative media.

What is important for the use of 3D technologies in cultural heritage is the augmentation of user experience, namely, the virtues of these applications can be listed also as non-invasive, reliable, sustainable, attractive, immersive and interactive [4, 5].

Before interpretation can be performed, the data about the object should be documented and archived. When there is a need of 3D reconstruction methods that is often the case in documentation of cultural heritage, special care should be applied to the processes of capturing, acquisition, registration, integration, texturing reproduction [6].

3D interpretation is a reproduction of a cultural heritage object that is not intended only to digitally preserve the object but also to interpret some defined feature, properties, manifestation of the object to promote, disseminate, popularize and to add value of their usability and user experience [7]. Usually, the techniques of digital interpretation reuse the data about the object of cultural heritage that were documented and preserved and represent them with the additional explanation and in the concept of additional purposes. In these procedures personal and non-personal methods can be applied depending on the purpose of the interpretation.

In cultural heritage different interpretative mediation can be used: landscape design, road infrastructure and design, art and sculptures, events, multimedia and technology [8], reinterpretation of historic structures or items [9], panels and signage and publications [10].

Interpretation can be divided in six main steps: identification of the opportunity, development of the scope, develop the concept and design, production and installation, maintenance and evaluation [10].

1.2. Aim of the Research and its Background

The aim of the research was the 3D interpretation of the Snežnik Castle and its near surroundings with a scale model. Snežnik castle is located in Notranjska region, southern Slovenia, in the Lož Valle in the municipality of Loška Dolina (Slovenia) [11]. The castle dates to the 13th century and was reconstructed in the second half of the 19th century, so that the interior parts date from this period. The castle features a defensive wall, a placement in natural rock, castle estates, various meadows, a tree-lined lane of chestnut and linden trees and two artificial lakes. As an representative and important cultural heritage object of the southern Slovenia, an initiative for its reproduction came from the Ars Viva Institute, i.e. a culture center and incubator active in the field of social issues, integration of disadvantaged groups into society and awareness of local cultural and natural heritage that offers also the accommodations - a Youth Hostel Ars Viva completely adapted for the physically impaired individuals and suitable also for persons with other disabilities (blind and visually impaired). With the installation of the scale model in the meeting room of hostel, the institute could offer to the disabled and non-disabled visitors the possibility of touching, feeling and experiencing the interpretation of the castle so on a macro scale - on a level of disposition and placement of the castle, its surroundings and the morphology of the terrain as on a micro scale - experiencing the details, textures and reliefs of the castle's features. This contribution presents a part of the results of the project entitled Equipping the Ars Viva Institute with target communication channels of new media (ŠIPK 2016-18) that involved ten students (graphic design, multimedia and architects) and three of them, also the authors of this research work, were with the project work educated in the field of additive technologies and their application.

2. EXPERIMENTAL

The research included following steps of 3D interpretation:

- *scope*: definition of the opportunity,
- *concept*: documentation and paper prototyping,
- *design*: 3D presentation and interpretation: 3D modelling main topology and details of the castle,

- *production – part 1*: 3D virtual reproduction: rendering shaded visualizations without the use of textures,
- *production – part 2*: 3D physical reproduction: production of a 3D scale model composed of a printed version of the castle and its surroundings constructed of plywood in plexiglass and
- *installation and evaluation*.

2.1. Scope of the interpretation

The scope of the research was defined in collaboration with the Institute Ars Viva. The aim was the 3D interpretation of a Snežnik Castle and its surroundings in a form of a scale model and consequently giving to the disabled and non-disabled visitors and tourists of Slovenian southwest Karts region the opportunity of experiencing and with their senses interpret the representative object of cultural heritage on a macro and a micro scale. The physical representation of the castle and surroundings was meant to preserve important aspects of the original and to represent some features with the interpretation of the terrain morphology and castle details.

2.2. Documentation and paper prototyping

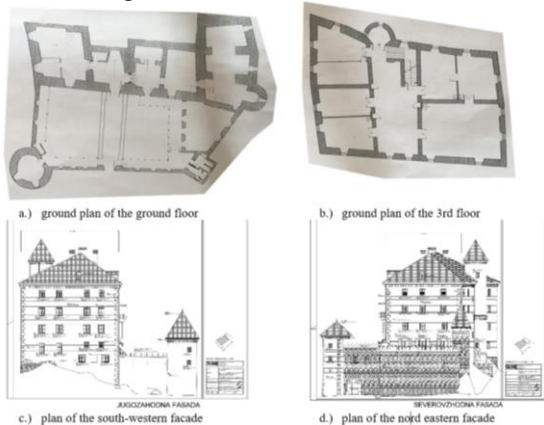
The documentation of the castle and its surroundings included three types of documents: photos of the on micro and macro scale, 2D plans of the building and 2D drawings of topological layers.

For the acquisition of the photos the camera NIKON D700 (NIKON CORP., Japan) with macro objective. Photos were acquired on a macro level for the analysis and reproduction of the textures and details and on a distance from an object (with the purpose to use image references in 3D environment from different views), as is presented in Figure 1a, 1b and 1d. For the use in 3D CG environment the perspective was extracted from the images (Figure 1c).



Figure 1. Photos of the castle; a.) and b.) distant views, facade with the windows and details and d.) relief and texture details of the roof and bridge.

In the next phase of the documentation, the collecting of and searching for material and accessible documents of the castle occur. 2D plans of cross sections of different segments of the castle were provided by Museum of Snežnik Castle that is situated in the castle. These plans served as a reference for the volume and spatial parts of the model and are presented in Figure 2a and 2b. More detailed surface 2D drawings of different facade sides were given by the Ministry of the Environment and Spatial Planning. These plans offered the perspective of the castle in the different viewports of 3D environment and are presented in Figure 2c and 2d.



*documents given by Museum of Snežnik Castle and Ministry of the Environment and Spatial Planning

Figure 2. 2D plans of cross sections of different segments of the castle and detailed surface 2D drawings of different facade sides.

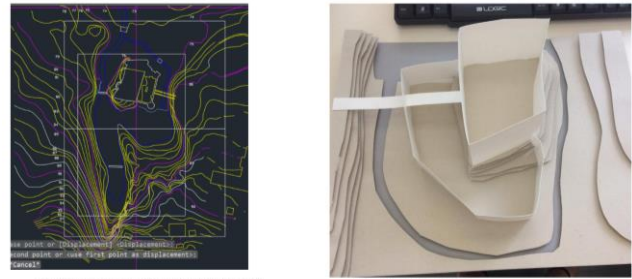
2D drawings of topological layers of the castle surroundings in CAD format were provided by the GEA-Consult and are presented in the Figure 3a. The drawings that were provided were very exact and they represent very accurately morphology of the place. This was not what was needed for the interpretation of the castle's surrounding. Consequently, the drawings were simplified in the software AutoCAD and only the layers that were important for our interpretative concept were extracted and further process. The analysis of documents and plans led the procedure in the creation of the paper prototype that served as a raw model for the disposition and the composition of the parts of the scale model, as is presented in Figure 3b.

2.3.3D presentation and interpretation: 3D modelling main topology and details of the castle

3D modelling was performed in Blender opensource software for 3D computer graphic, texturing, animation, special effects and rendering.

3D presentation and interpretation were divided in two main phases, i.e. 1. presentation - modelling of the main structure in right proportions, sizes and dispositions

(Figure 4) and 2. interpretation – fine modelling of modelling of the details (Figure 5).



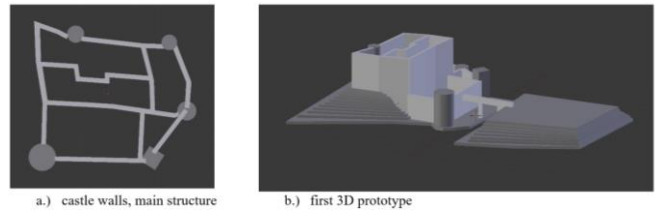
a.) 2D drawings of topological layers*

b.) paper prototype

* interpretation of the document given by GEA-Consult, Inženiring, projektiranje in svetovanje d.o.o.

Figure 3. a.) CAD drawings of topological layers of the castle surroundings and b.) a paper prototype.

Castle walls were modelled from the 2D plans of cross sections (Figure 1). They were extruded on the exact height according to the 2D planes of different facade sides. 3D prototype was prepared with the arrangements of the walls, the corrections of their sizes and the settlement of the surroundings, as is presented in Figure 5.



a.) castle walls, main structure

b.) first 3D prototype

Figure 4. 3D modelling of castle's main structure.

The interpretation phase included the definition of a particular parts of the model (i.e. stone bridge and defense wall) and interpretation of the building's features that includes the development of the procedure for the 3D modelling of the relief details and textures.

Stone bridge was modelled with the special attention to its architecture and redefined with cell fracture function that enabled its relief. Cell fracture is a Blender's Add on that enables detailing the fractures with the particle system, i.e. computer computation of a large number of very small 3D models, objects or sprites that simulates a specific kind of phenomena such as natural phenomena, chaotic systems etc. The shapes of the stones and other textures and relief details were redefined with the modifiers as displace, decimate and subdivision surface (Figure 5a). The final topological corrections of the castle and its parts occurred manually with fine polygonal modelling (Figure 5b).

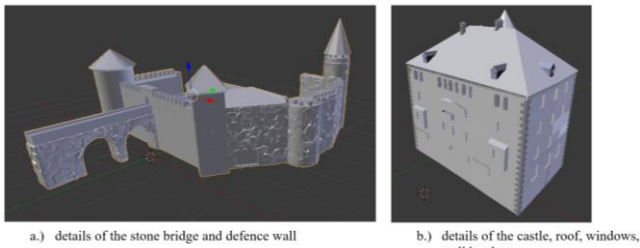


Figure 5. Fine solution with the 3D geometry of walls, windows, roofs.

2.4. 3D virtual representation: rendering shaded visualizations without the use of textures

After modelling, 3D virtual reproduction was visualized with the use of Cycles renderer and path tracing rendering technique. This phase was performed without texturing and texture and the relief and details were solved with the geometry of the polygonal mesh. Consequently, it served as detailed prototype before final step of 3D printing. In Figure 6 visualization of Snežnik castle and its relief details (stone in the defense walls, details of the windows, structure of the roofs of the castle and towers).

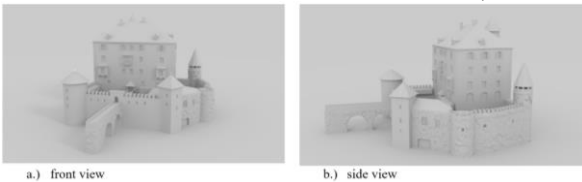


Figure 6. Visualization of the 3D modelled part of the scale model: castle, towers and the defense bridge and walls.

2.5. 3D printed representation of a castle and its parts

After 3D virtual prototyping, preparation of the model for 3D printing was performed. The 3D model of the castle was divided (carefully cut) in 11 parts, i.e. castle's roof, castle's main structure, many parts of the defense wall and the small stone building that was placed in the other part of the scale model. Each part was prepared for printing with the elimination of intersecting surfaces and non-manifold mesh geometry and saved as .stl format.

Printing occurred approx. 100 hours on two Z-morph multitool 3D printers with white PLA material. The most challenging was the printing of the roof due to its dimensions that had to match the structure of the main building and the achievements of the accuracy of the relief details on the castle surface.

In Figure 7 printing process (a-c) and final separate printed parts of the castle (d-f) are presented.

Our 3D interpretation of the surroundings of the castle included, besides printed parts, two other different materials, i.e. plywood with the acacia tree origins that served for the surrounding terrain and semi-transparent plexiglass for the lake.

The layers were 4 mm and were according to 2D drawings of the plans of the topology cut on HyperCut Pro 6090 as is shown in Figure 8.

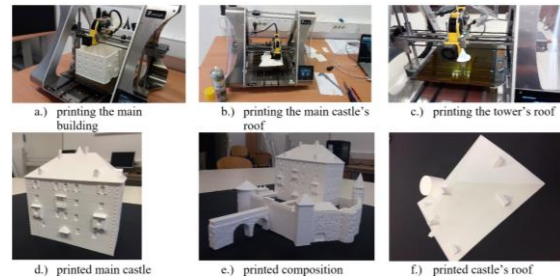


Figure 7. Presentation of the printing process (a-c) and final separate printed parts of the castle (d-f).

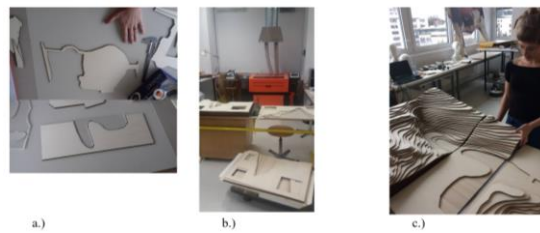


Figure 8. a.) Planning the laser cutting, b.) laser cutter and c.) the compositing of the terrain layers.

3. RESULTS AND DISCUSSION

3.1. Installation of the scale model

3D printing technology based on thermoplastic extrusion, fused deposition modeling does not allow the printing of overhanging parts without supporting structures, so we had to adapt the architecture of model in certain parts to avoid support. More appropriate 3D-printing technology for final reproduction of a castle would be binder jetting or three-dimensional printing, 3DP. In this way, the model could be printed in one piece without any support structures for certain overhanging details.

Final compositing of the scale model was a detailed task as each part had to completely match with others. The layers and parts were bind together with the glue paying attention to the interpretative style that we wanted to achieve in the final composition. The process of compositing and final settlement of the scale model in presented in Figure 9.

The scale model was placed in a solid table frame and exhibited in hostel's meeting room of the Ars Viva Institution.



Figure 9. Compositing of different parts and layers and final settlement of the scale model.

In Figure 10 the main printed structure and some representative details of the 3D prints can be observed.

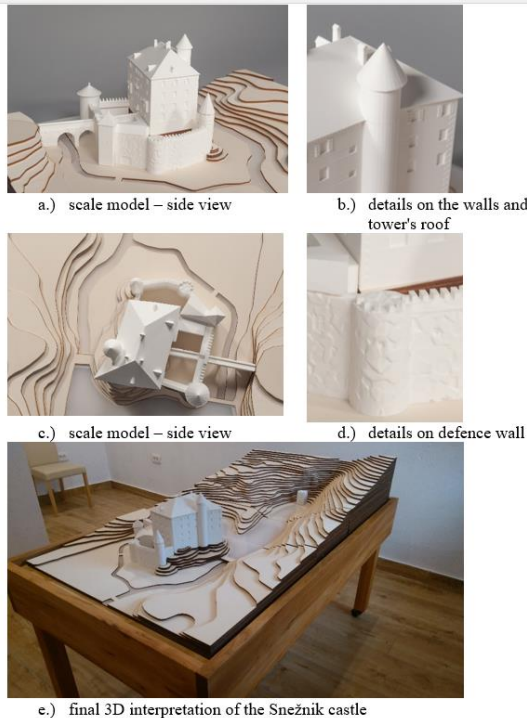


Figure 10. Final scale model and its installation.

3.2. Evaluation of a geometrical accuracy

The presented scale model is a construction made of 3D printed elements, i.e. architectural objects in PLA, wooden layers that present nearby landscape of the castle and Perspex presenting water and lake. Three constructional parts obviously differ in material structure, in resolution and details reproduction forming a contrast when observing at longer and near distance but also during tactile interaction. As it can be observed in Figure 10 and as it was evaluated by the institute representatives, architectural details as windows, doors, roof and wall structure are reproduced accurately, giving the experience of the building's topology, yet for some elements (rock wall) still missing the finest sharpness.

By all means, the installation and the exhibition of the scale model allow to the visitors and tourists an immersive experience of observing and touching natural (landscape) and cultural (castle) heritage from all the directions and planes.

4. CONCLUSIONS

In the conclusions the evaluation of the research can be presented. With the applied framework including methodologies of documentation, prototyping, virtual and physical production and installation the important Slovenian cultural heritage object was interpreted. The 3D interpretation of the object was not only a presentation of

the historic monument, but especially a representation with enriched visual and tactile communicative value. Besides the implemented 3D interpretation style that the authors gave to the representation of the castle, the visitors have an opportunity to experience and develop their own interpretation.

ACKNOWLEDGEMENT

The presented research work was financed by Public Scholarship, Development, Disability and Maintenance Fund of the Republic of Slovenia, Ministry of Education, Science and Sport (Republic of Slovenia) and European Social Fund. The authors of this contribution would like to thank them for the financial support.

Authors would like to thank also all the dedicated participants of the Ars Viva Institute that were involved in the project.

Special thanks are expressed also to GEA-Consult (Inženiring, projektiranje in svetovanje d.o.o.), Public Institution Snežnik (Snežnik Castle Museum) and the Ministry of the Environment and Spatial Planning (Republic of Slovenia) that provided the documentation for the project work.

5. REFERENCES

- [1] Ozbek, K. 2013, *3D vizualizacija antičnega Rima – 3D Visulisation of Antique Rome*, Diploma Thesis. Ljubljana, 41 p.
- [2] Stylianidis, E. , Remondino, F. 2016, *3D Recording, Documentation and Management of Cultural Heritage*, 1st ed., Whittles Publishing, 388 p.
- [3] Ioannides, M., Quak, E. 2014, *3D Research Challenges in Cultural Heritage, A Roadmap in Digital Heritage Preservation*, Springer-Verlag Berlin Heidelberg, 142 p.
- [4] Bekele, M. K., Pierdicca, R., Frontoni, E., Malinverni, E. S. and Gain, J. 2018, A Survey of Augmented, Virtual and Mixed Reality for Cultural Heritage, *Journal on Computing and Cultural Heritage*, Vol. 11, No. 2, pp.1-36, doi: 10.1145/3145534
- [5] Machidon, O. M., Duguleana, M. and Carrozzino M. 2018, Virtual humans in cultural heritage ICT applications: A review, *Journal of Cultural Heritage*, Available: <https://doi.org/10.1016/j.culher.2018.01.007>
- [6] Gomes, L., Silva, L., Regina, O. and Pereira Bellon, P. 2014, 3D Reconstruction Methods for Digital Preservation of Cultural Heritage: A Survey, *Pattern Recognition Letters*, Vol. 50, pp. 3-14
- [7] Interpreting Heritage Places and Items - Guidelines, 2005, *NSV, Heritage Office*, 2005, Available: <http://www.environment.nsw.gov.au/resources/heritagebranch/heritage/NSWHeritageOfficeGuidelinesinfointerpreting.pdf>
- [8] *Virtual Reconstructions and Computer Visualisations in Archeological Practice*, 2017, University of Ljubljana, Faculty of Arts Press, Eds.: Predrag Novaković, Nenad Tasić, Milan Horňák, 114 p. Available: https://issuu.com/znanstvenazalozbaff/docs/virtual_reconstructions_final_e-ver
- [9] Kočever, T. N., Naglič, B., Gabrijelčič Tomc, H. 2018, 3D Visualisation of a Woman's Folk Costume, *Digital Cultural Heritage*, Springer, pp. 304-323.
- [10] VicRoads Cultural Heritage Interpretation Guidelines, VicRoads, 2013, Available: <https://www.vicroads.vic.gov.au/>
- [11] Snežnik Castle Museum, National Museum of Slovenia, Available: http://www.nms.si/index.php?option=com_content&view=article&id=325&Itemid=0&lang=en

Additive Manufacturing – a system theoretic approach

Bernhard Heiden, Ulrich Leitner, Industrial Engineering and Management, FH Kärnten University of Applied Sciences, Villach, Austria,

Abstract—This paper sketches a system theory approach with methods of state theory and as systems in general can be characterized by an energy efficiency characteristics with extended thermodynamic sentences and in the special application case how this can explain additive manufacturing processes versus subtractive manufacturing processes. A first try to demonstrate the added value of this theory to additive manufacturing together with an outlook for future applications, possibly beyond additive manufacturing, is given.

System Theory; Thermodynamics; Industry 4.0; Self-Organizing Systems; Additive Manufacturing; Subtractive Manufacturing;

1. INTRODUCTION

Firstly a short introduction is given over some basic concepts of system theory (1), thermodynamics (2) and Additive Manufacturing (AM) (3) that are used subsequently to give a short systemic approach of explanation of AM. (1) There are different methods available to model systems. The here used method uses on the one hand block diagram illustration and on the other hand the *state theory* – (see e.g. [1]) which is a later branch in development of *system theory*, where Kalman and Zadeh have formulated a common understanding for the theory of non-linear control- and network systems [2],[1]. System theory lets analyze, among others, information, stability, linked-ness, observability, by identifying the direction of “flow” (e.g. information, material, energy), as well as the state itself. A weak connection is characterized by a one-directional “linking”, a strong coupling by a bi-directional coupling. (2) Thermodynamics as a scientific discipline is dealing with the “dynamics of systems” mainly due to temperature variation. (3) AM itself is the now common

term, for a production process also called popularly 3D-printing, with respect to industrial production (e.g. [3]).

2. STATE THEORY

The state theory – can be used to describe systems. Very useful in the context here is the composition of systems with regard to their structural coupling ([1] p. 64ff and 168 f.).

3. THERMODYNAMICS

Following the first three main sentences of thermodynamics are depicted in equations (1),(2) and (3) (see eg.[4]).

$$dU+dA=dQ+dE_A \tag{1}$$

$$dS \geq 0 \tag{2}$$

$$(T \rightarrow 0) \rightarrow (S \rightarrow 0) \tag{3}$$

Equation (1) means the energy conservation law. Energy forms can be transformed, while energy stays in the system always the same. Equation (2) means that the entropy S is always increasing or staying the same in closed systems. Equation (3) means that the entropy tends to zero when the temperature tends to zero [K].

An additional main sentence can now be introduced combining the second (2) and the first (1) sentence together in a self-referential process of feed-back, applied to the physical system itself, here called the fourth sentence (see later in equation (4)).

It means that when you apply the order to system (1) the energy balance, that consists of energy components that can be transformed into each other, then each energy form has its own “order”, in the sense, that it is more or

less ordered or in other words, it can be transformed in the other energy forms more or less easily, meaning efficiently. The potential to transform the energy with less energy effort – syntropy (or negentropy) production (2) – is following straightforward. The fourth main sentence has the form (4), where S is the entropy function, dE is the individual energy component of the system and the index i , vs. $i+1$

$$S(dE_{i+1}) < S(dE_i) \quad i: 1 \dots n \tag{4}$$

$$E = m \cdot c^2$$

$$E [J] = [kg \cdot m^2 / s^2] \sim E [Mass \cdot Room / Time^2]$$

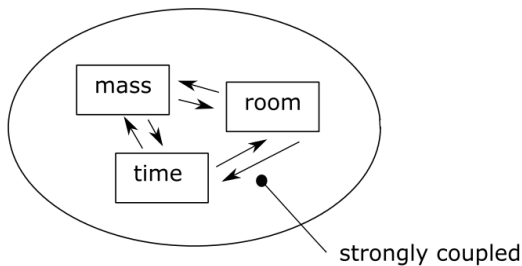


Figure 1 First Sentence of thermodynamics described with regard to physical dimensions

denotes the energy form with less “entropy” itself – or more syntropy - meaning, that the energy forms are ordered with respect to order.

When the reference to the energy system is reapplied in that sense that Self-Organizing (SO) systems are increasing their order, when they are far from thermodynamic equilibrium, then the fifth main sentence of thermodynamics equation (5) can be introduced,

$$S(dE_{i+1})_{-i} < S(dE_i)_{-i} \quad i: 1 \dots n \tag{5}$$

meaning that a further self-referencing of energy takes place, so to speak with increasing “feed-back” order, using the nomenclature of Förster [5] for the cybernetics of second order systems. Here i denotes the feedback order till the order n , in an evolutionary sense of the system, meaning i feedback loops. This is also in accordance with the possible order increase according to Prigogine in Bertalanffy [10] p. 144.:

$$dS = d_e S + d_i S \tag{6}$$

Equation (6) means that for open systems the entropy S can be divided in a term $d_e S$ which is importing entropy. This can be positive or negative. The negative case would lead to an order increase. The internal entropy is staying the same or increasing due to the Clausius equation (2) $dS \geq 0$. So in this context in an open system that evolves energy forms from evolutionary development, can form higher energy forms, meaning that the entropy term $d_e S$ is

decreasing. In fact this evolution is indicated in equation (5) together with the self-referencing process.

4. DEDUCTION OF THE FIRST SENTENCE OF THERMODYNAMICS

As can be seen in Figure 1 the first sentence of thermodynamics (1) can be assembled to one “physical system” when applying only the dimensions as entities that can be regarded as coupled systems. The physical dimension itself plays also a reducing role, according to the Buckingham’s Pi-Theorem (see also [6]). All three dimensions, Room [m^3], Time [s] and Mass [kg] give together one strongly coupled system, e.g. in the form of energy. This variable contains all three dimensions and acts simultaneously as one system. The resulting main sentence of thermodynamics is that “all” systems stay conserved with respect to energy (equation (1)), at least when mass, time or room stay existent or have a value big enough that strong coupling is true.

5. APPLICATION TO AM

The previously defined sentences of thermodynamics have obvious applications in technology development,

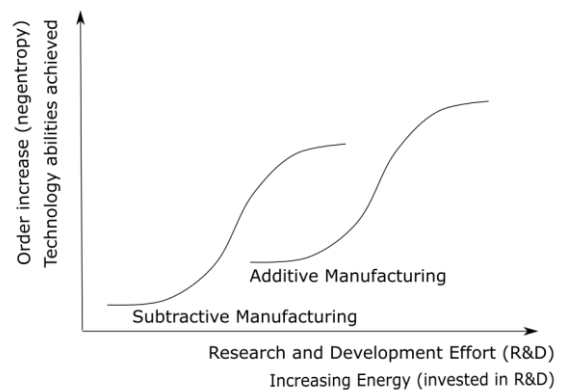


Figure 2 Technology life cycle curve for Subtractive and Additive Manufacturing (SM&AM) – Two “S-Curves”

as can be seen in Figure 2 for the Subtractive and Additive Manufacturing (SM&AM). Firstly the technology life cycle curve is spanned into two dimensions, that of the technology that has been achieved, with respect to its potential and secondly to the R&D effort. These curves are both “S-curves”, depicting limited growth curves, which are also solutions of the logistic equation, meaning, one exponential growth, meets one exponential decay (see also [7]). Both dimensions simultaneously have an order increase, meaning, that a dimensional reduction takes places, while the technology change from subtractive to additive manufacturing increases the order with respect to an integral fifth main sentence (5) of thermodynamics. AM is based on existing CNC-technology, therefore the R&D

begins at a higher level, as well as this is a base technology for both. On the other hand the potential of AM is higher, as the “production process itself” is more integrated (more parts can be printed together without assembling them), as the possible building complexity is higher. Therefore the energy efficiency of the process is also higher (4) leading to more efficient production. That means that the AM-Process itself has a new quality in the sense of (4) leading to higher total system order with (5).

To demonstrate that the process of AM itself follows a rule according to the fourth (4) and fifth (5) main sentence of thermodynamics an illustration is given in Figure 3. In a first feedback loop there takes place a first phase transition from liquid to solid, the filament is produced (depicted with the sign \downarrow_1). In a second loop, the order is increased by reheating the nozzle and the filament, and pressing it through the nozzle into a new order, the form of the workpiece (depicted by the sign \downarrow_2). All this is fully in coherence with equations (4) and (5).

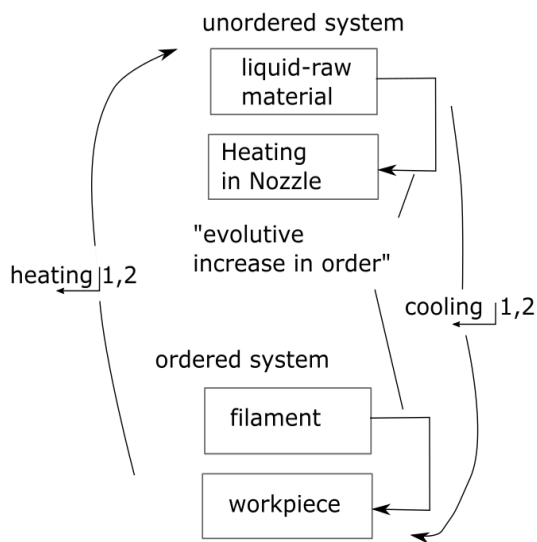


Figure 3 AM process evolution with second order cybernetics according to adapted self referential nomenclature from Förster [5], denoting here the first and second feedback loop in the AM

6. CONCLUSIONS, ADDED VALUE TO AM & OUTLOOK

Finally the conclusions of the above given deduction are drawn, will there be shown the added value of system theory to AM as well as will be given an outlook of possible future application of AM by means of the approach given here.

6.1. Conclusions

From the development of AM out of SM, a system change took place, meaning that a phase transition is necessary for the production process. This also indicates simultaneously the production technology transition from SM to AM, which is also closely linked to the paradigm 4.0 (see also [1], [8] and [9]). As was shown, this leads to a more efficient production in principle by means of equation (5). The recursive AM process hence leads to the order increase with regard to production, meaning that AM will be in “principal” have a higher potential saving energy costs, by a more efficient production process. The order increase hence is also coupled with an *information compaction or distillation*, or also the same with process, hence *process distillation*, meaning that to produce parts with AM is physically more simple than with SM. But it is far more reaching. Potential applications of AM include multiple parts printed in one process step, whereas with SM each part has to be produced separately and assembled later on to have comparable results. All this is “indicating” the higher order of the production process. The order itself can then be simple explained by a more “efficient” process, as a potential process solution.

6.2. Added Value of this approach to AM

The system theory that investigates the structure of systems therefore can be applied to AM as well as to other disciplines. (1) The first added value can be then to give a better understanding of interdisciplinary processes that occur with AM, as disciplines, like physics, information-, material technology and many others are important for AM. (2) The second added value is to explain more easily the AM process itself as a structural process in the world. To explain why or why not it is an efficient production process. (3) The approach given here allows for predictions how to improve AM: With regard to more energy efficiency, and also with regard to structured feedback systems, necessarily, as well as with phase transitions.

6.3. Outlook

Some questions with the above given approach arise: How can we measure objectively the order increase of the process itself, microscopically and macroscopically and also in an interdisciplinary way? To find methods to prove that the energy order increase is an essential part of

production efficiency, will practically prove the above stated sentence, which is now, more or less a hypothesis. So let me wish good luck to the researchers out there, to find corresponding experimental solutions. To make a prediction: A further increase in order – surely you have to solve the problem of measure order - would extend Figure 3 with (4) and (5) to the paradigm 5.0, meaning a SO production process. And each time a fundamental system change occurs, one “variable” has to be overcome, leading to a third S-Curve with regard to Figure 3, or a new attractor with chaos theory (see eg. [11]), even going sometimes beyond the production efficiency potential of AM. And last but not least one open question there is at the moment: How does the *process compaction, crystallization or distillation* take place and how can it be described more accurately?

ABBREVIATIONS & SYMBOLS

<i>Symbol</i>	<i>Description</i>
A	Work (J)
AM	Additive Manufacturing
c	Speed of Light (m/s)
CNC	Computer Numerical Control
d _i S	Differential Change of Imported Entropy
d _i S	Differential Change of Internal Entropy
dX	Differential of Variable X
E	Energy (J)
E _A	External Energy (J)
i	Index
n	Order of Feedback System
Q	Heat Energy (J)
R&D	Research and Development
S	Entropy (J*K ⁻¹)
S-Curve	Growth Curve
SM	Subtractive Manufacturing

SO	Self-Organizing (Systems)
T	Temperature (K)
U	Internal Energy (J)

REFERENCES

- [1] Lunze, J. (2008) *Automatisierungstechnik*, Oldenburg Verlag, München, 2nd ed.
- [2] Wunsch, G. (2000) *Grundlagen der Prozesstheorie: Struktur und Verhalten dynamischer Systeme in Technik und Naturwissenschaft* Teubner Verlag, Stuttgart.
- [3] Heiden B., Sun X., Decleva M. (2018) *Qualitätssicherungs-labor-konzept für 3-D-Druck*. In: Granig P., Hartlieb E., Heiden B. (eds) *Mit Innovationsmanagement zu Industrie 4.0*. Springer Gabler, Wiesbaden, p. 213-225, DOI: [10.1007/978-3-658-11667-5_17](https://doi.org/10.1007/978-3-658-11667-5_17)
- [4] Mattis, D. C. 2004, *Statistical Mechanics made Simple* World Scientific, New Jersey, University of Utah
- [5] von Förster, H.; H. Schmidt, S. J. (Ed.) (1993) *Wissen und Gewissen: Versuch einer Brücke*, Suhrkamp Taschenbuch Wissenschaft
- [6] Zlokarnik, M. (1991) *Dimensional Analysis and Scale-up in Chemical Engineering*, Springer Verlag, Berlin
- [7] Soldov, A. & Ochkov, V. (2005) *Differential Models*, Springer Verlag
- [8] Heiden, B. (2016) *Wirtschaftliche Industrie 4.0 Entscheidungen - mit Beispielen - Praxis der Wertschöpfung*, Akademiker Verlag, Saarbrücken
- [9] Bauernhansl, T.; ten Hompel, M. & Vogel-Haeuser, B. Vogel-Heuser, B. (Ed.) (2014) *Industrie 4.0 in Produktion, Automatisierung und Logistik* Springer Vieweg Verlag, Wiesbaden 2014
- [10] von Bertalanffy, L. (2009), *General System Theory*, George Braziller, New York, 7th Ed.
- [11] Hilborn, R. C. (1994) *Chaos and Nonlinear Dynamics - An Introduction for Scientists and Engineers*, Oxford University Press, New York

Development of an Additive Manufacturing education and training strategy for South Africa, using the I2P Lab concept

Havenga, S.P.*¹, Department of Technology Transfer and Innovation, Vaal University of Technology, Vanderbijlpark, South Africa, mercurion222@gmail.com; sarelh@vut.ac.za

De Beer, D.J.², DST Chair: Innovation and Commercialisation of Additive Manufacturing, Centre for Rapid Prototyping and Manufacturing, Central University of Technology, Free State, Bloemfontein, South Africa, ddebeer@cut.ac.za

Van Tonder, P.J.M.³, Department of Technology Transfer and Innovation, Vaal University of Technology, Vanderbijlpark, South Africa, malanvt@vut.ac.za

Campbell, R. I.⁴, Department of Technology Transfer and Innovation, Vaal University of Technology, Vanderbijlpark, South Africa, R.I.Campbell@lboro.ac.uk

Van Schalkwyk, F.⁵, Department of Design & Studio Art, Central University of Technology, Free State, Bloemfontein, South Africa, fvschalk@cut.ac.za
email

Additive Manufacturing, in South Africa, progressed significantly from its inception in the early 1990's. Recognised by the South African academia, government and industry as a necessary strategic component of Industry 4.0. Investment in research-and-development led to a nationally accepted implementation strategy for participation in the expansion of a new industry programme for SA. However, suitable training and educational programmes still need to be developed and implemented. Presently, the educational resources and syllabi for manufacturing subjects are outdated. Limited focus has been placed on the formal education of advancing methods for manufacturing or on accessing new techniques for classroom knowledge creation. This study aims to investigate pedagogical solutions to promote additive manufacturing knowledge transfer from within the existing curriculum. The Idea2Product laboratory will be used as a vehicle to facilitate knowledge dissemination and avoid becoming disruptive in an already overburdened environment. These laboratories support educators of technology with learner and teacher support material in a pilot project, in collaboration with the Gauteng Department

of Education. The project, indicates positive results but also identifies obstacles for the assimilation of emerging technologies. Resolution recommendations are made for inclusion in a future curriculum advisory white paper to the Gauteng Department of Education.

Keywords: Additive manufacturing, Idea2Product laboratories, Technology pedagogy, Education, Curriculum development, Technology transfer

1. INTRODUCTION

The Idea2Product (I2P) laboratory model was originally created in 2011 out of the need to uplift a very impoverished Southern Gauteng region and to effectively introduce additive manufacturing (AM) principles through open sourced models to anybody interested in product development. As stipulated in the I2P's social objectives, indirect job creation, economic empowerment, human capital, small and medium-sized enterprise (SME) development, hybridized education and educational

infrastructure are some of the focus areas to effect technology transfer [1].

The I2P model was created with the intention to support any product development from the beginning stage (idea), right through to the final prototype. To minimize cost, open sourced software was used and as long as the prototyping took place inside the I2P model/ laboratory, the training and support was free of cost to the client/student. Although the model is very successful, it was still marginalized in its output/ outreach towards technology transfer. This in part was due to restrictions such as geographical location (laboratories mostly based at higher education institutions), from where funding was raised to operate these facilities.

This, however, severely limits the full extent to which technology transfer can effectively be imparted on potential new clients and especially emerging undergraduate students of technology and users of AM. This has brought about the decision to adapt a formal pedagogical approach for the I2P laboratories to address emerging limitations.

2. BACKGROUND TO STUDY AND LIMITATIONS

2.1. Limitations

AM has not been successfully accepted by some manufacturing and educational industries in South Africa due to its perceived high costs and a lack of knowledge on emerging techniques in the education sector [2, 3]. Current educational manufacturing resources and syllabi for subjects such as technology, design and engineering are outdated. Very little, to no focus has been placed on new advanced methods of manufacturing or accessing new techniques for knowledge creation in the classroom environment [4]. This points to limitations in the current curricula and severely hampers technological advancement and puts high school learners and tertiary students at a critical disadvantage in the global manufacturing market.

The Department of Science and Technology (DST), National System of Innovation (NSI), Department of Education (DoE) and the Southern Gauteng Science and Technology Park (SGSTP), have continuously identified the need to align technological advancement with international standards and imperatives. Outcomes to date, according to reports from the DST, have not been met, to keep up with the rest of the world and the question was raised why the system is not advancing [5].

Problematic areas stand out, why the current education system in South Africa, is not advancing towards the acceptance of AM in the further education and training (FET) phase. These are, the presence of outdated curricula that does not include advancing technology practicum and educators that are unaware and/or not skilled with knowledge of advancing technology. This in turn stops the acceleration of technology transfer which could create and inform industry-ready participation from school leavers.

Furthermore, it should be noted that it becomes problematic to deal with the integration of adaptive pedagogical practices when working with the inclusion of emerging additive manufacturing techniques/ practices in an already overburdened education system. Without very clearly constructed integration methods, the implementation of any supplementary knowledge will become disruptive to the core of the subject matter itself. This concept of disruption can also be interpreted as positive from a disruptive innovation point of view.

2.2. Theoretical Grounding

The theory behind this specific investigation was formulated on philosophical pedagogies, by known scholars of education that are specific to digital fabrication and technology [6, 7, 8 and 9].

The theories that received the most attention to create the teaching practicum and survey, were the 3 pillars of technology pedagogy, additive vs disruptive practices in the classroom, constructionism, constructivism, social constructivism and most importantly the Conceive, Design, Implement and Operate (CDIO) approach principle to technology pedagogy (see page 3).

Schelly mentions that open sources additive manufacturing could potentially improve education by empowering educators through active participation and cross-curricular engagement [7]. They list the cost of science, technology, engineering, arts and manufacturing (STEAM) related equipment as one of the reasons why development has slowed down, but by making use of open sourced free software and entry level material extrusion (ELME) printers in the classroom, costs can dramatically be decreased. Schelly also believes that a student-centred-approach will best suit the introduction of three-dimensional printing (3DP) to the classroom.

One of the leading modern theories to approach 3DP education is Blikstein's Three Pillar teaching model. He states that these three pillars of 3DP learning consists of experiential education, constructionism and critical thinking pedagogy [8]. He bases his theories on three sets of thinking from different schools of thought:

- 1) Education should be experiential and connect to real-world objects based on the theories.
- 2) Critical pedagogy thinking [6].
- 3) Constructionism claims that the construction of knowledge happens remarkably well when students build, make, and publicly share object.

This study will therefore aim to predict if an additive or disruptive system will be more conducive to reach the objectives set by the study. "Disruptive" pedagogy is described as a process whereby technology integration creates "change in teaching approaches because it encourages new ways of teaching and learning" [10]. "Additive" pedagogy as an antithesis, refers to a process

whereby technology is integrated to support existing, often teacher directed and classroom practice.

To investigate this further the research needs to consider other technological pedagogy systems found around the world that does include computer assisted design (CAD) classroom practicum or at the very least, some or other form of digital fabrication construction in the classroom environment. To do so, the questions should be asked where and how 3DP is used in different education systems around the world? Some literature indicates the direct use of 3DP in the classroom as well as indirect use as learner and teacher support materials (LTSMs). However, it is still in the infancy stages and limited due to financial and infrastructure constraints [9].

Ford identifies that a number of studies into 3DP indicate that a lack of education and skills can present barriers to the adoption of technology [11, 12, 13, 14 and 15], which is exactly the state currently experienced in the South African education field.

The CDIO principle approach for technology pedagogy was investigated [16]. These researchers created an experimental course for 3DP pedagogy in Israel. The is to: “Conceive, Design, Implement and Operate”. This approach focuses on five pillars namely: constructivism, social constructivism, instructional scaffolding, constructivism and experiential learning. Verner says that visual literacy is also a key component of the technological literacy and its development is one of the main goals of technology education [p183].

3. METHODOLOGY

This paper introduces a section of an extensive pilot program, through the I2P laboratory in collaboration with the Gauteng Department of Education. The study follows a mixed methods research paradigm, underpinned with principles of experiential learning. In-depth qualitative data collection was collected by means of an anonymous online survey supplied to a closed population group, consisting of facilitators and educators for technology-based subjects. This survey was introduced after the first phase of the pilot project was executed.

This initial phase included both theoretical and practical training followed by formative and summative assessments. The first pilot workshop took place over the course of 5 days and the following workshops took place as two, one day workshops every month, over 6 months.

Out of an initial 70 educators/ schools identified, 15 partook in the final pilot study.

The data was extrapolated from the online surveys to make predictive interpretations and suggest implementation in secondary schooling system for STEAM subjects. The study includes descriptive material collected and then extracted from the surveys after the first phase of the pilot project was concluded.

The main author made use of primary research data collecting by means of learning material development, fieldwork, conducting interviews, constructing a pilot project, implementation of the pilot and analysing all data to construct the survey. Specific questions were formulated to gain insight into providing a syllabus suggestion for STEAM subjects, in the form of learner teacher support material (LTSM). These LTSMs will then be constructed and implemented in participating schools in the next phase.

The above theories and principles were experimentally introduced during the educators’ workshops to investigate its effectiveness in a South African social-economic and geographical setting. The outcomes were then investigated for successes, failure-to-implementation and written up.

A BETA curriculum model is being constructed and will be suggested for a future inclusion in an educational advisory white paper for the South African Department of Education.

4. RESULTS

During the first cycle of the pilot study (6 months), the project was implemented and monitored on a bi-monthly basis and the following results were collected after the anonymous online survey, containing reflective questions, were completed by all the active members in the pilot population group.

The first question asked what the respondents have learned so far, by attending the 3DP educator workshops at the Vaal University of Technology (figure 1).

An overall of forty percent of the respondents felt that they have acquired CAD skills while eighty percent of them documented learning more about 3DP operations and practice. A further forty-seven percent expressed learning

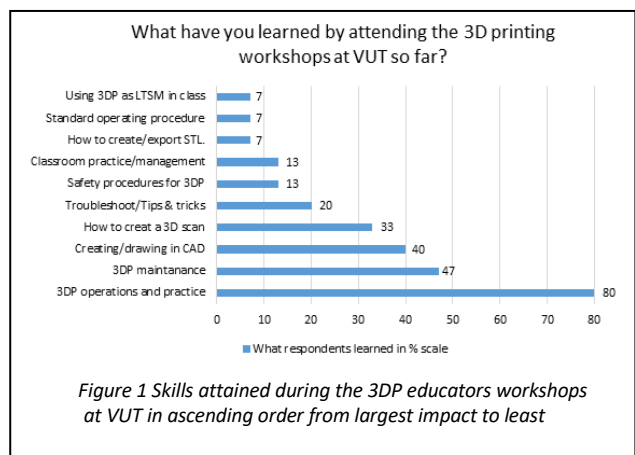


Figure 1 Skills attained during the 3DP educators workshops at VUT in ascending order from largest impact to least

about appropriate maintenance and thirty-three percent remarked learning about 3D scanning.

Twenty percent of the respondents said they learned how to troubleshoot and received valuable tips and tricks to address working with 3DP technology. A further thirteen

percent said they learned how to safely operate 3DP equipment and also learned improved classroom management and practice.

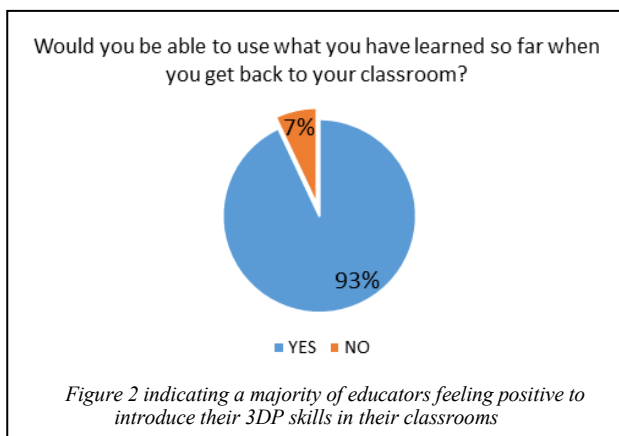
A much smaller group of only seven percent indicated 3DP as LTSM, standard operating procedures (SOPs) and stereolithography (STL) file creation were learned during the workshops. One respondent overcame their fear of the technology and stated they now realize the technology not just for engineers and can be used at any age by any gender.

The relatively small influence of managing classroom 3DP practice, SOPs and safety procedures can be ascribed to being a new idea and uncertainty experienced amongst the educators. Therefore, pointing to a lack of 3DP classroom pedagogy.

It is important to observe that sixty-seven percent of the educators felt that they acquired CAD skills from the open-sourced package used for this pilot study. Almost half of the educators have been exposed to other proprietary CAD training software, through projects such as the graphic activities for a new generation (GANG) initiative.

The second question asked whether the respondents would be able to take back to their classrooms what they have learned. If, they answered YES, they were asked how they would do it and if the answer was NO, they were asked, WHY?

Overall, ninety-three percent of the respondents felt that they will be able to integrate what they learned in their classrooms (figure 2). Some respondents said they will introduce it into their learning material but a majority said they would use it as LTSMs (figure 3). LTSMs seems to be a favourite for educators that feel there are time constraints but that physical 3DP models will be an advantage in the classroom as sensory aids.

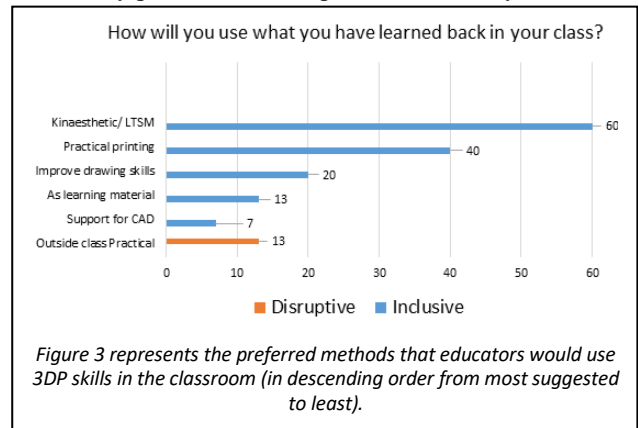


Further suggestions were made to select the most advance learners and permit them-only to use the technology, but other research suggest that it will be more advantageous if all the learners are exposed [8]. This inclusion also suggests to will improve learners drawing skills and heighten their performance in the classroom.

Furthermore, abstract visualization of more complex shapes will be helped by including LTSMs.

Figure 3 shows in descending order the popular choices of implementation as discussed by the respondents. Although ninety-three percent of the respondents indicated that they wish to use this technology in their classrooms, sixty percent of them indicated that this should be done as LTSMs and only forty percent are feeling confident to use it in a practical lesson.

Twenty percent of the respondents said they will use it

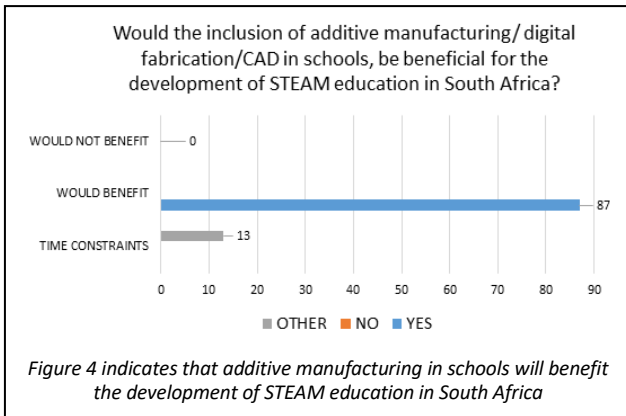


to enhance the learners instrument drawing skills, a further thirteen percent said they will use it as learning material in the classroom and only seven percent felt it should be used as a support to CAD. It should also be noted that thirteen percent of the respondents felt that it would be disruptive to the classroom and should only be used extracurricular.

The third question asked whether the inclusion of additive manufacturing/ digital fabrication/ CAD into school curriculum would benefit the development of STEAM education in South Africa.

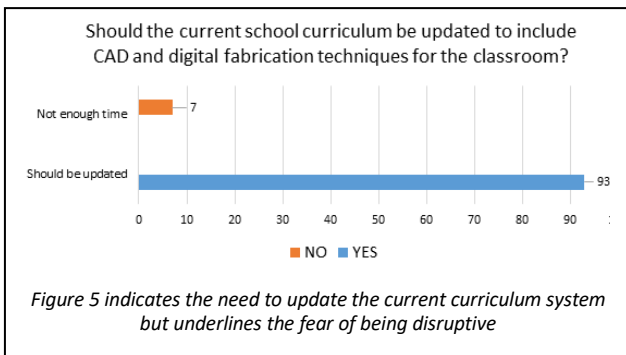
One-hundred percent of the respondents agreed that the inclusion of AM, digital fabrication (DF) and CAD in schools will promote STEAM education in South Africa. Eighty-seven percent said it will have a positive outcome, but thirteen percent cautioned against the disruption that this inclusion might cause due to restrictive donation hours available for instruction (figure 4). One respondent suggests that notional time be allocated for this and not be moved to extracurricular time.

It is clearly indicated that all respondents feel that AM/DF will benefit the development of STEAM education in South Africa, but that caution should be heeded to avoid becoming disruptive due to limited instruction time in the classroom



The fourth question asked whether the current curriculum should be updated to include CAD and digital fabrication in the classroom environment.

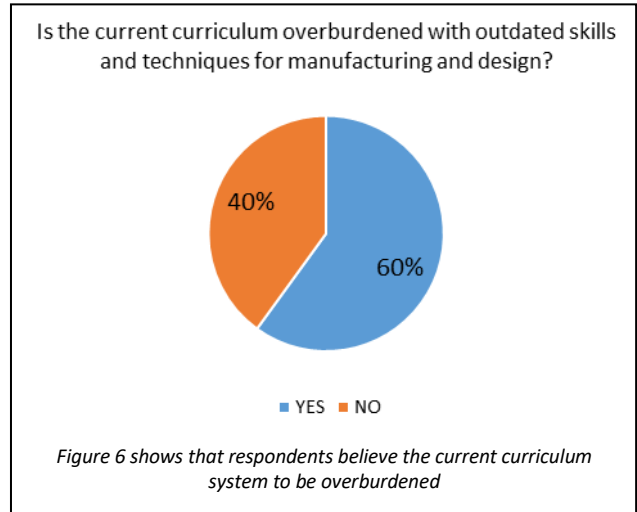
Ninety-three percent of the respondents felt that the current curriculum should be updated for both the Technology and Engineering, Graphics and Design (EGD) subjects (figure 5). They also agreed that it should include CAD and digital fabrication. In the senior phase where Technology is presented neither CAD nor DF is presented. In the FET phase only CAD is presented minimally. Seven percent of the respondents remarked that the notional time for the subjects should be increased before it can be included.



Question five asked if the current curriculum is overburdened with outdated skills and techniques; and furthermore if there is enough time to introduce new principles during instruction time.

Sixty percent of the respondents felt that the curriculum is overburdened and that some of the skills and techniques for manufacturing could become outdated.

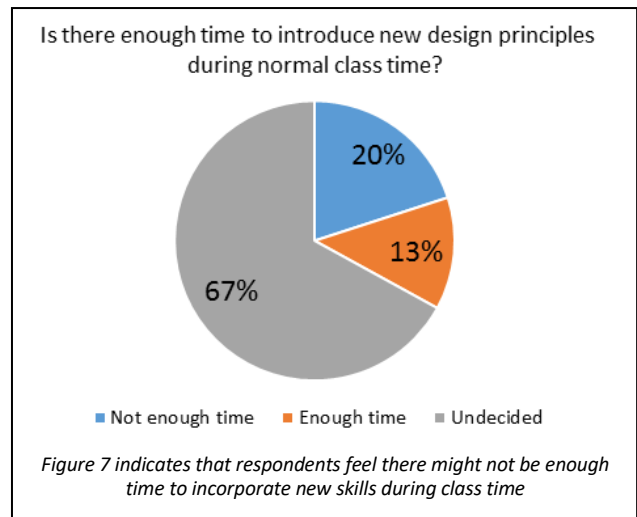
The further forty percent of the respondent remarked that although basic skills create the foundation, emerging technology is advancing past the current curriculum inclusion (figure 6). This remaining forty percent also argues that the basic skills pave the foundation for technology and warns against the disruption that a lack of notional hours could cause.



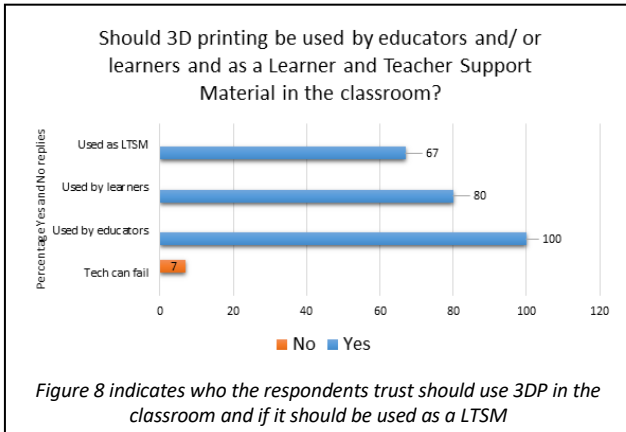
This can be observed in figure 7 where a total of twenty percent believes there to be a shortage of notional instruction time, versus thirteen percent saying there is enough time if the lesson is planned properly. Sixty-seven percent of the respondents decided not to comment, indicating the delicate nature of the debate.

Most surprisingly some respondents feel that the current electricity infrastructure system in South Africa poses a problematic obstacle for the inclusion of 3DP/ DF and that traditional hard skills will empower the students more than advancing tech.

Question six asked if the use of DF/ 3DP in the classroom should be restricted to the educator or used but learners too; OR should it only be used as a learner teacher support materials LTSMS in the classroom?

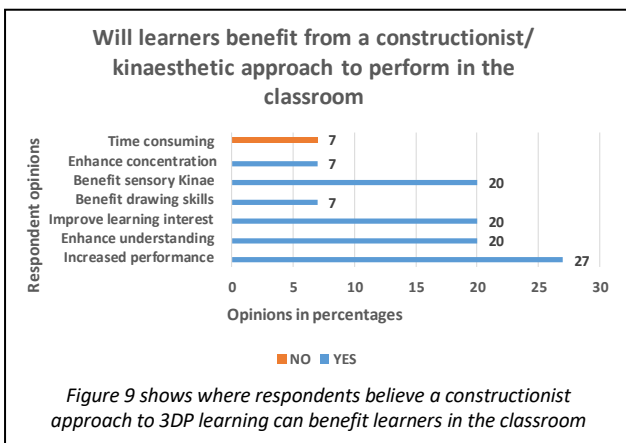


In figure 8 it is shown that one hundred percent of the respondents feel that educators should use 3DP in the classroom. Eighty percent of the respondents trust learners to be capable to use 3DP in the classroom, however some respondents are reluctant to let learners use it in class due to fears that the technology might fail in classroom. Sixty-seven percent of the respondents feel 3DP/DF should rather be used as LTSMs in the classroom.



Question seven addressed whether the respondents agreed that learners will benefit more from a constructionist/ kinesthetic learning approach. The respondents were also asked to identify how this will benefit the learners.

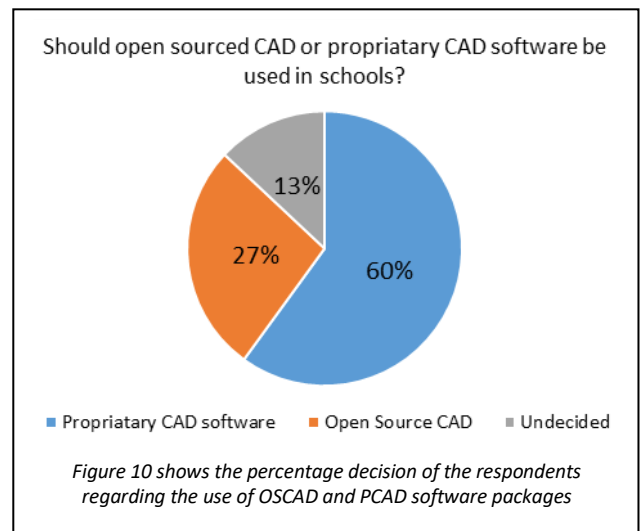
One hundred percent of the respondents feel that a constructionist/ kinaesthetic approach to learning in the classroom would be more conducive for knowledge absorption than traditional linguistic reading. Below in figure 9 all the areas are indicated where the respondents felt this could benefit.



Seven percent of the respondents said it would enhance the concentration of the learners and instrument drawing skills. It was also identified that the increased experience of technology exposure would benefit learner-centered-teaching, according to twenty percent of the respondents. Twenty percent of the respondents believed it improves the

learners' subject understanding. Twenty percent felt that constructionist learning enhance sensory interaction. Another twenty-seven percent said that constructionist learning will benefit the performance in classroom without any further explanation. Only seven present of the whole survey group felt that a constructionist approach would be disruptive due to time constraints.

Question eight asked whether respondents prefer open sourced CAD (OSCAD) software or proprietary CAD (PCAD) software. Twenty-seven percent of the respondents feel that OSCAD will benefit learners and that it will not restrict schools with the use of expensive proprietary software (figure 10).

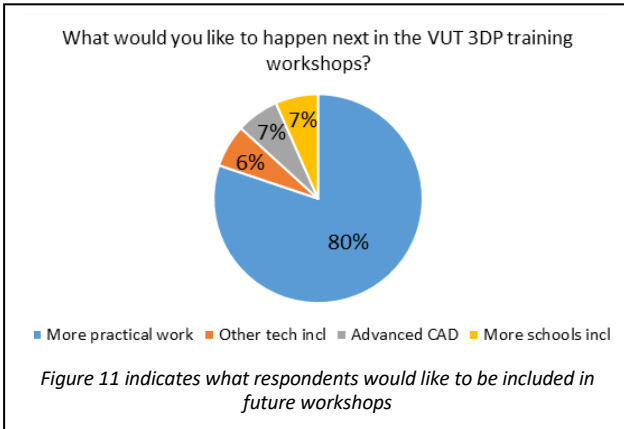


However, sixty percent of the respondents felt that formal training and specific proprietary CAD packages such as AUTOCAD should be used. According to these respondents such training would benefit educators most to empower them with the skills needed, but at a much higher cost, that some educators and learners cannot afford. It should be noted that most PCAD packages have restricted-function educational licences available where schools cannot afford the software. Thirteen of the respondents refrained from answering directly.

OSCAD software could be more readily available in the schools. The leading author is of the opinion that educator opinions may be biased here, due to exposure/intervention of the pilot program where they do not have to provide infrastructure for their schools. Some opinions are also biased as part of the overall pilot population has been exposed to PCAD through the GANG program.

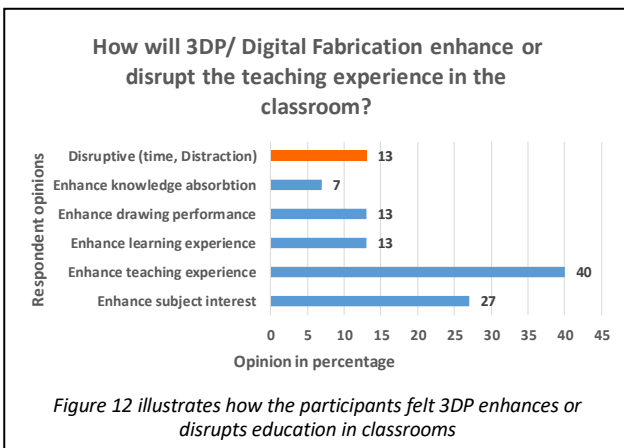
Question nine asked the respondents what they felt would be the most important to address next in the future 3DP workshops at the Vaal University of Technology.

Eighty percent of the respondents suggested more practical exercises for the pilot educators program (figure 11). Seven percent of the respondents suggested more exposure to other complimentary tech such as seen in the FabLab/ Makerstation models. Another seven percent of the respondents suggested more advanced CAD drawings and more schools should be involved in the study.



Question ten asked whether the respondents felt that the inclusion of 3DP in the classroom will enhance or disrupt knowledge absorption and how.

One-hundred percent of the respondents felt that 3DP in the classroom would enhance the teaching experience, empower learners to take control of their creations, help them to absorb information, enhance performance, form better subject understanding and improve lessons (figure 12).



This can be divided into thirteen percent of the respondents saying it will enhance the learning experience; forty percent feeling it will enhance the teaching experience; thirteen percent says it will enhance learning through LTSMs; another thirteen percent believe it will enhance instrument drawing; and seven percent believes it will enhance knowledge absorption and twenty-seven percent subject interest.

However, thirteen percent of the respondents felt that it might be disruptive due to time constraints and learners that will become distracted (not focus on lesson/ or keychain-consumer syndrome).

5. CONCLUSION AND RECOMMENDATIONS

It is evident that most participants felt that 3DP workshops/ training helped educators to operate, make use of and maintain 3D printers. Over ninety-three percent of the participants felt confident that they will be able to use their new skills in the classrooms.

There is a sixty to forty percent ratio favoring the use of 3DP for LTSMs rather than using it for classroom practicum, which mostly points to frustration experienced due to time constraints.

But when asked whether the inclusion of AM/CAD in schools will be beneficial for the development of STEAM education in South Africa, eighty-seven percent of the participants agreed. An even larger ninety-three percent of the participants said the curriculum should include digital fabrication and CAD.

More than half of the participants feel that the current curriculum system is outdated but at the same time they feel that there is not enough time to introduce new ideas during instructional time. Most of the participants feel that both educators and learners can use digital fabrication and CAD in the classroom, however, mostly as an LTSM.

All participants except seven percent, felt that learners benefit from a constructionist/ kinesthetic learning approach, which clearly points to a shift towards a more organic learner-centered teaching approach.

Surprisingly, a majority of participants favored proprietary CAD software above open sourced software, even though a large number of schools are burdened by funding and other social economic limitations.

A majority of the participants favored more practical instruction during the workshop time to improve their skills and confidence.

Even though a lack of knowledge on emerging techniques in the education sector are present, it is very clear that educational practitioners are eager for the inclusion of AM into their subjects. Although, the current curriculum contains limited literature on digital fabrication/ AM, this obstacle can be overcome by integrating technology into the current pedagogy by means of LTSMs.

The FET phase are not equipped to introduce CAD and AM as a separate subject but the principles taught through constructionist LTSMs, in the STEAM subject band, will enable school-leavers with critical knowledge on emerging technologies.

From the survey feedback it is evident that the DSTs need to align technological advancement with international standards and imperatives for South Africa could be

achieved when more people are exposed to technology in an educational capacity in the FET band. Learners should not just be exposed to 3DP technology through technology transfer alone, but taught the principles and operations of emerging technology. Blikstein states: "...avoid the "keychain syndrome" in the classroom, where learners want to use 3DP only to mass produce cheap trinkets instead of developing ideas" [8].

Educators are eager to learn and adapt with the new skills and technologies and more formal training material (LTSMs) and practical workshops are suggested to develop and streamline a workable teaching model that can be recommended to the department of education in South Africa.

REFERENCES

[1] De Beer, D. and Campbell, R., 2017. Using Idea-2-Product Labs ® as a strategy for accelerating technology transfer. *International Journal of Technology Transfer and Commercialisation* 14(3-4), pp.249-261.

[2] Pacey, E. 2013. Additive manufacturing: Opportunities and constraints. Published by Royal Academy of Engineering, Prince Philip House. Available from: www.raeng.org.uk/AM ISBN: 978-1-909327-05-4

[3] Serlenga, P & Montaville, F. 2015. Five questions to shape a winning 3-D printing strategy. Bain & Company, Inc.

[4] EGD CAPS. 2011. National Curriculum Statement policy (Final draft). Accessed on 21 April 2018. Available from: <https://www.education.gov.za/LinkClick.aspx?fileticket=pqcxCwUTO98%3D&tabid=570&portalid=0&mid=1558> ISBN: 978-1-4315-0583-8

[5] Department of Science and Technology. 2017. The Ten-Year Plan for Science and Technology. Available from: <http://www.dst.gov.za/index.php/resource-center/strategies-and-reports/143-the-ten-year-plan-for-science-and-technology> Accessed on: 10 June 2017

[6] Freire, P. (1974). *Pedagogy of the oppressed*. New York,: Seabury Press.

[7] Schelly, C., Anzalone, G., Wijnen, B. and Pearce, J. M (2015). Open-source 3-D printing Technologies for education: Bringing Additive Manufacturing to the Classroom. *Journal of Visual Languages & Computing*. 28 (2015) 226–237. DOI: 10.1016/j.jvlc.2015.01.004

[8] Blikstein, P. (2013). Digital Fabrication and 'Making' in Education: The Democratization of Invention. In J. Walter-Herrmann & C. Büching (Eds.), *FabLabs: Of Machines, Makers and Inventors*. Bielefeld: Transcript Publishers.

[9] Ford, S. and Minshall, T. 2016. 3D printing in education: a literature review. Institute for Manufacturing. University of Cambridge, United Kingdom. Centre for Technology Management. Accessed on the 5 May 2018. Available from: https://www.researchgate.net/publication/308204294_3D_printing_in_education_a_literature_review DOI: 10.13140/RG.2.2.16230.83526

[10] Hedberg, J. G., & Freebody, K. (2007). Towards a disruptive pedagogy: Classroom practices that combine interactive whiteboards with TLF digital content. Retrieved 15.08.07, from Melbourne: Le@rning Federation. Available from: http://www.thelearningfederation.edu.au/verve/_resources/towards_a_disruptive_pedagogy.pdf

[11] Royal Academy of Engineering (2013). Additive manufacturing: opportunities and constraints. A summary of a roundtable forum held on 23 May 2013 hosted by the Royal Academy of Engineering.

[12] Government Office for Science (2013). What are the significant trends shaping technology relevant to manufacturing? Future of Manufacturing Project: Evidence Paper 6.

[13] EC (2014). Additive Manufacturing in FP7 and Horizon 2020: Report from the EC Workshop on Additive Manufacturing held on 18 June 2014.

[14] Despeisse, M. & Ford, S. 2015. The Role of Additive Manufacturing in Improving: Resource Efficiency and Sustainability. Institute for Manufacturing. University of Cambridge, United Kingdom. Centre for Technology Management working paper series. ISSN 2058-8887

[15] Despeisse, M., Baumers, M., Brown, P., Charnley, F., Ford, S.J., Garmulewicz, A., Knowles, S., Minshall, T., Mortara, L., Reed-Tsochas, F. & Rowley, J. (2016). Unlocking value for a circular economy through 3D printing: a research agenda. *Technological Forecasting & Social Change*, Forthcoming.

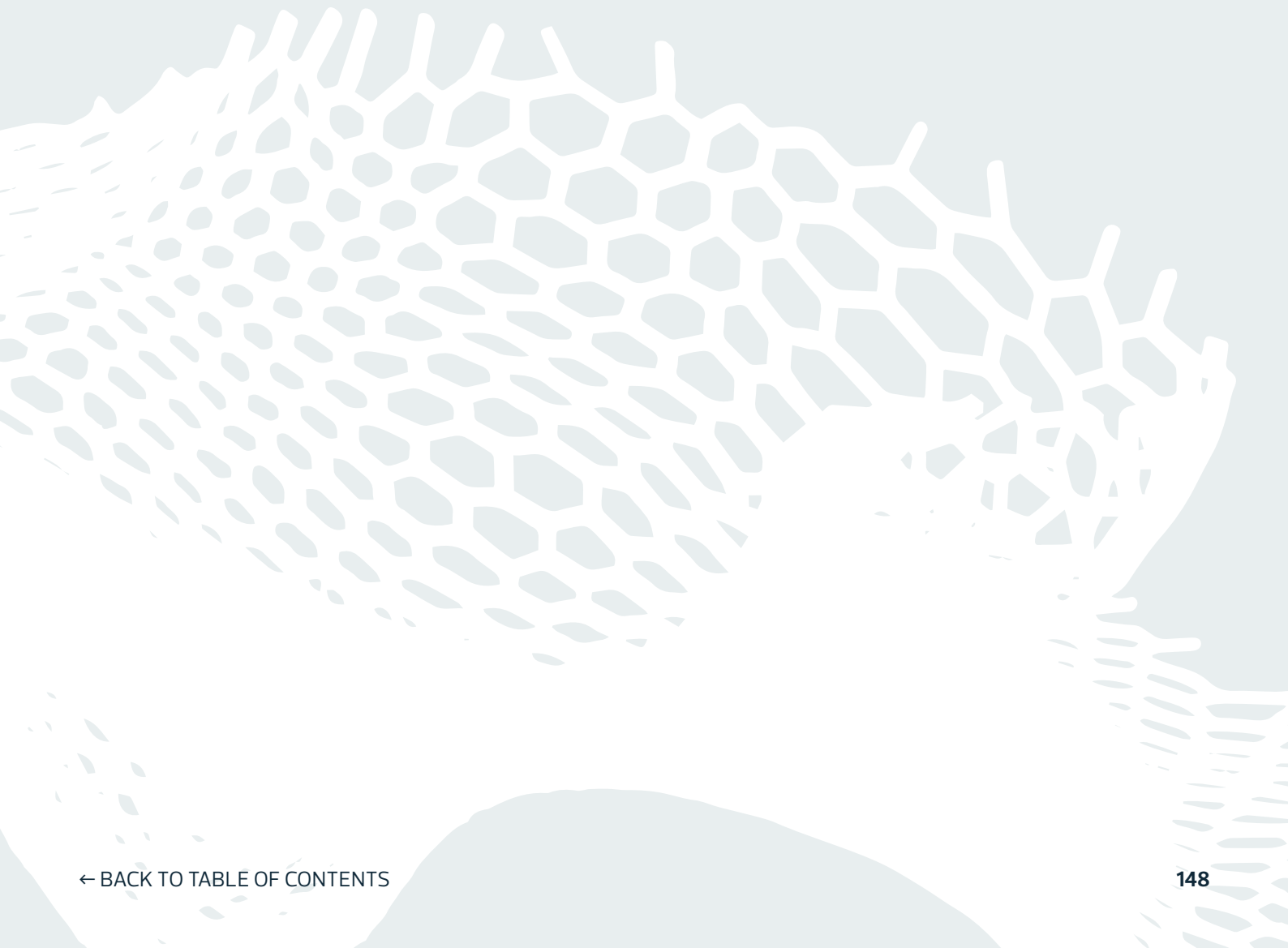
[16] Verner, I., & Merksamer, A. (2015). Digital Design and 3D Printing in Technology Teacher Education.

LIST OF FIGURES

- Figure 1 Skills attained during the 3DP educators workshops at VUT in ascending order from largest impact to least.
- Figure 2 indicating a majority of educators feeling positive to introduce their 3DP skills in their classrooms
- Figure 3 represents the preferred methods that educators would use 3DP skills in the classroom (in descending order from most suggested to least).
- Figure 4 indicates that additive manufacturing in schools will benefit the development of STEAM education in South Africa
- Figure 5 indicates the need to update the current curriculum system but underlines the fear of being disruptive
- Figure 6 shows that respondents believe the current curriculum system to be overburdened
- Figure 7 indicates that respondents feel there might not be enough time to incorporate new skills during class time
- Figure 8 indicates who the respondents trust should use 3DP in the classroom and if it should be used as a LTSM
- Figure 9 shows where respondents believe a constructionist approach to 3DP learning can benefit learners in the classroom
- Figure 10 shows the percentage decision of the respondents regarding the use of OSCAD and PCAD software packages
- Figure 11 indicates what respondents would like to be included in future workshops
- Figure 12 illustrates how the participants felt 3DP enhances or disrupts education in classrooms

CHAPTER 5.

AM Process - Polymers



Thermal rounding of particles in a downer reactor: Direct vs. indirect heating

Manufacturing and Characterization

J.S. Gómez Bonilla, A. Chiappina, M.A. Dechet, J. Schmidt, A. Bück, K.-E. Wirth, W. Peukert*,
Institute of Particle Technology (LFG), Friedrich-Alexander-Universität Erlangen-Nürnberg, Erlangen,
Germany, wolfgang.peukert@fau.de

Abstract—In this work we present a study on operating a downer reactor for thermal rounding of polymer particles with direct, convective and indirect heating of the material. We show for high density polyethylene (HD-PE) that convective heating is beneficial with respect to yield and flowability of the product, conserving the degree of crystallinity, but leading to a significant change in particle size distribution and subsequently in the degree of shape transformation. Conversely, indirect heating of the reactor shows better results in terms of particle size and shape, but with lower product yield and flowability.

Keywords- polymers; rounding; downer reactor; convective heating; contact heating; radiation

1. INTRODUCTION

Spherical particles of defined size are sought in many applications due to their superior flowability, resulting in easy transport and dosing of the particulate material.

Dosing behaviour is of high importance in the field of additive manufacturing by selective laser sintering (SLS) or melting (SLM). There, a part is created layer-by-layer by sintering (or melting and subsequent constitution) of a dosed powder layer [1, 2, 3]. For uniform structure of the created part, a uniform powder distribution is required.

Polymer powders used in SLS can be created by different routes, e.g. by direct polymerization, cryogenic grinding or precipitation [1, 4], melt emulsification [5], or wet grinding [6, 7]. Especially the latter process generates non-spherical particles of irregular shape (Fig. 1), which are difficult to handle and dose and require further treatment.

One route to obtain spherical particles from non-spherical primary particles is by thermal rounding in a downer (tubular) reactor which has recently been developed and tested for a wide range of polymers. In the downer reactor, the material is exposed to heat provided by

wall heating in a falling motion. It partially melts and due to fluid and gravitational forces takes a spherical shape. The operation of such a downer reactor has recently been characterised with respect to the required exposure time and temperature profile along the downer reactor length [8]. Figure 2 shows exemplarily the outcome of the processing of the initial material shown in Fig. 1.

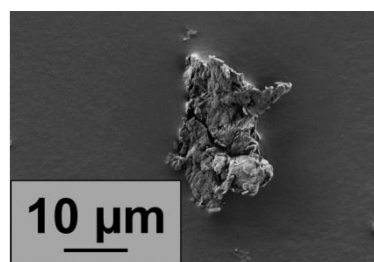


Fig. 1. Primary polymer particle (PBT) after wet milling [8].

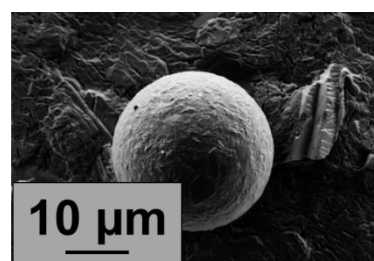


Figure 2. Particle after thermal treatment in downer reactor [8].

Although the quality of the obtained product was very good in terms of shape, the flowability, dosing behaviour and the yield of the process was very low, in some cases even less than 35 mass-% related to the supplied mass of polymer powder. This observation may in part be attributed to the indirect heating of the processed material.

In this contribution, we present a study of direct convective heating of the polymer particles by the transport gas, comparing heat transfer characteristics for both, direct and indirect (wall) heating. We finish with the presentation of improved flow behaviour and yield while simultaneously preserving product quality, for example crystallinity.

2. EXPERIMENTAL METHODS AND MATERIALS

This section provides an overview of the methods and equipment used to perform the design optimization study.

2.1. Description of downer reactor

Rounding of the host particles can be achieved in the downer reactor shown in Fig. 3. It has an inner diameter of 100 mm and a total length of 1.2 m. The downer walls are heated by an electric heater, consisting of several heating elements, which can be controlled independently. The particles are conveyed as an aerosol to the pre-heated downer reactor and the polymer is transferred to semi-molten state along the heat transfer routes wall-gas-particle (indirect) and particle-wall-collisions and to a certain extent, radiation. Surface tension and gravitational force allow the formation of a spherical shape on its trajectory along the downer length. Reducing the temperature towards the outlet allows cooling and consolidation of the spherical particles, which are then separated from the process gas by a cyclone. The proof-of-principle and a preliminary characterisation of this reactor concept have been reported in Sachs et al. (2017) [4].

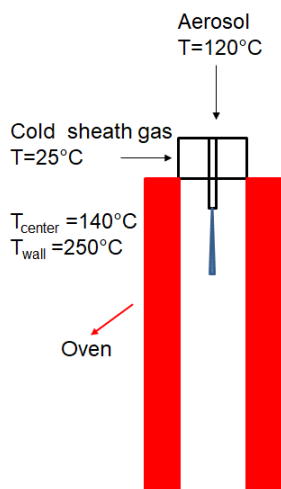


Figure 3. Design of the downer reactor with indirect (wall) heating. Note the significantly higher wall temperature required to achieve the centre temperature of 140 °C.

In the modified downer reactor (Fig. 4), wall heating is not used but the sheath gas used to convey the particles into the reactor is heated. In that way direct heat transfer from the gas to the particle dominates. Due to the lower wall temperatures, radiation is not a significant heat transfer mechanism. The conveyed particles are heated by the gas and a semi-molten state is achieved which again

yields a spherical shape under the action of surface tension and gravity.

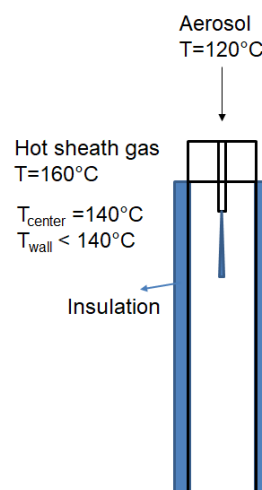


Figure 4. Design of the downer reactor with direct convective heating of the particles by the heated sheath gas.

In order to have comparable process results, flow conditions are identical in both designs and the gas temperature at the particle inlet are identical. (This requires a much larger wall temperature as indicated in Fig. 3.)

2.2. Materials

For the experiments, high-density polyethylene HD-PE (Coathylene® NB 6454-F, Axalta polymers powders, Switzerland) particles with the particle size distribution (number density, q_0) shown in Fig. 5 are used. The melting of HD-PE is initiated at a temperature of 130 – 145 °C; glass transition of the pure component (without any plasticiser) is reported to occur at 70 °C [9]. The feed rate of PE is approximately 200 g/h. The process is operated in a nitrogen (N_2) atmosphere with a sheath volume flow rate of 7 Nm³/h.

2.3. Characterisation

Particle size distributions are measured by laser diffraction (Mastersizer 2000, Malvern Panalytical GmbH, Germany); flowability, expressed by the Jenike flow function ffc , is measured by a Schulze ring shear tester (RST-01, Dr.-Ing. Dietmar Schulze Schüttgutmesstechnik GmbH, Germany). The higher the value of the ffc function, the better the flow behaviour. Crystallinity of the material before and after processing is assessed by evaluating changes in specific melting enthalpies obtained from differential scanning calorimetry DSC (DSC 8000, PerkinElmer GmbH, Germany).

3. RESULTS

3.1. Particle size distribution and shape

The normalised number-based particle size distribution densities q_0 of the initial PE powder, the

powder thermally rounded in the downer reactor with wall heating and rounded by convective heating are shown in Fig. 5. One can observe that initially, a bi-modal distribution is present in the reactor, which is shifted towards the coarse fraction during rounding. The main difference between the two designs is that in case of the indirectly heated reactor still a large portion of small particles is present in the product, which can also be seen in the SEM image (Fig. 6), whereas in case of the convectively heated process, all small particles have been eliminated and all sizes are concentrated in the size range of the initial coarse fraction. This means that particles predominantly agglomerate (either by sintering of primary particles or melting of small particles and coalescence of droplets). Consequently, the achieved shape transformation is not as complete as in case of the indirectly heated process (SEM image, Fig. 6). Control of agglomeration and shape transformation require a more in-depth look into the occurring micro-processes and are the topic of separate, on-going work.

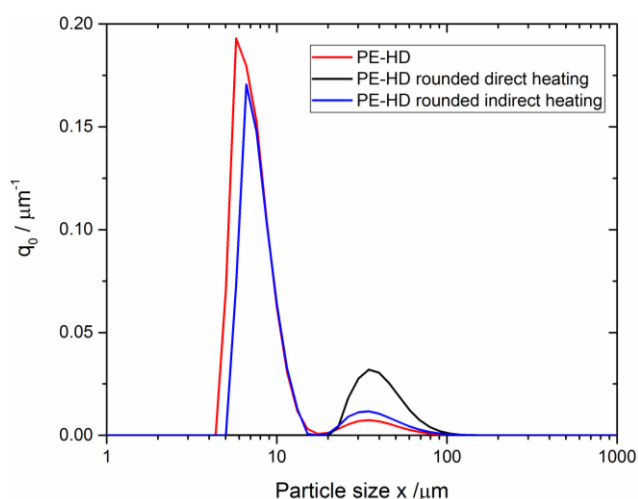


Figure 5. Normalised number-based particle size distribution densities (q_0) of the initial and treated PE powder.

In terms of product yield, measured with respect to the initial mass of PE supplied to the process, in the indirectly (wall-)heated configuration approximately $(32 \pm 6)\%$ (three repetitions) of the initial material is recovered. The remaining 68% (on average) are deposited at the reactor walls, requiring high-temperature cleaning of the apparatus after each experiment.

In the directly heated configuration ca. $(85 \pm 1)\%$ of the initial mass is recovered. This huge improvement in yield can be explained with the lesser risk of sticking of partially molten polymer particles at the (colder) reactor walls.

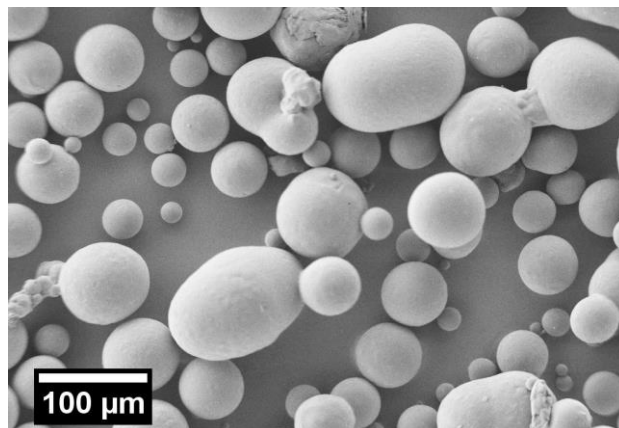


Figure 6. SEM image of product particles obtained from thermal rounding with indirect heating, showing a large variety of particle sizes.

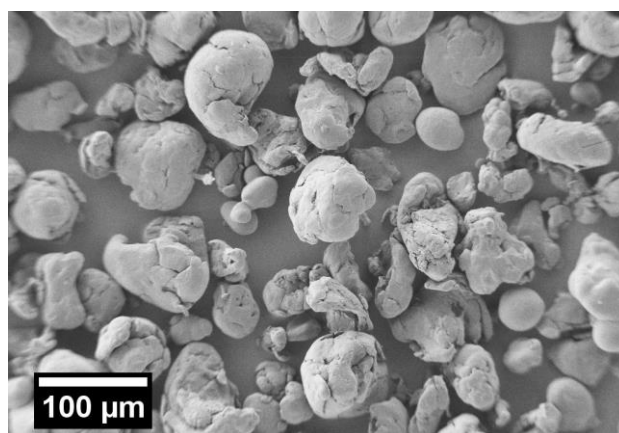


Figure 7. SEM image of product particles obtained from thermal rounding with direct heating (same magnification as in Fig. 6).

3.2. Flowability (ffc function)

With respect to the heating mode, the design with direct (convective) heating of the polymer particles provides a better flowing product in terms of the value of the ffc function (Fig. 8). A slight decrease in the flowability is observed for the material treated in the indirectly heated reactor. This is due to the large spread in particle size distribution, with significant amounts of fines and agglomerates at either end of the size spectrum (see Fig. 5). Compared to this, the particle sizes are much more concentrated in case of the convectively heated particulate material.

3.3. Crystallinity

Results for the changes in crystallinity are obtained from the DSC plots shown in Fig 9. The measured specific melting enthalpies are 167.93, 161.44 and 169.54 J/g for the un-treated material, the rounded product with direct heating and the rounded product with indirect heating, respectively. The measured specific melting enthalpies are related to the melting enthalpy of fully crystalline HD-PE (290 J/g) [10] to obtain the crystallinity.

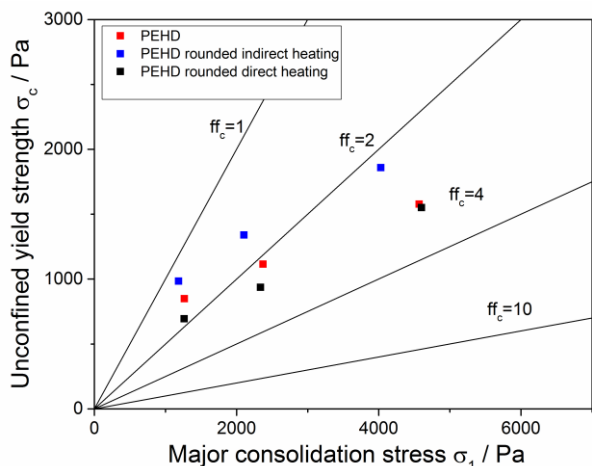


Figure 8. Results of the flowability measurements after Jenike (ffc function) for the un-treated and the two treated PE powders.

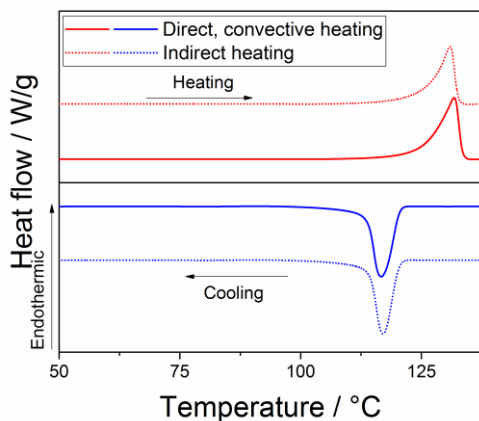


Figure 9. Heat flow vs. temperature diagram obtained from DSC measurement for rounded material with direct and indirect heating.

The initial degree of crystallinity was determined to be 58 %; the crystallinity of the powder rounded in the apparatus with direct heating was 58 %; in the downer reactor with indirect heating a value of about 55 % was obtained, showing no drastic change in either configuration but with a slight advantage of the indirectly heated design with respect to conservation of the degree of crystallinity.

4. CONCLUSIONS AND OUTLOOK

In this work, we presented an experimental study on operating a downer reactor for thermal rounding of polymer particles with direct, convective and indirect heating of the material. We showed for HD-PE that convective heating is beneficial with respect to yield and

flowability of the product, conserving the degree of crystallinity, but leading to a significant change in particle size distribution and subsequently in the degree of shape transformation. Conversely, indirect heating of the reactor shows better results in terms of particle size and shape, but with lower product yield, flowability and crystallinity.

With respect to agglomeration of the material, especially in the directly heated configuration, an in-depth study of the micro-processes taking place, for example partial melting, sintering of solid primary particles, coalescence of fully molten droplets, sticking to apparatus walls etc., has to be performed. Furthermore, full care of the particle size and shape distribution of the initial material as well as the flow field in the reactor has to be considered, to a) be able to design thermal rounding processes and b) control the degree of agglomeration.

ACKNOWLEDGMENT

This study has been supported by Deutsche Forschungsgemeinschaft (DFG) within the framework of the collaborative research center CRC 814 “Additive Manufacturing” (project A2). Financial support is gratefully acknowledged.

REFERENCES

- [1] Wohlers, T.T., 2016, ‘Wohlers Report 2016’, Wohlers Associates inc., Fort Collins.
- [2] Schmid, M., 2015, ‘Selektives Lasersintern (SLS) mit Kunststoffen: Technologie Prozesse und Werkstoffe’, Hanser, Munich.
- [3] Goodridge, R.D., Tuck, C.J., Hague, R.J.M., 2012, ‘Laser sintering of polyamides and other polymers’, *Progress in Material Science*, vol. 5, pp 229–267.
- [4] Kloos, S., Dechet, M.A., Peukert, W., Schmidt, J., 2018, ‘Production of spherical semi-crystalline polycarbonate microparticles for Additive Manufacturing by liquid-liquid phase separation’, *Powder Technology*, vol. 335, pp. 275-284.
- [5] Faselow, S., Ehsan Emamjomeh, S., Wirth, K.-E., Schmidt, J., Peukert, W., 2016, ‘Production of spherical wax and polyolefin microparticles by melt emulsification for additive manufacturing’, *Powder Technology*, vol. 141, pp. 282-292.
- [6] Schmidt, J., Sachs, M., Blümel, C., Winzer, B., Toni, F., Wirth, K.-E., Peukert, W., 2014, ‘A novel process route for the production of spherical LBM polymer powders with small size and good flowability’, *Powder Technology*, vol. 261, pp. 78-86.
- [7] Schmidt, J., Plata, M., Tröger, S., Peukert, W., 2012, ‘Production of polymer particles below 5 μm by wet grinding’, *Powder Technology*, vol. 228, pp. 84-90.
- [8] Sachs, M., Friedle, M., Schmidt, J., Peukert, W., Wirth, K.-E., 2017, ‘Characterization of a downer reactor for particle rounding’, *Powder Technology*, vol. 316, pp. 357-366.
- [9] RIWETA 4.2 Material Database, Kern GmbH, Germany
- [10] Richardson, M. J., 1972, ‘Precision differential calorimetry and the heat of fusion of polyethylene’, *Journal of Polymer Science Part C*, vol. 38, pp. 251-259.

Influence of powder bed surface on part properties produced by selective laser beam melting of polymers

Sandra Greiner, Institute of Polymer Technology, Friedrich-Alexander-Universität Erlangen-Nürnberg, Collaborative Research Center 814 – Additive Manufacturing, Germany, greiner@lkt.uni-erlangen.de

Lydia Lanzl, Institute of Polymer Technology, Collaborative Research Center 814 – Additive Manufacturing, Friedrich-Alexander-Universität Erlangen-Nürnberg, Germany, lanzl@lkt.uni-erlangen.de

Meng Zhao, Institute of Polymer Technology, Collaborative Research Center 814 – Additive Manufacturing, Friedrich-Alexander-Universität Erlangen-Nürnberg, Germany, zhao@lkt.uni-erlangen.de

Katrin Wudy, Institute of Polymer Technology, Collaborative Research Center 814 – Additive Manufacturing, Friedrich-Alexander-Universität Erlangen-Nürnberg, Germany, wudy@lkt.uni-erlangen.de

Dietmar Drummer, Institute of Polymer Technology, Collaborative Research Center 814 – Additive Manufacturing, Friedrich-Alexander-Universität Erlangen-Nürnberg, Germany, info@lkt.uni-erlangen.de

Abstract— The process of selective laser beam melting can be divided into the three process steps powder coating, exposure and consolidation. To increase process reproducibility, basic knowledge about the mutual interactions within the sub-processes is of major interest. However, as the powder coating provides the initial state for the following steps, a relevant influence can be assigned to it. Within this work, the influence of powder coating speed on the part bed surface is highlighted for a defined blade geometry, qualifying an optical measurement technique. According to the shown findings, an increased coating speed leads to higher surface roughness and inhomogeneity of the powder bed. This behavior can be linked directly to the resulting part roughness. Considering part density, the major influence can be attributed to exposure parameters and melt formation, whereas coating speed has a minor impact on it.

Keywords- Additive manufacturing, Selective laser beam melting, Powder coating, Surface topology, Part density.

1. INTRODUCTION

Additive manufacturing techniques, such as selective laser beam melting of polymers (SLS) offer the possibility to generate customized parts and assemblies of high complexity in one single fabrication process [1]. Despite the

huge variety of additive manufacturing processes, especially the SLS process has shown great potential to overcome the gap between rapid prototyping and rapid manufacturing [2]. Therefore, the main drawbacks of this technique, such as low diversity of available materials and the lack in reproducibility have to be overcome [3]. In general, the process of selective laser beam melting can be divided into the three main process steps powder coating, exposure and consolidation, which are affecting each other.

For this reason, the powder coating process provides the initial state for the subsequent exposure and is essential for the generation of part properties. Commonly, so-called blade or rake systems as well as counter-rotating rollers are applied within the process, having inherent advantages and disadvantages. Within most of the commercial systems, the rotational speed is directly linked to the translational coating speed [4]. In [5], Drummer showed that depending on coating speed, a slightly higher part density for the rake system can be observed. However, the counter-rotating roller has proven to be the more process-tolerant recoating system, as exposed layers with slight curling do not necessarily lead to process abortion. This is of particular importance, especially when new materials are introduced within the pro-

cess and new processing windows are to be tested. The differing performance within the recoating mechanisms can be assigned to varied force transmission and therefore result in altered powder bed densities, which corresponds to the powder bed surface [5]. To date the influence of coating speed on the powder bed surface has not been studied yet. For this reason, within this study the roughnesses of the powder bed, achieved by speed dependent coating strategies are correlated to different part properties.

2. STATE OF THE ART

In [4], limited possibilities to optimize the coating parameters of commercial systems are mentioned. Therefore, new regulating parameters were realized by decoupling the translational coating speed and rotational speed. Especially the influence of the coating mechanism on part roughness was highlighted, mentioning a major influence on the surface roughness in build height direction. Furthermore, an existing influence of roller size and roller surface structure was addressed, as results generated by two different laser beam melting systems have led to incomparable outputs values. In [6], a model for the counter-rotating roller was developed. According to this model, the main parameters of the counter-rotating coating process are powder layer thickness, roller radius and friction between both, roller-powder and powder-powder. In contrast to the aforementioned experiments of [4], the density does neither depend on coating nor rotational velocity of the roller.

Niinoo [7] introduced an experimental compaction method, which consists of two subsequent processes. In the first process, a counter-rotating roller spreads the powder on the part bed surface. In the following process, the part piston is heightened and the roller is forward rotating in the direction of powder coating to compresses the powder. Under certain processing conditions, such as equalizing the rotational speed and coating speed of the roller, this compaction process indicates potentials to rise the powder bed density, reduce curl distortion and improve specific mechanical properties. Nevertheless, in [5, 8, 9], an influence of powder bed density on optical and thermal material properties was mentioned affecting the processing conditions and the quality of the resulting parts. In [10], different coating strategies, such as blade, counter-rotating rollers of different size, forward-rotating roller and the combination of a blade with forward-rotating roller with gypsum as material system, aiming for powder compaction, were tested. The highest values for the bulk density and the best surface quality were achieved using a counter-rotating roller with a diameter of 22 mm. The combination of a blade and forward-rotating roller was highlighted to be promising for achieving high powder bed densities, but requires wide ranging material-specific optimization of the coating process. As the powder coating is thought to have a main influence on powder bed density and therefore on the resulting surface topology, surface roughness, especially on the top and on the bottom layer has to be considered. However, as powder is covering the whole surface of selective laser

beam molten parts, a certain surface roughness is always present. Schmid [11] summarized that for polyamide 12 (PA12) with a particle size $d_{50,3}$ of around 60 μm , the resulting values of the arithmetic average roughness (R_a) vary in the range of around $10 \pm 3 \mu\text{m}$ and the values for the mean roughness depth (R_z) can be expected to vary in the range of 50 to 150 microns. However, these ranges are valid for the top and the bottom layer of the fabricated parts and correlate to the particle size of the used powders. As shown in [12], surfaces of beam molten polymer parts were characterized by means of tactile profilometry and optical measurement techniques, such as focus variation, confocal laser scanning microscopy and fringe projection leading to different scales of the measured surface roughness. In general, optical measuring procedures tend to lead to higher measured values of surface roughness, as no smoothing is induced by the probe tip. In addition to that, the specific advantages and drawbacks of four measurement techniques are discussed. Nevertheless and in contrast to [13], tactile profilometry was recommended as it is a fast and reproducible method to characterize the surface topology, even though the tip scratching over the plastic surface could affect the measured values.

Within this article, the influence of varied coating speed on the powder bed and the part surface is shown for a blade system as to date low scientific effort has been made to analyze this basic process. As shown before, most groups focus on rotating rollers, making it difficult to separate observed effects according to roller size, rotational and translational speed. The consideration of a stiff blade geometry allows back tracing of the results to the basic powder coating itself and the varied parameters. Furthermore, the interaction between powder coating speed, part density and impact time is highlighted. The importance of the heating rate on part properties has been shown in literature [14-16] and is considered within this work.

3. MATERIALS AND METHODS

3.1. Material system

Within the experiments, the well characterized polyamide 12 (PA12) powder (PA2200, EOS GmbH, Krailling, Germany), was applied with a refreshing rate (new/recycled powder) of 50/50 wt.-%. The altered powder was taken from overflow of build jobs with maximum durations of two hours to minimize the aging influence. In order to characterize the powder flowability the bulk density ρ_b was measured according to DIN EN ISO 60 [17] for new and reused powder and the resulting mixture of both components. In addition to that, the tapped density ρ_t was acquired according to DIN EN ISO 787-11[18]. By using the results of the bulk and the tapped density, the Hausner factor (HF) of the applied material can be calculated according to the following equation:

$$HF = \frac{\rho_t}{\rho_b} \geq 1 \quad (1)$$

3.2. Laser beam melting system

For achieving homogeneous and constant experimental boundary conditions between different experiments, it is necessary to use a special temperature stabilized and homogenized laser beam melting system. An eight-zoned heating system guarantees a homogeneous temperature distribution along the build chamber. Moreover, a laser system with nearly constant intensity over the complete building chamber is used (F-theta lens). The scanning system guarantees short acceleration times as well as high precision in beam guiding. The focus diameter d_f is determined to 400 μm . For the experiments, a blade system was utilized. Its cross-sectional geometry can be extracted from Fig. 1, whereas the concave structure is present for loosening the bulk powder and to establish powder revolution. For all investigations, the powder coating speed v_c was varied between 125, 250 and 500 mm/s, respectively. Compared to the highest coating speed of 500 mm/s, the layer time is increased for 1.2 s at 250 mm/s and 2.4 s for 125 mm/s. In general, the single layer time should be kept as short as possible to avoid enhanced process durations. A layer time increase of 1.2 s would lead to a by 20 min increased build time for a build job with a z-height of 10 cm, which is corresponding to 1,000 single layers. However, especially for blade systems, the assessment of the influence of powder coating speed on part bed surface and part properties is useful, as influences can be directly linked to it.

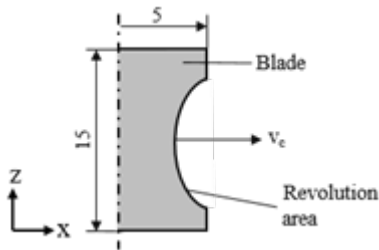


Figure 1. Schematic presentation of the used blades cross-sectional geometry

3.3. Powder bed characterization

The quality of the powder coating was measured optically by using the fringe projection technology. The COMET LED 5M (Carl Zeiss Optotechnik GmbH, Neubuern) with a measuring field of 74 x 62 x 45 mm³ and a 3D point spacing of 30 μm was equipped to quantify the influence of powder coating speed on the powder bed surface. For reproducibility purposes, a reference frame as depicted in Fig. 2 was applied. For every coating speed and direction three measurements were performed and the mean roughness values R_a and the average roughness depth R_z was calculated according to (2) and (3) given in DIN EN ISO 4287 [19]. Within shown investigations, a differing profile length of 50 mm with a sampling length L_R of 10 mm was applied.

For all samples, the assessed profiles were located at equal positions.

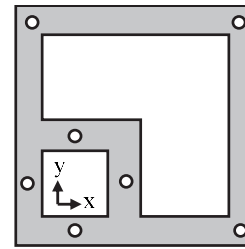


Figure 2. Schematic image of applied reference frame

$$R_a = \frac{1}{L_R} \int_0^{L_R} |z(x)| dx \quad (2)$$

$$R_z = \frac{1}{5} \cdot (R_{z1} + R_{z2} + R_{z3} + R_{z4} + R_{z5}) \quad (3)$$

3.4. Processing experiments

As shown in Fig. 3, two different kinds of test geometries were applied for the present experiments. On the one hand, density cubes with an edge length of 6 mm were fabricated to study the influence of coating strategies on part density, layer structure and morphology.

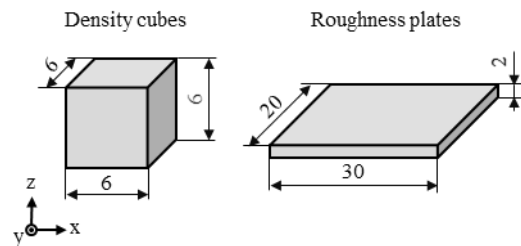


Figure 3. Schematic illustration of the applied test geometries, density cubes (left) and roughness plates (right)

On the other hand roughness plates were produced with dimensions of 30 x 40 x 2 mm (l x w x h) to analyze the topography induced by powder coating speed. Within shown experiments, the top and the bottom side were assessed, whereas higher roughness values are expected for the top side of the parts as lower gravitational forces and reduced coalescence behavior is expected. The laser beam melting experiments were performed with different scan parameters, which can be extracted from Table 1. As the interaction between laser and material is strongly time dependent, the influence of impact time, which can be calculated according to (4), was considered. For all of the shown experiments, the volume energy density E_D , which can be determined according to (5), was kept constant at a level of 0.4 J/mm³, which is a typical value for the fabrication of PA12 parts.

$$t_{im} = \frac{d_f}{v_s} \tag{4}$$

$$E_D = \frac{P_L}{v_s \cdot d_h \cdot d_l} \tag{5}$$

The layer thickness d_l was set to 0.1 mm and the hatch distance d_h to 0.2 mm at a laser spot diameter of the CO₂ laser d_f of 0.4 mm. The parameter study was performed to analyze the influence of impact time on part properties.

TABLE 1. STUDIED PARAMETER SETS FOR EXPOSURE EXPERIMENTS AT AN ENERGY DENSITY OF 0.4 J/MM³

Parameter set	Scan speed v_s [mm/s]	Laser power P_L [W]	Impact time t_{im} [ms]	Energy density [J/mm ³]
1	1540	12.3	0.39	0.4
2	2015	16.1	0.30	
3	2475	19.8	0.24	
4	2875	23.0	0.21	
5	3225	25.8	0.19	

3.5. Part characterization

The density of the cubes was determined by buoyancy method in ethanol directly after processing to avoid humidity influences. Previously, adhesive powder was removed carefully with a brush. To study the part morphology, the cubes were embedded in epoxy resin for subsequent microtome examinations. Thin cuts of 10 μm were prepared for the analysis of porosity and layer connectivity. The surface of the produced specimens had to be measured by a tactile approach. Therefore, the contact profile method (Hommel Tester T1000, Osterwalder AG) was used on the basis of DIN EN ISO 4288 [20]. For the experiments a 5 μm hard metal probe tip with 90° opening angle (Jenoptik Industrial Metrology Germany GmbH, Jena) was employed. In order to evaluate the influence of the flow behavior, the surface roughness was determined three times in direction of powder coating (Fig. 4).

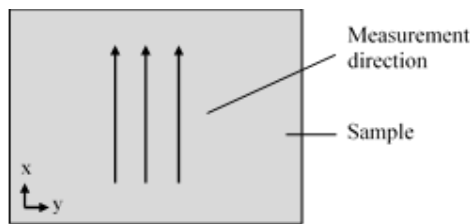


Figure 4. Measuring sections for tactile analysis of laser beam molten parts (roughness plates)

Within these investigations, the average roughness value R_a and the more sensitive mean roughness depth R_z were evaluated for the top and bottom side. The measuring

section was 20 mm including 5 mm cut off. The vertical measuring range was 320 μm and the sample size n was three. Finally, the values of the optical and tactile measurements were compared to each other and the powder beds influence on part density was derived and evaluated in order to derive an optimized coating strategy.

4. RESULTS AND DISCUSSION

4.1. Powder characterization

The powder rheology of the applied material is one of the most influencing factors for the quality of parts produced by selective laser beam melting. Besides particle shape, size and the particle size distribution, usually the bulk and tapped densities, as well as the Hausner ratio are considered to characterize the flowability of powder materials for SLS purposes. The results depicted in Fig. 5 indicate a similar flowability for the used materials compared to new powder as the bulk density remains at around 0.45 g/cm³, respectively.

However, a slight decrease in bulk density can be observed which is induced by the thermal influence of the materials first processing. An increase of tapped density was achieved by the particle smoothening of recycled powder and the resulting increase of packing density. Nevertheless, good powder flowability and reproducibility is indicated throughout Hausner ratios varying between 1.15 and 1.19, for new and recycled powder, respectively. The following results are evaluated for a powder system with good flowability and high packing density. Considering particle systems with reduced flowability the impact of the recoating strategy on powder bed surface or part properties might be enhanced.

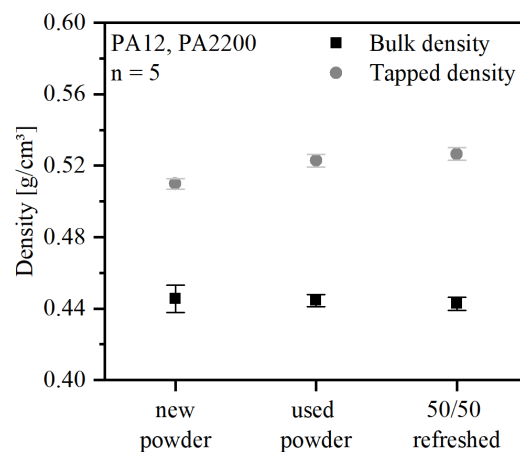


Figure 5. Results of the powder characterization

4.2. Powder bed characterization

The powder bed surface was analyzed optically by fringe projection technology to obtain three-dimensional surface data. The evaluated results for the surface roughness can be extracted from Fig. 6. The mean roughness R_a , is ranging between 30 and 40 microns. Increasing the coating speed leads to an increase of the R_a value from 30 μm to around 37 μm . at low standard deviations.

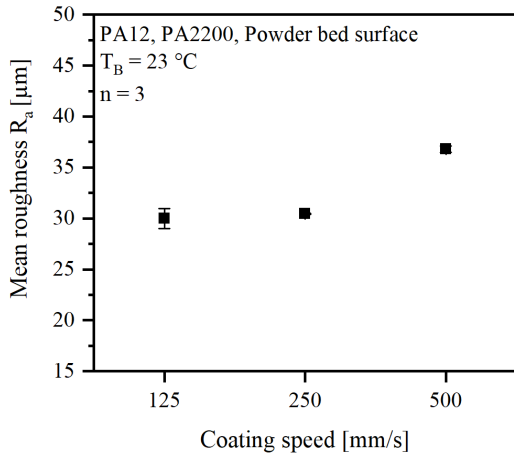


Figure 6. Results of the powder bed surface characterization (R_a) for different coating speeds and directions

This phenomenon can be explained by the particles randomly arranging on the powder bed surface. Increasing coating speed decreases the time for the particles to sort to an optimal position, leading to higher surface roughness values. The authors estimate, that surface roughness can directly be correlated to the density of the powder bed, as for subsequent layers, this rough surface structure propagates to a porous powder bed with reduced powder bed density. However, the resulting values of the R_a value can be correlated to the half of the mean volumetric particle diameter $d_{3,50}$, which is measured to be around 60 μm (see Fig. 7).

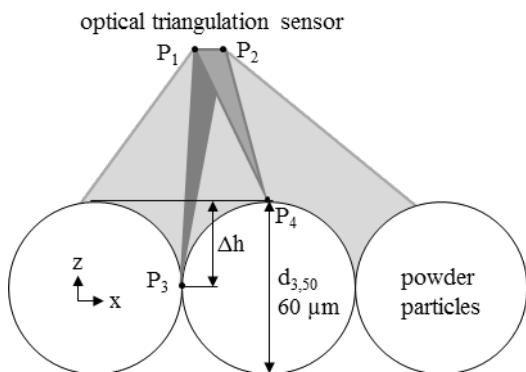


Figure 7. Schematic representation of the optically measured height difference Δh for optimally arranged or smoothed powder surface

Considering an optimum packing of the PA12 powder with contact to neighboring spherical particles, the measurable height difference Δh would be $d/2$. This value lies within the range of the results of the shown investigations. As R_a is an averaged value, the influence of lower irregularities are smoothed and the detected roughness mainly depends on the particle diameter.

The results for the R_z values can be extracted from Fig. 8. As this characteristic value is determined by the difference between the averaged minimum and maximum value of five measuring sections, much higher roughness values of around 200 μm are measured. Furthermore, this parameter is known to be more sensible for the detection of surface changes. However, only a slight increase of the mean roughness depth can be observed for increased coating speeds, which is in accordance with the shown results for the R_a value. Nevertheless, differences regarding the resulting standard deviations are present, because of the voids higher influence on the R_z -value.

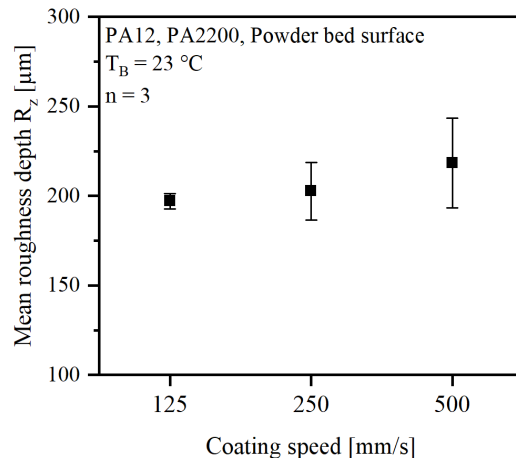


Figure 8. Results of the powder bed surface characterization (R_z) for different coating speeds and directions

Especially for higher coating speeds, a higher degree of surface variations can be observed, which can be assigned to local imperfections of the powder bed. Fig. 9 schematically explains the high R_z values. As the particles are randomly distributed on the surface, gaps between two neighboring particles are likely to occur, especially for higher coating speeds. These imperfections are detected by stripe light projection and can be made visible by using the mean roughness depth R_z as output value. An increase in coating speed from 125 to 500 mm/s will lead to higher values of surface roughness, whereas the standard deviation of the R_z values is the highest for the maximum coating speed. A possible reason for this could be, that the high velocity of the blade reduces the probability of powder particles to randomly sort ideally. Hence, the likeliness for voids within the powder bed is increased. For this reason,

the influence of the powder coating and the powder bed surface on the part properties are of particular interest.

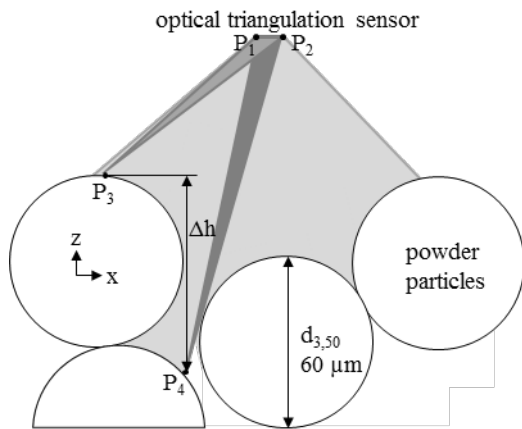


Figure 9. Schematic representation of the optically measured height difference Δh randomly packed particles

4.3. Part characterization

The results for the density measurements in dependency on laser power are shown in Fig. 10. For all experiments, the energy density was kept constant at 0.4 J/mm^3 but the laser power and scan speed were varied, so influences depending on impact time can be distinguished. High values for part density of over 0.96 g/cm^3 can be observed for all specimens, which can on the one hand be assigned to high density parts and on the other hand to the buoyancy testing method, which in general leads to slightly higher part densities, because of the surface roughness, which might lead to air pockets. Furthermore, it can be seen, that with increasing laser power and scan speed, the density of the tested specimens decreases. In addition, the standard deviation increases with decreasing impact time indicating inhomogeneous melting behavior. Considering the influence of coating speed, only minor influences can be observed. Especially for higher scan speeds, the coating speed influences the part density.

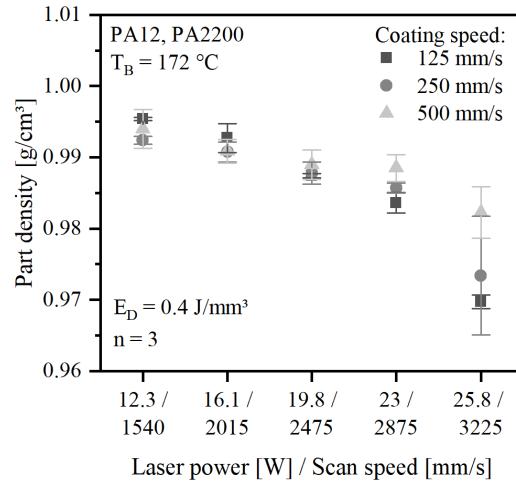


Figure 10: Part density in dependency on laser power and coating speed

In this case, a lower coating speed results in lower density values, whereas higher coating speed leads to a higher stability in part density values. It is expected, that this can be traced back to the thermal household being influenced by powder coating and the variation the of the powder pre-heating time due to changed heat transfer conditions between powder bed and blade system. For that reason, intensive thermographic studies will be performed, focusing powder coating process.

Microscopic images of thin cuts in polarized light under variation of coating speed can be seen in Fig.11. For all thin cuts, a certain porosity is visible, which can be correlated to the short duration of the build job and the resulting reduced morphology development, e.g. pore dissolution or remelting of the layers. The visibility of the layer structure in Fig. 11 c) can be assigned to the cutting direction, which is perpendicular to that of a) and b). However, low porosity of the parts can be confirmed by the shown images for the highlighted parameter set. In addition to that, the low deviation in density is visible as well.

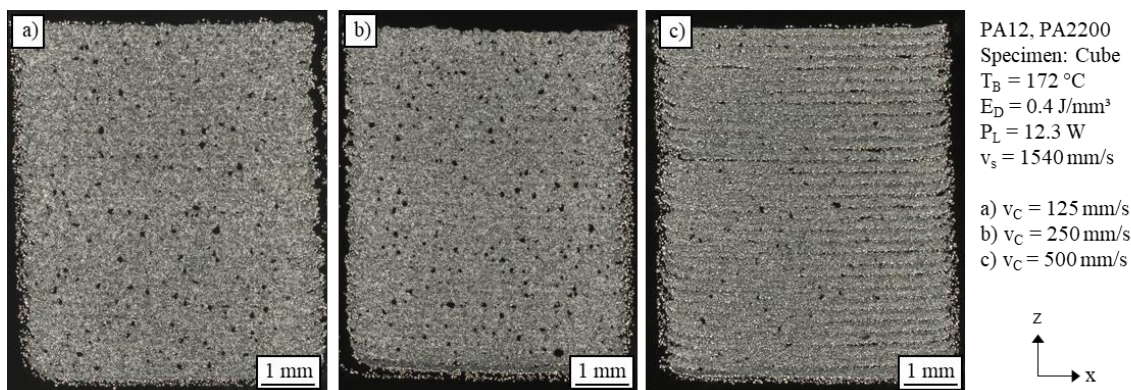


Figure 11. Microscopic images of thin cuts under polarized light under variation of coating speed

Within Fig. 12 to 14, the resulting part surface roughnesses values R_a and R_z are shown and subdivided according to the applied coating speeds. In general, the measured R_a and R_z values fit well to the range of values summarized in [11]. Regarding the upper and bottom side of the parts, the mean values of all parameter sets and coating speeds show similar effects. Due to infiltration of the melt, the surface roughness at the bottom side is lower compared to the upper side. In addition, the gravitational forces are higher on the bottom supporting this theory. For the lowest coating speed of 125 mm/s, the resulting R_a and R_z values show similar effects. For all exposure parameters, a certain offset in surface roughness is present comparing the upper and bottom sides. A minor influence can be assigned to the different scan parameters, as the mean values for R_a and R_z , as well as the standard deviations are in the same range. The highest deviations are detected on the upper side for the parameter set with the fastest scan speed of 3225 mm/s.

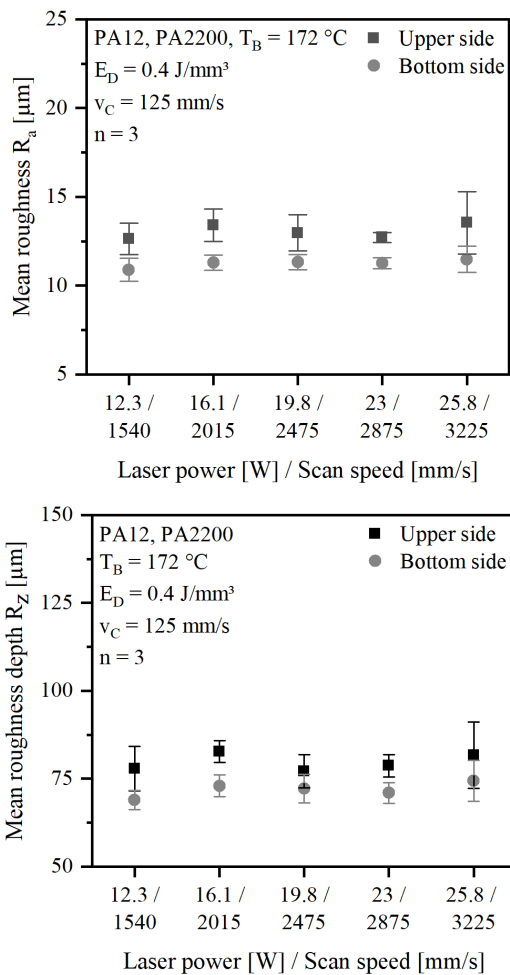


Figure 12. Part surface roughness at a coating speed of 125 mm/s considering mean roughness R_a (above) and mean roughness depth R_z (below)

As this phenomenon is present for all coating speeds, a systematic cause is indicated. It could be explained by the interaction between melt and coated particles, which is in this case mainly viscosity driven. If the melt viscosity is too high, adherence and coalescence of the particles is reduced, leading to enhanced surface roughness caused by local surface inhomogeneities such as superficial voids.

In Fig. 13, the influence of the medium coating speed of 250 mm/s is shown. For the lower scan speed the mean roughness values and the offsets between of the upper and bottom side are lower. At a higher coating speed, higher forces act upon the particles, which are pressed deeper into the viscous melt. For higher scan speeds, this cannot be confirmed, but as described earlier this can be assigned to a varied melt viscosity. As melt formation and the linked viscosity reduction takes longer for higher scan speed, higher surface roughnesses are the result for reduced particle adhesion.

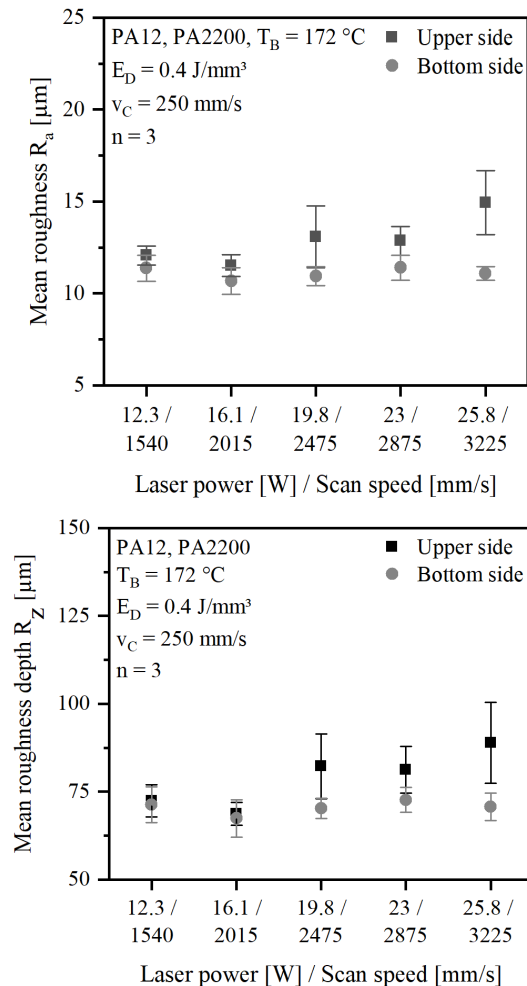


Figure 13. Part surface roughness at a coating speed of 250 mm/s considering mean roughness R_a (above) and mean roughness depth R_z (below)

In Fig 14, the influence of the highest coating speed of 500 mm/s on the surface roughness is shown. Again, the upper side of the part can be characterized by higher surface roughness and by higher standard deviations. In addition to that, a higher gap between the surface roughness of the upper and the bottom side can be recognized, as well as increasing surface roughness with increasing scan speed. Due to faster processing, the former described influence of reduced melt formation and intensified infiltration, a higher variation of the surface topology is resulting.

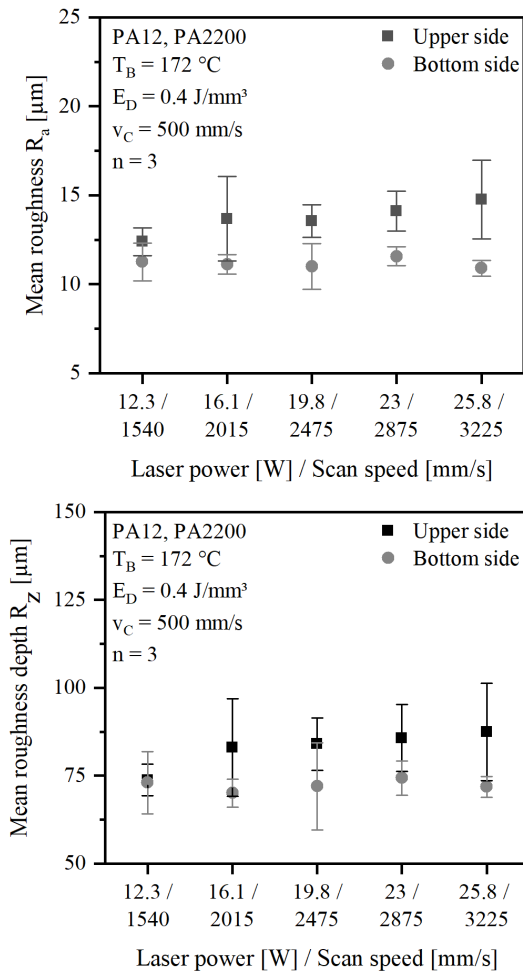


Figure 14. Part surface roughness at a coating speed of 500 mm/s considering mean roughness R_a (above) and mean roughness depth R_z (below)

5. SUMMARY

The shown investigations focus on the impact of powder coating on part bed surface and the resulting part properties, such as part density and surface roughness. For analyzing the surface of the powder bed, the fringe projection method was introduced. Veritable results could be generated, indicating a correlation between increasing coating

speed and surface roughness of the powder bed. In general, higher coating speed and scan speed leads to higher surface roughnesses and standard deviation. For this reason in terms of coating speed, a compromise has to be made between process acceleration and homogeneity of the resulting part properties. Even though the impact of some effects seems to be small, wider influences can be expected when powders with reduced flowability are processed.

ACKNOWLEDGEMENT

The authors want to thank the German Research Foundation (DFG) for funding the Collaborative Research Center 814 (CRC 814) – Additive Manufacturing, sub-projects B3, A3 and A6.

REFERENCES

- [1] Gebhardt, A., 2013, *Generative Fertigungsverfahren Additive Manufacturing und 3D Drucken für Prototyping, Tooling, Produktion*, 4., neu bearbeitete und erweiterte. Auflage. München: Hanser.
- [2] Wohlers, T., 2014, Wohlers Report 2014: ‘3D Printing and Additive manufacturing state of the industry - Annual worldwide progress report’, Wohlers Associates.
- [3] Wegner, A. and Witt, G., 2013, Ursachen für eine mangelnde Reproduzierbarkeit beim Laser-Sintern von Kunststoffbauteilen, *RTJournal - Forum für Rapid Technologie*, vol. 2013, no. 1.
- [4] Khaled, S. A, Burley, J. C., Alexander, M. R. and Roberts, C. J., 2014, ‘Desktop 3D printing of controlled release pharmaceutical bilayer tablets’, *International Journal of Pharmaceutics*, vol. 461, no. 1–2, pp. 105-111.
- [5] Drummer, D., Drexler, M. and Wudy, K., 2015, ‘density of laser molten polymer parts as function of powder coating process during additive manufacturing’, *Procedia Engineering*, vol. 102, pp. 1908-1917.
- [6] Shanjani, Y. and Toyserkani, E., 2008, ‘Material spreading and compaction in powder-based solid freeform fabrication methods: mathematical modeling’, *Proc. Solid Freeform Fabrication on Symposium 2008*, vol. 399, p. 410.
- [7] Niino, T. and Sato, K., 2009, ‘Effect of Powder Compaction in plastic laser sintering fabrication’, *Proc. Solid Freeform Fabrication Symposium*, pp. 193-205.
- [8] Drummer, D., Drexler, M., Wudy, K. and Kühnlein, F., 2013, ‘Effects of powder bulk density on the porosity of laser molten thermoplastic parts’, *Proceedings of the Polymer Processing Society 29th Annual Meeting*, Nuremberg, Germany, vol. 29.
- [9] Greiner, S., Lanzl, L., Wudy, K., Drexler, M. and Drummer, D., 2017, ‘Study on the powder compaction potential induced by the powder coating process of selective beam melting’, ‘Untersuchungen zum Potential der Pulververdichtung durch den Pulverauftrag beim selektiven Laserstrahlschmelzen von Kunststoffen’, *Proceedings of Rapid Tech 2017*.
- [10] Budding, A. and Vaneker, T., 2013, ‘New strategies for powder compaction in powder-based rapid prototyping techniques’, *Procedia CIRP*, vol. 6, pp. 527-532.
- [11] Schmid, M., ‘*Selektives Lasersintern (SLS) mit Kunststoffen*’, 1 ed. München: Carl Hanser Verlag, 2015.
- [12] Launhardt, M. et al., 2016, ‘Detecting surface roughness on SLS parts with various measuring techniques’, *Polymer Testing*, vol. 53, pp. 217 -226.

- [13] Grimm, T., Wiora, G. and Witt, G., 2015, 'Characterization of typical surface effects in additive manufacturing with confocal microscopy', *Surface Topography: Metrology and Properties*, vol. 3, no. 1, p. 014001.
- [14] Drummer, D., Drexler, M. and Wudy, K., 2014, 'Derivation of heating rate dependent exposure strategies for the selective laser melting of thermoplastic polymers', *Proceedings of the Polymer Processing Society 30th Annual Meeting*, Cleveland, Ohio, USA.
- [15] Drummer, D., Drexler, M. and Wudy, K., 2014, "Impact of heating rate during exposure of laser molten parts on the processing window of PA12 powder," *Physics Procedia*, vol. 56, no. 0, pp. 184-192.
- [16] Drexler, M., Lexow, M. and Drummer, D., 2015, 'Selective laser melting of polymer powders – part mechanics as function of exposure speed', *Physics Procedia*, vol. 78, pp. 328-336.
- [17] N. N., 2000, 'DIN EN ISO 60 - Kunststoffe- Bestimmung der scheinbaren Dichte von Formmassen, die durch einen genormten Trichter abfließen können (Schüttdichte) (ISO 60:1977)', *Beuth Verlag GmbH*.
- [18] N. N., 1995, 'DIN EN ISO 787-11: 1995 - Allgemeine Prüfverfahren für Pigmente und Füllstoffe - Teil 11: Bestimmung des Stampfvolumens und der Stampfdichte (ISO 787-11: 1995)', *Beuth Verlag GmbH*.
- [19] N. N., 2009, 'DIN EN ISO 4287 - Geometrische Produktspezifikation (GPS) - Oberflächenbeschaffenheit: Tastschnittverfahren - Benennungen, Definitionen und Kenngrößen der Oberflächenbeschaffenheit (ISO 4287:1997 + Cor 1:1998 + Cor 2:2005 + Amd 1:2009)', *Beuth Verlag GmbH*.
- [20] N. N., 1997, 'DIN EN ISO 4288 - Geometrische Produktspezifikation (GPS) - Oberflächenbeschaffenheit: Tastschnittverfahren - Regeln und Verfahren für die Beurteilung der Oberflächenbeschaffenheit (ISO 4288:1996)', *Beuth Verlag GmbH*.

Glass-Filled Polypropylene-Systems for Enhancing Reproducibility during Selective Laser Beam Melting and Effect of the Mixing Strategy on Powder Properties

Lydia Lanzl, Institute of Polymer Technology, Collaborative Research Center 814 – Additive Manufacturing, Friedrich-Alexander-Universität Erlangen-Nürnberg, Germany, lanzl@lkt.uni-erlangen.de

Sandra Greiner, Institute of Polymer Technology, Collaborative Research Center 814 – Additive Manufacturing, Friedrich-Alexander-Universität Erlangen-Nürnberg, Germany, greiner@lkt.uni-erlangen.de

Katrin Wudy, Institute of Polymer Technology, Collaborative Research Center 814 – Additive Manufacturing, Friedrich-Alexander-Universität Erlangen-Nürnberg, Germany, wudy@lkt.uni-erlangen.de

Dietmar Drummer, Institute of Polymer Technology, Collaborative Research Center 814 – Additive Manufacturing, Friedrich-Alexander-Universität Erlangen-Nürnberg, Germany, info@lkt.uni-erlangen.de

Abstract—Filled systems in selective laser beam melting of polymers (SLS) can be used to set tailored properties depending on the powder properties such as material, shape, aspect ratio and particle size. For example, glass-filled systems are used to increase mechanical properties, like stiffness or tensile strength. However, fillers might change the process behavior, like the optical properties, flowability and crystallization behavior, which leads to a decreased process robustness. In this study, the influence of the mixing strategy and the influence of two different filler shapes on the powder flowability and the crystallization behavior are investigated. Therefore, glass fibers and glass particles prepared as dry-blends in contrary to incorporated fillers in the polymer particles are analyzed. The study shows that particle filled systems minimize negative influences by fillers on the process behavior.

Keywords - selective laser beam melting; filled systems; polypropylene; glass fiber, crystallization rate

1. INTRODUCTION

Selective laser beam melting of polymers (SLS) offers a high degree of individualization in production. While the applications of selective laser sintering are increasing and the technology has already been transferred from rapid prototyping to small batch production, the material variety is still limited [1]. Filled polymer systems offer the advantage of setting

tailored properties. By adding metal fillers, the parts offer metal appearance and machinability is enhanced [2, 3]. Also, thermal or electrical conductive parts can be realized [4]. Glass fillers are used to improve stiffness, exemplarily for housing in automotive, or tensile strength. Nevertheless, most of the filled systems are mechanically mixed, i.e. the fillers are added to the matrix powder and an elementary mixing is produced having a distinct influence on the process behavior of SLS. For example, fillers with a different material or shape change the optical properties of the powder composition [5] leading to a changed energy input and makes individual process parameters necessary. In addition, the flowability decreases adding fillers with an irregular shape. Decreased flowability might result in reduced mechanical properties due to higher part porosity [6]. To avoid the fillers' negative effects on the process, particle filled systems are investigated in this paper. Hereby, the fillers are incorporated in the polymer particles, having the effect that the process is mostly dominated by the behavior and the properties of the polymer particles and the influence of fillers is minimized. In this study, two different glass filled (glass fibers (GF) and glass particles (GP)) polypropylene (PP) systems are analyzed. The mixing strategy, i.e. dry-blends and the mentioned particle systems is compared with respect to flowability and crystallization behavior.

2. STATE OF THE ART

A few approaches were made to processing glass filled polymer systems in SLS. Kleijnen et al. [7] investigated the mechanical properties of short-fiber reinforced PP. In this study, various short fibers, like glass and wollastonite fibers are added to PP aiming to enhance mechanical properties. It was found that by adding 30 wt.-% glass fibers with a mean particle size of 50 μm, the tensile modulus can be improved by 59 % with a reduction of the ultimate tensile strength [7]. Moreover, glass fibers were used to reinforce polystyrene in [8] to improve the bending strength. At a concentration of 10 %, the best strengthening effect could be found. Tensile tests, compression and bending tests were conducted on commercial glass-filled fine polyamide PA3200GF in [9]. The effect of coupling agents and of two different types of glass beads in polyamide 12 (PA12) were under investigation in [10]. It was discovered that the flexural modulus increased from 77 to 91 MPa and the flexural modulus from 2500 to 3800 MPa with a glass bead content from 10 to 40 wt.-%. Wudy et al. also investigated different sizes of glass beads and their effect on PA12 concerning bulk density, optical and thermal material behavior [11]. As a result, the diffuse reflection is decreased with higher filler content with no difference of the two filler types and the crystallization temperature increases. This indicates that the glass fillers have a nucleating effect, which might lead to faster curling. With a smaller size of the glass beads, only porous networks could be realized due to a higher surface to volume ratio [11]. The effect of short-glass fibers on copolymer poly (butylene terephthalate) (cPBT) in SLS was evaluated by Arai et al. [12]. In this study, the content of short-glass fibers was varied between 15, 30, 45 and 60 wt.-% and it was found that with increasing filler content the flowability is decreased and the maximum values for tensile strength and flexural strength was reached at a glass fiber content of 30 wt.-% and highest impact strength with a content of 45 wt.-%. Furthermore, the parts exhibited higher porosity, improved thermal properties and reduced shrinkage. The crystallization properties were hardly affected with adding short-glass fibers [12]. Nevertheless, all the composites were prepared by mechanical mixing in all the studies above. The effect of the fillers on the process behavior has been analyzed hardly and mixing strategies have not been investigated so far. Therefore, this paper deals with the effects of two different feeding strategies for PP-composites.

3. MATERIALS AND METHODS

3.1. Materials

For this study, polypropylene by NeuMat Shanghai Advanced Materials Co as the matrix and two shapes of glass fillers are used. Therefore, glass fibers and glass particles are investigated to compare the effect of the filler shape on the powder and processing properties during selective laser beam melting. Information about the raw- and bulk density as well the medium particle size of the material systems can be seen in Table 1. Since the mixing strategy is under investigation, particle filled systems, with the fillers incorporated in the polymer particles and dry blends with the very same matrix and

fillers are compared. The particle-filled systems are provided by the supplier. The dry blends are produced by mixing the systems in a rotary mixer.

For both systems, a filler concentration of 10 and 30 wt.-% is used.

TABLE I. Material information of the polymer and fillers

value	Materials		
	PP	glass fibers	glass particles
supplier	NeuMat Shanghai Advanced Materials Co	--	--
raw density	0.92 g/cm ³	2.50 g/cm ³	2.50 g/cm ³
bulk density	0.47 g/cm ³	0.94 g/cm ³	0.84 g/cm ³
d _{50,3}		33.80 μm	15.90 μm

3.2. Methodology

Particle shapes are investigated by scanning electron microscopy (SEM), (Ultra Plus, Carl Zeiss, AG) at a magnification of 1,000 x. The maximum resolution for the SEM is 1.0 nm dependent on the working conditions. The volumetric particle size distribution of the fillers are measured by an optical system, Morphologi G3, Malvern Instruments. For the measurement 80,000 particles are used. The flowability of the particle filled systems and dry-blends is evaluated by the Hausner ratio, which is the ratio of the bulk- and stamping density. Therefore, the bulk densities are determined with a fluometer measurement set-up by Emmeram Karg Industrie-technik according to DIN EN ISO 60 [13] and the stamping densities according to DIN EN ISO 787-11 [14]. Fillers often act as nucleating agents and increase the crystallization behavior of polymer systems. For the selective laser beam melting process, a faster crystallization during isothermal conditions might lead to curling and therefore to a smaller processing window. Isothermal DSC (Differential Scanning Calorimetry)-measurements are conducted to evaluate the crystallization behavior. The temperature profile of the measurements is as following: the temperature is held at 200 °C for one minute for erasing the temperature history of the material and is then cooled down to the isothermal holding temperature of 131 °C, or 132 °C respectively, with a cooling rate of 60 K/min. The chosen isothermal temperature is dependent on the single powder composition and its individual behavior during cooling. The temperature is held for 60 min, in which crystallization takes place. Afterwards, the temperature is heated to 220 °C, above the melting temperature, with a heating rate of 10 K/min. For the dry-blend preparation, the single fillers and neat PP powder are mixed in a rotary mixer for 30 min and 300 rpm. The powders are processed in a DTM Sinterstation 2000 machine to tensile bars according to DIN EN ISO 3167, type A [15]. The used parameters can be seen in Table 2. Powder and filler orientation in the parts are analyzed by polished sections. Therefore, the powder particles and cross section of a tensile bar are embedded in epoxy, grinded, polished and analyzed in bright field microscopy, (AxioImager M2m, Carl Zeiss AG).

TABLE II. Processing parameters

Processing parameters			
T_B (°C)	P_L (W)	v_s (mm/s)	d_H (mm)
131	16.3	1900	0.25

T_B : build temperature
 v_s : scan speed

P_L : laser power
 d_H : hatch distance

4. RESULTS AND DISCUSSION

4.1. Material characterization

In the following, the used polymer systems are presented. The powder shapes are investigated by SEM, see Figure 1 and Figure 2. Spherical particles can be observed being important for a smooth powder surface during coating in SLS.

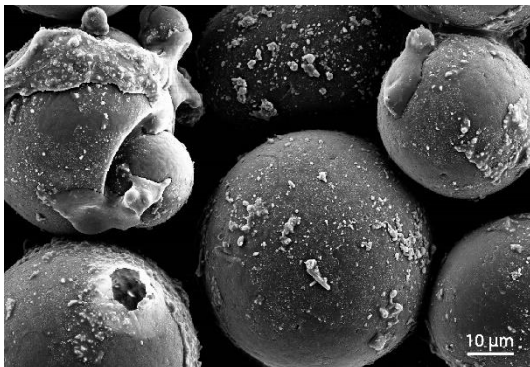


Figure 1. SEM- image of particle filled PP-GP30 (PP + 30 wt.-% glass particles).

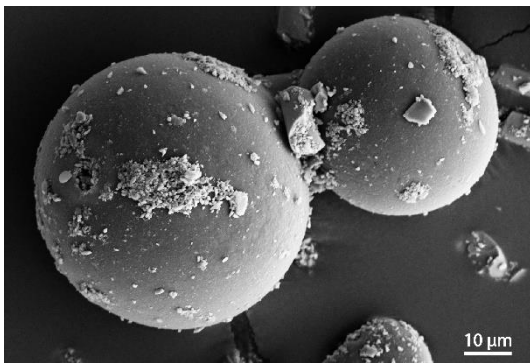


Figure 2. SEM-image of particle filled PP-GF30 (PP + 30 wt.-% glass fibers).

The particles are supposed to be within the polymer particles. By SEM, only the particle shapes can be evaluated. Consequently, a polished section of the powder particles is made to evaluate if the fillers are incorporated in the particles, which can be proved in Figure 3. Since the glass fillers are incorporated in the particles, it is assumed that they do not affect the process behavior. There should be no change in the optical behavior as well as the flowability and the reproducibility of filled polymer systems during SLS can be enhanced, which will be investigated in the following chapters.

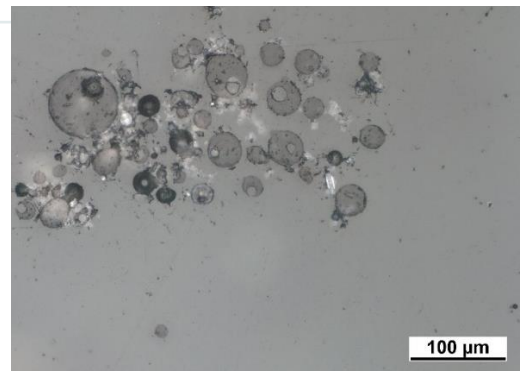


Figure 3. Polished section of particle filled polymer powder.

4.2. Flowability

Flowability of the powder is essential for the quality of the powder coating and therefore the parts' quality. Cohesive powder might lead to porous parts or even process breakdown. Fillers having a rugged shape or a high aspect ratio, like glass particles or glass fibers in this study, can decrease the flowability in dry-blends. The higher the concentration of the filler, the higher is the effect on influencing the powder bed. Incorporated fillers in the polymer particles are therefore compared to dry blends.

The flowability is evaluated by the Hausner ratio (HR). The HR of the dry blends in dependence of the filler content is depicted in Figure 4.

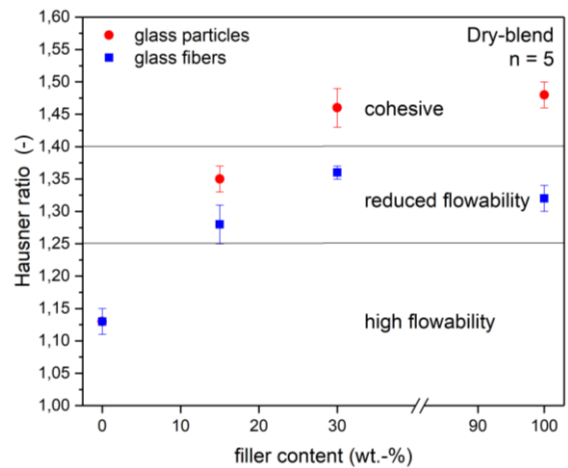


Figure 4. Hausner ratio of dry-blend powder systems in dependence of the filler content.

It can be seen that the Hausner ratio is increased with higher filler content. The pure PP exhibits excellent flowability with a Hausner ratio of 1.13. Adding glass fibers or glass particles as dry blend, the flowability is reduced and at a content of 30 wt.-% of glass particles, the powder gets cohesive avoiding process stable powder coating. The reason for the decreased flowability is the high fine content of the glass particles leading to agglomerations and to an undefined and inhomogeneous filler distribution in the powder.

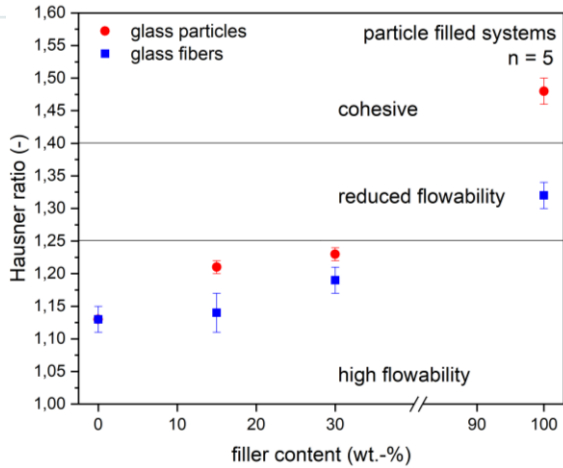


Figure 5. Hausner ratio of particle filled systems in dependence of filler content.

In case of particle-filled systems, the flowability is dominated by the shape and powder properties of the polymer particles, as can be seen in Figure 5. Some fillers lie next to the polymer, resulting in a slight increase of the Hausner ratio. Nevertheless, up to a filler content of 30 wt.-%, all powder compositions exhibit a high flowability and the powder coating is virtually not affected by additional fillers. For the process, high flowability results in a smooth powder bed surface even at higher filler concentrations, which might result in a lower part porosity and therefore improved mechanical properties compared to physical mixing.

4.3. Isothermal crystallization behavior

Fillers often act as nucleating agents and increase the crystallization speed. For the SLS process, an accelerated crystallization at isothermal conditions would lead to early curling at actually suitable processing temperatures and therefore to process break-off.

The crystallization rate can be evaluated by the half crystallization time $t_{c,0.5}$, which is the time, for the crystallization process to be finished to 50 %, as can be seen in Figure 6. This figure shows the relative crystallization turnover of the dry-blend systems, which are integrated and normed crystallization curves at T_{iso} , the holding temperature. The higher the filler content is, the slower is the crystallization turnover.

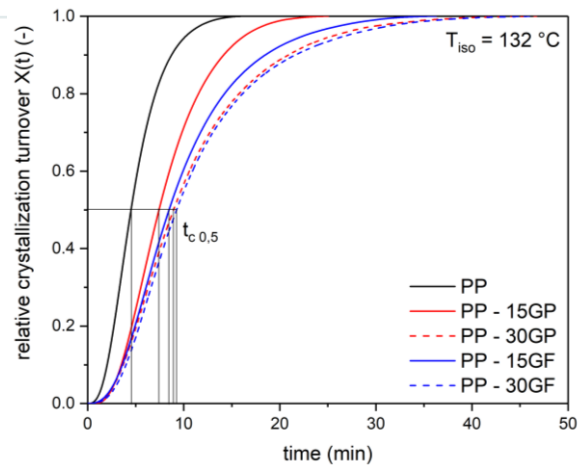


Figure 6. Relative crystallization turnovers of dry-blend powder systems in dependence of filler content and filler shape.

Figure 7 depicts the half crystallization time of particle-filled systems in dependence on the temperature. With increasing temperature (T_{iso}) the half crystallization time is enhanced exponentially. The systems with a filler content of 30 wt.-% crystallizes slower. Comparing the filler shape, the glass particles also lead to a detention of the crystallization. The higher amount of fillers might prevent the rearrangement of the molecular chains during crystallization and therefore lead to higher half crystallization times.

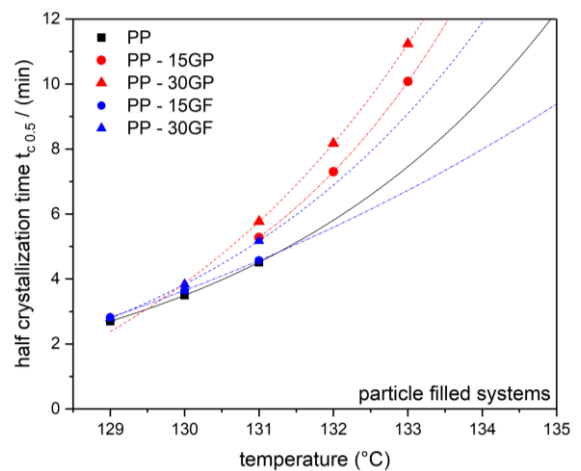


Figure 7. Half crystallization time of particle-filled systems in dependence on the temperature.

The comparison of the fillers as dry-blend is depicted in Figure 8. It can be seen that with increasing filler content the crystallization half time also rises. No accelerated crystallization by the glass fillers can be detected at a processing temperature of 132 °C. Moreover, no major difference between the two powder shapes is present. The same tendency to a lower crystallization rate and therefore an increasing half crystallization time is valid for the particle-filled systems, see Figure 9. The crystallization rate is also decreased for these systems.

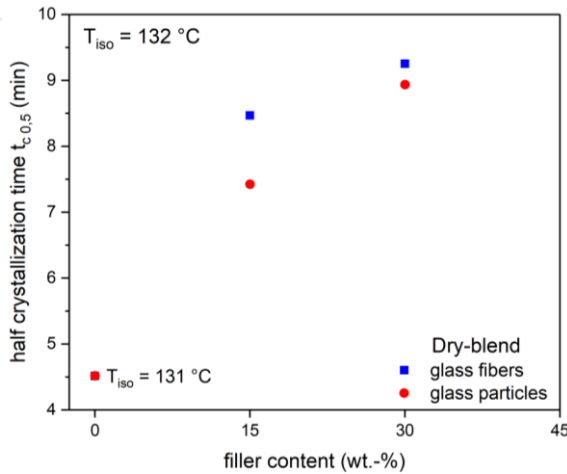


Figure 8. Half crystallization time of glass fibers and glass particles with various content prepared as dry-blend.

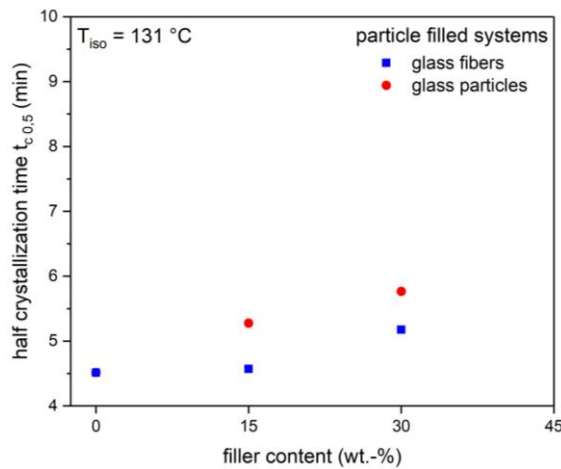


Figure 9. Half crystallization time of glass fibers and glass particles with various content as particle-filled systems.

Regarding filled systems it is known from literature that fillers might have a nucleating effect on polypropylene. However, a decrease of the crystallization rate could also be detected in PP with hemp fibers as filler in [16]. It was found that a sufficiently high density of nuclei prevents transport of PP chains to crystal surface. Due to the high fine content in the glass fillers, this might also be a reason for the decreased crystallization rate. Moreover, the filler surface also plays a role on the nucleation behavior in PP. The nucleation activity of sized and unsized glass fibers towards PP was investigated by Bogoeva-Gaceva in [17]. It could be found that unsized glass fibers depress the nucleation of polypropylene. In addition to that, the cooling rate in dynamic regime and undercooling in the isothermal regime greatly affect the morphology during crystallization. In addition to that, the crystallization is mainly governed by the viscosity of the melt, temperature and pressure [17]. The time-temperature profile during SLS obviously leads to a depressing of the nucleation and a slower crystallization behavior.

Figure 10 depicts the comparison of the two feed systems to investigate the effect of the composite preparation method on the crystallization behavior of the material. Both values

for the particle-filled systems and the dry-blend lie in the same order of magnitude. No effect of the feeding strategy on the crystallization behavior can be detected.

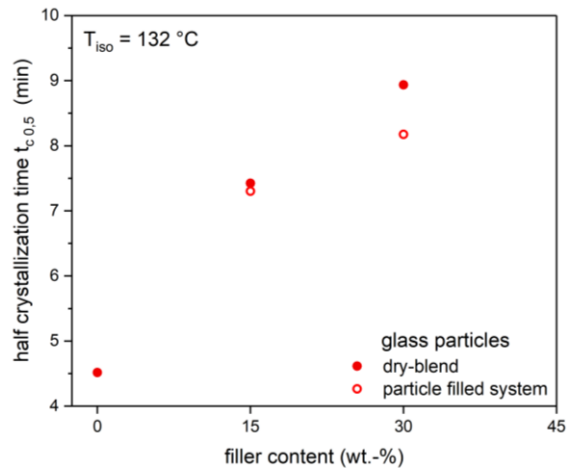


Figure 10. Half crystallization time of glass particles with various contents comparing the mixing strategy.

4.4. Part characterization

The cross-section of a tensile bar of PP-GF30 material is depicted in Figure 11. The polished section shows the distribution of the fillers throughout the part. It becomes obvious that the glass fibers are regularly distributed over the cross-section and no segregation occurs. In addition, no major porosity can be detected in the parts.

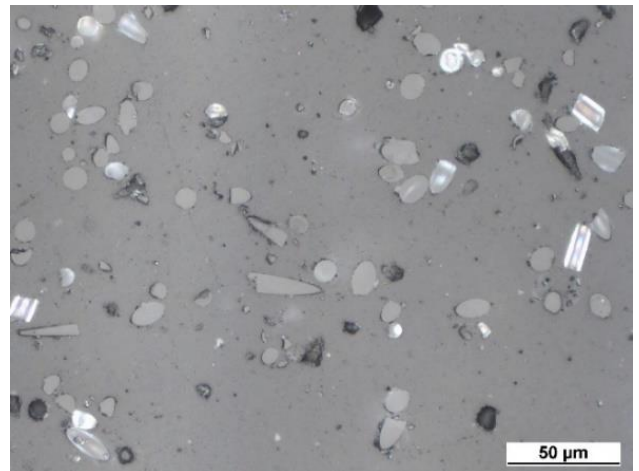


Figure 11. Cross-section of a tensile bar built with an energy density of $E_D = 0.04 \text{ J/mm}^2$ of PP-GF30.

5. CONCLUSION

The study introduced particle-filled PP/glass systems, which have a high potential to enhance the reproducibility of filled systems. The flowability of the particle-filled systems is high and hardly changed with increasing filler content in contrary to dry-blends, which shows a significant increase of the Hausner ratio due to cohesive glass fillers. It could be shown that the glass fillers do not have a nucleating effect on

PP at isothermal conditions. Therefore, no accelerated crystallization can be detected, which might lead to curling effects during processing and therefore to a process break-off. Rather a lower crystallization rate with increasing filler content is observed. No influence of the filler shape and the mixing strategy can be detected, leading to a higher process robustness.

Perspectively, the mechanical properties will be determined as well as the filler orientation and distribution within the part comparing particle-filled systems and physical mixtures.

ACKNOWLEDGEMENT

The authors would like to extend their thanks to the German Research Foundation (DFG) for funding the Collaborative Research Center 814 (CRC 814) – Additive Manufacturing, sub-project A6. This support has enabled the investigations in the area of additive manufacturing, which have led to the results presented in this article.

REFERENCES

- [1] Wohlers, T.T. 2016, 'Wohlers Report 2016: 3D Printing and Additive Manufacturing State of the Industry Annual Worldwide Progress Report', Wohlers Associate.
- [2] Mazzoli, A., Moriconi G. and Pauri, M.G. 2007, 'Characterization of an aluminum-filled polyamide powder for applications in selective laser sintering', *Materials & Design*, vol. 28, no. 3, pp. 993-1000.
- [3] Goodridge, R.D., Shofner, M.L., Hague, R.J.M., McClelland, M. Schlea, M.R., Johnson, R.B., and Tuck, C.J. 2011, 'Processing of a Polyamide-12/carbon nanofibre composite by laser sintering', *Polymer Testing*, vol. 30, no. 1, pp. 94-100.
- [4] Salmoria, G.V., Paggi, R.A., Beal, V.E. 2017, 'Graded Composites of Polyamide/Carbon Nanotubes Prepared by Laser Sintering', *Lasermed. Immunopatol. Manuf. Mater. P. V.*, vol. 4, no. 1, pp. 36-44.
- [5] Kozhukharov, V., Dimitrov, D., Tonchev, D. 1989, Interaction of CO₂ laser radiation with glasses, *Infrared Physics*, vol. 29, no. 2, pp. 415-422.
- [6] Ziegelmeier, S., Christou, P., Wollecke, F., Tuck, C., Goodridge, R., Hague, R., Krampe, E., and Wintermantel, E. 2015, 'An experimental study into the effects of bulk and flow behaviour of laser sintering polymer powders on resulting part properties', *Journal of Materials Processing Technology*, vol. 215, pp. 239-250.
- [7] Kleijnen, R.G., Sesseg, J.P.W., Schmid, M. and Wegener, K. 2017, 'Insights into the development of a short-fiber reinforced polypropylene for laser sintering', in: *AiP Conference Proceedings*, vol. 1914, American Institute of Physics Inc.
- [8] Yang, L., Wang, B. and Zhou, W. 2017, Study on selective laser sintering of glass fiber reinforced polystyrene, Institute of Physics Publishing, 2017.
- [9] Bajerski, P., Pęcherski, R.B. 2017, Influence of additive manufacturing technology on mechanical properties of glass-filled fine polyamide PA3200GF, *Eng. Trans.*, vol. 65, no. 1, pp. 155-161.
- [10] Mousa, A.A., 2014, 'The Effects of Content and Surface Modification of Filler on the Mechanical Properties of Selective Laser Sintered Polyamide12 Composites', *JJMIE* vol. 8, no. 5.
- [11] Wudy, K., Lanzl, L. and Drummer, D. 2016, 'Selective Laser Sintering of Filled Polymer Systems: Bulk Properties and Laser Beam Material Interaction', *Physics Procedia*, vol. 83, pp. 991-1002.
- [12] Arai, S., Tsunoda, S., Yamaguchi, A., Ougizawa, T. 2018, 'Effects of short-glass-fiber content on material and part properties of poly(butylene terephthalate) processed by selective laser sintering', *Additive Manufacturing*, vol. 21, pp. 683-693.
- [13] DIN EN ISO 60 - Kunststoffe - Bestimmung der scheinbaren Dichte von Formmassen, die durch einen genormten Trichter abfließen können (Schüttdichte) (ISO 60:1977); Deutsche Fassung EN ISO 60:1999, in: Beuth Verlag GmbH (Ed.) DIN EN ISO 60, 2000-01-00.
- [14] ISO 787-11 Norm ISO 787-11 . Allgemeine Prüfverfahren für Pigmente und Füllstoffe; Teil 11: Bestimmung des Stampfvolumens und der Stampfdichte, Oktober 1981.
- [15] DIN EN ISO 3167: Kunststoffe – Vielzweckprobekörper (ISO/FDIS 3167:2014) Deutsche Fassung FprEN ISO 3167:2014, Beuth Verlag GmbH, 2014.
- [16] Pengfei, N., Xiaojun, W., Baoying, L., Shengru, L., Jie, Y. 2011, Melting and nonisothermal crystallization behavior of polypropylene/hemp fiber composites, *Journal of Composite Materials*, vol. 46, no. 2, pp. 203-210.
- [17] Bogoeva-Gaceva, G., Janevski, A., Mader, E. 2001, Nucleation activity of glass fibers towards iPP evaluated by DSC and polarizing light microscopy, *Polymer* vol. 42, no. 9, pp. 4409-4416.

Spherical Blend PBT-PC Particles for Selective Laser Sintering

Manufacturing and Characterization

Maximilian A. Dechet, Juan S. Gómez Bonilla, Jochen Schmidt, Andreas Bück, Wolfgang Peukert*.
Institute of Particle Technology, Friedrich-Alexander Universität Erlangen-Nürnberg (FAU), Erlangen,
Germany, wolfgang.peukert@fau.de

Abstract—Polymer powder-based additive manufacturing technologies yield excellent mechanical and functional part qualities. One of these technologies is selective laser sintering (SLS), a process employing polymer particles, which are selectively fused by a laser. However, hardly any blend materials are available; mostly, the processing of multi-material systems via SLS is achieved by simply mixing different polymer powder materials. In this contribution, a novel approach to obtain spherical blend particles is introduced. Via co-grinding and subsequent rounding, manufacturing of spherical particles consisting of semi-crystalline polybutylene terephthalate (PBT) and amorphous polycarbonate (PC) thermoplastic is possible. The polymers are jointly comminuted and mixed in a planetary ball mill and the product particles are rounded in a heated downer reactor. PBT-PC composite particles are characterized regarding size and morphology via electron microscopy. Intermixing of the polymers is investigated via staining techniques and Raman spectroscopy. Furthermore, flowability and size distribution of the blend particles are examined. This way, we show the high potential of our process route for the production of novel polymer blend particle systems for SLS.

Keywords—additive manufacturing; selective laser sintering; spherical blend particles; polybutylene terephthalate; polycarbonate; SEM staining;

1. INTRODUCTION

The application of polymer-based technologies for additive manufacturing is steadily increasing. With technologies like fused deposition modeling, stereolithography or binder jetting, a wide variety of solid to flexible parts are becoming available [1]. However, if functional parts with excellent mechanical properties are needed, only few additive manufacturing technologies are feasible. Among these are mainly powder-based technologies like selective laser sintering (SLS) [2]. While nearly no boundaries regarding part design exist, there are quite some restrictions in the variety of commercially

available SLS materials. As of yet, the most widely used polymeric material for SLS is polyamide 12 (PA12) with a market share of roughly 90%. Other technologies, e.g. filament-based additive manufacturing, offer already a wide variety of different materials including blends and composites. In SLS however, hardly any blend materials are available; mostly, the processing of multi-material systems via SLS is achieved by simply mixing different polymer powder materials [3].

In this contribution, we present a novel process route to obtain spherical blend particles, based on co-grinding [4] and subsequent thermal rounding. As a blend system, polybutylene terephthalate (PBT) and bisphenol A-derived polycarbonate (PC) was selected, as the combination of a semi-crystalline (PBT) and an amorphous (PC) thermoplastic yields excellent mechanical properties. The PBT-PC blend combines the chemical and thermal resistance of PBT with the impact resistance and toughness of PC [5]. Most commercially available bulk material (granules) is mixed 50/50 (wt.%). While a transesterification reaction between the polymers upon melt mixing is well known [6,7], it is often deliberately inhibited, as the formation of the random copolymer impairs the blend properties [5].

The comminution of polymers often yields powders made up of irregular shaped particles [8] with a low bulk density and a bad flow behaviour, which cannot be processed efficiently in SLS machines. Flowability and packing density of the comminution product can be improved by a thermal process for shape modification, namely the thermal rounding in a downer reactor [9]. This process has been applied successfully e.g. for the rounding of grinded particles of polystyrene (PS) [9], polybutylene terephthalate (PBT) [10] or PBT/glass composite particles [11].

2. MATERIALS AND METHODS

2.1. Materials

Injection-grade PBT (Ultradur B 4520 HS, BASF, Germany) and injection-grade Bisphenol-A-based amorphous poly-carbonate (Makrolon 2405, Covestro, Germany) was used as feed material.

2.2. Experimental Methods

Co-grinding in a planetary ball mill

The feed material granules were pre-comminuted in a rotary impact mill (Pulverisette 14, Fritsch, Germany) operated with a pin rotor speed of 20000 rpm equipped with a 0.5 mm sieve ring, to obtain coarse powders of PBT and PC needed for the co-grinding step. Comminution and simultaneous intermixing of the pre-comminuted polymers was achieved using a planetary ball mill (Pulverisette 7 classic line, Fritsch, Germany), as these mills provide high energy input and are capable of mechanical alloying [12,13].

Grinding vessels (Yttria-stabilized zirconia) with 12 mL volume were equipped with 50 grinding balls (5 mm, Yttria-stabilized zirconia) of 5 mm size. Two vessels could be used in parallel and were filled with 1 g of each of the polymers. Co-grinding was performed at a rotational speed of 600 rpm. For each full revolution of the central “sun”, the grinding vessels, i.e. the “planets”, are rotated twice, leading to high stress energies. After 20 minutes of grinding, a waiting period of 2 minute was applied to allow the system to cool down, in order to avoid excessive thermal stressing of the polymers. The direction of rotation was changed after each pause. A size distribution suitable for SLS was achieved after 15 hours of total milling time (c.f. Figure 1 & 3).

Rounding of particles in a downer reactor

The downer setup is composed of a heated stainless steel pipe, an aerosol generator unit and a separation system to recover the rounded particles. The dried comminuted particles are dispersed in nitrogen (5.0, Linde) at 1 bar by means of a brush disperser unit (RGB 100, Palas GmbH, Germany). The aerosol is centrally fed into the head of the reactor. A nitrogen sheath flow is employed to reduce the interactions of the particles and the wall. The volumetric flow of the sheath gas is controlled by a mass flow controller (EL-Flow, Wagner Mess-und Regeltechnik, Germany). The sheath gas is homogeneously distributed over the downer cross-section surrounding the aerosol gas by means of a sintered metal plate (SIKA-R20, GKN Sinter Metals GmbH, Germany). Heating of the reactor is realized by a three-stage oven (Thermal technology GmbH, Germany). The temperature of the upper section is set above the melting point of the polymer. The function of this section is to heat the gas and the particles from room temperature to the melting point of the polymer. The temperature in the second section is set to the melting point of the polymer such that all

particles are in the molten state. The molten particles acquire progressively a spherical shape driven by the surface tension of the melt. In the third heating section, the temperature is set below the melting point of the material, such that the particles crystallize. The last cooling step is achieved at the lower unheated end of the reactor. Finally, the rounded particles are separated from the gas flow by means of a sintered metallic plate (SIKA-R20, GKN Sinter Metals GmbH, Germany). A detailed description of the geometry of the downer can be found elsewhere.[14]. The temperature profile at the center of the downer is measured by thermocouples (Typ K, TC Mess-und Regeltechnik GmbH, Germany) installed at 0, 1, 2, 3, 4, 5, and 6 m from the head of the downer

In the current investigation, the temperature of the three sections of the oven was set at 280°C, 230°C and 150°C ($T_{m,PBT} = 223^\circ\text{C}$) respectively. In order to investigate the influence of the volumetric flow rate of sheath gas on the process, it was varied between 3 (low flow rate) and 7 m³/h (high flow rate).

2.3. Characterization Methods

Laser diffraction particle sizing

Particle size distribution was determined by laser diffraction (Mastersizer 2000, Malvern Panalytical GmbH, Germany) the wet dispersing unit Hydro 2000. Before measuring, the powders were pre-dispersed in water with approximately 1g of SDS (sodium dodecyl sulfate, Merck, KGaA, Germany) and a few milliliters of ethanol (96%, denatured) in an ultrasonic bad for a few minutes. The wet measurements were carried out with a stirring rate of 3500 rpm and using the ultrasonic finger at 100% power.

Scanning Electron Microscopy (SEM)

Particle shape and surface morphology were characterized by scanning electron microscopy (SEM) (Gemini Ultra 55, Carl Zeiss AG, Germany) operated at an acceleration voltage of 1.0 kV. A SE2 detector was used for the imaging of unstained samples, while an InLense detector was used for stained samples.

Raman spectroscopy

Spectra were collected with a LabRAM HR Evolution Raman micro-spectrometer (Horiba, Japan) equipped with a frequency-doubled Nd-YAG laser ($\lambda = 532$ nm; grating 1800 gr/mm; 50X large working distance (LWD) objective) for Raman shifts between 100 cm⁻¹ and 3200 cm⁻¹.

Staining

Rounded samples were stained, in order to visualize the distribution of PBT and PC in the scanning electron microscopy. In general, SEM staining techniques are based on the differences in the diffusion speed of heavy atoms into different polymers. In our case, staining with

in-situ formed RuO₄, as described by Brown and Butler [15], based on the work by Trent [16], was applied.

3. RESULTS

3.1. Particle Shape and particle size distribution

A SEM picture of the co-comminuted PBT/PC after 15 h of comminution is shown in Fig 1. Co-comminuted blend particles have a flake-like, irregular shape and rough surface. Powders from such particles are characterized by a low flowability and packing density leading to problems in processing in SLS machines and may result in components with disadvantageous mechanical properties [17].

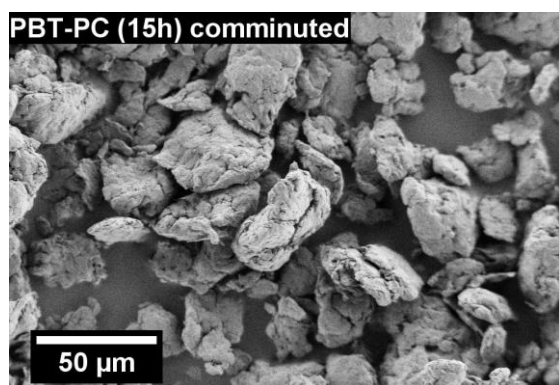


Figure 1. SEM image of co-grinded PBT-PC particles after 15 hours milling time in a planetary ball mill.

Figure 2 presents an SEM picture of the rounded product for the PBT/PC blend after 15 h of co-comminution. Independent of the volumetric flow rate of sheath gas, after rounding, the particles have predominantly a spherical shape and a smooth surface.

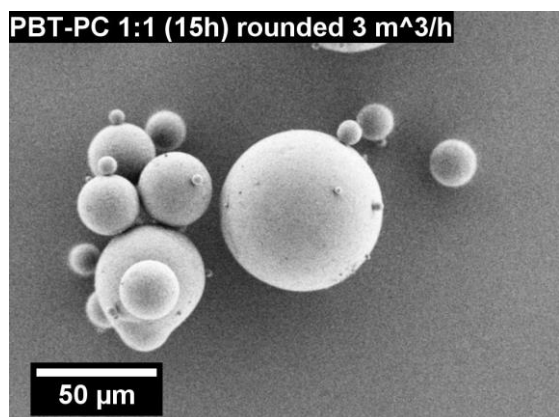


Figure 2. PBT-PC particles rounded with a volumetric sheath gas flow of 3 m³/h

The particle size distributions of the co-comminuted powders after 15 h process time are depicted in Figure 3 (black line). Powders with broad particle size distributions between 1 to 400 μm are obtained. After comminution, the powders have a bimodal particle distribution with two

maxima, with the first at approximately 3 μm and the second one at 25 μm.

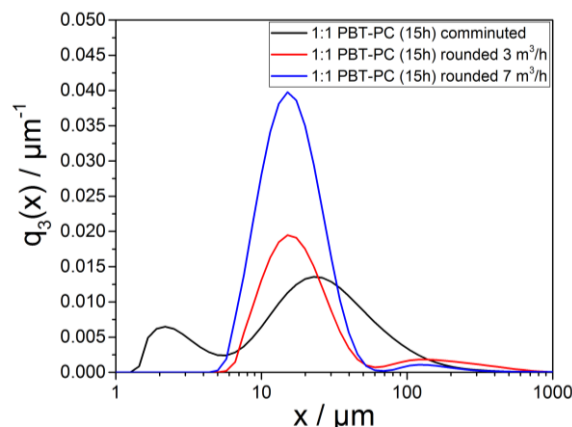


Figure 3. Particle size distribution of co-grinded (15h) and rounded PBT-PC particles

The effect of the rounding process on the particle size distribution can be observed in Figure 3, which presents the normalized volume-based particle size distribution q_3 . The peak at 3 μm disappears, the second peak moved toward lower values (20 μm approximately) and a peak appears at approximately 150 μm. According to these results, a fraction of particles of approximately 20 μm escapes the downer without agglomeration, while the rest of the agglomerates form the peak at 150 μm. This leads to a certain number of partially rounded agglomerates in the product. The fines fraction ($x < 10$ μm) agglomerates to bigger particles and disappears completely. The influence of the sheath gas on the particle size can also be observed in Figure 3. The high volumetric flow of 7 m³/h (blue line) reduces the agglomeration of particles in comparison to 3 m³/h (red line). This is due to the lower residence time of the particles in the downer at the higher volumetric flow of the sheath gas.

3.2. Vibrational spectroscopy

Identification of PBT and PC is possible based on their distinct Raman spectra. Both polymers show many identical bands in their spectra, due to their structural resemblance (e.g aromatic groups and carboxylate ester groups). However, the location of a few bands is unique for the respective polymer (e.g. the C-O and the C=O stretching bands), allowing precise identification. The C-O stretching band is located at 1280 cm⁻¹ and 1235 cm⁻¹ for PBT and PC, respectively. The C=O stretching band is located at 1720 cm⁻¹ for PBT and at 1775 cm⁻¹ for PC.

Investigation of the presence of both polymers in a single particle can be achieved by Raman micro spectroscopy, where the laser is focused through an objective (i.e. 50X LWD objective) onto a single micron-sized particle. A comparison of single particle Raman

spectra of the pure polymers, the particles after grinding and the rounded particles is depicted in Figure 4.

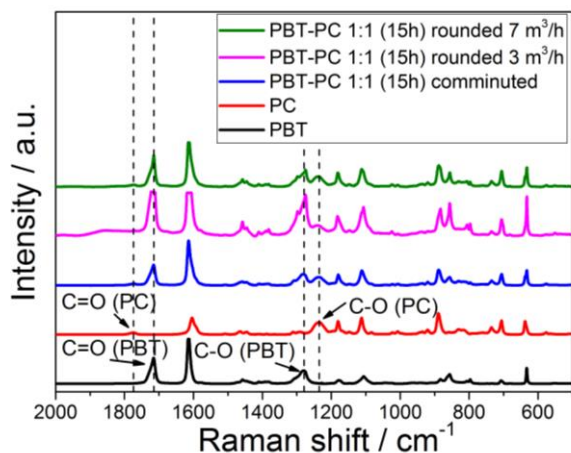


Figure 4. Raman spectra of pure PBT, pure PC, the comminuted blend particles and the blend particles rounded with 3 m³/h and 7 m³/h. The location of the specific C-O and C=O bands for PBT and PC is indicated by dashed lines.

As can be seen, the specific bands for the C-O and C=O stretching of PBT and PC both appear in the comminuted product, supporting the observation in Fig. 1, that intermixed PBT-PC blend particles are readily obtained after co-grinding in a planetary ball mill. While the C=O band of PC is intrinsically weak and therefore hard to identify, the respective C-O band of PC is much stronger and can be easily identified in the depicted spectra. Same holds for the strong C=O band of PBT. After the rounding process, no separation of the polymers can be observed; i.e. intermixed spherical PBT-PC blend particles with a size distribution suitable for SLS are obtained applying a process route based on dry co-grinding of both polymers and subsequent thermal rounding of the comminuted particles. In all the recorded spectra, no signs of significant transesterification of PBT and PC could be found [18].

3.3. SEM Staining

The rounded particles were stained with in-situ formed RuO₄, making it possible to differentiate both polymers based on their contrast in the SEM. The contrast is caused by the differing diffusion speed of the RuO₄ into the two polymers. The heavy ruthenium atoms induce more backscattered electrons, whereby, if a detector sensitive to backscattered electron (e.g. InLens) is used, a difference in contrast or brightness can be observed in areas with varying quantities of ruthenium. Based on preliminary staining experiments with comminuted PC and rounded PBT particles, an assignment of the polymers in relation to their contrast in SEM could be achieved. The PC appears bright, correlating to a higher quantity of ruthenium, while the PBT appears darker, indicating a lower quantity of ruthenium. In Figure 5 an ensemble of

stained rounded particles (3 m³/h), recorded using a SE2 and an InLens detector, is shown. The staining effect is visible in the images recorded with the InLens detector, clearly visualizing the bright PC and the darker PBT areas on the surface of single spherical particles.

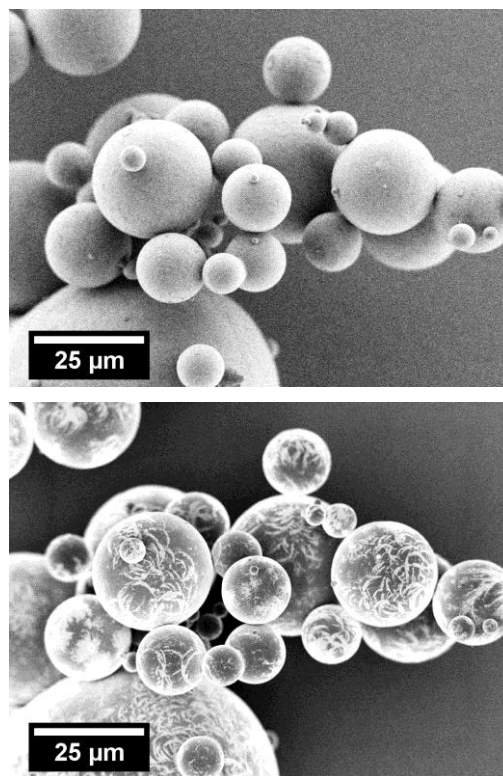


Figure 5. SEM images of stained spherical PBT-PC particles rounded with 3 m³/h. Top: SE2 detector. Bottom: InLens detector.

Upon closer inspection, as shown in Figure 6, some larger PC areas and many small crescent shaped PC areas are observable on the particle surface.

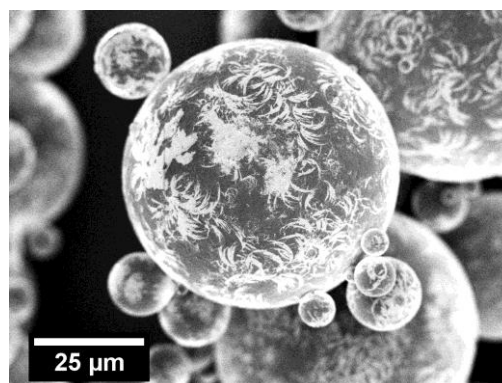


Figure 6. SEM image, recorded with an InLens detector, of a stained spherical PBT-PC blend particle.

Investigations of the stained particles are in agreement with the results of the vibrational spectroscopy, leading to the conclusion, that we were able to manufacture

intermixed spherical PBT-PC particles by applying a process route consisting of dry co-grinding and thermal rounding in a downer reactor.

4. SUMMARY AND CONCLUSIONS

In this contribution, an approach to obtain spherical intermixed PBT-PC particles with a size distribution suitable for selective laser sintering was presented. The intermixing could be achieved by comminution and simultaneous mechanically alloying of the polymers in a planetary ball mill. The subsequent shape control, i.e. rounding, could be performed by introducing the particles to a heated downer reactor operated with a well-defined laminar sheath gas flow. A grinding time of 15 hours led to a particle size distribution well suited for SLS applications, while the rounding with 3 m³/h or 7 m³/h ensured spherical shape of the particles. Characterization of the obtained particles after comminution, as well as after rounding, with Raman micro spectroscopy shows, that PBT and PC are present in single particles already after comminution. Finally, the presence of both polymers in the rounded particles was made directly observable in the SEM by applying a staining technique.

ACKNOWLEDGMENT

This study has been supported by Deutsche Forschungsgemeinschaft (DFG) in the framework of the collaborative research center CRC 814 “Additive Manufacturing” (project A3 and A2). Financial support is gratefully acknowledged.

REFERENCES

[1] I. Gibson, D. Rosen, B. Stucker, Additive manufacturing technologies, 2. ed., Springer, New York, NY, 2015.

[2] B. Wendel, D. Rietzel, F. Kühnlein, R. Feulner, G. Hülder, E. Schmachtenberg, Additive processing of polymers, *Macromol. Mater. Eng.* 293 (2008) 799–809. doi:10.1002/mame.200800121.

[3] D. Drummer, K. Wudy, F. Kühnlein, M. Drexler, Polymer Blends for Selective Laser Sintering: Material and Process Requirements, *Phys. Procedia.* 39 (2012) 509–517. doi:10.1016/j.phpro.2012.10.067.

[4] J. Schmidt, S. Romeis, W. Peukert, Production of PBT/PC particle systems by wet grinding, in: *AIP Conf. Proc.*, AIP Publishing LLC, 2017: p. 050003. doi:10.1063/1.5016720.

[5] J.M.R.C.A. Santos, J.T. Guthrie, Polymer blends: the PC–PBT case, *J. Mater. Chem.* 16 (2006) 237–245. doi:10.1039/B502036K.

[6] I. Hopfe, G. Pompe, K.J. Eichhorn, L. Häußler, FTIR spectroscopy of PC/PBT melt blends: Influence of crystallite

morphology and copolyester content, *J. Mol. Struct.* 349 (1995) 443–446. doi:10.1016/0022-2860(95)08804-5.

[7] S.B. Tattum, D. Cole, A.N. Wilkinson, Controlled Transesterification and Its Effects on Structure Development in Polycarbonate–Poly(Butylene Terephthalate) Melt Blends, *J. Macromol. Sci. Part B.* 39 (2000) 459–479. doi:10.1081/MB-100100399.

[8] J. Schmidt, M. Plata, S. Tröger, W. Peukert, Production of polymer particles below 5µm by wet grinding, *Powder Technol.* 228 (2012) 84–90. doi:10.1016/j.powtec.2012.04.064.

[9] J. Schmidt, M. Sachs, C. Blümel, B. Winzer, F. Toni, K.-E. Wirth, W. Peukert, A novel process route for the production of spherical LBM polymer powders with small size and good flowability, *Powder Technol.* 261 (2014) 78–86. doi:10.1016/j.powtec.2014.04.003.

[10] J. Schmidt, M. Sachs, S. Fanselow, M. Zhao, S. Romeis, D. Drummer, K.E. Wirth, W. Peukert, Optimized polybutylene terephthalate powders for selective laser beam melting, *Chem. Eng. Sci.* 156 (2016) 1–10. doi:10.1016/j.ces.2016.09.009.

[11] J. Schmidt, J. Gómez Bonilla, M. Sachs, L. Lanzl, K. Wudy, K.-E. Wirth, D. Drummer, W. Peukert, Production of polybutylene terephthalate glass composite powders and characterization for processing in selective laser sintering, in: *Proc. 26th Annu. Int. Solid Free. Fabr. Symp.*, 2016: pp. 989–997.

[12] M. Abdellaoui, E. Gaffet, The physics of mechanical alloying in a planetary ball mill: Mathematical treatment, *Acta Metall. Mater.* 43 (1995) 1087–1098. doi:10.1016/0956-7151(95)92625-7.

[13] P.P. Chattopadhyay, I. Manna, S. Talapatra, S.K. Pabi, Mathematical analysis of milling mechanics in a planetary ball mill, *Mater. Chem. Phys.* 68 (2001) 85–94. doi:10.1016/S0254-0584(00)00289-3.

[14] M. Sachs, J. Schmidt, W. Peukert, K.-E. Wirth, Design and scale-up of a semi-industrial downer-reactor for the rounding of irregular polymer particles, in: *AIP Conf. Proc.*, AIP Publishing LLC, 2016: p. 070003. doi:10.1063/1.4942289.

[15] G.M. Brown, J.H. Butler, New method for the characterization of domain morphology of polymer blends using ruthenium tetroxide staining and low voltage scanning electron microscopy (LVSEM), *Polymer (Guildf).* 38 (1997) 3937–3945. doi:http://dx.doi.org/10.1016/S0032-3861(96)00962-7.

[16] J.S. Trent, Ruthenium tetraoxide staining of polymers: new preparative methods for electron microscopy, *Macromolecules.* 17 (1984) 2930–2931. doi:10.1021/ma00142a087.

[17] S. Dadbakhsh, L. Verbelen, T. Vandeputte, D. Strobbe, P. Van Puyvelde, J.-P. Kruth, Effect of Powder Size and Shape on the SLS Processability and Mechanical Properties of a TPU Elastomer, *Phys. Procedia.* 83 (2016) 971–980. doi:10.1016/J.PHPRO.2016.08.102.

[18] M. Pellow-Jarman, P. Hendra, M.J. Hetem, Poly(butylene terephthalate) polycarbonate transesterification: monitoring its progress with Fourier transform Raman spectroscopy, *Spectrochim. Acta Part A Mol. Biomol. Spectrosc.* 51 (1995) 2107–2116. doi:10.1016/0584-8539(95)01472-3.

Cork-based filaments for Additive Manufacturing

The use of cork powder residues from stoppers industry

T. Antunes, Department of Materials and Ceramic Engineering, Aveiro Institute of Materials (CICECO) University of Aveiro, tatiana.antunes@ua.pt

S. P. Magalhães da Silva, School of Design, Management and Production Technologies, Aveiro Institute of Materials (CICECO), University of Aveiro, Oliveira de Azeméis, Portugal, sarapms@ua.pt

M. E. V. Costa, Department of Materials and Ceramic Engineering, Aveiro Institute of Materials (CICECO) University of Aveiro, elisabete.costa@ua.pt

J. M. Oliveira, School of Design, Management and Production Technologies, Aveiro Institute of Materials (CICECO), University of Aveiro, Oliveira de Azeméis, Portugal, martinho@ua.pt

Abstract— An increasing demand is arising for new additive manufacturing (AM) materials seeking for improved surface finishes, higher mechanical performance and more versatile properties. The present work intends to present a green composite material solution for fused filament fabrication (FFF), an AM technology. This solution consists on the combination of cork powder residues and biodegradable polymeric matrices based on functionalized polylactic acid (PLA). This work also provides a comparative study between the mechanical behaviour of FFF printed specimens and injected specimens. The mechanical properties of the printed specimens are promising results while indicating that the unique combination of cork properties is maintained.

Keywords – cork; additive manufacturing; cork-polymer composites (CPC); green composites; filaments

1. INTRODUCTION

Industry is constantly seeking for processes that allow an effective reduction of the product development time allied with a sustainable use of materials. The incorporation of lignocellulosic materials in biopolymers has become an effective approach to develop new sustainable materials. Biodegradable polymers offer a complete degradation at ambient conditions, without toxic compounds emissions. Polylactic acid (PLA) is one of the most promising biopolymers, since it is produced from annually renewable available resources and the industrial technology needed for its processing is relatively low cost, when compared to petrol-based plastics [1], [2].

Cork stoppers industrial production generates about 30 wt % of low granulometric cork powder residues [3]. In Fig. 1 it is displayed an overview of cork stoppers production.

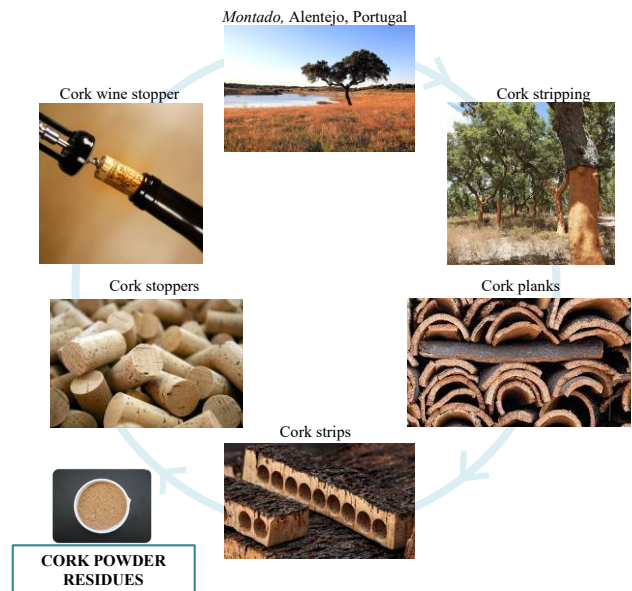


Figure 1. Overview of cork stoppers production.

Cork is a natural, versatile and sustainable material, being an emblematic material in Portugal. It is the outer bark of the oak tree *Quercus suber* L. and its main chemical composition is based on suberin (33-50%), lignin (20-25%), polysaccharides (12-20%) and extractives (14-18%). It presents tiny hollow cells of hexagonal shape in a closed-cell foam, similar to a honeycomb structure [4]. The combination of its chemical composition with its honeycomb structure leads to a unique set of properties, including low density, high recovery after impact and thermal and acoustic insulation, among others. [4].

Considering the actual technological demand for new materials in additive manufacturing (AM), the

development of cork-polymer composites (CPC) is envisaged to open new horizons in AM. The use of CPC filaments for Fused Filament Fabrication (FFF) can potentiate new design freedom solutions and products through the combination of cork unique properties and aesthetics. FFF is an AM technique based on an extrusion process, in which a thermoplastic filament is melted and selectively extruded via nozzle, deposited layer by layer [5].

The present study aims to explore the mechanical properties of the CPC printed parts and compare the results with similar parts obtained by injection moulding. Furthermore, in this study, PLA was functionalized with maleic anhydride (MA) in order to improve the interfacial adhesion of cork powder to the polymeric matrix.

2. MATERIALS AND METHODS

2.1. Cork

Cork powder residues from a Portuguese cork producer were used. The as-received material was fractionated through sieving (Retsch, Germany) using a vibrational sieve shaker. The amplitude used on sieve shaker was 70. Four sieves mesh size were used, namely 100 (0.42), 80 (0.28), 63 (0.18) and 40 (0.15) μm . Values in brackets correspondent to the mesh values in mm. The particle size distribution (PSD) was determined by measuring the powder retained in each sieve and determining the cumulative curve, as described in Fig. 2.

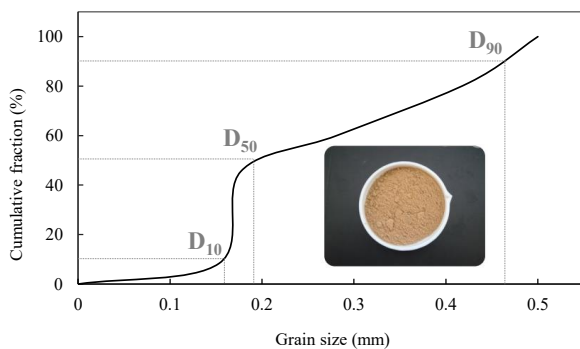


FIGURE 2. Cumulative curve of cork powder.

The cumulative curve corresponds to the average of 3 trials. Through Fig. 2, it is seen that 10% of the sample has an average size equal or smaller than 40 μm .

For the composite preparation, the cork powder retained in the 40 μm sieve was used. The reason for the selection of this particle size was related to the typical nozzle size of an FFF extrusion system.

The average pore diameter as well as the bulk density of cork powder were determined by mercury intrusion porosimetry. The experiment was conducted in a Micromeritics Auto-pore IV 9500 apparatus. Cork powder was dried in vacuum oven (70 $^{\circ}\text{C}$) for 24 h, evacuated to 0.1Pa. Mercury was then forced to enter the pores under the

pressure from 0.3 MPa to 227 MPa. Density and average cork density values are presented in Table 1.

TABLE I. Cork powder properties.

	Cork Powder
Average pore diameter (μm)	23.3
Bulk density (g/cm^3)	0.1555
Apparent Density (g/cm^3)	0.69
Porosity (%)	77.6

2.2. Polymeric Matrices

An IngeoTM biopolymer PLA 4032D purchased from NatureWorks with a stereoisomer composition of 1.2-1.6 % D-isomer lactide was used. It presents a melting point between 155-170 $^{\circ}\text{C}$ and a melt flow index (MFI) of 4.60 g/10 min (190 $^{\circ}\text{C}$, 2.16 Kg). A functionalized PLA with MA was used and it was prepared by melt functionalization. The selected MAgPLA formulation was based on a Taguchi design experiment (study not shown).

2.3. Composites formulation

Before compounding, the cork powder and the PLA were dried at 70 $^{\circ}\text{C}$ during 24 h in a vacuum oven (Carbolite AX60 model), to remove the moisture content. CPC formulations were prepared using a Brabender type internal mixer. Initially, PLA and MAgPLA were charged and melted at 190 $^{\circ}\text{C}$, during 2 min at 40 rotations per minute (rpm), and then cork powder was added for additional 8 min. After compounding, the mixture was granulated in a Dynisco granulator into small granules. Table II shows the formulation composition.

TABLE II. CPCs formulation composition.

Samples	PLA (wt %)	Cork (wt %)	MAgPLA (wt %)
CPC	81	15	4

In terms of volume, it corresponds to 45 vol % of polymeric matrix and 55 vol % of cork powder, respectively.

2.4. Filament production

CPC filament was prepared using a 3Devo NEXT 1.0 extruder with the conditions exhibited in Fig. 3.

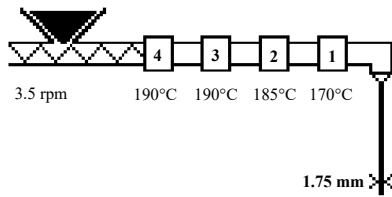


FIGURE 3. Filament extrusion conditions.

Filament thickness of 1.75 mm was obtained with a tolerance deviation of 5 μm.

2.5. FFF printing conditions

The composite filaments were printed into specimens according the standard ISO 527-2:1996 (specimens type IV). A Delta WASP 3D printer was used with a stainless steel nozzle with 0.4 mm diameter. The printing head was set at the rate of 40 mm/s. The nozzle temperature was set at 190°C. Double-sided tape was used as a printing substrate with the printing bed temperature set at 40°C to prevent the printed material from warping. Concentric infill pattern with a layer height of 0.06 mm and a fill percentage of 100% were chosen. The G-code was generated by Cura software. Fig. 4 shows images of the specimens printing process and the obtained printed specimens.

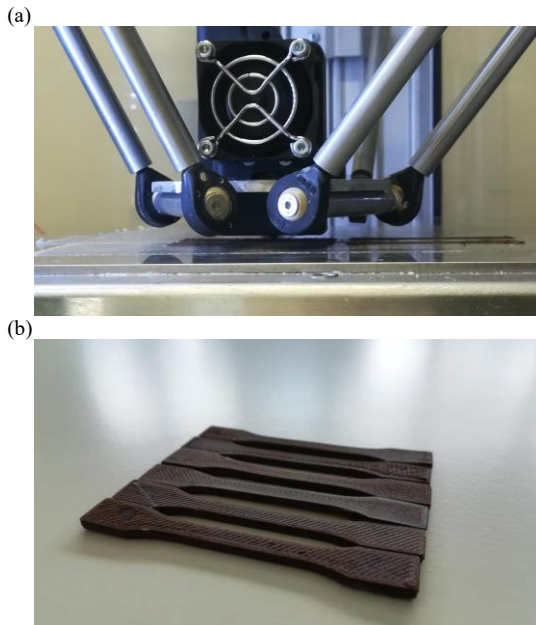


FIGURE 4. Images of (a) specimens printing process and (b) obtained specimens.

2.6. Mechanical analyses

Mechanical tests were performed on a universal testing machine Autograph AG-IS (Shimadzu) with a 10kN load cell with a constant crosshead speed of 1 mm/min. All measurements were done at ambient temperature and the results here reported are averaged values of at least six samples.

A comparative analysis between printed and injected specimens was performed. The injected specimens were prepared using a Babyplast 610P with the conditions presented in Table III. The mould cavity was designed considering the standard ISO 527-2:1996 for the preparation of specimens type IV.

TABLE III. Injection moulding conditions.

	Conditions
Temperature profile (°C)	180-185-190
Injection pressure (bar)	130
Second injection pressure (bar)	100

3. RESULTS AND DISCUSSION

3.1. Mechanical Analyses

The stress-strain curves of i-PLA and the average curves for i-CPC and p-CPC are presented in Fig. 5. Note that i-PLA represents the injected PLA, and i-CPC stands for the injected CPC specimens, while p-CPC is related to the printed CPC specimens. The tensile properties of these materials and its standard deviations, including tensile strength, maximum strain and Young modulus are given in Table IV.

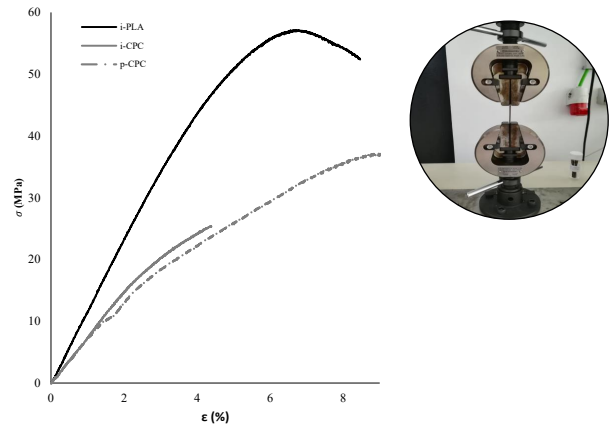


FIGURE 5. Tensile stress-strain curves of pure i-PLA, i-CPC and p-CPC.

Pure i-PLA exhibited higher tensile strength when compared to composites, and also showed its brittle behaviour. The addition of cork led to the reduction of tensile strength. i-CPC presented a ≈54% reduction of tensile strength against the ≈37% shown by p-CPC.

TABLE IV. Tensile properties of pure i-PLA, i-CPC and p-CPC.

Samples	σ_{max} (MPa)	ϵ_{max} (%)	E (MPa)
i-PLA	55.4 (2.2)	8.8 (1.2)	1110.9 (40.3)
i-CPC	25.7 (1.4)	4.4 (0.6)	743.5 (26.4)
p-CPC	34.8 (1.2)	7.8 (0.1)	790.2 (32.7)

This reduction can be due to the lower mechanical properties of cork as compared with pure PLA. It is known that other mechanisms can also influence the mechanical behaviour of CPC, namely (1) type of matrix; (2) compatibility between polymeric matrix and cork and (3) cork content, dispersion within the matrix and homogenization [6]. In relation to the compatibility, 4 %wt of compatibilizing agent was used in this study. Nevertheless, a study concerning the optimal amount of MAGPLA added to PLA is running. Insufficient or excess amount of MAGPLA can result in lower mechanical properties caused by the lack of interaction of MAGPLA with cork powder, resulting on the disruption of PLA matrix [7]. The maximum strain also decreased when cork was added. This reduction is more significant for the injected specimens. Additionally, it was observed a decrease in Young modulus when cork was present. This can be attributed to the lower stiffness and to the foamed structure of cork, which exhibits a lower Young modulus when compared to neat biopolymers.

On the other hand, comparing both CPCs, it can be seen that the printed specimens revealed a higher mechanical performance. This result might indicate that the pressure applied during the injection moulding process has more impact on CPC mechanical properties than the very low pressure associated with the 3D printing process. More specifically, the pressure applied compresses the honeycomb cork structure. Morphological analyses to evaluate the surface fracture of specimens are now ongoing.

4. CONCLUSIONS

A functionalized CPC was prepared with 4 % wt of MAGPLA. Tensile properties were determined for the FFF

printed parts and compared with similar parts obtained from injection moulding technology. From this study, it can be concluded that the presence of cork resulted in a decrease on mechanical properties when compared with pure PLA. The addition of MAGPLA to the polymeric matrix was done to decrease the gap between the pure matrix and CPC mechanical behaviour.

An interesting observation was perceived when comparing the behaviour of both the printed and the injected specimens. The mechanical properties of the printed specimens are promising results while indicating that the unique combination of cork properties is maintained.

ACKNOWLEDGMENTS

THIS WORK WAS SUPPORTED BY COMPETE 2020 – PROGRAMA OPERACIONAL COMPETIVIDADE E INTERNACIONALIZAÇÃO WITHIN TT@ESAN PROJECT (NORTE-01-0246-FEDER-000001).

REFERENCES

- [1] V. K. Thakur, 2015, *Lignocellulosic Polymer Composites: Processing, Characterization and Properties*. Scrivener Publishing, Wiley, New Jersey.
- [2] J. P. Greene, 2014, *Sustainable Plastics: Environmental Assessments of Biobased, Biodegradable, and Recycled Plastics*. New Jersey: John Wiley & Sons, Inc., New Jersey.
- [3] E. M. Fernandes, I. M. Aroso, J. F. Mano, J. A. Covas, and R. L. Reis 2014, 'Functionalized cork-polymer composites (CPC) by reactive extrusion using suberin and lignin from cork as coupling agents', *Composites Part B Engineering*, vol. 67, pp. 371–380.
- [4] H. Pereira, 2017, *Cork: Biology, Production and Uses*. Elsevier, Amsterdam.
- [5] S. B. Gibson I, Rosen D, 2015, *Additive Manufacturing Technologies: 3D Printing, Rapid Prototyping, and Direct Digital Manufacturing*, 2nd ed., Springer, New York.
- [6] E. M. Fernandes, V. M. Correlo, J. F. Mano, and R. L. Reis 2015, 'Cork-polymer biocomposites: Mechanical, structural and thermal properties', *Materials and Design*, vol. 82, pp. 282–289.
- [7] M. E. González-López, J. R. Robledo-Ortiz, R. Manríquez-González, J. A. Silva-Guzmán, and A. A. Pérez-Fonseca 2018, 'Polylactic acid functionalization with maleic anhydride and its use as coupling agent in natural fiber biocomposites: a review', *Composite Interfaces*, pp. 1–24.

ICAT 2018

